Theoretical and experimental study of the behaviour at service and failure of partially prestressed concrete beams under flexure and shear

PHD Dissertation

Doctoral Thesis by:

Ulric Celada Blesa

Supervisors:

Prof. Jesus Miguel Bairán García

Prof. Eva Oller Ibars

Barcelona, October 2019

Universitat Politècnica de Catalunya, Barcelona Tech

Doctorat en Enginyeria de la Construcció

Departament d´Enginyeria Civil i Ambiental

Escola Tècnica Superior d'Enginyers de Camins, Canals i Ports de Barcelona

UNIVERSITAT POLITÈCNICA DE CATALUNYA

Theoretical and experimental study of the behaviour at service and failure of partially prestressed concrete beams under flexure and shear

Author:

Ulric Celada Blesa

Supervisors:

Jesús Miguel Bairán García

Eva Oller Ibars

Ph.D. Program:

Doctorat en Enginyeria de la Construcció

Barcelona, October 2019

Universitat Politècnica de Catalunya, Barcelona Tech

Departament d'Enginyeria Civil i Ambiental

Acknowledgments

I would like to start thanking Dr. Anonio R. Marí and Dr. Jesús M. Bairán for the confidence they placed in me in 2014, when they presented to me the opportunity of doing a PhD research over a very interesting topic. They have always trusted me and gave me all the resources I needed.

Dr. Jesús M. Bairán has been my supervisor and mentor since before starting this journey. He has always helped me and guided me; supporting my ideas and giving me advices to accomplish the different goals of this thesis. Although, he has allowed me to explore very different topics, he was always able to discuss the discoveries and present with refreshing approaches to solve the problems found in this investigation.

Dr Eva Oller has helped me to develop this thesis and has been a crucial support to the writing and correcting of this document. I am truly thankful for her time and dedication to correct this document.

Special thanks to my colleague and officemate Noemí Duarte. From the first day she has been a wonderful colleague, helping me with any doubt (even the most ridiculous ones) and especially when I broke my leg and she took over my experimental campaign and had to do the heavy lifting for several tests. Her company and discussions has been a vital part of this thesis.

To all the technicians of the lab, especially to Carlos Hurtado, without whom the experimental campaign could not have been done. Remembering all the trips and lunches we had still makes me smile. Thank you for all your support while performing the experimental campaign and during my stay in the UPC.

Such a huge campaign could not have been possible without the help of: Carlos, Noemí, Tomás, Gerard, Sandra, Gerardo, Luis, Noa, Jordi and Robert. Thanks to all of you for helping me instrument, build or tests que beams of this thesis.

I would like to thanks also Dr Yuguang Yang and Dr Dick Hordijk for accepting me into their department in TU Delft. This exchange was very important to me and they made me feel very welcomed. One of the best experiences of my academic and personal life.

I would like to express my gratitude to the Ministerio de Economía y Competitividad for granting me a pre-doctoral grant from the Plan Estatal de Investigación Científica y Técnica y de Innovación 2013-2016 (BIA2012-36848). To VSL for donating all the prestress components, to BASF for the injection material and to Norden, Prainsa for they work with the construction and casting of the beams.

To all my friends, without whom this PhD journey could not have been possible. To all those moments when, even without noticing it, they recharged my energies to go up against this task.

To Lara, we started this journey only two years ago but I feel this is how I want to keep going forever. You really helped me finish this project and I am thrilled to start the next project with you.

A mis padres, los verdaderos héroes de esta historia. Derrochando amor sin pedir nada a cambio y haciendo posible que haya llegado hasta aquí.

Abstract

Partially Prestressed Concrete (PPC) is an intermediate design approach between reinforced and totally prestressed concrete, that enables controlled cracks in service phase. Conversely, totally prestressed concrete is design to prevent cracks in service. This design strategy can be useful for structural optimization, as allows for more freedom in the variation of stiffness, crack opening, stress level and resistance. This technique has been studied during the past decades. However, its extensive use has been limited due to the lack of methodologies to control the crack width. This thesis aims to analyse the behaviour of PPC under flexural and shear forces.

In this research, the behaviour of PPC elements in bending and shear is investigated through an experimental campaign of sixteen tests. The specimens were design to represent the webs of a girder box bridge, hence the I section of the beams. From the sixteen tests, twelve studied the shear behaviour of PPC beams and the influence of web width, prestress ratio, stirrup ratio and lay out. The remaining tests were four-point bending tests. The aim of these tests was to evaluate the flexural behaviour at service and failure by changing the prestress and longitudinal reinforcement ratios.

For each test, the loading protocol performed cyclic loads to analyse the evolution of the behaviour of the specimens at service. The cycles presented three steps corresponding to quasi-permanent, frequent and characteristic load level. Each step was used to analyse and compare the evolution of the main parameters that characterise the behaviour of the beams. After the cycles, the load was monotonically increased until failure.

Several models have been presented to explain the shear resistance mechanism for sections with flanges, with very different results. The Compression Chord Capacity Model (CCCM) presented the best predictions for this experimental campaign.

A photogrammetric technique was developed to analyse the shear crack pattern. This technique obtains from the pictures the crack spacing, the crack angle and the crack width. With this tool, an equation to predict the $\cot\theta$ at service and failure was obtained. The equation relates the angle of the cracks with the ratio between compression due to prestress and tensile strength and the ratio of stirrups. This technique allowed to obtain the influence of the reinforcements over the crack shear width.

A model to predict the average shear crack width in service was developed using the average strain of the stirrups, the experimental crack spacing and the angle of the cracks. Strains were calculated taking into account the shear contribution of the stirrups.

From the experimental results, it was evidenced that in the shear tests at service, the strains in the stirrups were over the yielding threshold. Therefore, the shear cracks were large. Meanwhile the strains in the four-point bending tests only reached the yielding level in failure, being stable for the service part of the test.

Resumen

El Hormigón Parcialmente Pretensado (HPP) es una estrategia de diseño intermedia entre el hormigón armado y el pretensado total el cual permite la fisuración controlada en fase de servicio; en contraposición, el hormigón totalmente pretensado se dimensiona para evitar la fisuración en servicio. Esta estrategia de diseño puede ser de gran utilidad para la optimización estructural, ya que permite una variación gradual en la rigidez, apertura de fisura, niveles tensionales y resistencia. Esta técnica ha sido estudiada durante décadas; sin embargo, su uso extensivo se ha visto limitado por la falta de metodologías para controlar el ancho de fisura. Esta Tesis busca analizar el comportamiento del HPP sometido a esfuerzos de flexión y cortante.

En esta investigación, se estudia el comportamiento de elementos de hormigón parcialmente pretensado, a flexión y cortante, mediante un estudio experimental de dieciséis ensayos. Los especímenes fueron diseñados para representar las almas de puentes en cajón, de ahí la sección en doble-T de las vigas. De los dieciséis ensayos, doce estudiaron el comportamiento a cortante del HPP y la influencia del ancho del alma, el grado de pretensado, la cuantía de armadura transversal y el trazado del pretensado. El resto de casos fueron ensayados a flexión. El objetivo de estos últimos casos fue evaluar el comportamiento a flexión, en servicio y rotura, con diferentes cuantías de armadura pasiva y activa.

Para analizar el comportamiento en servicio, el protocolo de carga constaba de ciclos de carga. Los ciclos recorrían tres niveles de carga, casi-permanente, frecuente y característico. En cada nivel se analizó y comparó la evolución de los principales parámetros para caracterizar el comportamiento de las vigas. Después de los ciclos, se aplicó una carga monotónica hasta rotura.

Se analiza la bondad de diferentes modelos de resistencia a corte para el caso de elementos pretensados con alas comprimidas. De entre los diferentes modelos estudiados, el modelo de "Capacidad de Cordón Comprimido" o *"Compression Chord Capacity Model"* (CCCM) presentó las mejores predicciones para esta campaña experimental.

Así mismo, se desarrolló una técnica fotogramétrica para analizar el patrón de la fisuración a cortante. Esta técnica permite obtener de las imágenes la separación entre fisuras, el ángulo de las fisuras y el ancho de fisura. Esta herramienta permitió generar una ecuación para predecir la $\cot\theta$ en servicio y rotura. La ecuación relaciona el ángulo de las fisuras con las tensiones de compresión en el hormigón por el pretensado y su resistencia a tracción y la cuantía de armadura transversal. Con esta técnica se obtuvo la influencia entre los estribos y el ancho de las fisuras a cortante.

Posteriormente, se propuso un modelo para predecir el ancho medio a cortante en servicio, usando la deformación media de los estribos, la separación entre fisuras y la inclinación de las fisuras. Las deformaciones se calcularon teniendo en cuenta la contribución a cortante de los estribos.

De los resultados experimentales se concluye que, para los ensayos a cortante, las deformaciones en los estribos superan la deformación de plastificación en servicio. Lo que conlleva a grandes oberturas de fisura. Mientras que las deformaciones en la armadura longitudinal de los ensayos a flexión solo llegan a la deformación de plastificación en rotura, manteniendo deformaciones controladas en servicio.

Table of Contents

List of tables

List of figures

1 Introduction

1.1 General introduction

With the actual situation of the global economy, the optimization of structures has become of paramount importance. Developing and perfecting efficient building methods allows saving important resources. Partially prestressed concrete (PPC) is a known methodology that allows to reduce the use of materials maintaining the performance level of the structures.

PPC is prestressed concrete that allows decompression on the concrete and the generation of cracks during the service loads. Therefore, the prestressing loads, the area of prestressing reinforcement or the concrete section can be reduced respect a more classical approach to prestressed concrete. Multiple combinations of ordinary and prestress reinforcement can be defined to resist the service and failure loads. The optimization of the reinforcements minimises the cost and the use of resources.

Allowing cracks to appear in service means that the PPC analysis has to be non-linear. The non-linearity has presented several problems to the engineering world, since the design. Nowadays, there is no consensus on specific criteria to design PPC. Each approach uses different assumptions, providing different solutions. Moreover, the existing codes do not present solutions to aspects directly related to the design of PPC.

The range of PPC uses is very suitable for large structures such as bridges, in particular precast girder bridges. These girders usually are T or I shaped to reduce self-weight, maintaining the shear and bending resistance. The shear resistance of this kind of girders has been underestimated when applying the existing codes. The formulations do not take into account correctly the concrete in the flanges of the compression chord.

Since shear failures are more brittle than flexural failures, the safety margin for shear has always been larger. Nonetheless, the underestimation of shear resistance for T-shaped concrete beams by the codes is too important and new formulations, which consider the flange contribution to the shear resistance, have significantly improved the shear strength assessment.

1.2 Motivation

The limitations for PPC in the codes are the maximum crack width that can appear in service. This is a durability criteria and does not take into account the origin of the cracks. The cracks are originated by normal or shear stresses. The codes have formulations to predict the crack width for normal stresses using the crack spacing and a mean value for the reinforcement strain along this length. Not all the formulations agree on the definition of the crack spacing, resulting on different results. Only a very few number of codes present a formulation to calculate the crack width of shear cracks. These cracks are not perpendicular to the reinforcements and show a different behaviour compared with normal cracks.

There is no consensus on the formulation to calculate the diagonal cracking (distribution and width). Several formulations have been presented but with very different results. The formulations use the same approach used in normal stresses, the crack spacing and strains. Each formulation uses different parameters, which entails to a wide range of results.

Cracks are discrete elements that change significantly the strain and stress state of all the surrounding materials. Even if the conditions that generate cracks are very simple (tensile stress of the concrete superior to its tensile resistance), it is very complicated to predict the exact position where they are going to appear. Moreover, pre-existing cracks will affect the strain and stress distribution of the element, affecting the appearance of new cracks. Diagonal cracks are more complicated than flexural cracks because they can appear in mid-high of the web and their angle is unknown.

Obtaining the crack properties from experimental tests has been a very complicated task. Locating properly the instrumentation was not possible and the evolutionary character of the cracks implied its properties changed during the tests. Methods that analysed a region of the beam have been developed but can be dangerous to use when the specimens are under important loads and are very time consuming. Even though, these methods do not obtain the crack patterns.

In civil engineering research area, several methods involving the use of digital cameras have been developed to obtain trough pictures, information to characterise the behaviour of the specimen. The most important method has been Digital Image Correlation (DIC), which has not been used extensively due to its very significant cost. New methods can be developed to acquire relevant information from tests to study shear cracking patterns specifically.

In PPC beams, the interaction between the shear strength component due to the capacity of the compression chord and the influence of the prestress has to be analysed to present a reliable formulation to obtain the shear capacity of this type of structures.

Therefore realizing an experimental campaign of PPC beams with I section to study their behaviour in shear and bending moment tests, focusing in their resistance, behaviour and the crack pattern could provide with important information to clear up some of the unknowns. The use of new technologies would allow to obtain more information from the tests, to use for the analysis.

1.3 Objectives

The main goal of this study is to analyse the behaviour and performance of PPC beams with an I-shaped section under bending and shear stresses in service and failure.

To achieve this main objective, specific objectives were targeted:

- Analyse the influence of cracks in cyclic load and how the response of the beam evolves.
- Compare different shear formulations with the experimental results and obtain the best approach.
- Analyse the shear pattern of diagonal cracking to finally obtain a formulation to predict the crack width.
- Develop a software to obtain the crack width of experimental campaigns.

1.4 Structure of the thesis

This document is divided in seven chapters. Chapter 1, “Introduction”, presents the PPC which can optimize the reinforcements used in regular prestressed structures to obtain cheaper and sustainable structures. In addition, this chapter presents the research motivation and the main and specific objectives of this work.

The second chapter summarises the state-of-the-art related to PPC, shear capacity of concrete structure and crack width. Some design criterion for PPC are presented as well as the non-linear Magnel diagram. A new approach for shear resistance taking into account the influence of the flanges in the compression chord with an analytical model. It also presents the formulations used for normal and shear cracking to calculate the crack spacing and crack width.

In the third chapter, the experimental campaign is described. Geometry and material properties of each beam set as well as instrumentation are presented. In addition, the different test set-ups to perform both shear tests and four-point bending tests are described. The load protocol to analyse the effect of cycling loads and the effect on the PPC are also described.

The fourth chapter gives a discussion of the results obtained in the four-point bending tests. This chapter is divided in two sections: failure and service results analysis. In this chapter the influence of the cyclic loads are analysed as well as ductility and damping of PPC.

The fifth chapter presents the results of the twelve shear tests. It is also divided between failure and serviceability. When analysing the ultimate limit state, failure modes are discussed and failure loads are compared with the different existing models. A relationship between the prestressing area, the transversal reinforcement and the angle of cracks is obtained. In service, the information gathered by the strain gauges and by the pictures, taken during the test, is presented to explain maximum crack spacing, crack angles and the increase of strain due to the cycling process. A relationship between the observed crack width and its analytical calculation is obtained. As well as in failure, a relationship between prestressing, transversal reinforcement and angle of the cracks was obtained for service.

Chapter six presents the software created in this thesis to perform the photogrammetric analysis used for the shear tests to analyse shear cracks. A step by step explanation of the use of the method is presented. The internal proceedings of the software to calculate the crack width using the pixels of the picture .

Finally, chapter seven describes the conclusions that have being obtained after the experimental campaign and the analysis of results. There is also a section about the future lines of research.

2 State of the art

2.1 Introduction

The use of concrete structures is widely established in civil engineering and building construction and has been deeply investigated. All existing codes present formulations and models of how to design concrete structures; although, disagreement exist in some areas. Two subjects that are still not solved are the calculation of crack patterns and the shear capacity of concrete structures.

Figure 2.1-1 shows the division of concrete structures depending on the amount of active and ordinary reinforcement. Reinforced concrete (RC) elements only contain passive reinforcement. Prestressed concrete (or totally prestressed concrete TPC) beams contain active steel. This typology presents camber under dead load and will remain uncracked under full service loads. Partially prestressed concrete is a midpoint between reinforced and totally prestressed concrete. The resistance of the beam is obtained due to active and ordinary reinforcement and the structure is allowed to have cracks in service. This configuration allows the optimization of the section and the materials. The condition to use this configuration is to have a precise control over the crack width.

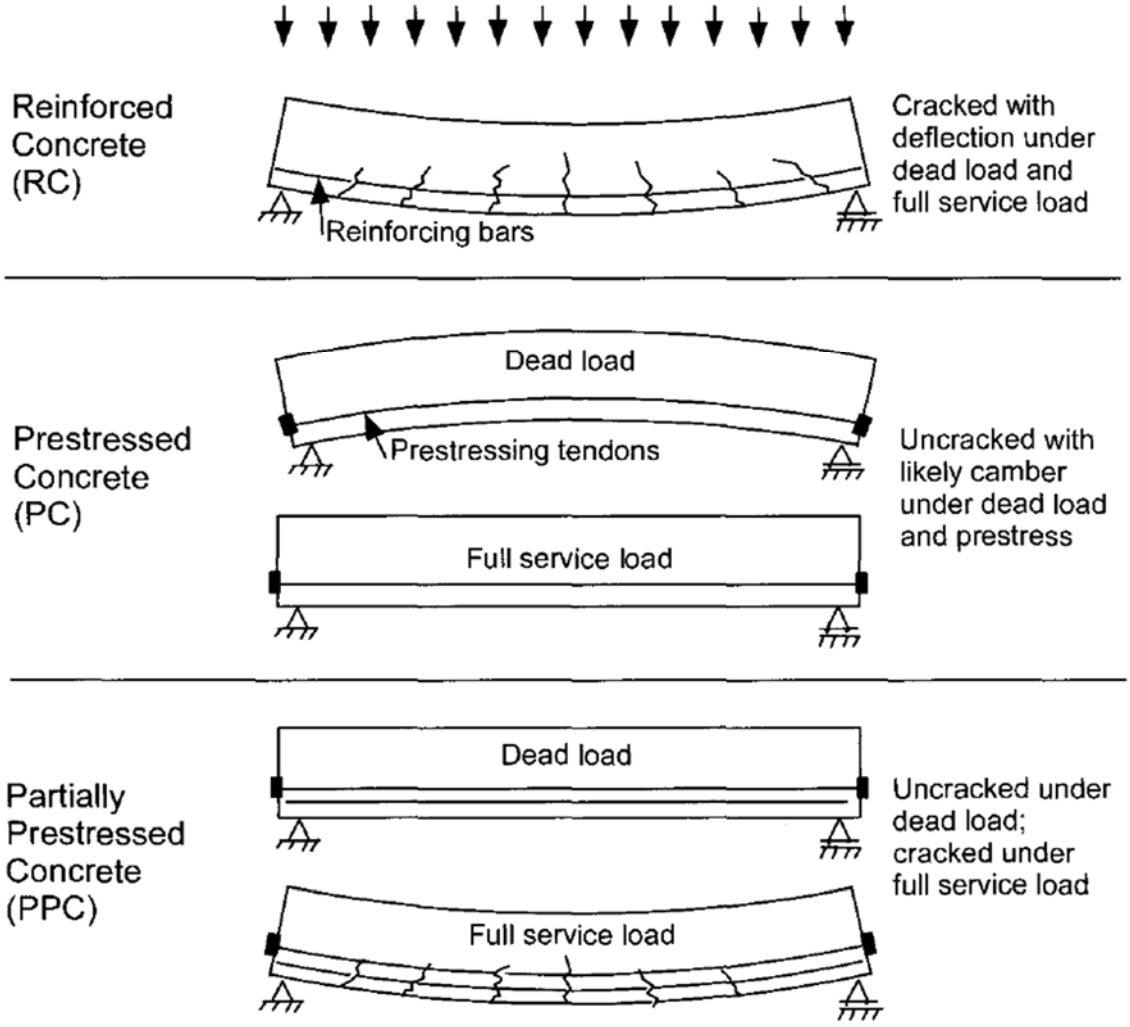

Figure 2.1-1 Comparison of the behaviour of reinforced, prestressed and partially prestressed beams (Naaman, 1983)

Prestressed concrete is usually used to build bridges and beams of a relevant size. These elements are regularly build in T or I section as a way of reducing the self-weight of the structure. The shear capacity of these sections has been discussed recently in (Tureyen, 2003; Tureyen and Frosch, 2003; Tureyen, Wolf and Frosch, 2006; Zararis, Karaveziroglou and Zararis, 2006; Wolf and Frosch, 2007). New tests carried out in (Zararis, Karaveziroglou and Zararis, 2006; Ribas, 2013; Pujol, 2018) showed that the codes underestimate the shear resistance of sections with non-constant width. The increase of resistance could come from the compression chord or from the crack capacity, but in either case the size of the diagonal cracks could increase significantly.

2.2 Partially prestressed concrete

Prestressed elements have been used in our societies for a long period. When Eugène Freyssinet (Freyssinet, 1933) published its classical study, the idea was to take advantage of the excellent behaviour of the concrete when it is under compression. Since concrete has a very low tensile stress, he argued that keeping the material under compression stresses would increase the range of use. The

compression forces were introduced by prestressing regular steel bars and cables. The target was to avoid cracks under service load so that the concrete would work as a homogeneous material.

In the 1940's, in England, Abeles suggested in (Abeles, 1940, 1945) that eliminating the tensile stress and cracking was unnecessary in many cases. His approach was to control part of the tensile stresses and cracking with the prestressed elements. He established that under dead load only, no tension stresses should be allowed to ensure the closure of the cracks. Extra non-prestressed reinforcements could be used to help controlling the cracking of the member. He termed this approach as Partially Prestressed Concrete (PPC) and the approach of Freyssinet was called Totally Prestressed Concrete (TPC) (ACI-ASCE Committee 423, 2000).

During the rest of the 20th century, studies were made around the world to characterise the behaviour of PPC structures; although, the exact concept of PPC was not uniform. (Lin and Burns, 1981) defined it as of members with some tensile stresses under working load. According to (Naaman, 1983), a PPC implied a combination of prestressed and non-prestressed reinforcement that would allow tension and cracking under full service loads. In (ACI-ASCE Committee 423, 2000), the report about the state of the art on partially prestressed concrete, PPC was defined as: "An approach in design and construction in which prestressed reinforcement or a combination of prestressed and non-prestressed reinforcement is used such that tension and cracking in concrete due to flexure are allowed under service dead and live loads, while serviceability and strength requirements are satisfied".

These studies were meant to analyse the properties of the steel and the concrete. Since the effect of been compressed for a long period, would induce creep effects on the material. The reduction of the stiffness would increase the deformation of the concrete, reducing the prestressing force and could induce the failure of the structure. The relaxation of the prestressed bars and tendons could also produce important reductions of the prestressing force. The failure of the structure could also come from problems of durability on the tendons. The ratio of corrosion for the steel increases when the material is under important tensile stresses, stress corrosion affects steel prestressed over 50% of its strength. Cracks on the concrete could allow oxygen to reach the strands, and the consequent initiation of corrosion.

Since the end of the 20th century, partially prestressed concrete has been studied all over the world (Santamaria and Arenas, 1985; De Silva, 2008; Nakamura, Bayrak and Avendaño, 2013) but a unique and definitive design formulation has not been found. Mainly due to the non-linear behaviour of the materials. Recently researchers had studied crack control, the influence of unbounded tendons, ductility, fatigue, tangent stresses, design in serviceability levels and durability under aggressive environments

In (Chowdhury, 2001), a formulation to predict the maximum crack width was presented. The formulation was statistically derived and unified the behaviour of reinforced and partially prestressed concrete beams. It related the average crack width with the maximum crack width using a multiplication factor of 1.5. (Naaman *et al.*, 2002) analyses the stress increment in unbounded tendons. They present a new formulation to predict the increase of tension. The formulation takes into account the elastic modulus of prestressing tendons, the distance of the spans and the distance between anchorages, to establish the stress increment. For small ratios between span and anchorage distance, they propose a minimum increment that depends on the modulus. This minimum increase is due to the friction in the duct.

In (Casas and Crespo-Minguillon, 1998) analyses the fatigue in prestressed structures due to fretting effects. Using tests involving fretting fatigue tests, probabilistic curves for reinforced and prestressing steel were developed. While, in (Marmo, Serpieri and Rosati, 2011) were analysed the behaviour of the prestressing element in ultimate limit state, for the cases of axial and biaxial bending moment. (Darmawan, 2009) presents a modified structural framework to study the effect of marine environment in partially prestressed concrete structures. The study used corrosion models previously developed for reinforced and prestressed to predict the behaviour in partially prestressed.

The Model Code for Concrete Structures (CEB FIP, 1978) established three classes of prestressed structures.

- Class I: No tensile stress is permitted in the concrete under full service load (TPC)
- Class II Limited tensile stress is permitted in the concrete under full service load, but no visible cracks.
- Class III: Crack widths of 0,2 mm are permitted under full service load (PPC).

The Spanish code (Comisión permanente del Hormigón, 2008) and the Eurocode 2 (EC 2) (European Committee for Standardization, 2004) have a classification of the exposure of concrete elements. There are three levels depending on the aggressiveness of the environment. Both codes establish for prestressed elements the maximum crack width limitation under a frequent load combination

Table 2.2-1 EuroCode 2 exposure classification and maximum crack width limitation

Table 7.1N Recommended values of w_{max} (mm)

Exposure Class	Reinforced members and prestressed members with unbonded tendons	Prestressed members with bonded tendons
	Quasi-permanent load combination	Frequent load combination
X0, XC1	0,4[1]	0,2
XC2, XC3, XC4	0,3	0,2[2]
XD1, XD2, XS1, XS2, XS3		Decompression

Note 1: For X0, XC1 exposure classes, crack width has no influence on durability and this limit is set to guarantee acceptable appearance. In the absence of appearance conditions this limit may be relaxed.
Note 2: For these exposure classes, in addition, decompression should be checked under the quasi-permanent combination of loads.

Table 2.2-1 is Table 7.1N from EC2 that defines the limits for the maximum crack widths for reinforced concrete (RC) and prestressed concrete (PC). Most of the codes establish 0.2mm as the maximum crack width that the structures could have for a frequent load combination. This limitation should be applied to cracks due to all kinds of stresses.

The behaviour of PPC is between RC and TPC. Allowing tensile stresses or cracking in the concrete increases the range of feasible solutions for the prestress force that can be used. Prestressing is viewed as a way of controlling the deformation and the cracking in the members. If needed, additional non-prestressed reinforcement will be added to reach the required strength.

In PPC, the element is not in linear range and the behaviour of the materials and the position of the neutral axis is not fixed. From the beginning, PPC has been designed using the method of the effective stress in the concrete, without taking into account that the section was cracked. It is a widely used method that represents an iterative process and produce good estimations for design purposes.

Allowing cracking introduces an important non-linear problem, which requires a high control on the stress state and a deep understanding of the sectional behaviour. Cracking will affect calculations and may induce durability problems in the tendons. As seen in Table 2.2-1 the TPC does not allow decompression, this eliminates the durability problem and implies that the range of deformation is smaller. In PPC, the stress introduced to the cables would be inferior but the range of deformations is superior due to the decompression and crack opening. This could generate a fatigue problem in the cables.

In most elements, the designed live loads often exceed the normally applied loads. This is to take into account the peak live actions or other exceptional loads. Using PPC, a higher flexural tension is allowed and a more economical design is achieved reducing the size of the section and the amount of reinforcement.

When using TPC, the designer may have problems to control the camber and deflection. With the reduction of the prestressed reinforcement and the inclusion of ordinary reinforcement, the resulting section will have smaller camber and stiffer sections. The new eccentricities and loads will help in multi span structures where different cambers should be obtained. In this sense, PPC can solve deflection and camber problems of TPC.

The presence of active steel can also present some inconveniences. In the case of corrosion, ordinary reinforcements are less affected by stress corrosion than prestressed steel (Duro *et al.*, 2016). In case of fire, the presence of a higher amount of mild reinforcement will provide a longer resistance of the structure. As explained in existing codes (PCI, 1989, 1992, chap. 9), the fire-resistance rating increases with the amount of mild reinforcement. As it can be seen in EC-2 part 1-2 (European Committee for Standardization, 2011), the decrease of yielding stress due to temperature is more important for active steel. For ordinary reinforcement the decrease is 10% and 30% for 400 and 500ºC, respectively; for active reinforcement the decrease is 50 and 75% for at the same temperatures.

During service life, cracks may take place in PPC, so cyclical loads will produce that the cracks open and close. The interaction between the sides of the crack generates a damping effect that did not appear in TPC due to the uncracked section or in the RC, since in this case the cracks remain open after appearing. However, when facing repeated loads, fatigue might be a real concern. As Namaan (Harajli and Naaman, 1985; Naaman, 1989; Naaman and Founas, 1991) studied on the eighties, the fatigue strength depends on the range of stresses.

The codes EC-2 and EHE-08 establish a limitation of the crack width for PPC (Table 2.2-1). This is due to durability problems, since the concrete is not protecting the reinforcement from the different agents of the environment when it is cracked. The calculation of crack width due to normal stresses has been widely studied.

The final target of the PPC is to obtain a structure more balanced between service and failure, being sure all the requirements are granted without wasting geometrical or mechanical properties. For classes I and II, the area of prestressed steel is designed following serviceability criteria and checked at ultimate limit state. On the other hand for class III, the PPC behaves like a mix between RC and TPC, both criteria have to be used to design the structure and the ratio between active and passive steel reinforcement will determine the behaviour.

2.2.1 Prestress indicators

The prestress indicators show the level of prestress that has been applied to the concrete element. It indicates the possible non-linearity of the section. There are several approaches and formulations to obtain such indicators, the most popular expressions on the literature are the degree of prestress established by the Swiss school and Hugo Bachman (Bachmann, 1984), and the partial prestress ratio (PPR). These indicators would help to compare elements with similar materials but their simplicity does not allow a more complex comparison (such as deformations or crack width).

Bachmann proposes the service load degree of prestress (Equation 2.2-1), which is the ratio between the decompression moment (M_{dec}) and the dead-load moment plus the live-load moment (M_D and M_L respectively). According to this equation, when κ is equal to zero the section is not prestressed, when κ is equal to one, the section is TP.

$$\kappa = \frac{M_{dec}}{M_D + M_L} \qquad 2.2\text{-}1$$

In (Pisani, 2000), the PPR was proposed. The PPR (Equation 2.2-2) compares the ultimate bending moment of two sections. A theoretical section with only the prestressed steel is compared with the real section, with active and ordinary reinforcement. If the section is made of reinforced concrete, the ratio is zero. If there is no passive steel, the ratio is one. This method only takes into account the ultimate state.

$$PPR = \frac{M_u(A_p)}{M_u(A_p + A_s)} \qquad 2.2\text{-}2$$

This method also establishes a ratio of 0 for RC and 1 for TPC.

2.2.2 Design criteria of PPC

Most of the design methods for PPC impose the equilibrium between moments and forces. For rectangular sections and when cracked is allowed, the solution to the equilibrium is a 3rd degree equation. Each method will try to find a value of the prestressing load (P) that satisfies a certain crack width or stress on the reinforcement criteria. This is an iterative process until a prestressing load and an amount of passive and active steel is obtained. The first iteration usually uses the tensile stress of the concrete as a reference.

2.2.2.1 Swiss school design criteria

The Swiss school opened up the way for the design and construction of PPC in Europe. In (Bachmann, 1984), Bachmann proposed a practical design method to find the amount of prestressed steel (Ap) and passive steel (As). The design checks the ultimate state and verifies the serviceability state. The method is based on the following steps:

1. Determine the decompression bending moment (M_{Dec}), usually the bending moment due to permanent load (M_D)

2. Find P in elastic range for M_{des} taking into account prestressing losses and the initial stress of the tendons. Obtain A_p from P.

4. Find A_s using ultimate state criteria (Equation 2.2-3)

$$A_s = \frac{M_u - A_p f_{pyd} j_p}{f_{yd} j_y} \qquad 2.2\text{-}3$$

Where j_p and j_y are the lever arms from the line of action of the compressive force to the centroid of the prestressed reinforcement and the mild reinforcement, respectively.

5. Meticulous detailing of the non-prestressed reinforcement. A close distribution of reinforcement (longitudinal and vertical) will reduce significantly the size of the cracks.

6. If the crack width is larger than the limits established in the codes, an iterative process starts. The parameters that have to be changed are A_s or P.

2.2.2.2 Spanish design criteria

(Santamaria and Arenas, 1985) presents the state of the art of PPC. The technique they propose is the same as in the Swiss school but with an recommendation of limiting the PPR to 0.80 for PPC.

2.2.2.3 Japan standard (JGC15) design criteria

Since the Japanese codes are performance based design, the PPC is widely used in Japan. The code establishes two groups of structures, those which are allowed to crack in service and the ones that are not allowed to crack in service. JGC15 (Japan Society of Civil Engineers, 2007) allows any combination of A_s and A_p, covering the full range, from RC to TPC. The code uses the same criteria than the European codes. They establish the PPC limitations as the crack width and the ultimate bending moment.

2.2.3 Linear and non-linear Magnel diagram

The design of prestressed sections has been usually done using the Magnel diagram (Magnel, 1950) (Figure 2.2-1). The diagram presents the relationship between the isostatic bending moment due to the prestressing force ($P \cdot e$) and the prestressing force (P). The inequalities of Table 2.2-2 generate a solution space of P and e. For each value of the eccentricity (e), two prestressed forces may be found. The typical ratios between minimum and maximum forces are 30-35%.

This method controls the compression stresses during transfer situation and in service. The stresses cannot exceed 0.6 the concrete resistance to ensure no micro cracks damage the concrete. In turn, for the other side of the beam, the method controls the tensile stresses. Depending on the Class of the structure, the stresses are limited by the traction strength of the concrete or they have to be always in the compression range.

The first two equations (Equation 2.2-4 and Equation 2.2-5) represent the situation of the element in the prestressing transfer situation, i.e. loaded under self-weight and the prestressing force. When prestressing, the tensile stress in the top fibre of the concrete (2.2-4) is limited to the maximum allowable stress. This equation is meant to control the possible cracking of the beam during the prestressing of the beam. 2.2-5 uses as pivot the maximum allowable stresses on the lower fibre of the concrete. This equation will check that the compression on the concrete does not increase, overcoming the admissible stress and damaging the concrete.

The last two equations take into account the service life situation. 2.2-6 limits the compression on the top fibre in the characteristic combination. The compression on the concrete is checked to ensure no compression damage occurs. The last equation checks the tensile stress on the bottom part of the section under the frequent combination. This stress has to be zero in Class I prestressed concrete section.

Table 2.2-2 Inequations of linear Magnel for prestressed concrete

1: Maximum tensile stress in empty situation	$\sigma_{c\,top} = -\frac{P}{A_c} - \frac{Pev}{I_c} - \frac{M_0 v}{I_c} \leq \sigma_{c\,adm,t}$	2.2-4
2: Maximum compression in empty situation	$\sigma_{c\,bot} = -\frac{P}{A_c} - \frac{Pev'}{I_c} - \frac{M_0 v'}{I_c} \leq \sigma_{c\,adm,c}$	2.2-5
3: Maximum compression in serviceability	$\sigma_{c\,top} = -\frac{P}{A_c} - \frac{Pev}{I_c} - \frac{M_2 v}{I_c} \leq \sigma_{c\,adm,c}$	2.2-6
4: Maximum tensile stress in serviceability	$\sigma_{c\,bot} = -\frac{P}{A_c} - \frac{Pev'}{I_c} - \frac{M_1 v'}{I_c} \leq \sigma_{c\,adm,t}$	2.2-7

where M_0, M_1 and $\mathrm{M}_2$are the different moments used to design the element. These moments are in growing order and represent different serviceability states. In EHE 08 [REF], M_0 is the bending moment in transfer situation, M_1 is for the frequent combination and M_2 is the moment of full service load.

For the four equations (Table 2.2-2), all points defining the maximum allowable working stresses are on top or bottom of the section and in the concrete. Because the traditional approach assumes linear elastic behaviour, the inertia of the section is always taken as uncracked. Figure 2.2-1 shows a representation of the 4th inequality and the solution space of combinations of P and e.

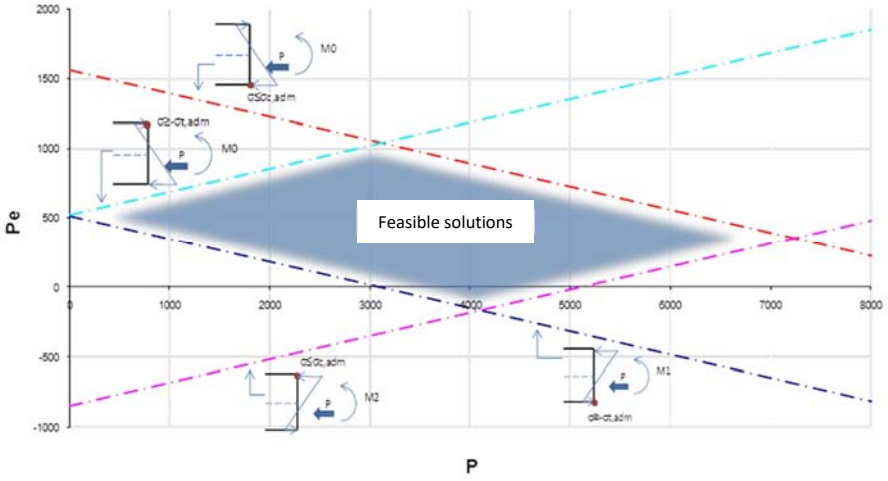

Figure 2.2-1 Magnel diagram for linear behaviour on prestressed sections

One possible upgrade of the Magnel diagram, when applied to PPC, is to take into account that the section will be cracked and the inertia for every combination of prestressed forces would be different. Figure 2.2-2 presents a new solution space when the variation of the inertia is taken into account. The inequalities presented in Table 2.2-2 are also plotted in this figure, and it can be seen how the area of feasible solutions has increased. A broader solution space allows to design sections where the position of the cable allows a smaller amount of prestressing load, so a smaller area of prestress, and therefore a reduction of the costs of the structure. Since the two solution spaces are similar, the use of linear simplification is accepted.

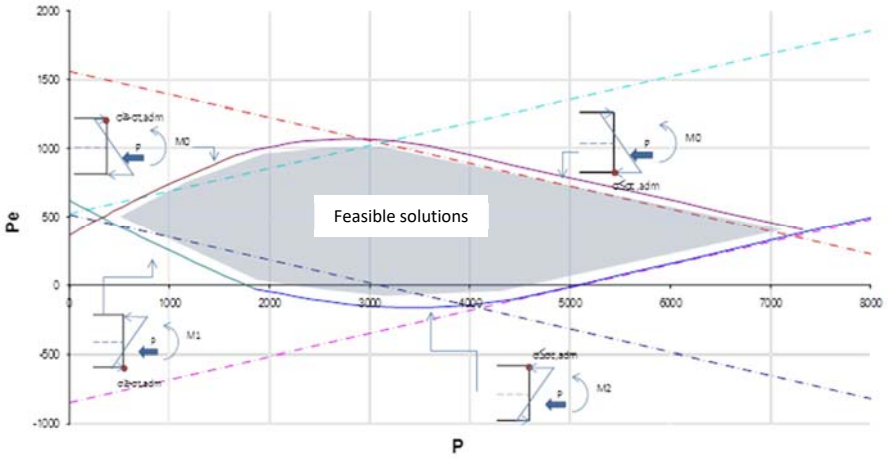

Figure 2.2-2 Magnel diagram taking into account cracked inertia

(Bairán, Marí and Duarte, 2011) presents a design proposal for PPC, where the optimal degree of prestressed can be found for a design value of the crack width taking into account the non-linear part of the problem. The methodology is based on the analysis of cracked prestressed sections. When the external bending moment (M_{ext}), the passive reinforcement (A_s and A'_s) and the strain plane distribution are known, the equilibrium of forces and moments can be calculated to determine the value of the prestressing force (Figure 2.2-3).

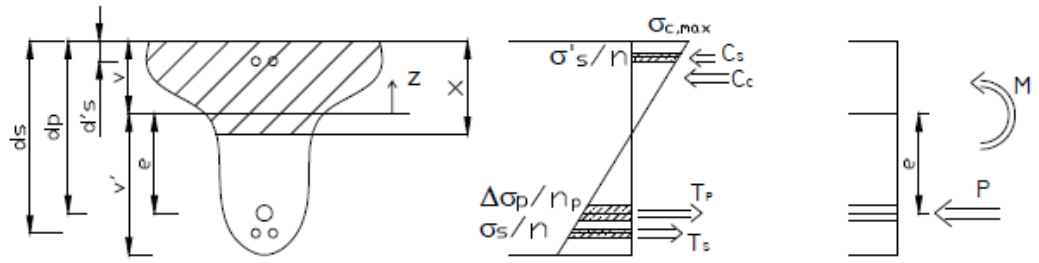

Figure 2.2-3 Internal equilibrium in a PPC section

$$\sum F = P = \int_{v-x}^{v} \sigma_c(z)b(z)dz + A'_s\sigma'_s - A_s\sigma_s - A_p\Delta\sigma_p \qquad 2.2\text{-}8$$

$$\sum M = M_{tot} = M - Pe = \int_{v-x}^{v} z\sigma_c(z)b(z)dz + (v - d'_s)A'_s\sigma'_s - (d_s - v)A_s\sigma_s - eA_p\Delta\sigma_p \qquad 2.2\text{-}9$$

The non-linear diagrams are built by changing, in each combination of P and e, the position of the neutral axis and the position of the different fixed-points, for each load situation, i.e. prestress transfer and service life (Figure 2.2-4). For each curve of the diagram, the fixed-point will be in a specific position and each plane of strain will define a combination of P and e.

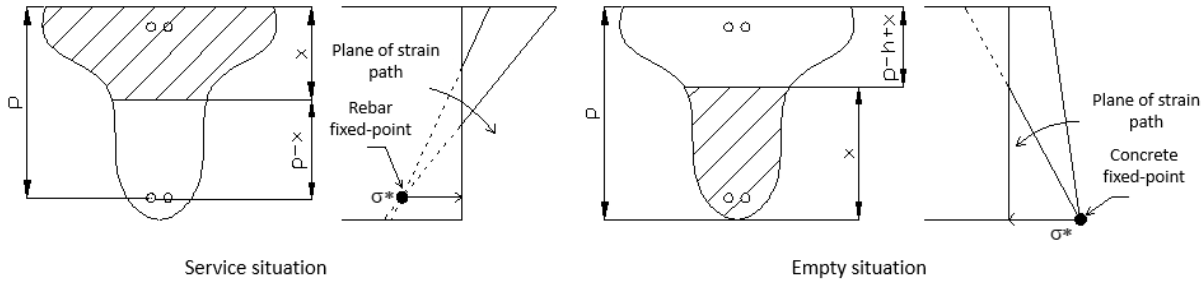

Figure 2.2-4 Different plane of strain fixed-points and neutral axis position will generate the diagrams

When P is known, the A_p can be computed (Equations 2.2-10 to 2.2-13) (Bairán, Marí and Duarte, 2011, 2012). The formulation to obtain A_p depends on the bonding condition of the strands and on the constructive process used on the member. In the pre-tensioned case, A_p is related to P and the variation of prestressed force ($\Delta\sigma_p$) (Equation 2.2-10). For post-tensioned elements with unbonded strands, the area is directly related to the load and the initial stress (Equation 2.2-11). In the case of bonded tendons, the calculation involves a 2nd degree equation and the concrete area.

$$A_p = \frac{P}{c\sigma_{p0} + \Delta\sigma_p} \qquad 2.2\text{-}10$$

$$A_p = \frac{P}{c\sigma_{p0}} \qquad 2.2\text{-}11$$

$$A_p = \frac{c\sigma_{p0} + \Delta\sigma_p}{2cn\sigma_{p0}} \; A'_c \left[-1 + \sqrt{1 + 4\frac{P}{A'_c}\frac{cn\sigma_{p0}}{\left(c\sigma_{p0} + \Delta\sigma_p\right)^2}} \right] \qquad 2.2\text{-}12$$

where c is the percentage of long-term prestressing force minus the losses; σ_{p0} is the initial stress introduced to the cable and $\Delta\sigma_p$ is the variation of tension due to the compatibility of strains; n is the factor between the modulus of steel and concrete; and finally A'_c is:

$$\frac{1}{A'_c} = \frac{1}{A} + \frac{e^2}{I} \qquad 2.2\text{-}13$$

In most cases, this process will increase the area of the space of feasible solutions. Hence, the range of e and the difference between P_{max} and P_{min} will increase significantly. Figure 2.2-5 shows the difference between using the linear or the non-linear diagram. The new approach changes significantly the possible combinations.

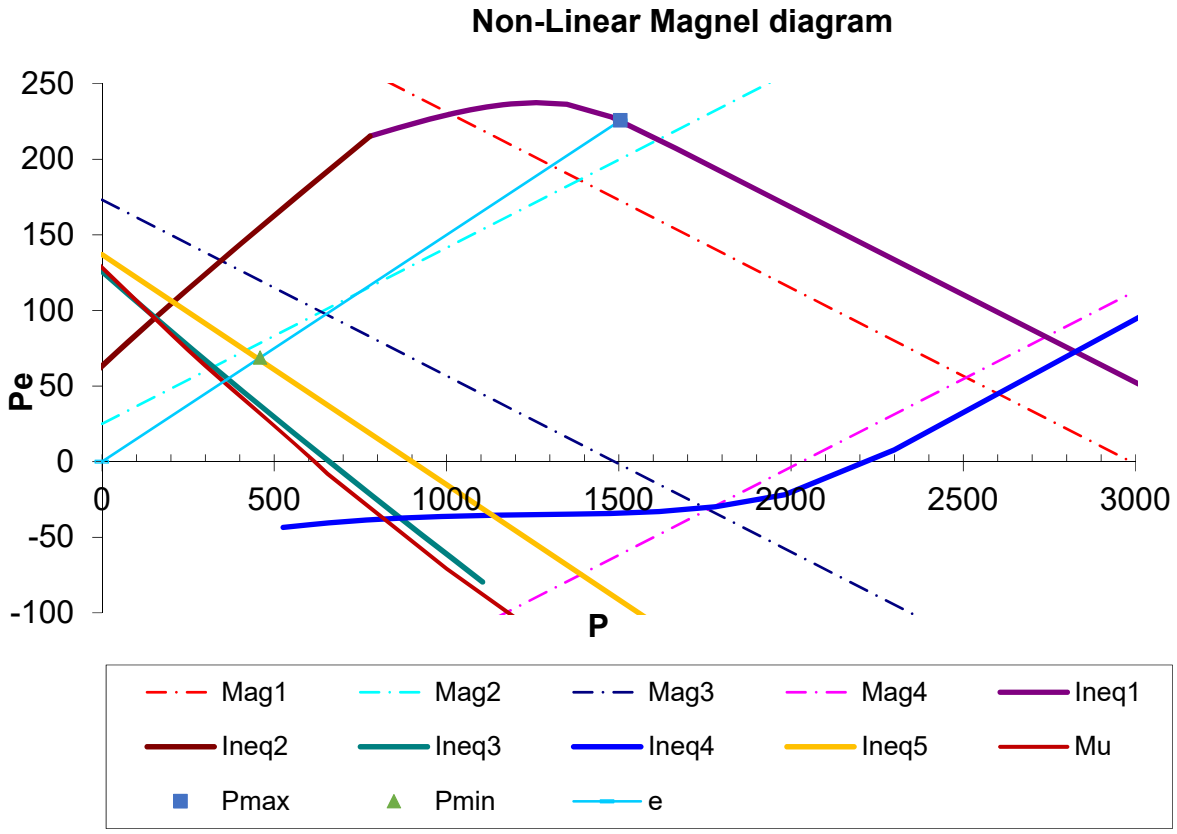

Figure 2.2-5 Non-linear Magnel diagram increases the solution area for a double T section

In addition to the four inequalities of traditional Magnel diagram, this method considers two new conditions for the situations of tendon decompression under permanent load (Ineq 5) and the ultimate bending strength (M_u) (Table 2.2-3). The fifth inequality (Ineq 5) has its fixed-point on the prestress tendon, and checks that the duct will never be in a decompression situation under the quasi-permanent combination. This limitation could define the design of the section depending on the percentage of permanent load and life load.

In PPC structures the amount of prestressed reinforcement required to resist the service combination may not be enough at ultimate limit state. In these situations, the ordinary reinforcement A_s is usually increased; however, this may not be the most economical solution, and an increase of the active reinforcement (A_p) may be more adequate. In the latter case, the fixed-point is placed on the top of the section and the limit value is defined in terms of the concrete strain; in particular, it is fixed to the ultimate concrete strain, which takes a value of 0.0035 for ordinary strength concrete. For concrete strength higher than 50 MPa, the corresponding limit strain should be adapted accordingly. With the process of load and moment equilibrium, P and e are found. To include this information on the diagram, P is multiplied by σ_{p0}/f_{pyd}, the prestressed in service over the reduced failure stress.

In many cases this two new conditions are more restrictive than inequality number 3 (Ineq 3). In those cases, the minimum P is defined by the stress on the duct or the ultimate resistance of the section.

Table 2.2-3 Fixed-point definitions for the inequations

Inequation	*Description*	*Fixed-point position*	*Fixed-point value*
1	Compression in transfer situation	$p = h$	$\sigma_c = 0.6 f_{ck,j}$
2	Traction in transfer situation	$p = d'$	$\sigma_c = \frac{1}{n}\sigma'_c$
3	Traction in frequent combination	$p = d$	$\sigma_c = \frac{1}{n}\sigma_c$
4	Compression in characteristic combination	$p = 0$	$\sigma_c = 0.6 f_{ck}$
5	Traction in quasi permanent combination	$p = duct$	$\sigma_c = 0$
6	Ultimate bending moment	$p = 0$	$\varepsilon_c = 0.0035$

The design criteria consist of fixing a minimum passive reinforcement area to determine the area of prestressed steel to maintain the crack width between the range of the codes. Crack width depends on the stresses of the rebars crossing the cracks and the spacing between cracks. The stress of the rebars is related to the behaviour of the concrete, the contribution of the tension stiffening, the slip on the bars and other effects. To obtain accurate crack width, a deep knowledge of these effects has to be acquired.

2.3 Shear resistance

The behaviour of concrete beams in flexure is completely different to the shear behaviour. One of the most important differences is that shear failures tend to be abrupt. The evolution of the cracks is much faster and can reach wider widths. As it can be seen in Figure 2.3-1, concrete beams can have different shear failures modes. The amount of parameters intervening in the shear resistance is very large, which makes the design of shear resistance very complicated. Most of the codes propose models that are based on experimental results and can produce wrong solutions when applied to new situations (like new materials or geometrical configurations).

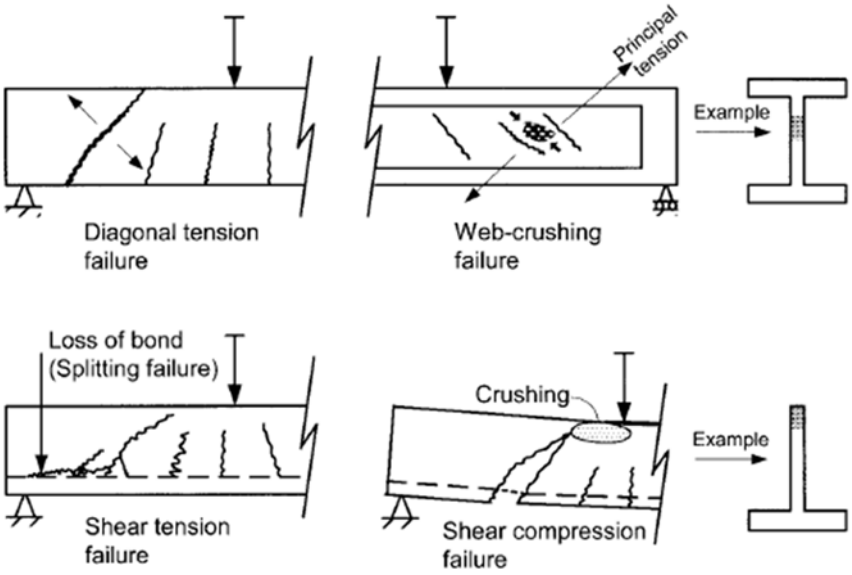

Figure 2.3-1 Different modes of shear failures (Naaman, 1983)

The different failure modes represent very different situations and have to be address accordingly. The beam will fail by the weakest mode. The diagonal tension failure is the mode where the concrete undergoes shear stresses that could lead to diagonal cracking. If this occurs, and the correct amount of transverse reinforcement has not been placed, the beam will fail in a brittle mode.

The minimum shear reinforcement to control diagonal cracking in reinforced concrete has been researched extensively; however, a satisfactory unique solution has not been found. Even fewer tests and studies have been developed for prestressed concrete (Choulli, 2005), hence the influence of the prestressing force in the minimum shear reinforcement has not been established yet.

The use of transversal reinforcement will allow more ductile failure modes, and a more controlled evolution of the crack width until the maximum load. As in the case of bending, this is desirable because it will provide a warning of the state of the member. The study of cracked reinforced concrete and how does it resist shear stresses has been a major focus of the community. The models and formulations use the friction between the lips of the crack and the concrete in the compression chord as mechanisms of shear resistance. The aggregate interlock takes into account the shear resisted by the cracks. The amount of tensile shear stresses that can be transmitted to the cracks is inversely proportional to the crack width. The concrete compressed in the chord provides shear resistance.

2.3.1 Analytical models

The first rational model taking into account the presence of the web was the truss analogy, developed by (Ritter, 1899; Mörsch, 1909) in the early twentieth century. This mechanism analyses the beams as a lattice, in which the concrete act has struts, resisting the compression in the parallel direction of the cracks. The reinforcement, longitudinal and transversal, act as the ties and resist the tensile stresses (Figure 2.3-2).

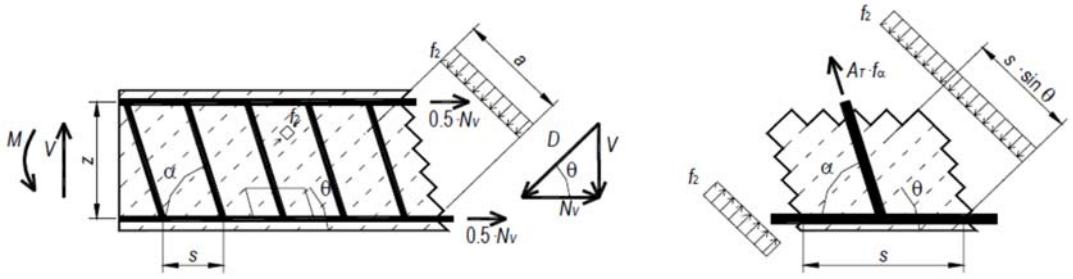

Figure 2.3-2 Lattice interpretation of the shear stresses

Figure 2.3-3 shows the force distribution of a section taking into account the stirrups and the truss analogy. The main contribution to the shear resistance is the vertical component of the stirrups force (V_s).

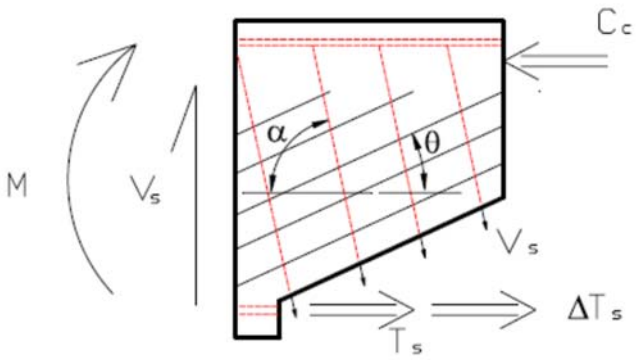

Figure 2.3-3 Shear transfer mechanisms considered on the truss analogy

The contribution of the stirrups to the shear resistance is presented in Equation 2.3-1. The ratio between the lever arm, the cotangent of the angles and the stirrup spacing will determine the number of stirrups crossed by the crack. The area of stirrups and their stress will determine the force in each stirrup. The combination of this two factors and the sinus of the stirrups determine the shear force in the vertical direction.

$$Vs = \frac{A_{st}}{st} f_{yd}\, z\, \sin\alpha\, (\cot\theta + \cot\alpha) \qquad 2.3\text{-}1$$

Since the shear tests in Stuttgart from (Leonhardt and Walther, 1962), the shear resistance process has been divided in two stages. The first stage is defined before the sections cracks, when the concrete is resisting all the stresses. In the second stage, after cracking, stirrups get loaded, and the shear strength of the section is provided by a combination of the cracked concrete and the stirrups.

Before cracking, the concrete is loaded in a multiaxial stress state. When the principal stress reaches the maximum tensile stress of the concrete, a pattern of cracks appears. Usually this crack develops as a continuation of the bending cracks. Figure 2.3-4 shows the interaction of the internal and external loads on a beam without stirrups.

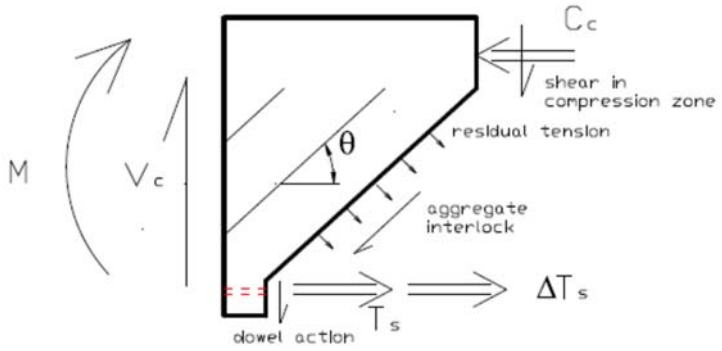

Figure 2.3-4 Shear transfer mechanisms

Four resisting actions are effective in resisting the external shear load. Namely, the non-cracked concrete of the compression zone is under a multiaxial state and provides shear resistance. On the crack, two effects generate shear resistance. The aggregate interlock and the tension stiffening produce shear stress parallel to the cracks. The residual tension due to the imperfections on the crack generate a tensile stress. In addition, the presence of the longitudinal tensile reinforcement generates a dowel action effect

As can be seen in Figure 2.3-4, the crack stresses produce a horizontal force. In order to have a self-balanced situation, a tension shift (ΔT_s) appear. ΔT_s is an increase in the load of the longitudinal reinforcements. The reinforcement stresses will be governed by the bending moment until the section cracks. After this point, the tension shift has to be added. The dowel action effects depends on the ability of the longitudinal reinforcement to maintain its position. In the cases where there are not stirrups, the orthogonal tensile stress between the concrete and the longitudinal bar is the only mechanism to provide resistance to the dowel; hence, this resisting action is brittle and may vanish after the inclined crack develops.

$$V = \frac{dM}{dx} = \frac{\partial M}{\partial T}\frac{dT}{dx} + \frac{\partial M}{\partial z}\frac{dz}{dx} = z\frac{dT}{dx} + T\frac{dz}{dx} \qquad 2.3\text{-}2$$

The applied bending moment can be taken as $M = Tz$, where T is the tensile force on the longitudinal reinforcement and z is the effective lever arm between the compression and tension forces due to bending. The equation 2.3-2 presents the evolution of the bending moment along the longitudinal axis. The first term represents the variation of the force on the reinforcement, the procedure used to explain the equilibrium of loads and moments. On the other hand, the second term of the equation represents a variation on the lever arm along the longitudinal axis.

This mechanism is also known as arch effect (Figure 2.3-5). When the bond of the longitudinal reinforcement is reduced, or the reinforcement has yielded, the variation of T is also reduced. In these cases, the second part of equation gains more relevance. The beams without transverse reinforcement should develop the arch effect to resist the shear loads. The shear resistance reached by this effect can be higher than the cracking shear strength. This effect appears when the distance between support and the loaded section is close enough.

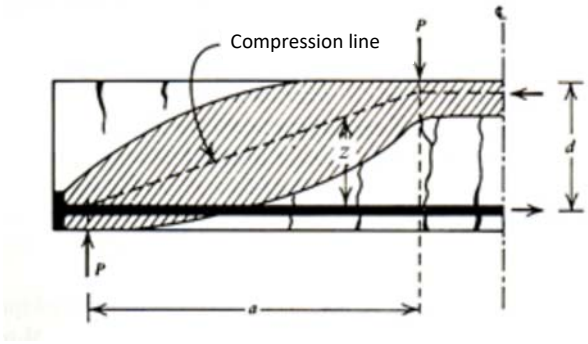

Figure 2.3-5 Evolution of the lever arm generating the arch effect

Equation 2.3-3 presents the variation on the force in the longitudinal reinforcement due to the compressive stresses in the web.

$$\Delta T_S = \frac{1}{2} * V_S * (\cot\theta - \cot\alpha) \qquad 2.3\text{-}3$$

The stirrups will also modify the stress distribution on the concrete and since the stirrups are going to undergo important tensile stresses, the longitudinal reinforcement have to anchor them. Figure 2.3-6 shows how the stress field on the concrete depends on the stirrup distribution.

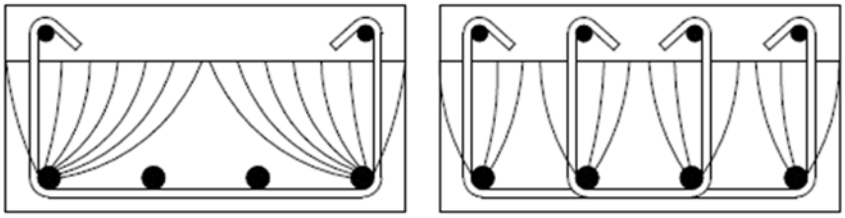

Figure 2.3-6 Influence of the stirrup distribution on the stresses on the concrete

The presence of transverse reinforcement changes significantly the behaviour of the section. The dowel action effect can completely develop. The stirrups will control the crack width, ensuring the aggregate interlock and the internal friction contribute to a larger shear resistance. Finally, the concrete of the compression chord will be confined; consequently, the new multiaxial situation will increase the shear resistance of the element (Marí *et al.*, 2015).

To compute the contribution of the concrete to the shear resistance, the codes take into account an area of concrete defined by the height of the section and the width of the web. They assume all the stresses flow through the web. When the section has different widths (like a double T section), the codes and formulation (EC-2 and EHE 08) (European Committee for Standardization, 2004; Comisión permanente del Hormigón, 2008) dismiss the flanges. After the development of several experimental campaigns (Zararis, Karaveziroglou and Zararis, 2006; Ribas, 2013; Pujol, 2018), with non-constant width sections, it was discovered that the shear resistance had been undervalued.

The T-section geometry is subject of recent research, to understand the concrete contribution to the shear resistance. Based on the cracks observed in the top of the flanges, (Zararis, Karaveziroglou and Zararis, 2006) proposed that the contribution of the flanges was not zero (Figure 2.3-7). In addition, an effective area will be used for the shear strength assessment taking into account part of the flanges.

When the section does not have stirrups, the effective area will be a trapezoid with the sides starting at the edges of the web and going to the top of the section at 45º.

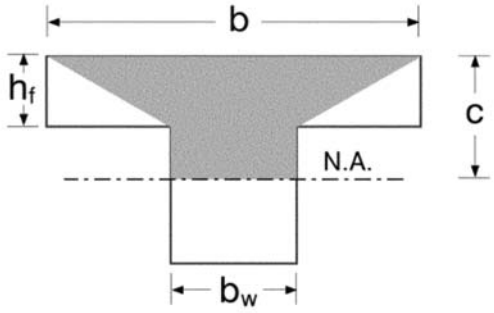

Figure 2.3-7 Shear effective area on T sections according to (Zararis, Karaveziroglou and Zararis, 2006)

The Compression Chord Capacity Model (CCCM) presented in (Marí *et al.*, 2015; Cladera *et al.*, 2016), is a conceptual model for the prediction of the shear-flexural strength reinforced concrete beams. It incorporates the shear transferred by the un-cracked concrete chord, along the crack's length by the stirrups. Figure 2.3-8 shows the distribution of the resisting mechanism. The model introduces an analytical approach to calculate the contribution of the concrete V_c, from the compression chord. This concrete is under compression due to the bending moment and confined due to the stirrups. Its multiaxial state would increase the shear resistance to that concrete. The rest of the mechanisms are equal to the previous models.

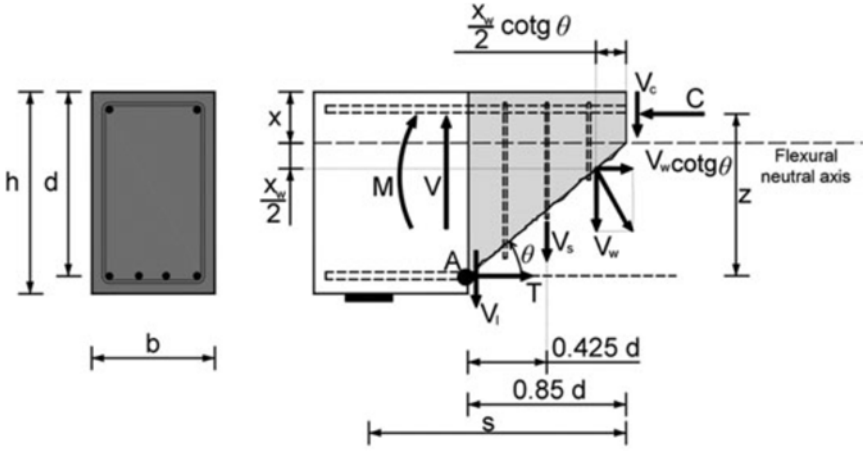

Figure 2.3-8 Shear transfer mechanisms considered on the CCCM

This model establishes a method to find the critical shear crack section. The method involves the bending moment applied to the beam, since the shear cracks start in flexural cracks. The crack of the critical section starts on the section where the bending moment reaches the cracking moment. In reinforced beams, the critical section will be placed at $0.85d$ from the cracked section in the direction of the applied load (Figure 2.3-9).

The shear contribution of the compression chord would depend on its area and on the compression stress. With this model, increasing the longitudinal reinforcement will move the neutral axis to a lower position augmenting the area of the chord. The increment of transversal reinforcement will increase the shear resistance of the beam in two ways. The principal improvement is due to the increase of V_s (Equation 2.3-1), like in previous models. The concrete shear resistance also increases since the

concrete in the compressive chord will be more confined. The maximum shear stress that it can reach will increase, producing a higher V_c. Since the area taken into account to calculate V_c is on the top of the section, the previously mentioned problem with the widths does not exist, even though when the sections involves a very wide section, like in bending moment problems, there is an effective width that has to be calculated.

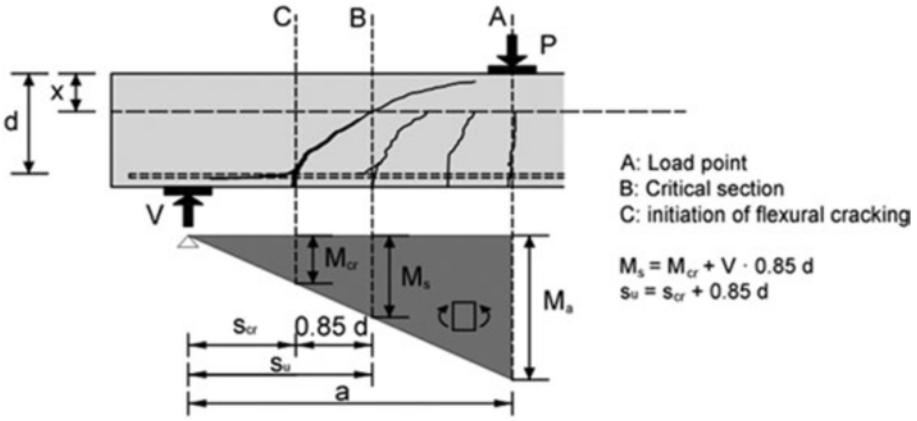

Figure 2.3-9 Critical section diagram

2.3.2 Shear resistance in PPC: minimum transverse reinforcement ratio

The dissertation (De Silva, 2008) compiles the work of the last fifty years over the relation between shear resistance and cracks and crack width for PPC. According to De Silva, the shear reinforcement configuration will affect the shear patterns but it is not relevant for the shear resistance. It is also emphasized that a minimum amount of transverse reinforcement has to be placed to ensure that the beam will not suffer a brittle failure when the first cracks appear.

The presence of prestressed tendons generates additional compression stresses in the strands direction. This will shift the angle of trusses and cracks to a more horizontal direction. The decrease of the angle increases the number of stirrups crossed by the critical shear crack. Therefore, the shear resistance of the section increases. In addition, the increase of compression stress in the concrete also increases its shear resistance.

The minimum transverse reinforcement should satisfy three conditions. The first aspect is to avoid the brittle failure of the beam. Secondly, to control the evolution of the cracks. Finally, to assure the concrete contribution to the shear resistance of the concrete until the yielding of the transversal reinforcement.

(Nakamura, 2011) analyses the different formulation (from USA, Canada and Japan) to establish the minimum transverse reinforcement. The formulations are divided in three categories, depending on the considered parameters. The first category only takes into account the geometry of the section (Equation 2.3-4). The second category adds the yielding stress of the steel (Equation 2.3-5). The last category uses also the tensile resistance of the concrete (Equation 2.3-6).

$$A_{v,\min} = K b_w s \qquad 2.3\text{-}4$$

$$A_{v.\min} = \frac{50 b_w s}{f_y} \qquad 2.3\text{-}5$$

$$A_{v.\min} = k\sqrt{f'_c}\,\frac{b_w s}{f_y} \qquad 2.3\text{-}6$$

In this study, the reserve of shear strength (RSS) ratio is defined. This ratio compares the failure shear force of a beam against the shear force that produces the first inclined cracks. Nakamura defined that a section with at least $RSS = 1{,}3$ will be ductile.

$$RSS = \frac{V_u}{V_{crack}} \qquad 2.3\text{-}7$$

Nakamura collected a database of shear tests that included the geometric and mechanical properties and V_u and V_{crack}. He compares the RSS and minimum reinforcement area of Equation 2.3-6 (Figure 2.3-10). He observed that the limits established by the codes did not guarantee the minimum RSS. Group I represents the beams that had a minimum transverse reinforcement area, $A_{v,min}$, over the limit established by the code but were not ductile. In this case, the prediction of the codes (European Committee for Standardization, 2004; ACI Committee 318, 2008; AASHTO, 2010; CSA, 2010; FIB, 2010) were unsafe (Figure 2.3-10). Conversely, group II contains the beams with ductile behaviour but that not guarantee the minimum transverse reinforcement area $A_{v,min}$.

In addition, Nakamura proposed a change on the K factor of the formulation of the minimum transverse reinforcement area, increasing it to $K = 0.85$. This change increases the smallest RSS of Group I from 1.04 to 1.14, increasing the security margin of the method. This increase on safety margin only will suppose an increase of 13% of the area of transversal steel.

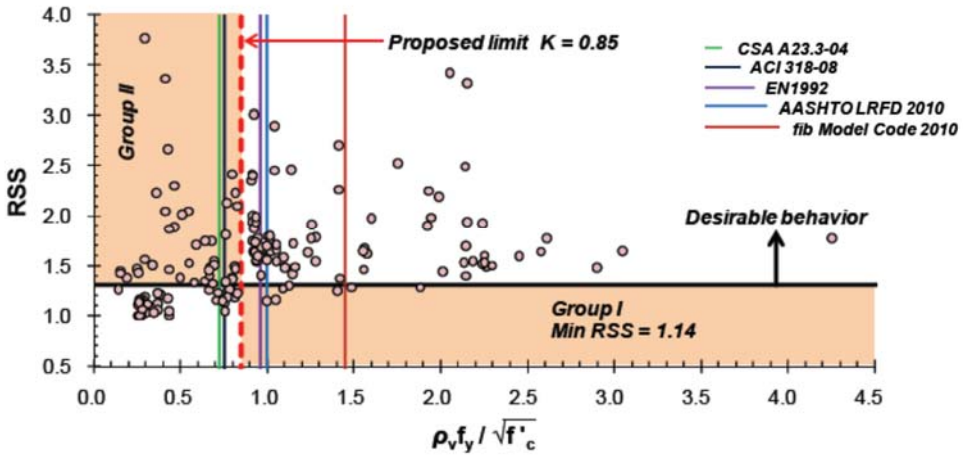

Figure 2.3-10 Influence of minimum transversal reinforcement on the RSS

2.4 Crack width

Cracks are generated by flexural and shear forces, since both develop tensile stresses. In most regular structures, both effects are present and their will produce cracks in the structure. Each force tend to

generate cracks in specific locations with different patterns. When the forces are combined, the cracks and patterns are mixed.

Flexural effects generate cracks in the tensile part of the member. Generally, these cracks are perpendicular to the longitudinal reinforcement. The cracks start at the tensile area of the beam and develop along the web, up to the concrete chord. The crack width reduces as the crack approaches the neutral axis of the beam. Shear cracking appears when the principal tensile stress exceeds the concrete strength. In RC beams, the angle of the shear cracks is close 45º in the mid-height of the cross-section, when no axial forces are applied. The axial force introduced by the PC reduces the angle of the compression strut, so the angle of the cracks is also reduced. Usually, the cracks appear in the centre of the web, starting in the mid-height and developing to the top and the bottom of the sections.

As can be seen in Figure 2.4-1, the diagonal cracking can appear in two different forms, depending on the relationship between shearing and flexural stresses. In the sections where the flexural cracks have appeared, the shear crack will develop from the flexural crack. These cracks have a characteristic shape, they start perpendicular to the axis of the beam and then turn to a diagonal orientation. They are referred as flexure-shear cracks.

If the relationship between moment and shear is smaller, the diagonal crack appear before flexural cracks. In these case, cracks are only in the web. In beams with I sections or prestressed, the shear cracks and the flexural cracks can be also independent. Web-shear cracks develop in the middle of the web and the ends of the cracks does not reach the sides of the beam. The cracks are wider on their centre.

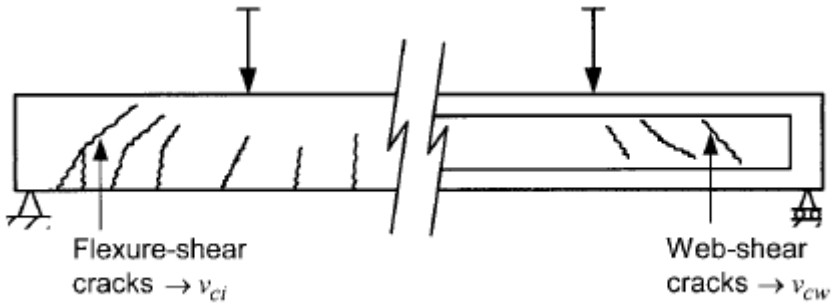

Figure 2.4-1 Different types of shear cracking (Naaman, 1983)

To design Class III structures under the codes regulation (Table 2.2-1), a formulation to obtain the crack width is essential. There are several approaches to calculate the crack width but the results of each formulation can be very different. The main reason is that there is no consensus on the definition of the parameters that affect the crack width.

2.4.1 Cracking under normal stresses

The classical approach for a distributed cracking method is to assume that the crack width is a mean value of the longitudinal reinforcement strain multiplied by the distance between cracks (Equation 2.4-1). This approach assumes all the strain is absorbed by the reinforcement therefore, the elongation of the rebars is equal to the crack width. The k factor is used to obtain the maximum crack width from the average strain and crack spacing.

$$w_k = kS_m\varepsilon_s \quad \text{2.4-1}$$

This equation is a simplification of a more complex problem, where the rebars do not have a constant strain and the spacing between cracks is not uniform. Some software (like DIANA, Midas Fea and ABAQUS) (Diana, 2019; Midas, 2019; Simulia, 2019) address the problem without simplifications. They take into account the bond slip between concrete and reinforcement to compute the stresses and strains of every part of the specimen to give the crack width. Both software require mechanical information of the concrete that is usually complicated to obtain and has a very disperse values, like the bond slip equations and the parameters of fracture mechanics. The value of these parameters are not uniform, they can change drastically inside the same element of study. Therefore, these programs are not useful for simple cases of daily engineering and are only used on very specific cases.

Most of the codes and formulation for PPC use a formulation similar to Equation 2.4-1, being the main difference between them, the way to calculate the crack spacing S_m. There is a huge range of formulations that include or exclude the different parameters affecting the crack-spacing; such as effective area, amount of reinforcement inside the effective area, cover or the influence of the stirrup spacing for the flexural cracking. Since different codes may propose different formulae, and the results from each one is very different, the crack spacing and, therefore, the crack width is a problem that has not been solved, even for reinforced concrete (RC).

In (Erlicher, 2014), the formulation of EC-2 and MC-2010 (European Committee for Standardization, 2004; FIB, 2010) are compared with the experimental results of the Concrack 4 (International Benchmark for Control of Cracking in R.C. Structures) performed by the French group CEOS. The study concludes that the codes overestimate the crack spacing but underestimate the stress on the reinforcements. This could mean that the tension stiffening has been overestimated, this should be taking into account in other calculations that take into account this tensile stress on cracked concrete.

2.4.2 Shear cracking

The shear cracking is more complex than normal stresses cracks. Shear cracks can have different directions, they are longer and the position of the wider part is not always at the end of the crack. Moreover, the stresses in the web are not always parallel to the cracks and the reinforcement is not placed at 90º of the crack.

due to the typical longer cracks, the more variation of its width along the same cracks and .

Cracks can be wider in the middle of the web and have their ends closed, but if there is interaction with the flexural cracks, this pattern can change. Figure 2.4-2 shows a typical example of diagonal cracking in beams with transversal reinforcement. The cracks run through the entire beam, reaching between them. Some of the cracks are concealed into the web without reaching the exterior. Every crack has multiple angles and they do not match with the angles that surround them.

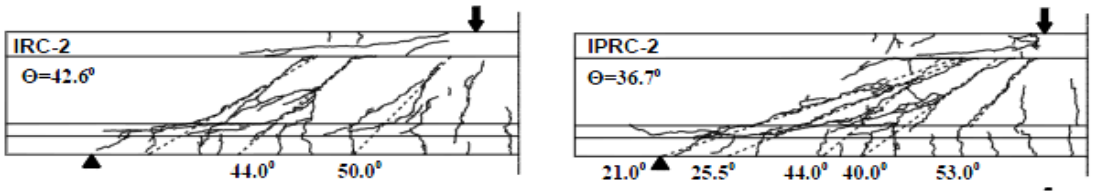

Figure 2.4-2 Difference between the crack pattern and angles of RC (left) and PPC (right) (De Silva *et al.*, 2006)

The Spanish code (Comisión permanente del Hormigón, 2008) uses Equation 2.4-1 to compute the crack with for normal stresses, but for diagonal cracking the approach is different. The code does not provide a formulation to compute the shear crack width, since the cracking serviceability limit state is directly verified if the conditions given for shear design for ultimate limit state are accomplished. When designing transversal reinforcement, the stirrup stresses are limited to control the shear crack width.

One may find two different approaches in the literature to compute the crack width for diagonal cracking. Both approaches are based on Equation 2.4-1, but one of them takes into account the principal strain of the concrete of the web (Equation 2.4-2) and the other one the stirrups strain (Equation 2.4-3). Both formulae use $S_{m\theta}$ as the spacing between the cracks, on the perpendicular direction of the cracks. The calculation of the spacing is where the different formulations differ.

$$w_k = kS_{m\theta}\varepsilon_{1m} \qquad 2.4\text{-}2$$

$$w_k = kS_{m\theta}\varepsilon_{wm} \qquad 2.4\text{-}3$$

ε_1 and $S_{m\theta}$ are calculated on the same direction (assuming the crack angle is very close to the truss angle), but the stirrup deformation and the crack spacing are usually not aligned. (De Silva, 2008; Zakaria *et al.*, 2009) establish an important relationship between the reinforcement ratios (transversal and longitudinal) and the crack width.

As is stated in (Collins and Mitchell, 1991; Witchukreangkrai *et al.*, 2006; Bairán *et al.*, 2014), two basic assumptions are established: a) The cracks are presented in a uniform pattern; and b) the cracks do not rotate. The spacing between cracks ($S_{m\theta}$) cannot be calculated directly. All the analysed formulations compute first the spacing on the horizontal (S_{mx}) and vertical (S_{my}) direction and compute $S_{m\theta}$ with Equation 2.4-4. Figure 2.4-3 shows the interpretation of the spacing in each direction.

$$S_{m\theta} = 1/\left(\frac{\sin\theta}{S_{mx}} + \frac{\cos\theta}{S_{my}}\right) \qquad 2.4\text{-}4$$

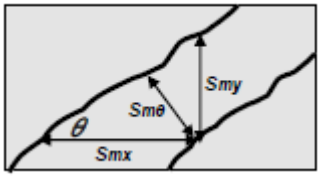

Figure 2.4-3 Representation of the crack spacing in the three directions

EC-2 EN-1992-1 presents a formulation to calculate the maximum spacing between the cracks in the two directions (Equation 2.4-5 and Equation 2.4-6). The spacing is function of the cover, parameters of stress, bar diameter and effective reinforcement ratio ($c, k_1, k_2, \emptyset_x, \emptyset_y$ and $\rho_{p,eff}$ respectively). But the EC-2 does not specify how to obtain the stirrups strain.

$$S_{max,x} = 3.4c + 0.425\, k_1 k_2 \emptyset_x / \rho_{p,eff,x} \quad \text{2.4-5}$$

$$S_{max,y} = 3.4c + 0.425 k_1 k_2 \emptyset_y / \rho_{p,eff,y} \quad \text{2.4-6}$$

$$\rho_{p,eff,x} = {A_{s,x}}\Big/{A_{c,eff,x}} \quad \text{2.4-7}$$

On the other hand, the CEB-FIP Model Code (1978), with its own average spacing formula, presented a way to calculate the stirrups strain. The crack spacing is defined for the two directions x and y, by using Equation 2.4-8 and Equation 2.4-9. In this case, the spacing is defined by the cover, the spacing of the rebars, the parameters of stress, the diameter of the rebars and reinforcement ratio (Equation 2.4-10 and Equation 2.4-11) ($c_{nx}, c_{ny}, S_x, S_y k_1, k_2, \emptyset_x, \emptyset_y, \rho_{cx}$ and ρ_{cy} respectively).

$$S_{mx} = 2\left(c + \frac{S_x}{10}\right) + k_1 k_2 \frac{\emptyset_x}{\rho_{cx}} \quad \text{2.4-8}$$

$$S_{my} = 2\left(c + \frac{S_y}{10}\right) + k_1 k_2 \frac{\emptyset_y}{\rho_{cy}} \quad \text{2.4-9}$$

$$\rho_{cx} = {A_{s,x}}\Big/{A_{c,eff,x}} \quad \text{2.4-10}$$

$$\rho_{cy} = {A_w}\Big/{(c + 8\emptyset_y)\,(15\emptyset_y)} \quad \text{2.4-11}$$

$$\varepsilon_{wm} = \varepsilon_w \left[1 - \left(\frac{V_{c0}}{V}\right)^2\right] \geq 0.4\varepsilon_w \quad \text{2.4-12}$$

Equation 2.4-12 presents the transformation between the strain obtained from the shear resistance of the beams and the value used in Equation 2.4-3. The strain is reduced based on the ratio of the shear resistance of the concrete over the applied shear of the section. There is a minimum transference ratio due to the shear cracking.

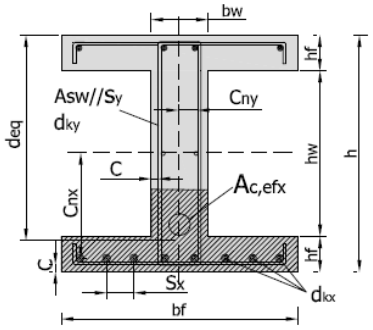

Figure 2.4-4 Geometrical parameters used to calculate the horizontal and vertical spacing

De Silva, in his dissertation, proposed a new formulation based on the previously presented of CEB-FIP Model Code. He multiplied the spacing by factors $\alpha = 0.4$ and $\beta = 0.35$. Like other formulations had done previously, he changed the cover by the distance from the reinforcement to the centroid of the section (Equation 2.4-13 and Equation 2.4-14) (Figure 2.4-4). To compute the stirrup strain for Equation 2.4-3, he uses directly the strain from the shear resistance equation (Equation 2.4-15). The innovation presented in (De Silva, 2008) was the addition of the prestressed reinforcement as part of the calculations to obtain the spacing.

$$S_{mx} = 2\alpha\left(c_{nx} + \frac{S_x}{10}\right) + k_1 k_2 \alpha \frac{\emptyset_x}{\rho_{cx}} \quad \text{2.4-13}$$

$$S_{my} = 2\beta\left(c_{ny} + \frac{S_y}{10}\right) + k_1 k_2 \beta \frac{\emptyset_y}{\rho_{cy}} \quad \text{2.4-14}$$

$$\varepsilon_w = \frac{V - V_{c0}}{\frac{A_w}{s} z(\sin\alpha_s + \cos\alpha_s)\cot\theta\, E_w} \quad \text{2.4-15}$$

(Bhide and Collins, 1989) proposed a formulation based on the principal strains of the concrete in the web (Equation 2.4-2). These authors assumed that the shear crack angle and the principal directions were similar. They introduced the change of the cover over the distance between the centroid and the reinforcements (Equation 2.4-16 and Equation 2.4-17). However, in this study, they did not presented an experimental verification for their model.

$$S_{mx} = 2\left(c_{nx} + \frac{S_x}{10}\right) + 0.1\frac{\emptyset_x}{\rho_{cx}} \quad \text{2.4-16}$$

$$S_{my} = 2\left(c_{ny} + \frac{S_y}{10}\right) + 0.1\frac{\emptyset_y}{\rho_{cy}} \quad \text{2.4-17}$$

$$\rho_{cx} = {}^{A_{s,x}}\Big/_{A_{c,eff,x}} : A_{c,eff,x} = 2.5\,(h-d)b_w \quad \text{2.4-18}$$

$$\rho_{cy} = {}^{A_w}\Big/_{b_w S_y} \quad \text{2.4-19}$$

(Yoon, Cook and Mitchell, 1996) presented a simplified version of the calculation. They consider the principal strain in the concrete was a reasonable approach to calculate the crack width (Equation 2.4-2). They reduced the number of factors to compute the spacing. They conclude that the horizontal

and vertical spacing of Equation 2.4-4 were the effective depth (d) and the distance between stirrups (S_y), respectively.

2.4.3 Strain variation in stirrups

As it has been previously described, several formulations use the strain of the reinforcement to predict the shear crack width. The formulations presented methods to obtain the strain from the applied shear and the shear resisted by the concrete. In (De Silva *et al.*, 2006; De Silva, 2008), it is presented an experimental campaign designed to analyse shear crack width in PPC beams. The stirrups of the beams were instrumented with strain gauges to analyse the strain in the reinforcements.

The strain gauges were placed in the stirrups at five different depths, to analyse the variation of the strain due to cracks and relative position in the web. As it can be seen in Figure 2.4-5, the variation of strain in a single stirrup is very important. The influence of the position and its proximity to a crack it is crucial.

The monotonic load applied in their campaign, produced the yielding of certain parts of the stirrup but maintained the rest of the stirrup in linear behaviour. There were important concentration of strains.

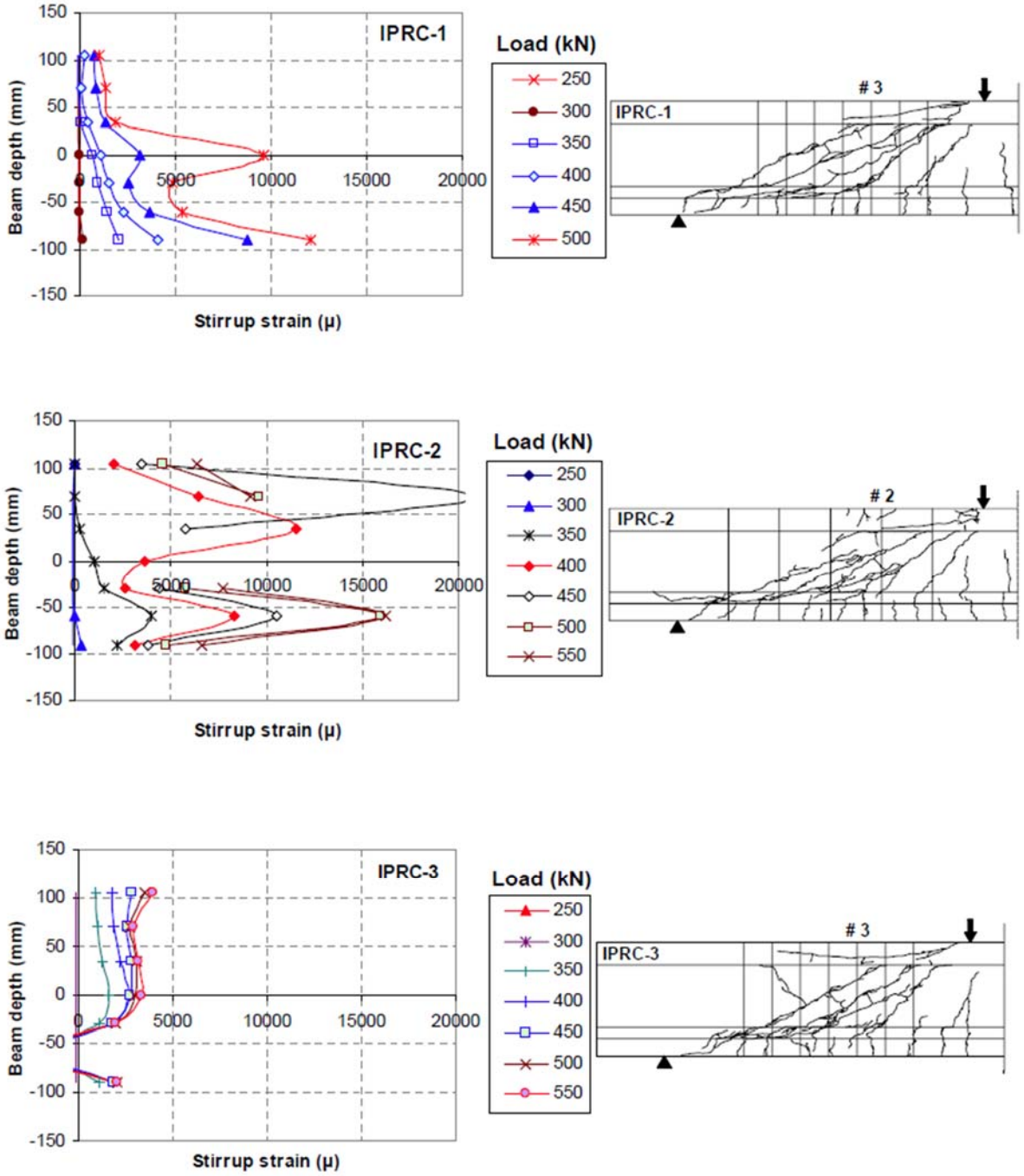

Figure 2.4-5 Stirrup strain variation along the beam depth at the critical section (De Silva, 2008, p. 65)

2.5 Conclusion

PPC is a technique that can provide more efficient structures. The use of TPC is more extended due to its simpler design. To obtain PPC structures, a new method (Bairán and Marí, 2011) had been presented allowing an easier approach without the need of an iterative process.

There are many models to describe the shear resistance of concrete structures. For T and I shaped beams the models provide very different results. An experimental campaign is required to compare

with the different formulation to provide a clearer understanding of the mechanical process and point out the best approach between the different formulations.

The main approach to calculate the average crack width in concrete is the product between the strain of the reinforcement and the crack spacing. To obtain the maximum crack width a statistical factor, obtained from experimental results, has to be applied. For cracks perpendicular to the reinforcement (bending moment cases) the formulation overestimate the crack spacing but underestimate the stress on the reinforcement.

To determine the width of the shear crack (diagonal cracking non-perpendicular to the stirrups) some models use the reinforcement strain and other use the principal strain of the concrete in the web. The calculation of the crack spacing has very different approaches, depending on the model and formulation. The parameters used to determine the crack spacing are very different between formulations. In this chapter, the calculation of the reinforcement strain was presented using different formulas in each model.

The strain distribution in the stirrups has been proved to be very dependent on the crack position. Moreover, the strain variation along the stirrups was significant. Some parts of the stirrups had yielded (with large deformations) while the rest of the stirrup was still in elastic domain.

Several methods have been proposed to define PPC structures. The method proposed in (Bairán, Marí and Duarte, 2011) was the most competent and practical to define PPC beams, since the process did not involved iterative calculation and it was very similar to the Magnel diagram.

3 Experimental Campaign

3.1 Introduction

The experimental campaign associated to this thesis was designed in 2013. The campaign consisted in 8 partially prestressed concrete (PPC) beams, of 8 meters long, with an I-shaped section, with a bonded post-tensioned system. The elements were casted at the precasting company Norden (Prainsa group).

The main objective of this campaign is to analyse the behaviour of PPC under pure bending moment and combined shear forces and bending moment. The beams were testes twice, 12 tests to study shear behaviour and 4 to study bending moment behaviour The tested elements are a representation of a prestressed bridge. The I-shape of the members represents the web of a box girder bridge or individual beams of an I shape girder bridge (Figure 3.2-1).

The tests were design to study the influence of web width, stirrup ratio, prestress tension and lay out over shear behaviour and the influence of longitudinal reinforcement and prestress tension over bending moment.

The first test was carried out on May 15th, 2015, and the experimental campaign finished March 1st, 2016.

3.2 Geometry

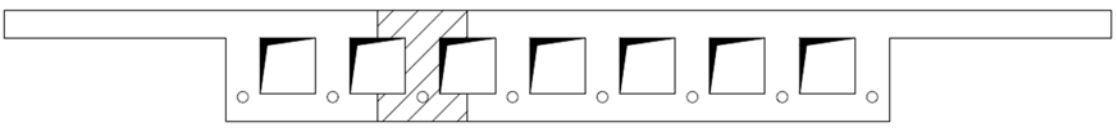

Figure 3.2-1 I shape girder bridge, with an individual girder highlighted.

Due to space limitations in the *"Laboratori de Tecnologia d'Estructures Lluis Agulló"* (LTE Lluis Agulló). and the size of its equipment, the length of the beams was set to 8m. The transverse section was 500 mm high, with identical top and bottom flanges of 100 mm thick and 500 mm wide, as shown in Figure 3.2-2. To study the influence of the web and the compression chord in the shear resistance, two

different widths for the web were chosen: 120 mm and 180 mm (Figure 3.2-3). End blocks of 50 cm long were provided at each end of the girders, with the same flanges width to accommodate the anchorage reinforcement.

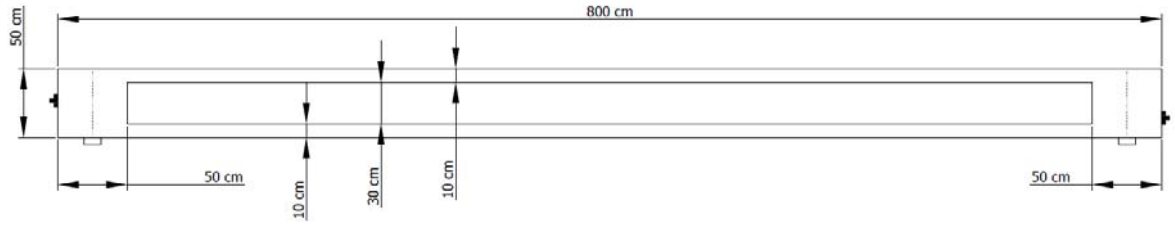

Figure 3.2-2 General description of the geometry of the beams.

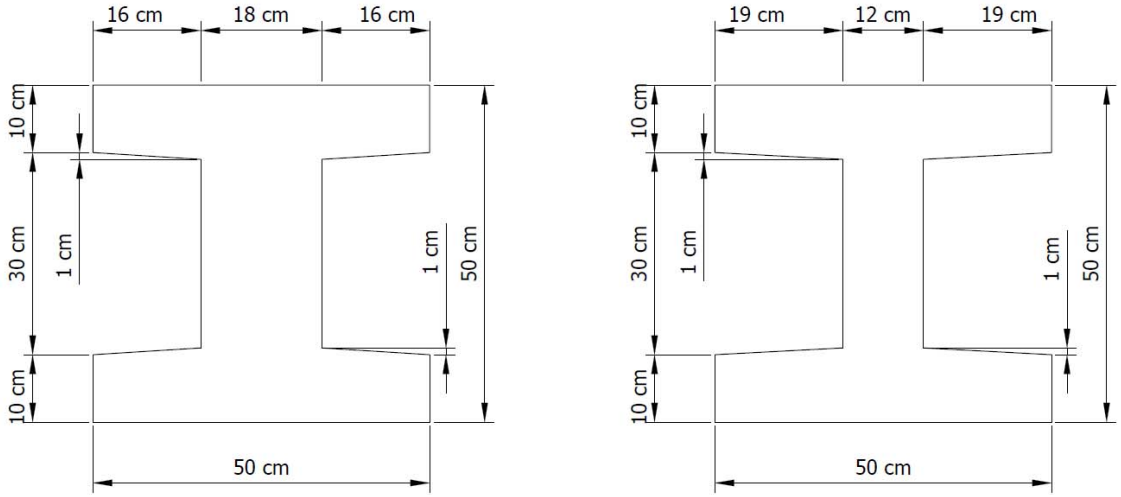

Figure 3.2-3 Transverse section of the beams.

In post-tensioned structures, the typical layout of the prestress reinforcement is not a straight line at a constant depth. Usually, the layout is used to balance the bending moment or the shear stresses. All the studied specimens had similar layout, with the aim of reproducing the behaviour of prestressing layouts in post-tensioned bridges. As shown in Figure 3.2-4, the polygonal layout of the prestress reinforcement consisted in four segments.

The first segment is on the left part of the beam (in Figure 3.2-4), with an inclined straight layout. The line goes from the anchorage height (27,1 cm) towards the bottom of the beam, at a length of 167 cm. The central straight segment has constant height, at 10 cm from the bottom. These two straight lines are connected by a parabolic segment of 800 cm radius. This segment leaves the first line at 167 cm from the anchorage and finishes at 235 cm in the second line. The second line reaches the third line segment 100 cm before the right end. The third line reaches the end in the anchorage (14,5 cm high). The inclination angle of the first straight segment is 5º. The left support is placed on the *I* section and the right one on the *R* section, the left and right support respectively (Figure 3.2-4).

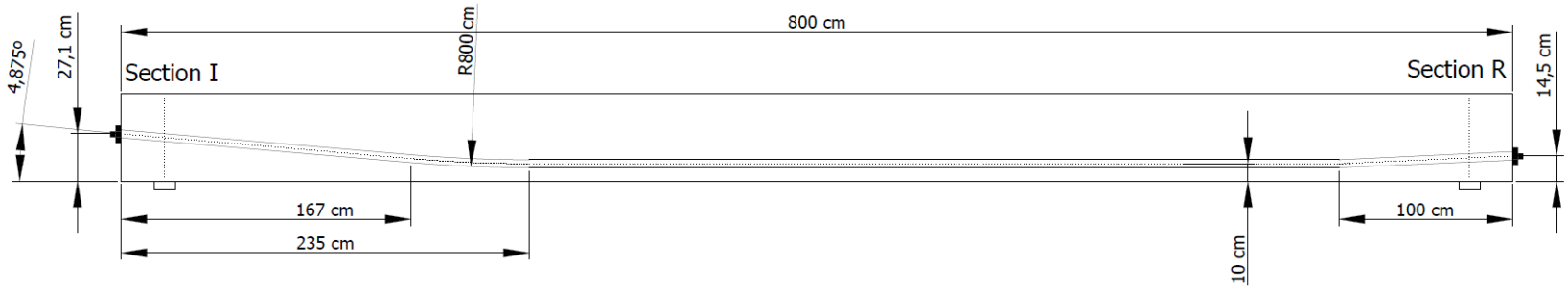

Figure 3.2-4 Lay out of the duct

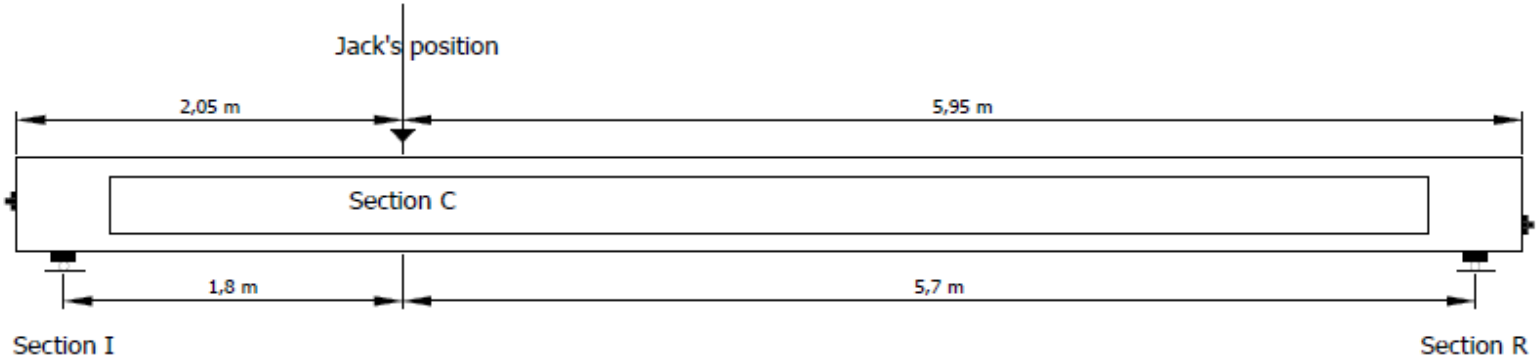

Figure 3.2-5 Set-up 1: long span shear test

In an isostatic bridge, the maximum shear stresses occurs near the supports where there is an inclined layout. In continuous bridges, the maximum shear force could occur also in the support, where the position of the cable is straight and the cables are not close to the centroid of the section. In turn, the maximum stresses due to bending moment tend to occur only at midspan, where the lay out is flat.

This configuration creates two different zones to study in each beam. The left side (I) with an inclined layout and the right part where the prestress is horizontal. This different layout configuration allowed testing each beam twice. For the first test, the full span of the beam (Figure 3.2-5) was used. Once the beam had failed, the set-up was changed, moving the left support and the beam was tested again focusing on the other side of the beam. The first test set-up had the supports placed at 25cm from the ends of the beam. The span of the beam was 7.5 m. This set up was used for the long span shear test. The jack was placed in section *C,* at 1,8 m from section *I.*

The second test of a beam was performed in the right part of the beam. Two test set-ups were designed for this second test, the set-ups shared the support disposition but with different load distribution. After the first test was performed, the left support was moved to section *C.* The second set-up was designed for a shear test; the jack was positioned at 2.1 m from the section *R*, section *M2 (*Figure 3.2-6). The third set-up was for four-point flexural test. In this case, an auxiliary steel beam was used to divide the jack load in two forces in middle of the span. The two forces were placed at 2.1 m from the sections *C* and *R,* 1.5m apart one from the other, sections *M1* and *M2* (Figure 3.2-7).

The distance between supports and load application point was related to the depth of the beam, in order to avoid arch effects and D regions on the test, especially on the shear tests. Section 3.4 Set-up contains a more detailed explanation of the Set-up

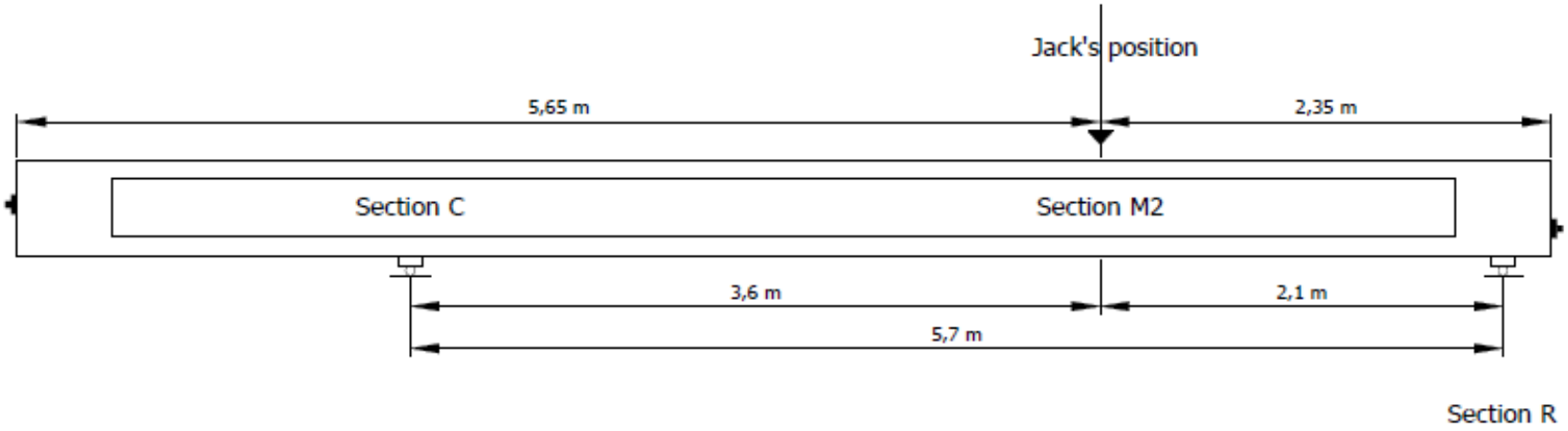

Figure 3.2-6 Set-up 2: short span shear test

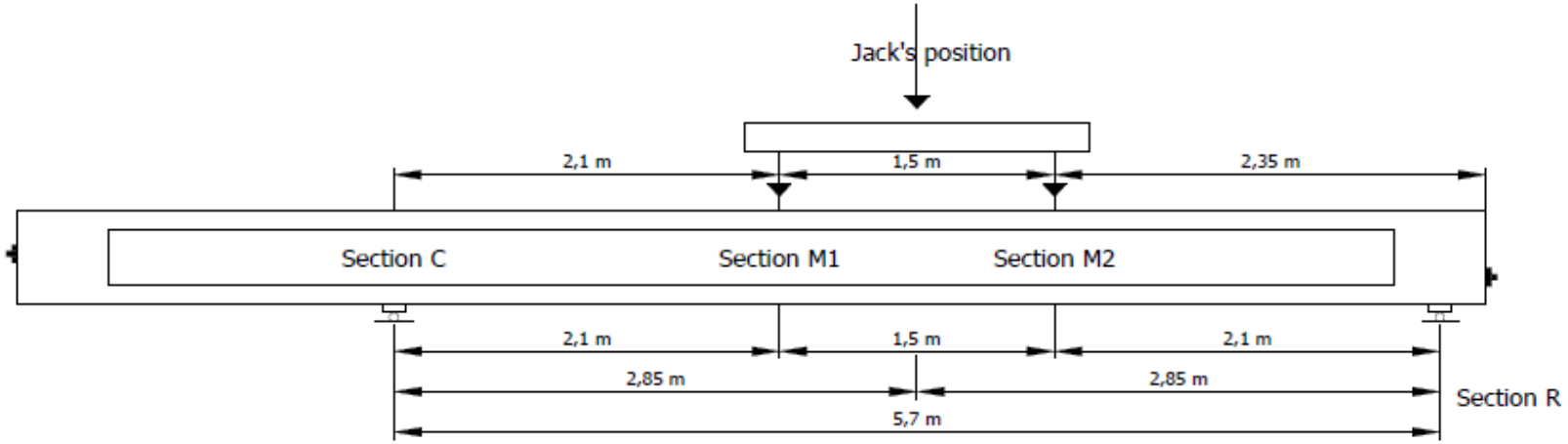

Figure 3.2-7 Set-up 3: bending moment test

The main factors to study during the shear test were: web width, prestressing force and transverse reinforcement. For each variable, two different values have been studied. For the prestressing reinforcement area, 2 or 4 strands of 140 mm^2 were stressed at the same initial tension, so there were two different initial prestressing forces. The initial stress of the cables was 1150 MPa. Therefore, a prestressing force of 294 kN or 588 kN was applied to the beams. The shear reinforcement consisted on rebars at 150 mm or at 250 mm. To cover all the combinations, 8 beams were built. This combination of specimens allowed to perform a parametric study of the influence of each parameter: web width, prestressing force and transverse reinforcement (Figure 3.2-9).

These eight combinations were tested under shear using the first set-up (inclined layout). To analyse the influence of the cable position in the shear tests, the four beams with 120mm of web width were shear tested again, using the second set-up (flat layout). To perform the layout influence analysis, the amount ordinary reinforcement (transversal and longitudinal) remained the same in both ends (Table 3.2-1).

The variation of other minor parameters was also analysed. Three parameters were selected, with two different values for each parameter. The parameters were 1) the amount of longitudinal reinforcement on the bottom flange, 2) the number of bars on the web, and, finally, 3) the horizontal transverse reinforcement cover in the web. The reinforcement on the bottom flange was 6Ø25 and 2Ø10 or 8Ø25 and 2Ø10. Both values largely ensured that the beam would not fail due to flexure. In the web, 2 or 6 longitudinal bars were placed, as can be seen in Figure 3.2-9. Even though the vertical cover was 25 mm for all the beams, the cover of the web for the beams was changed to evaluate its influence. The cover was reduced to 15 mm in half of the cases.

The bending moment tests were performed with the aim to analyse the relationship between crack patterns, stress in the longitudinal reinforcement and the prestress level of the strands. The objective was to compare beams with similar behaviour in service but different ultimate load, and, conversely, similar ultimate load but different behaviour in service.

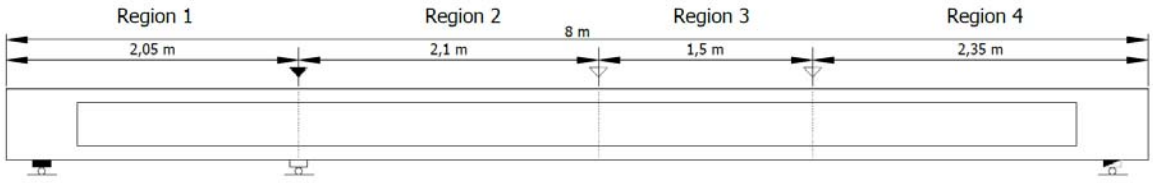

Figure 3.2-8 Regions of reinforcement of the beams

Four-point bending test were performed in the beams with 180 mm web width, using the third test set-up. In these beams, the longitudinal reinforcement of the right part of the beam (Region 3 and 4, Figure 3.2-8) was reduced and the transverse reinforcement increased. The former considerations were made to ensure that the failure mode and critical regions of the specimens were as expected.

There were three combinations of longitudinal reinforcement. The lower one consisted in 6 Ø10 rebars, the medium one 6 Ø16 rebars and the higher one the combination of 4 Ø25 and 2 Ø10 rebars. To obtain the two pairs of specimens with similar ultimate resistance, previously mentioned, the beams with 2 strands had the medium and the higher reinforcement rate and the beams with 4 strands, the lower and medium reinforcement rate (Table 3.2-1). To ensure the test failed in flexure,

the transverse reinforcement was upgraded to Ø8 at 200 mm in region 3 and at 100 mm in regions 2 and 4 (Figure 3.2-9).

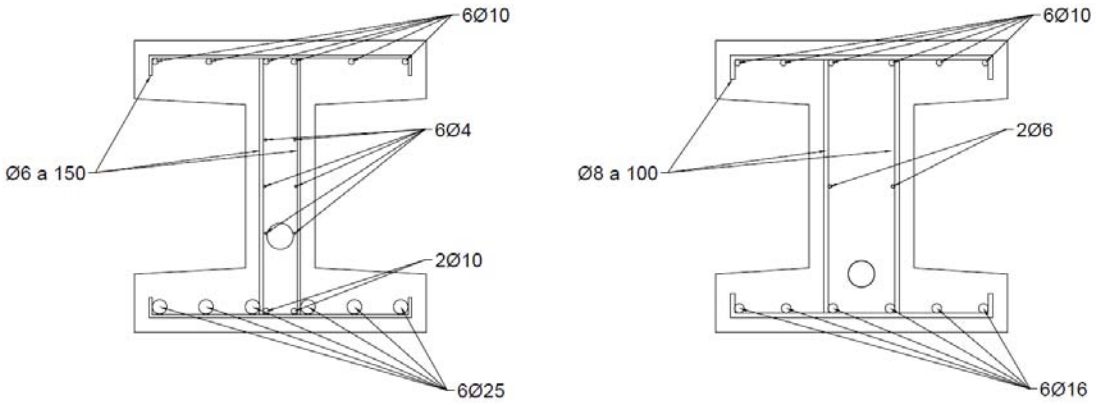

Figure 3.2-9 Region 1 Beam I123 (left) and Region 4 Beam I184 (right)

Two metallic supports were used in the beams of the shear tests. The support closer to the jack was a roller support to avoid arch effects (Figure 3.2-10). This support allowed the rotation and the displacement of the section. The other support was a pinned support, only allowing the rotation of the section. The jack was located on top of a rubber to apply the force over the beam. The bending moment test had 2 metallic supports and 2 rubbers. The pinned support was placed under section *C*. The roller support was placed under section *R.* The metallic beam, which distributed the single force of the jack to the 2 points load, was placed over two rubbers (Figure 3.2-11). A more extended explanation is presented in Section 3.4.

Figure 3.2-10 Detail of a rolled support

Figure 3.2-11 Metallic beam to distribute the jack load for the four-point bending tests

Since the beams were tested twice, maximum control of the failure location should be ensured. Therefore, the beams were divided in 4 parts (Figure 3.2-8). The first part was in between the end *I* and the load point *C1*. This region had to be weaker than the rest to ensure that the shear failure would occur inside this area. The second region went from the load section *C1* to section *M1*. This region had the same longitudinal reinforcement than the first one but with a higher amount of transverse reinforcement. The third region was in between sections *M1* an *M2*. This region was identical to the second region for 120 mm beams but had a lower amount of longitudinal reinforcement for the 180 mm width beams (4-point bending tests). The fourth region was identical to the first one in the 120 mm width beam and identical to the third for the 180 mm width beams. This configuration ensured failure of the beams happened on the region under control.

The labelling of the beams had the notation "IAAB". The "I" represented the shape of the cross section. "AA" was the width of the web, that could be 12 or 18 and "B" was a number between 1 and 4. "B" was an ordinal to refer to the beams. As it can be seen in Table 3.2-1, the "B" represented a combination of number of strands and spacing of stirrups. To identify the side of the beam where the test was performed, after the name of the beam four letters were added. For the test carried out with the load on point *C,* "*Incl"* was added at the end. For the test that was carried out on the part of the beam where the layout of the strands were horizontal, the code was "*Rect."*

Table 3.2-1 presents a summary of the geometrical properties of the beams and the typology of test that was performed on each end of the beams.

Table 3.2-1 Reference name and characteristics of the tests

Test	Typology	Prestress area (mm^2)	Web Width (mm)	Ssw (mm)	Asl Inf	Astw
I 121 Incl	Shear	560	120	150	6Ø25+2Ø10	Ø6
I 122 Incl	Shear	560	120	250	8Ø25+2Ø10	Ø6
I 123 Incl	Shear	280	120	150	6Ø25+2Ø10	Ø6
I 124 Incl	Shear	280	120	250	8Ø25+2Ø10	Ø6
I 181 Incl	Shear	560	180	150	8Ø25+2Ø10	Ø6
I 182 Incl	Shear	560	180	250	6Ø25+2Ø10	Ø6
I 183 Incl	Shear	280	180	150	8Ø25+2Ø10	Ø6
I 184 Incl	Shear	280	180	250	6Ø25+2Ø10	Ø6
I 121 Rect	Shear	560	120	150	6Ø25+2Ø10	Ø6
I 122 Rect	Shear	560	120	250	8Ø25+2Ø10	Ø6
I 123 Rect	Shear	280	120	150	6Ø25+2Ø10	Ø6
I 124 Rect	Shear	280	120	250	8Ø25+2Ø10	Ø6
I 181 Rect	Bending Moment	560	180	100	6Ø16	Ø8
I 182 Rect	Bending Moment	560	180	100	6Ø10	Ø8
I 183 Rect	Bending Moment	280	180	100	4Ø25+2Ø10	Ø8
I 184 Rect	Bending Moment	280	180	100	6Ø16	Ø8

3.3 Materials

The precasting company Norden made the reinforcement work and the installation of the duct for the strands during the third quarter of 2014. The casting process was made between November 7th and 21st of that year. The application of post-tensioning forces was performed by VSL prestressing systems; they also provided all the prestress devices such as ducts, strands and anchorages. All beams were prestressed in November 24th,2014.

Table 3.3-1 Casting date and days until prestressing

Beam	Casting date	Days to prestress
I121	07/11/2014	17
I122	11/11/2014	13
I123	05/11/2014	19
I124	12/11/2014	12
I181	19/11/2014	5
I182	21/11/2014	3
I183	17/11/2014	7
I184	14/11/2014	10

On January 8th, 2015, the beams were transported to the *"Laboratori de Tecnologia d'Estructures Lluis Agulló"* (LTE Lluis Agulló). On February, VSL came to the laboratory to perform the injection of ducts with a high strength cement, to activate bonding. The execution process of the 8 bonded post-tensioned concrete beams was then completed.

The campaign was designed with a unique concrete compression strength for all the tests. However, due to problems with the casting and variation during mixture, the final properties of the concrete presented a considerable variation in between all beams. The original characteristic compression strength was 45MPa. Compression tests performed 28 days after casting showed an average mean value of compression strength of 51.8 MPa and a characteristic compression strength of 35.9 MPa. Table 3.3-2 shows the Young modulus, compression strength and tensile strength of the concrete samples obtained the day of the test of the corresponding beams.

Table 3.3-2 Concrete properties the day of the test

	Ec	fc	fct
I121	36.0 GPa	69.7 MPa	3.8 MPa
I122	29.3 GPa	52.6 MPa	4.3 MPa
I123	27.3 GPa	43.9 MPa	3.5 MPa
I124	36.4 GPa	57.0 MPa	4.1 MPa
I181 Incl	33.2 GPa	59.0 MPa	4.1 MPa
I182 Incl	34.3 GPa	60.0 MPa	5.3 MPa
I183 Incl	30.5 GPa	45.3 MPa	4.4 MPa
I184 Incl	35.4 GPa	63.9 MPa	4.6 MPa
I181 Rect	33.4 GPa	62.3 MPa	4.2 MPa
I182 Rect	34.7 GPa	63.7 MPa	4.8 MPa
I183 Rect	30.0 GPa	47.4 MPa	4.2 MPa
I184 Rect	35.1 GPa	66.9 MPa	4.8 MPa

3.4 Set-up

This experimental campaign was carried out in the "*Laboratori de Tecnologia d'Estructures Lluis Agulló*" (LTE Lluis Agulló), and consisted of 16 tests. They were organized on three groups: 8 long span shear test, 4 short span shear test and 4 four-point bending test. The same jack was used for the 16 tests. A steel beam was used in the four-point bending moment test to split the jack load into two point loads.

The jack was fixed to a steel frame structure fixed to the strong floor of the LTE. It is a MTS jack with two fixed hinges, a load capacity of 1000kN and a range of movements of 500mm. When the rod is picked up, there are 1.5 m of free span under the jack. This free span limitation was enough to perform all the shear tests with the initial supports. To perform the four-point bending test, a beam to distribute the load into two points had to be added to the jack. To compensate the extra height, the supports were replaced by smaller beams.

There were two test sequences, one for the beams with a web width of 120 mm (I120) and one for the beams with 180 mm of web width (I180). The I120 were only subjected to shear tests. Due to the similarity in the configuration between long and short span shear tests and the available space for the storage of damaged beams, the two shear tests of each beam (one with long and the other with a short span) were performed one after the other. In turn, the specimens I180 had two very different configuration for each test, so the four long span shear tests were performed and then the four-point bending tests.

The first set-up (Set-up 1) (See Figure 3.4-1), was used to perform the long span shear tests. The support on section *I* was 1.8m apart from the position of the jack (section *C*). The other support for the section *R* end was 7.5 m from section *I* and 5.7 m from section *C*. The supports were made of several layers. The bottom layer was a metallic beam of 700x400x400 mm, stiffened with ribs. Over the metallic beam, load cells were placed. On top of the load cells, support devices were placed.

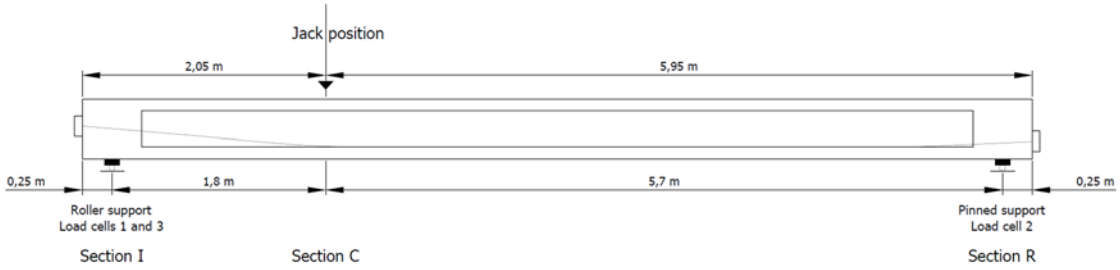

Figure 3.4-1 Set-up 1

The support devices featured three pieces. The bottom one was a steel plate with a cylindrical incision in the centre (Figure 3.2-10 Detail of a rolled support (Figure 3.2-10). The central part was a cylinder and was placed inside the incision. The top part was a simple plate or a plate with an incision, to generate a rolled or a pinned support, respectively. In support *I*, the steel plate was used to allow the rotation and displacement of the beam. In support *R*, the steel plate with incision was set, to allow the rotation but not the displacement of this section. On top of it, to guarantee the perfect contact between steel and concrete, a 10 mm rubber band was placed. In section C, to assure a good contact between the steel of the jack and the top of the beam a 100x300x250 mm rubber was placed. The rubber was changed after a number of test to avoid an excessive transversal deformation.

The Set-up 2 (Figure 3.4-2) was designed to perform the short span shear tests. After the long shear span test, the beam was moved 3.6 m. In the final position, the section *R* was 2.1 m away from the jack, section *M2*. Therefore, the supports were moved. The support that was under the section *I,* was moved 1.8m from its position. It was then located 3.6 m from the load and was under section *C,* where the load was applied in the long span test. The support on section *R* moved like the beam. In this set-up, the region 1 (between sections *I* and *C*) was in a cantilever configuration, and the damaged region did not affect the test. In this configuration, the type of supports were switched. The hinge was placed in section *C* and the plate to allow rotation and displacement was placed in the *R* support.

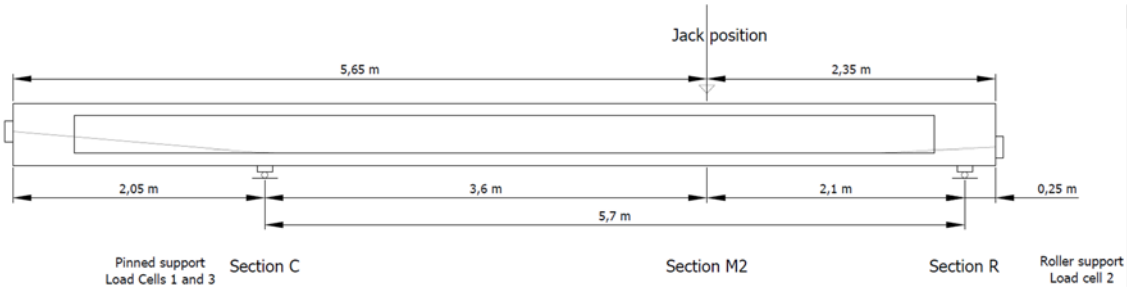

Figure 3.4-2 Set-up 2

The Set-up 3 (Figure 3.4-3) was designed to perform a 4-point bending test. These tests were the last set of the experimental campaign and were carried out without modifying the support configuration in between tests. The main difference between this configuration and the previous ones is the two load application points. To achieve it with only one jack, the jack was connected to the centre of a

200x26x20 cm steel beam (Figure 3.2-11). The interface between steel beam and the concrete beam was a 100x300x250 rubber. The rubbers were placed on sections *M1* and *M2*. Both *C* and *R* supports were located at 2.85 m from the jack, the four-point bending test schematic was symmetric. Due to this additional spacing between the jack and the beam, the supports used in the other set-up were too big. Consequently, the steel beams of the supports were changed to smaller beams. Due to the larger deflections that were expected and the reduction of the size of the supports, the Temposonics to register the vertical deflection were placed on the side of the flange.

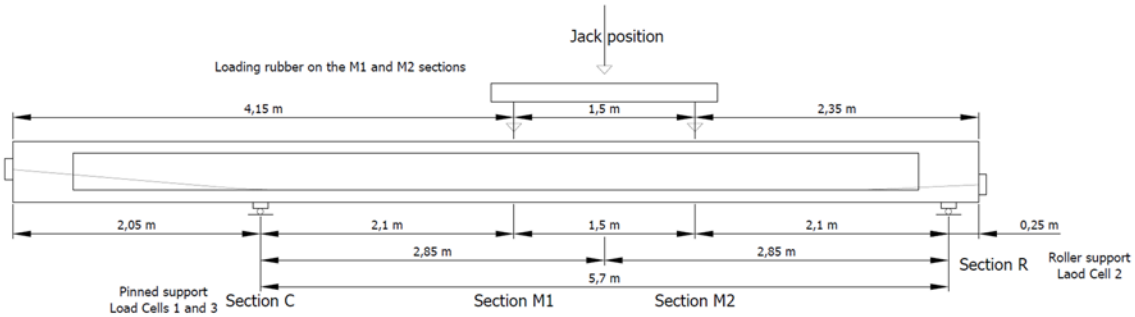

Figure 3.4-3 Set-up 3

3.5 Loading Protocol

This experimental campaign aimed to study the behaviour of PPC beam at service and failure conditions. Current codes establish serviceability limit state and ultimate limit state to represent the different situation that have to be taken into account when designing a structure. The serviceability state is a set of load combinations that represent different situations that will occur regularly to the structure. The ultimate limit state represent the loads that the structure has to endure before failure.

The goal of serviceability limit state is to control the parameters that affect the comfort, durability and aesthetic of the structures, checking the deflection of the beams or the crack opening. For partially prestressed concrete (PPC), cracks are allowed to be formed under the frequent load combination but the crack width and the stresses of the reinforcement would be within the standards.

For the experimental campaign, when designing the load protocol, a monotonic loading was discarded because the behaviour of the structures under low load levels varies significantly if the structures have been previously cracked. Since real bridges may have to resist important loads in early stages of their life span (like during the loading tests), the load protocol included load cycles from quasi-permanent level to characteristic level.

These cycles would allow us to analyse the variation on the behaviour of the PPC to control the cracking of the beams. To do so, force holds were introduced during the cycles. These holds maintained stable the readings of the sensors and allowed us to take pictures, during different cycles, at the same load. If differences were observed, it would imply a variation on the behaviour of the structure, due to the stabilization of the crack or due to the yielding of some reinforcement. These holds started when the desired load was reached and maintained the load for a specified time, as shown in Figure 3.5-1.

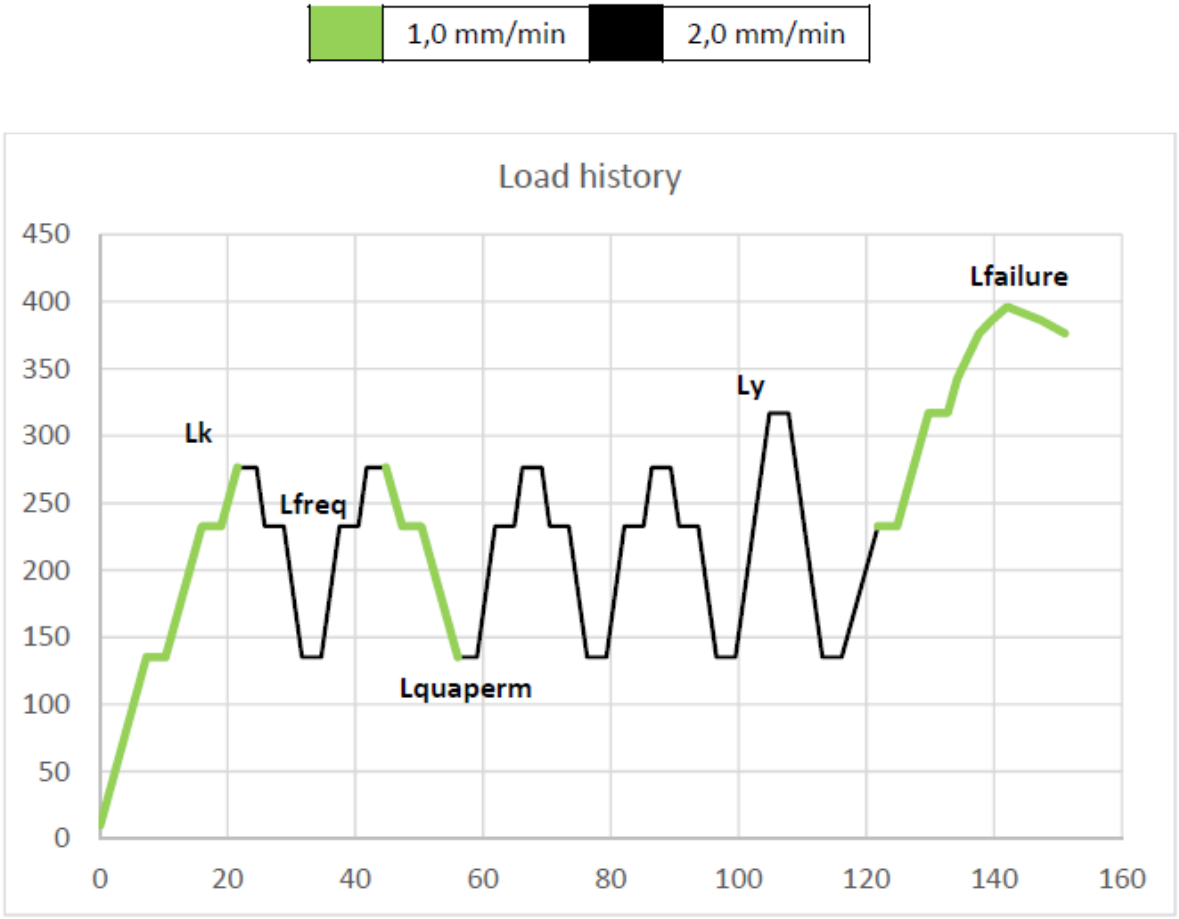

Figure 3.5-1 Load history for shear test

For the four-point bending test, four extra cycles were performed. The cycles were composed by 4 triangular waves. The first two cycles were centred on the quasi-permanent level and the last two on the frequent level (Figure 3.5-2). The amplitude of the first cycle in each load level was 10 kN, for the second cycle, it was increased to 40 kN. To conclude the tests, the beam was loaded up to the yielding load, then unloaded to the quasi-permanent level and finally it was loaded up to failure (see Figure 3.5-3).

The four-point bending test lasted longer than the shear tests and had to be split into two tests, performed in two consecutive days, The first day englobed all the service cycles (Figure 3.5-2) and the second day included the loading to yielding level plus the failure of the beam (Figure 3.5-3).

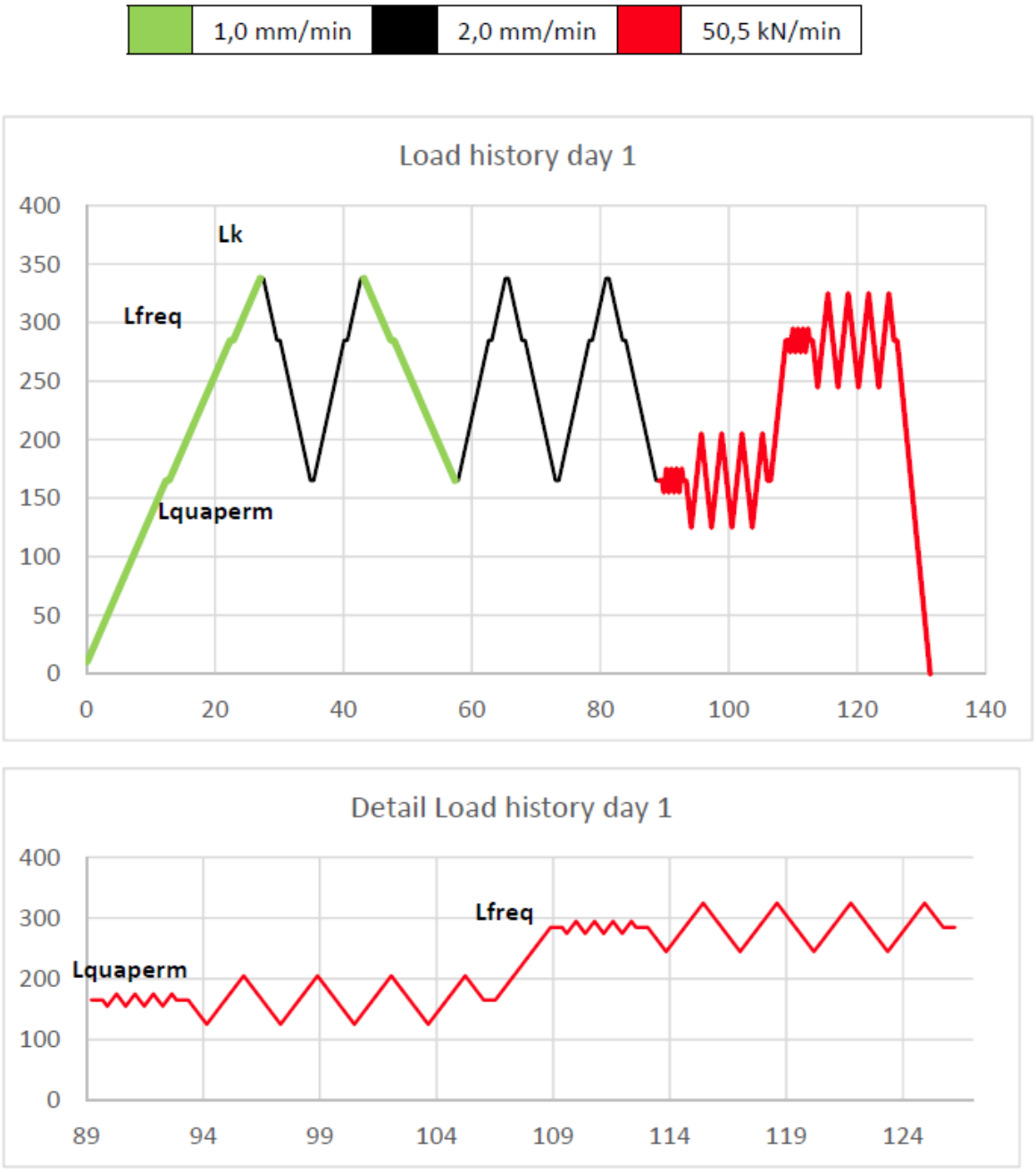

Figure 3.5-2 Load history for bending moment test, day 1

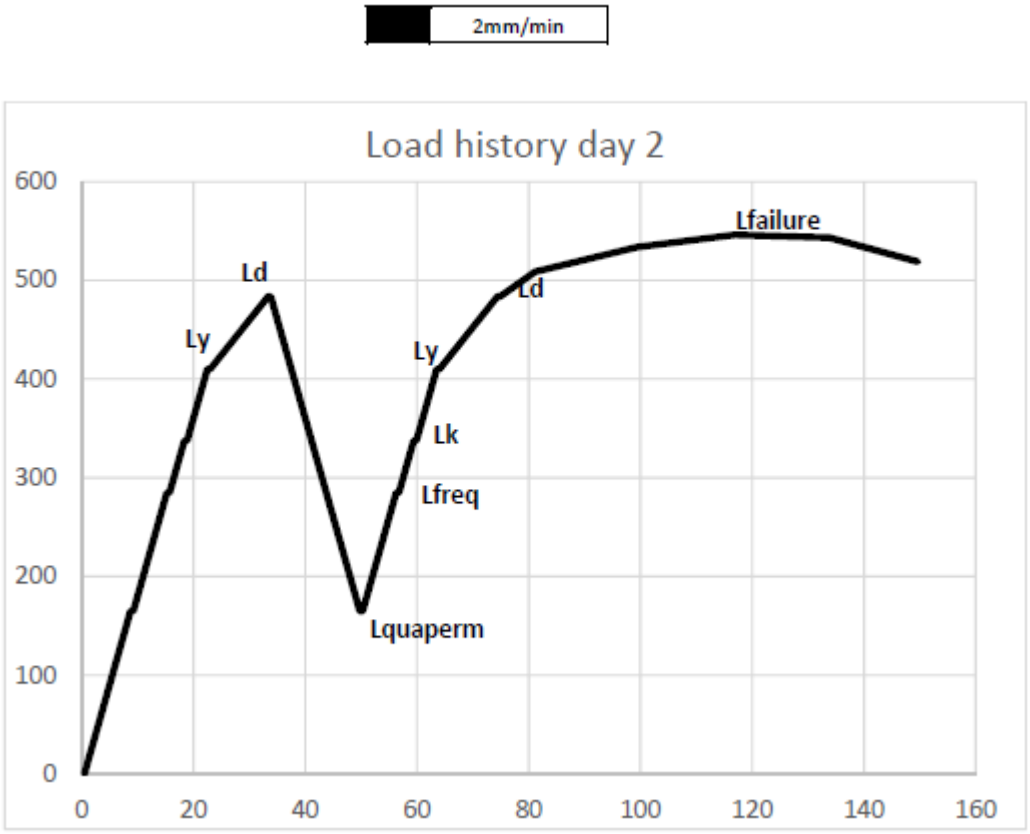

Figure 3.5-3 Load history for bending moment test, day 2

The load was applied using displacement control, but the holds were controlled by force. In the first test, the I122_Incl, a speed of 0.5 mm/min was applied at the beginning of the test. The speed was increased after the first cycle up to 1 mm/min. Then the speed ratio was decreased to 0.5 mm/min during the final ramp to ensure that the beam failure was accurately recorded. For the second test, I122_Rect, the speed of the test was 1mm/min during the initial and final ramp and the rest of the test was performed with a 2 mm/min speed. For the third test, I124_Incl, the same configuration of the first test was used. After analysing the results and taking in to consideration the duration of the tests it was decided to increase the speed load of the remaining test to 1 and 2mm/min, like in the second test.

The load protocol used for the rest of the tests had the first ramp at 1 mm/min, continued with 2 mm/min until the next pick. Decreased to 1 mm/min for the unloading and then proceeded at 2 mm/min until the last ramp where the ratio decreased again and became 1 mm/min until failure. For the extra cycles of the 4-point bending, force control was applied with a ratio of 50 kN/min, generating a faster loading process. After these cycles, displacement control was applied with a 2 mm/min speed ratio.

The last step to obtain the loading protocol was to establish for each test the load levels. An algorithm was developed to obtain the different load levels as a function of a theoretical load distribution. The algorithm had two steps, the first one divided the load it into three components (Table 3.5-1). The second step combined the components to obtain each load level (Table 3.5-2).

The components represents the distribution of the loads in a structure: permanent load (LPer), variable load (LVar) due to heavy vehicles (LHeaVeh) and the rest of variable loads (LRest). The weights for the LPer and LVar were assumed 40% and 60%, respectively. The weighted distribution between LHeaVeh and LRest was 70% and 30%, respectively. The combination of these coefficients gave us the weighted distribution of the three components, LPer, LHeaVeh and LRest equal to 0.40, 0.42 and 0.18, respectively. Each load level was a combination of the three components. The algorithm provided the combination factors to produce the load for the quasi-permanent level (Lquasiperm), the frequent level (Lfreq), the characteristic level (Lk) and the design level (Ld).

Table 3.5-1 Relationship between permanent and variable loads

LPer	LVar	
	LHeaVeh	LRest
0.4	0.6	
	0.7	0.3
0.4	0.42	0.18

Table 3.5-2 Combination factor for the different load levels

Combination factor	LPer	LVar	
		LHeaVeh	LRest
Ld	1.35	1.5	0.6
Lk	1	1	0.4
Lfreq	1	0.75	0.2
Lquaperm	1	0	0.2

For the shear tests, the level reference was Ld load, it had to match the failure load, establishing the rest of load levels. For the bending moment test, the set of load levels obtained with the algorithm was compared with the loads from the simulations. The load levels had to match with the expected behaviours (crack widths, tension on the reinforcements and stress on the compression chord), establishing all the load levels.

3.6 Instrumentation

The evolution of the strain in the reinforcement is an important feature to describe the behaviour of the beams. To take into account the strain variation in the stirrups, produced by the cracks, three strain gauges were placed in the stirrups. Moreover, the interest lied in knowing the strain and stress of the reinforcements in the cracks. Since the prediction of the exact position of the cracks was not possible.

To analyse the strain variation of the stirrups due to the cracks, three strain gauges were installed in the stirrups (in the web part). An additional strain gauge was also placed on the stirrup at the top flange level (Figure 3.6-1). To analyse the strain in the longitudinal reinforcement two bars were

instrumented. Strain gauges were also placed on the prestress strands, but the friction during the prestress, the duct injection and the during the test damage them.

Figure 3.6-1 shows the final position of the strain gauges on the stirrups and longitudinal rebars. For the stirrups four strain gauges positions were defined. The first one A was just above the flange, the second one B was at the centre of the web and the third one C was just below the flange. The fourth strain gauge D was only placed in the last stirrup, inside the compression chord to detect cracking.

In turn, two out of the total amount of longitudinal rebars were instrumented. The *e* strain gauge was placed at the most exterior rebar. The *i* strain gauge was placed on the closest rebar to the web. This lay out would allow to obtain the variation of the stresses along the flange. Figure 3.6-3 shows the position of the strain gauges in the longitudinal direction. The strain gauges were placed in the mid-height, between stirrups.

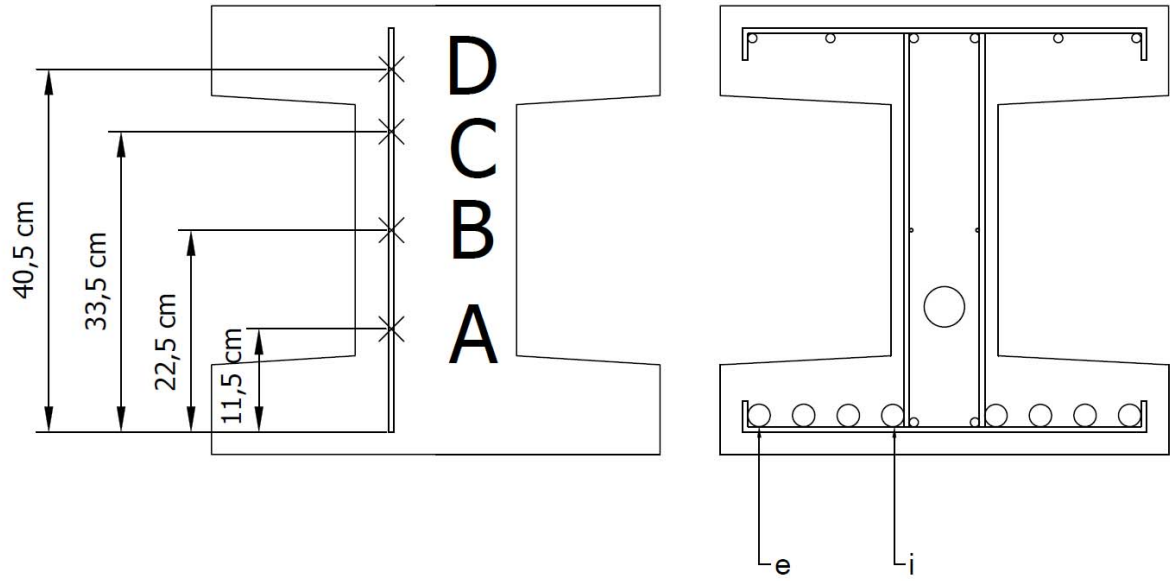

Figure 3.6-1 Strain Gauges position on the stirrups (left) and longitudinal reinforcement (right)

A codification was used to name the strain gauges. The first two letters are “GP” or “GA”, standing for strain gauges on a passive bar and strain gauge on an active strand, respectively. For the GP strain gauges (Equation 3.6-1), the next letter stands for the side of the beam where the strain gauge was placed. “I” if the beam was placed where the strand was inclined or “R” if the strain gauge was placed in the remaining part of the beam. Then, the following letter represented the rebar type: “S” or “L” for stirrups or longitudinal reinforcement, respectively. Then, a number was added to point out the relative position in relation to the support. The strain gauges placed closer to the support would receive the number 1 (Figure 3.2-2). Then, the position of the strain gauge in the section was specified. For the stirrups, it would be a letter between A and D and for the longitudinal reinforcement an *i* or an *e* (see Figure 3.6-1).

Equation 3.6-1 Codification to name strain gauges placed in passive reinforcement

$$GP - \begin{matrix} I \\ R \end{matrix} - \begin{matrix} S \\ L \end{matrix} - \begin{matrix} 1 \\ 2 \\ 3 \\ 4 \\ 5 \\ 6 \end{matrix} - \begin{matrix} A \\ B \\ C \\ D \\ i \\ e \end{matrix}$$

The strain gauges that started with GA were placed on the strands. Like for longitudinal reinforcement, two strain gauges were placed on each section. This configuration was necessary since the process of prestressing may damage the instrumentation. Setting the beam I182 apart, 8 strain gauges were placed in each beam, 2 strain gauges in every region (Figure 3.2-8). The ones placed on region 1 had the letter "I", the ones on region 2 had the letter "C", the ones on region 3 were named "F" and finally on region 4 "R". The pair of strain gauges of every section were differentiated using the letters "A" and "B". In beam I182, 22 strain gauges were placed. The first region had 4 sections (1 to 4) with strain gauges and the second region maintained the same configuration (see Figure 3.6-6). On the third region, 3 sections were instrumented as well as in region 4. For region 1, the number of the section was added starting in 1 for the section closer to the support. For the regions 3 and 4, the name counter started with the section closer to the support *R*. The last part of the name was be "A" or "B" (Equation 3.6-2).

Equation 3.6-2 Codification for the strain gauges placed on the active reinforcement

$$GA - \begin{matrix} I \\ C \\ F \\ R \end{matrix} - \begin{matrix} - \\ 1 \\ 2 \\ 3 \\ 4 \end{matrix} - \begin{matrix} A \\ B \end{matrix}$$

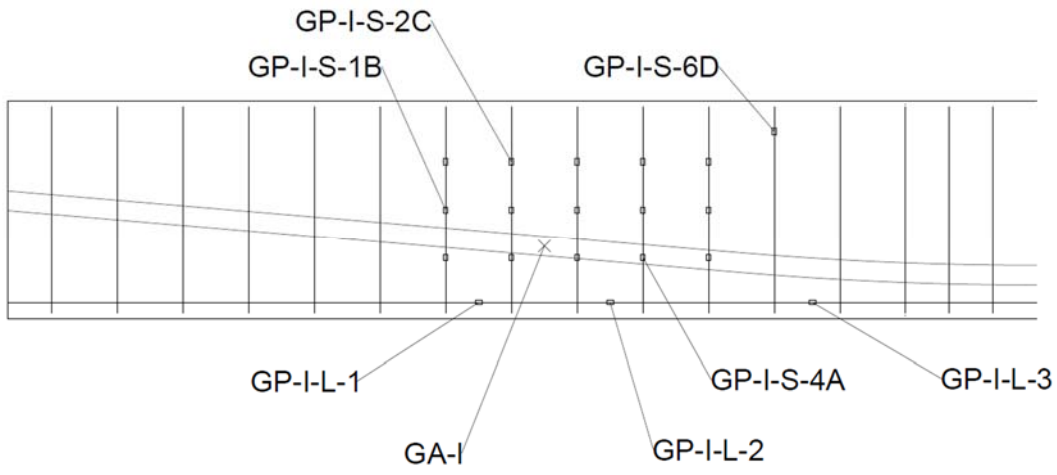

Figure 3.6-2 Name and position of the strain gauges

For the shear tests, strain gauges were placed on 5 or 6 stirrups, depending on the spacing stirrups (250 mm or 150 mm, respectively). The last instrumented stirrup had only one strain gauge in the

position D. The instrumented sections were consecutives. For beams with a spacing between stirrups of 150 mm, the last instrumented stirrup was at 300 mm from section *C*. For the beams with 250 mm of spacing, this distance was reduced to 250 mm. The sections with strain gauges for the longitudinal reinforcement were placed in between stirrups (see Figure 3.6-3 and Figure 3.6-4).

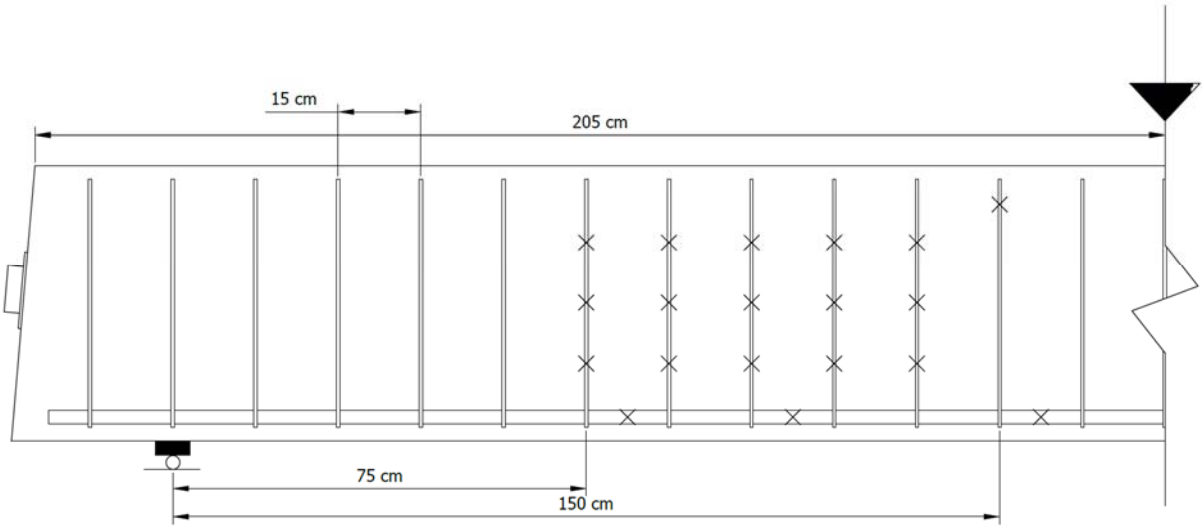

Figure 3.6-3 Strain gauge distribution for a 150mm stirrup spacing beam, on a long span shear test

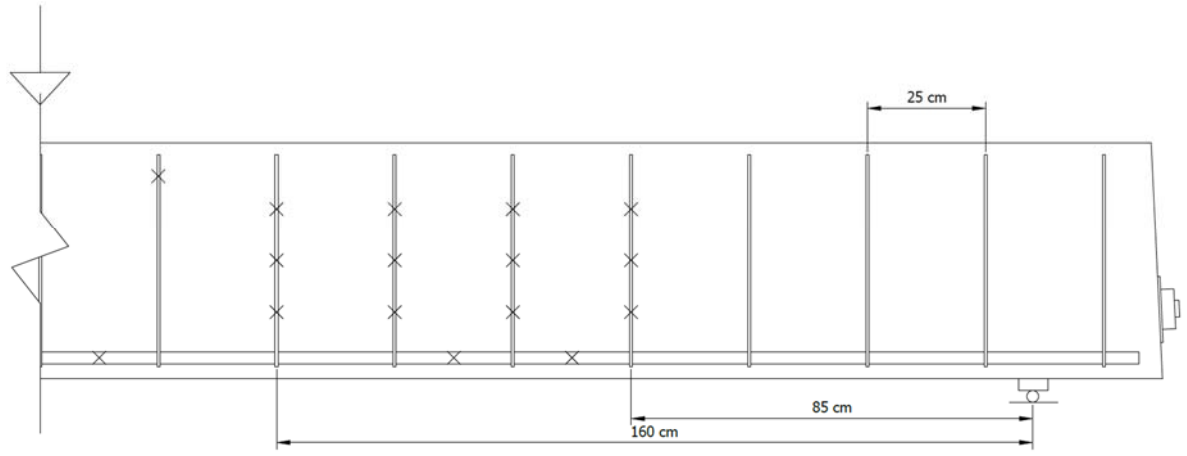

Figure 3.6-4 Strain gauge distribution for a 250mm stirrup spacing beam, on a short span shear test

For the 4-point bending tests, strain gauges were placed in regions 3 and 4. Strain gauges in region 3, were placed at the same distance from the load application point to compare the behaviour afterwards. In region 4, GP-R-L-3 was placed at 150 mm from section *M2,* and the three strain gauges were separated 400 mm from each other. We also placed a strain gauge (GP-R-S-1-B) on the stirrups, which was placed 500 mm from section *M2* (as shown in Figure 3.6-5).

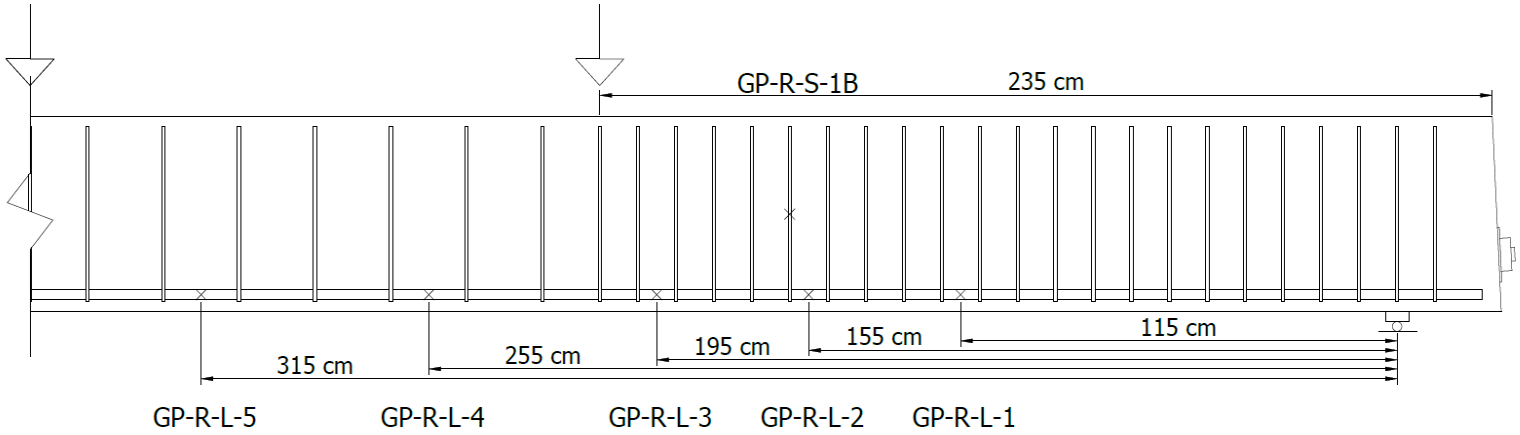

Figure 3.6-5 Strain gauge distribution, on the four-point bending test

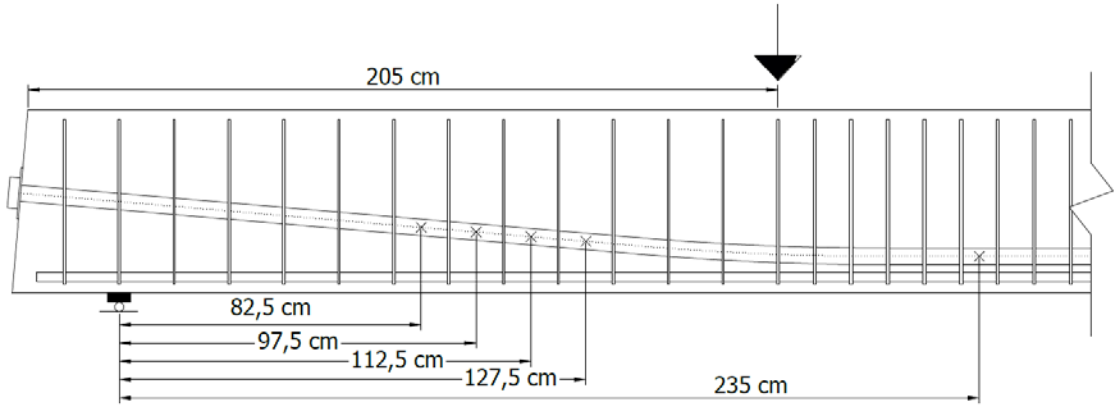

Figure 3.6-6 Strain gauges on the strands of the beam I182, region 1

All strain gauges were bonded before casting the beams. Their cables followed the reinforcement and went outside the beams from the top side. The strain gauges of the strands were glued through a small window made on the metallic duct. Their cables were then tied to the passive steel and followed the other cables. The window was closed to ensure that no concrete was getting inside the duct during casting.

To control the deflection of the beam, displacement transducers were placed in different beam sections. Two different technologies were used: laser measurement and magnetorestrictive displacement sensors (Temposonics). Temposonics were used to register the deflection of intermediate sections along the beam. Temposonics had a frame where a stem slips. The frame was attached to an auxiliary beam and the end of the stem was fixed to the beam. For the shear tests, in which the deflection of the beam was smaller, the shaft of the sensor was glued under the beam in the centre of the beam. However, in the 4-point bending test, the deflection of the beam was more important. Therefore, the sensors had to be bigger and they did not fit under the beams. In such tests, the sensor had to be fixed to the side of the flange. All sensors were placed on the same beam side.

Lasers sensors were placed over the beams, just on top of the support sections (*I, C or R*). These devices compute the deflection of the supports. The presence of rubbers in between the beam and the supports introduced relevant movement on the supports. These supports' displacements were transferred to the deflection of the beam, and should be corrected. Hence, they had to be subtracted to the total deflection of the beam.

In the first 4 tests (beams 122 and 124 tested twice once by side), the vertical movement of the support was measured by a Temposonic. The sensor was placed on the axis of the bottom of the beam, and as close as possible to the support. After analysing the data of the 4 tests, it was observed that the precision of the sensor was not enough to capture the settlement of the support; thus, these sensors were changed to laser devices. Laser sensors produced a light signal that rebounded on the top of the beam. Due to the small displacement that had to be recorded, the top surface of the beam was regularised by gluing an aluminium plate.

The Temposonic configuration to detect deflection for the shear tests consisted of 5 sensors. One sensor was placed under the load application point, another at the centre of the beam, two Temposonics were placed in the centre of each side of the beam. The fifth was placed near to the support closer to the load. For the beams without laser sensors, a sixth sensor was used on the other support. See Figure 3.6-7 for the name and position of the sensors.

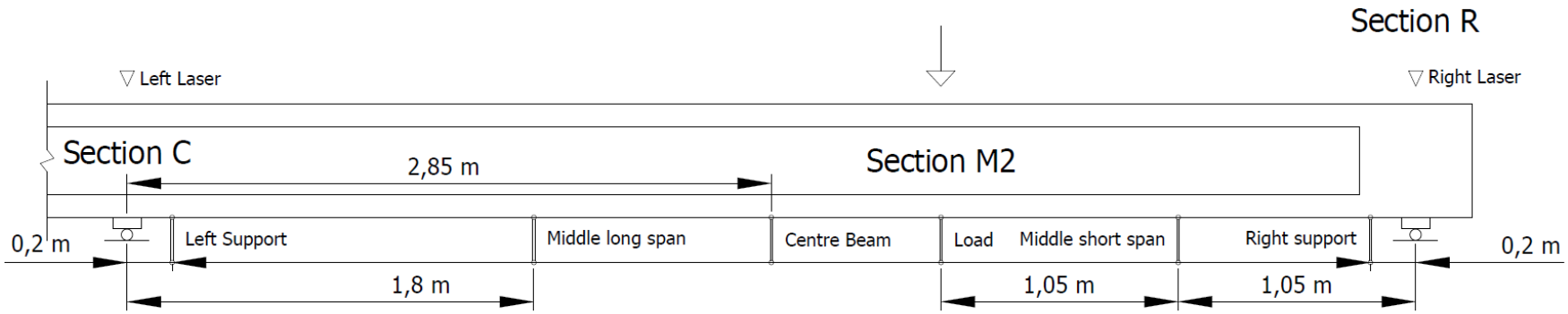

Figure 3.6-7 Distribution of the deflection sensor for the short span shear test

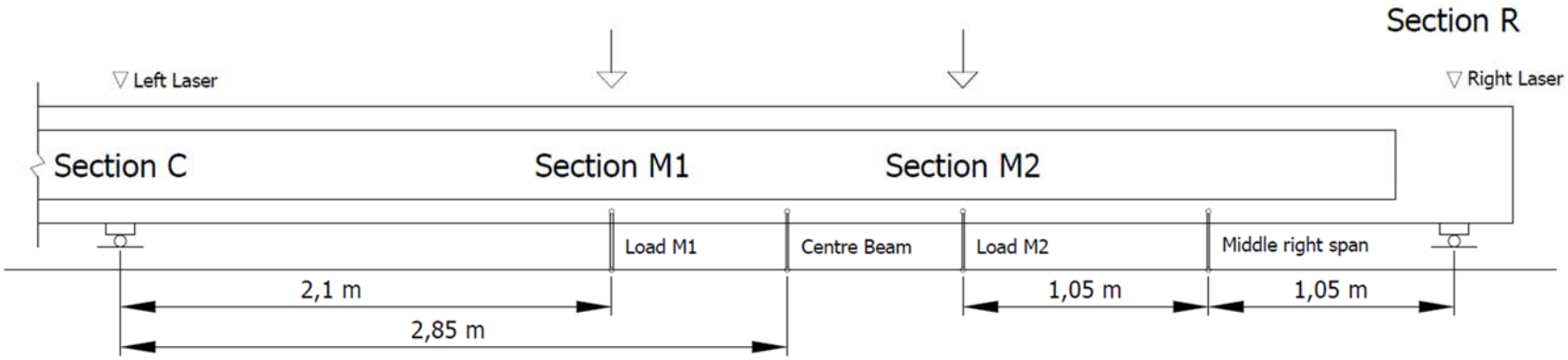

Figure 3.6-8 Distribution of the deflection sensor for the bending moment test

The Set-up 3, for the four-point bending test, had four sensors. Two sensors were under the rubbers of the metallic beam, under the points were the loads were applied to the beam. The third one was directly placed under the jack and the last sensor was placed in between points *M2* and *R.* As in the shear tests, the control of the support settlement was done by laser sensors (see Figure 3.6-8).

To register the rotation and curvature of the beams, displacement transducers were placed on the top and on the bottom of the beam, forming pairs. Each pair of sensors analysed the space between their end. They were placed on the longitudinal direction of the beam. The ones on the top controlled the shortening of the compression chord and the ones on the bottom side recorded the elongation of the bottom part of the beam. These sensors were recording the displacements of 2 points initially separated 300 mm. For the Set-up 1, 4 sensors were used. The two sections of analysis were between section *I* and load section *C*. The sections were located 96.5 cm and 131.5 cm from the support *I*. On the Set-up 2, the sensors were at the same distance from the load section *M2*, 126.5 cm and 161.5 cm from support *R* (Figure 3.6-10). For the Set-up 3, designed for the 4-point bending tests, more sensors were used: in addition to the two transducers placed at 125 cm, and at 161 cm from the support *R*, another transducer was placed between the loads, at 285 cm from *R* and at 75 cm from *M1* and *M2*. Another sensor was placed on the bottom flange at 90 cm from the support *R* (Figure 3.6-11).

To measure the relative displacements on the web of the beam, 45-degrees rosettes were used. Each rosette was made of 5 potentiometric displacement sensors (Potentiometers), 2 horizontal, 2 vertical and a diagonal one, depicting a square with a diagonal (see Figure 3.6-10). The diagonal one was in the opposite direction of the line that goes from the load application point to the support, this orientation was intended to capture elongation (tensile strains) of diagonal strain field. The displacement measured in this direction was the crack opening, the displacement measured on the perpendicular direction was the shortening of the struts. Since the elongation direction is always bigger than the shortening direction, the measurement error is inferior. Due to the limitations on the number of sensors and channels available, the number of potentiometers was limited to 14.

The sensors were placed on a double rosette and a simple one. The double rosette was the union of two rosettes, overlapping the central vertical sensors. The double rosette consisted of two 180mm squares. It was placed it in the middle of the web and always at the same distance from the load. For the Set-up 1, the centres of the squares were located at 88 cm and 106 cm from the support *I* (respectively) (Figure 3.6-9). On the Set-up 2 and 3, the centres of the squares were located at 118 cm and 136 cm form support *R* (respectively) (Figure 3.6-10).

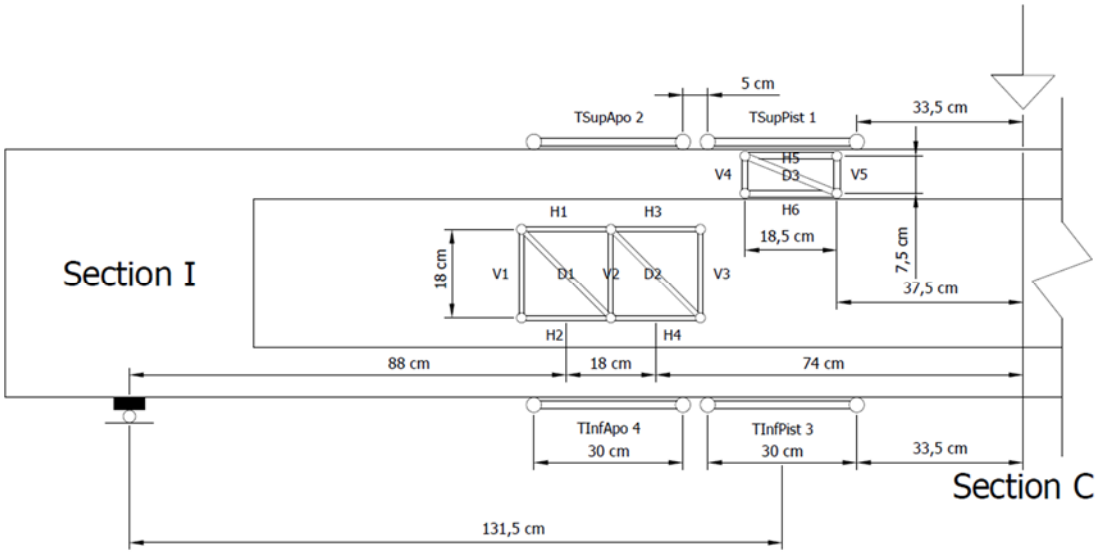

Figure 3.6-9 Sensors position on the short span shear test

The simple rosette was placed on the side of the top flange in the shear tests and on the web in the region 2 in the four-point bending test. The flange was 100 mm height, not allowing us to use the same square configuration. The fixing points were placed 75 mm apart vertically. On the horizontal direction, they were placed 185 mm apart. On those tests, the centre of the rosette was always placed 46.8 cm from the load application point. On the set-up 1, the centre was placed 133.2 cm from the support *I* (Figure 3.6-9). For the set-up 2 the distance was 163.2 mm (Figure 3.6-10). In the four-point bending test, the rosette was placed on the web. The rosette was placed 83 cm from point *M1* (Figure 3.6-11).

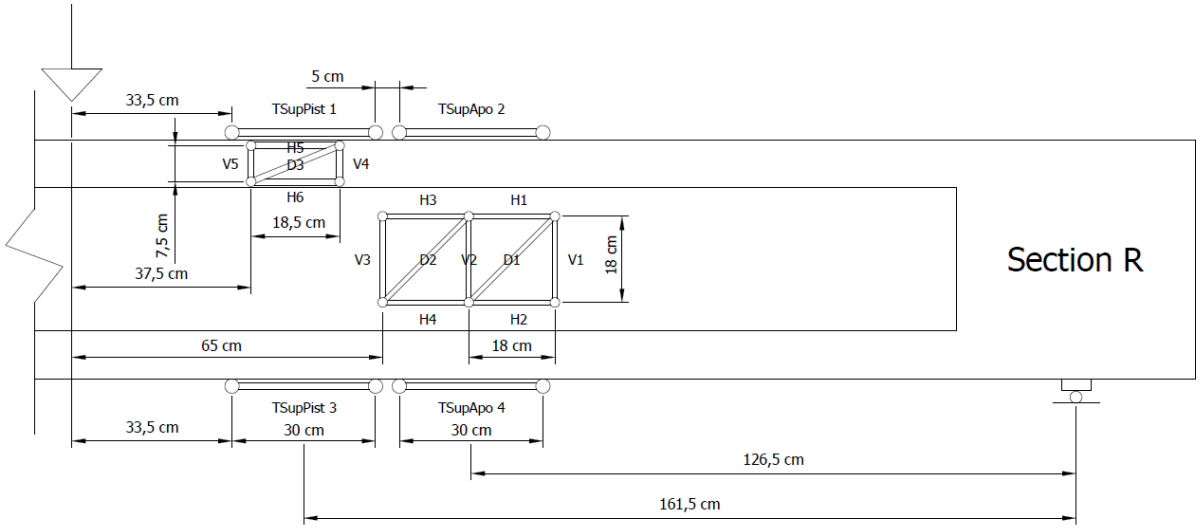

Figure 3.6-10 Distribution of Temposonics and potentiometers for a short span shear test

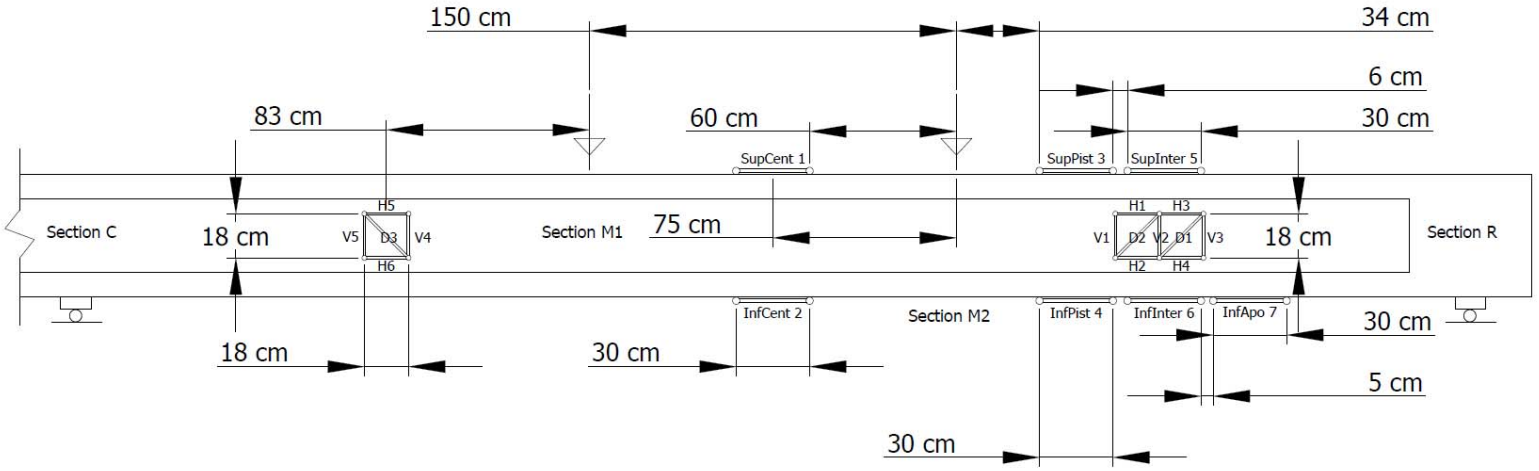

Figure 3.6-11 Distribution of Temposonics and potentiometers for a bending moment test

The loads were controlled through the internal load cell from the jack (1000kN) and through three load cells installed in the supports. The three load cells were identical and able to carry up to 1000 kN. One of the cells was placed at the *R* end and the two remaining cells in the other support. These loads cells had a small diameter and the transversal stability could be compromised. Using three load cells provided a more stable base to carry out the tests. To ensure the transversal stability and as a safety measure, the supports had two arms that reached each side of the beams.

In collaboration with another PhD study developed at the same department (Rodríguez, 2017), fibre optic sensors were employed in these tests. The sensors provided were fibre optic cables that were glued in their whole length of the steel and concrete. These sensors were able to detect strain every 1 cm of cable, allowing a continuous record of the strain. When applied to the reinforcement, the fibre had to be glued before the casting process. Over the concrete, the fibre was installed after hardening. Due to the continuous reading, the evolution of strains, cracking and yielding, could be analysed in a multitude of parts of the beams (Figure 3.6-12).

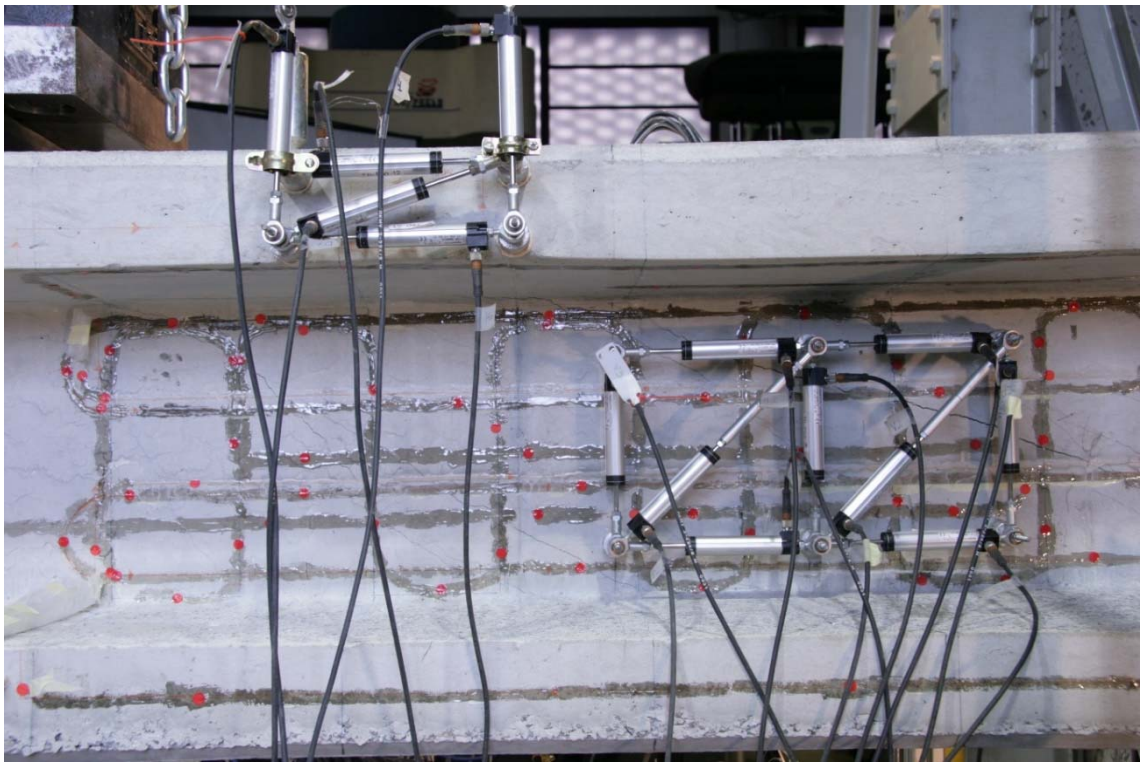

Figure 3.6-12 Fibre optic distribution in the web

The fibre optic sensors were very thin and could not be bended with small curvatures. One of the cables broke during the bonding operation of the fibre optic cable to the reinforcement. Since it was impossible to amend it, the rest of the cables were placed over the concrete and they were only used for superficial analysis. The fibres, which were stuck to the concrete, bear the initial loads but when the concrete started to crack, the pick deformation was obtained and the fibres ruptured. No information obtained with the fibre optics has been included in this document.

3.7 Photogrammetry

As previously stated, an important part of this study was to analyse the diagonal cracks. Through the instrumentation previously presented, cracking of the beam was detected. In order to obtain the spacing, angle, length and width of the cracks, these sensors were not enough. The usual procedure

to gather this information was to draw the pattern of the cracks in the beam for different load values and use a magnifier to measure the crack width. Once the test was over, the crack angle or the crack spacing of the tested beam was measured.

In the research group ATEM (Analysis and Technology of Structures and Materials) a code to detect and analyse cracks from pictures was developed (Sanchez, 2017). One of the features of the programme is to upload a set of pictures of a beam and detect the cracks and their corresponding angle and opening. From his software, a new programme was generated allowing the analysis of crack pattern.

The first step in this process was to select the part of the beam that would be of interest to be analysed, in our case, the web of the beam. We selected the free side without potentiometers. The camera was placed on a tripod. To ensure proper image quality, extra illumination was added to this side of the beam using two spotlights. The extra illumination homogenized the different pictures and increased the contrast on the concrete surface. Each spotlight was equipped with a halogen tubular lamp providing warm white light.

These techniques can analyse all the information gathered by the camera, but are dependent on the scale of the image. A trade-off between precision and amount of information has to be done. Taking into account that the deflection of the beam was important and the web was the main target for this analysis, the camera took pictures of the web and the bottom flange. No movements of the beam were expected on the horizontal direction.

This framing, resulted in a distance between the camera and the web from 1,5 and 2m. The distance had also to ensure the free movement of the laboratory personnel around the beam and a safety distance to protect the camera, in case of brittle failure. Using the optical zoom of the camera, the frame of the image at this distance included all the elements relevant for the analysis plus the vertical extra to compensate the deflection.

Initially photographs were taken manually on specific loads or deflection states. After several tests, auto-shoot was used, taking pictures at a specified time interval. This method improved the stability of the images and allowed a bigger amount of photos effortless. Therefore, the possibility of introducing angle or position variation between pictures, modifying the homogeneity of the set of pictures, was eradicated. The time interval between photographs (t) was related to the time between the load holds and its duration. The value of t was changed during the different tests and in some cases along the same test.

In order to associate each picture with the load applied by the load actuator, a display was set on top of the bottom flange. Similarly, the name of the beam and the type of test was written in the top flange. Then, every photograph could be easily sortable. To obtain the scale of the images and perform the photogrammetric analyse, a ruler was placed on the analysed surface in the first image to establish the scale of all the images.

4 Flexural Behaviour of Partially Prestressed Concrete Beams

4.1 Introduction

As previously described in Chapter 0, a set of tests was planned to analyse the behaviour of partially prestressed concrete (PPC) under bending stresses. They consisted of four specimens beams with 180 mm web width. The four specimens were grouped in pairs with the same active reinforcement, to obtain similar serviceability behaviour within the pairs. The pair of specimens I183 and I184 had 2 strands (280 mm^2). The pair of specimen I181 and I182 had 4 strands (560 mm^2). Different ordinary reinforcements were defined to have different ultimate bending moments. The combination of the two types of reinforcement led to a similar ultimate bending moment between the pair I181 and I183 and the pair I182 and I184. The first pair had a higher ultimate bending moment.

These tests were performed after the long span shear tests. In some cases, the shear tests produced cracks in the concrete of regions 3 and 4, the furthest end of the jack. Before performing the experimental tests, a numerical simulation of the beams was made. Predictions were made assuming that the prestressing force on the strands and the stiffness of the concrete will remain constant after realizing the long span shear test, described in Chapter 0. When the results were analysed, the behaviour of the beams was different from the predictions. In order to accommodate the behaviour of the experimental results with the simulations, the prestressing forces and the stiffness of the beams were reduced in the simulations.

The main configuration of the load protocol was divided into 4 steps (Section 3.5). An initial set of cycles at a low load velocity, using displacement control (1-2 mm/min). Two sets of cycles using load control, with a fast load velocity (50.5 kN/min). The first fast cycle was representative of the quasi-permanent load level and the second one on the frequent load level, based on typical combination factors on codes (Ψ_2, Ψ_1). Both sets were divided internally in 2 blocks of cycles. The cycles were up to 20 kN and up to 80 kN amplitude, small and large cycles, respectively. The last set used displacement control at a low velocity (1 mm/min). The load increased up to yielding, then unloaded to the quasi-permanent level and, finally, increased the load up to the failure of the beam.

4.2 Performance of tests specimens at failure

As it was already established, the purpose of this set was to have two pairs of beams with similar failure load but with different amount of prestressing force. Beams I181 and I184 had the same longitudinal ordinary reinforcement 6Ø16, but they had 4 and 2 strands, respectively. Beam I182, with 4 strands, had a longitudinal reinforcement of 6Ø10. Beam I183, with 2 strands, had a longitudinal reinforcement of 4Ø25 and 2Ø10 (2121 mm2), almost double of that of beams I181 and I184, as can be seen in Table 4.2-1.

Table 4.2-1 Amount of active and passive longitudinal reinforcement

Beam		Active steel	Passive steel
I181	**Rect**	560 mm^2	1206 mm^2
I182	**Rect**	560 mm^2	471 mm^2
I183	**Rect**	280 mm^2	2121 mm^2
I184	**Rect**	280 mm^2	1206 mm^2

Table 4.2-2 presents the comparison between the experimental bending moment and the numerical simulations. The simulation was performed with a multi-fibre non-linear analysis developed on our department. The tests I183 Rect had an important difference between experimental result and simulation. This is because the tests suffered a problem at its final stage and the beam fell off the supports. The top surface of the beam had imperfections and combined with the important deflection reached during the tests, it generated a torsion effect that threw the beam off, unloading it abruptly and ending the test.

Table 4.2-2 Bending moment results

	Bending Moment		
Beam	Experimental	Simulation	Ratio
I181 Rect	673,92 kNm	673,86 kNm	1.00
I182 Rect	531,09 kNm	522,32 kNm	1.02
I183 Rect	604,04 kNm	657,87 kNm	0.92
I184 Rect	513,23 kNm	497,07 kNm	1.03

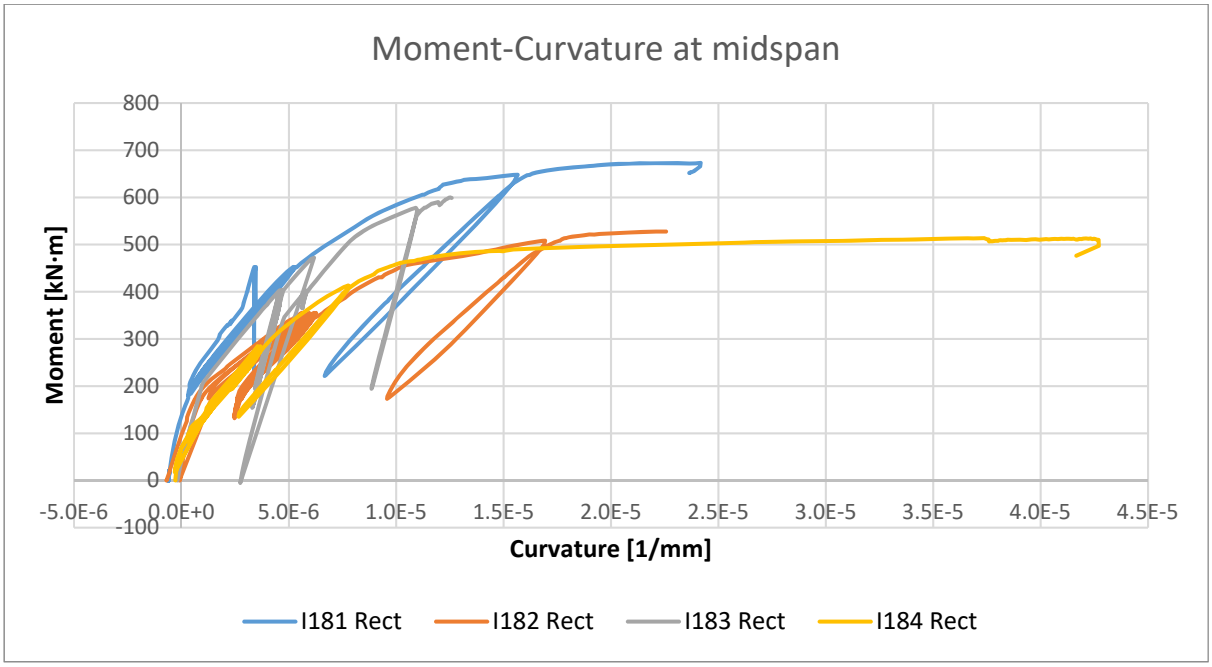

Figure 4.2-1 Experimental relation between bending moment and curvature

Figure 4.2-1 shows the moment-curvature relationship for the four tests. The curvature was computed using the displacement transducers SupCent1 and InfCent2 (Figure 3.6-11). It can be observed that beams I181 and I183 showed a similar response on their final stages. In addition, a similar failure load was observed in beams I182 and I184.

4.2.1 Tension shift influence in longitudinal reinforcement

For each tests, the yielding bending moment was calculated. When the strains from the longitudinal reinforcements were analysed, the strain gauges in sections 1 and 2 (Figure 3.6-5) showed higher strains than predicted by the bending moment. The strains for sections 3, 4 and 5 were as expected. Table 4.2-3 summarizes the difference between the experimental load and the predicted loads, presenting the percentage of bending moment reduction. The empty cells correspond to the cells without longitudinal reinforcement yielding.

Table 4.2-3 Difference between experimental and predicted yielding moment

Test		I181 Rect	I182 Rect	I183 Rect	I184 Rect
Predicted yielding moment		**540 kNm**	**391 kNm**	**583 kNm**	**409 kNm**
Section	1	352 kNm	287 kNm	-	-
		34.8%	26.8%	-	-
	2	422 kNm	307 kNm	-	329 kNm
		21.9%	21.5%	-	19.4%
	3	503 kNm	383 kNm	532 kNm	352 kNm
		6.9%	2.1%	8.7%	13.9%
	4	505 kNm	366 kNm	545 kNm	396 kNm
		6.4%	6.4%	6.4%	3.1%
	5	540 kNm	399 kNm	530 kNm	402 kNm
		-0.1%	-2.0%	9.1%	1.6%

The strain gauges of section 3 showed that the bending moment at yielding of the longitudinal rebar was similar to the predicted value, even though in the test I184 Rect, the bending resistance was 13.9% smaller than expected. The main difference can be observed for sections 1 and 2, where the influence of the shear stresses and the tension shift increased the tensile stress in the longitudinal reinforcements. In those sections, the strain of the longitudinal reinforcement exceeded the elastic limit for bending moments that are 20% to 35% lower than expected. This increase in the stress is related to the tension shift. The theoretical tension shift was calculated for the four tests and the results were similar to the experimental results.

4.2.2 Study of PPC ductility

The behaviour of the PPC beams after the yielding of the longitudinal reinforcements was studied using different approaches. The abrupt unload of test I183 Rect prevented its ductility studies, the final deflections and deformations were missing.

4.2.2.1 Ductility analysed using the deflection in centre beam

The deflection of the beams was registered in several sections. Figure 4.2-2 shows the relationship between the load and the deflection at midspan. The test I183 Rect is displayed until the abrupt unload. The final deflection observed in the other tests showed that the beams with higher amount of prestress reinforcement had inferior failure deflection. In turn, beams with smaller amount of ordinary reinforcement had larger deflections.

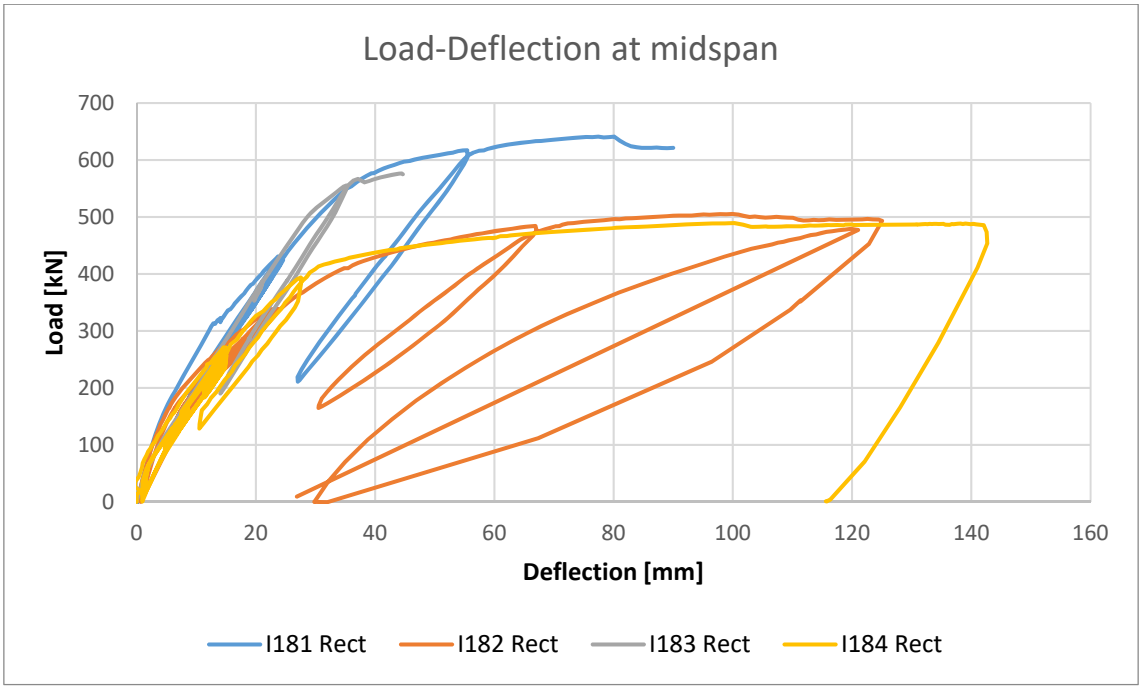

Figure 4.2-2 Relation between load and deflection in section Centre Beam, mid span

The displacement ductility of the beams was computed based on the deflection at midspan, by taking the ratio of the deflection at failure and the deflection at yielding. To define the yielding point, an ideal bilinear behaviour was assumed, and the area under the curve was made equal to the area of the actual load-deflection curve (see Figure 4.2-3). The difference between the bases of the trapezoid is the yielding point. The failure deflection is the deflection when the load decreases a 10% after having reached the maximum load.

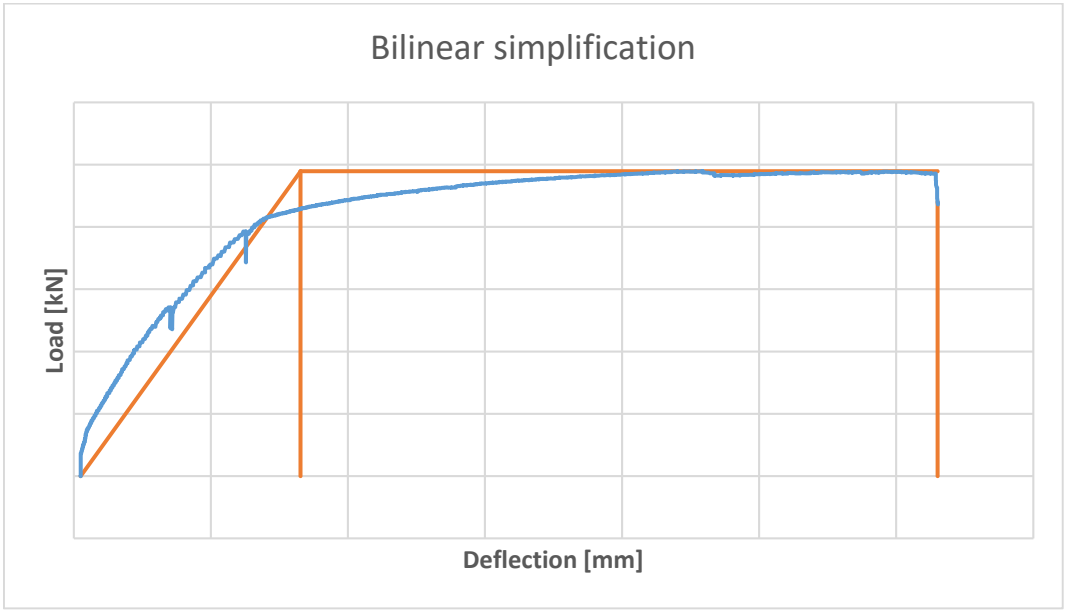

Figure 4.2-3 Bilinear behaviour simplification

The curve displayed in Figure 4.2-3 is the envelope of the load-deflection cycles. For the calculation of the ductility, the envelope of the load-deflection history is used. Figure 4.2-4 and Figure 4.2-5 show the envelope deflection for tests I181 Rect and I182 Rect, respectively. In both figures, the envelope

was computed from the deflection at midspan. Figure 4.2-4 shows the deflection of test I181 Rect, this test has the smallest ductility between the three remaining tests: 2.4. In Figure 4.2-5, the deflection of test I182 Rect after yielding was larger than in the previous case therefore the ductility was larger 3.1.

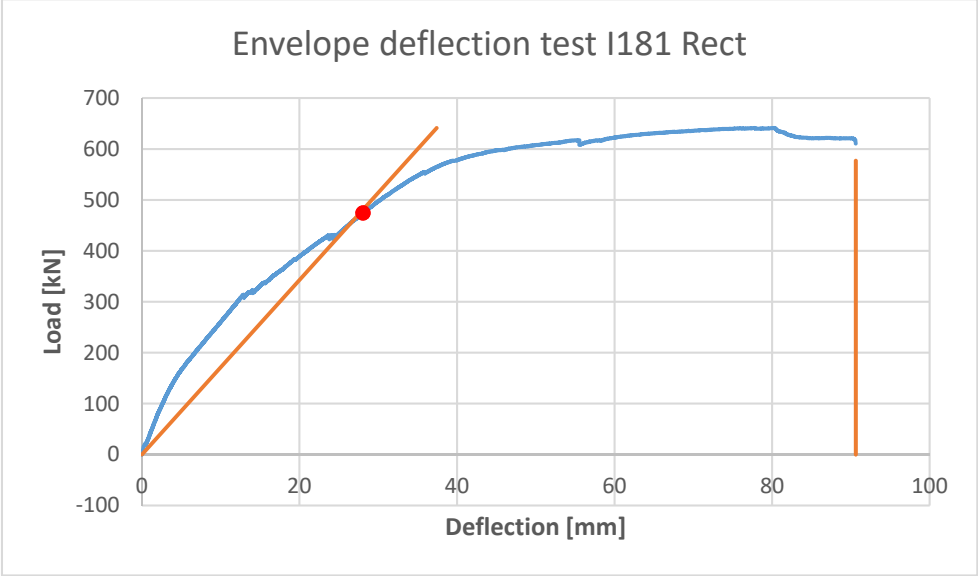

Figure 4.2-4 Deflection measured at midspan, ductility of 2.4

For both analyses, a bilinear behaviour was assumed to obtain the yielding point. The red dots mark the deflection for first yielding of a longitudinal reinforcement (sections 4 and 5). The deflection of these dots is always inferior to the deflection obtained by the bilinear behaviour. This is because the deflection takes into account the behaviour of all the sections and the strain gauges is a localized measure.

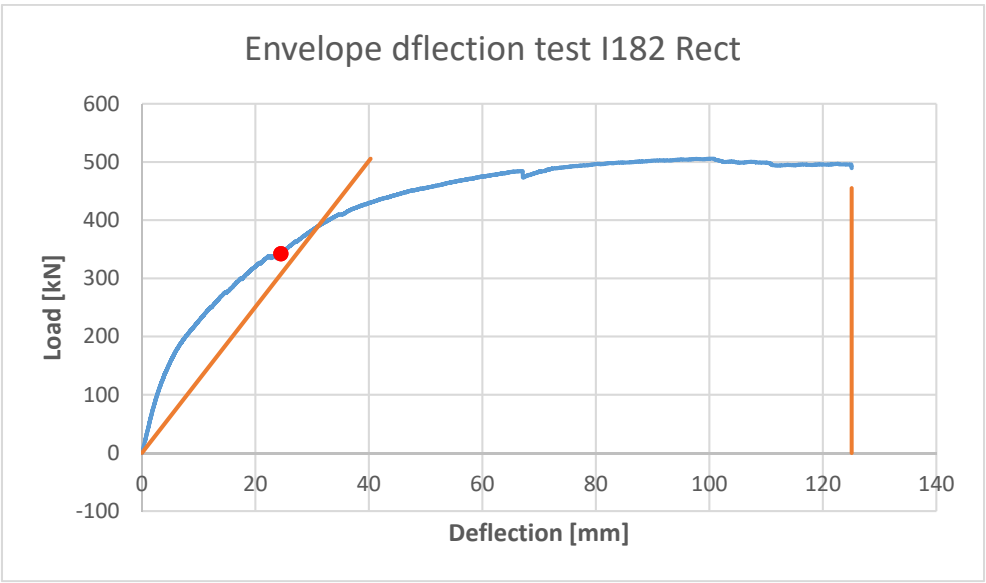

Figure 4.2-5 Deflection measured at midspan, ductility of 3.1

In order to obtain the influence of the prestress reinforced over the ductility of the beams, an equivalent area was developed. This area is a linear relationship between ordinary and prestressed reinforcement (Equation 2.2-1). The α factor represents the equivalence between areas of reinforcement.

$$A_{eq} = A_s + \alpha A_p \qquad 4.2\text{-}1$$

The factor α was obtained maximizing the coefficient of determination of the pair: equivalent area and ductility. For these three test, the α factor was equal to 5.29, therefore the beams with higher amount of equivalent area had higher ductility (Table 4.2-4).

Table 4.2-4 Beams sorted by deflection ductility and equivalent reinforcement

	I181 Rect	I182 Rect	I184 Rect
Ductility	2.4	3.1	3.8
Equivalent Area [mm²]	2876	2141	2041

The linear relationship presented in Equation 2.2-1 and the maximization of the coefficient of determination, was used in this Thesis in several occasion to obtain the relationship between areas of reinforcement and different variables.

4.2.2.2 Ductility calculated using the curvature

The curvature ductility was also calculated. The three pairs of horizontal displacement transducers placed on the top and bottom of the beams were used to calculate the curvature (Cent, Pist and Inter positions Figure 3.6-11). In this case, an important difference was observed between the curvature calculated between the two load points (Cent) and the curvature calculated between the load point *M2* and the supports (Pist and Inter). In the first case a wide range of ductility was obtained, for the other two cases, the range was smaller (as can be seen in Figure 4.2-6). This is because curvature is a property of the section, and since these sections did not fail, they were not showing important deformations. The last curvature registered did not represented the failure of the section.

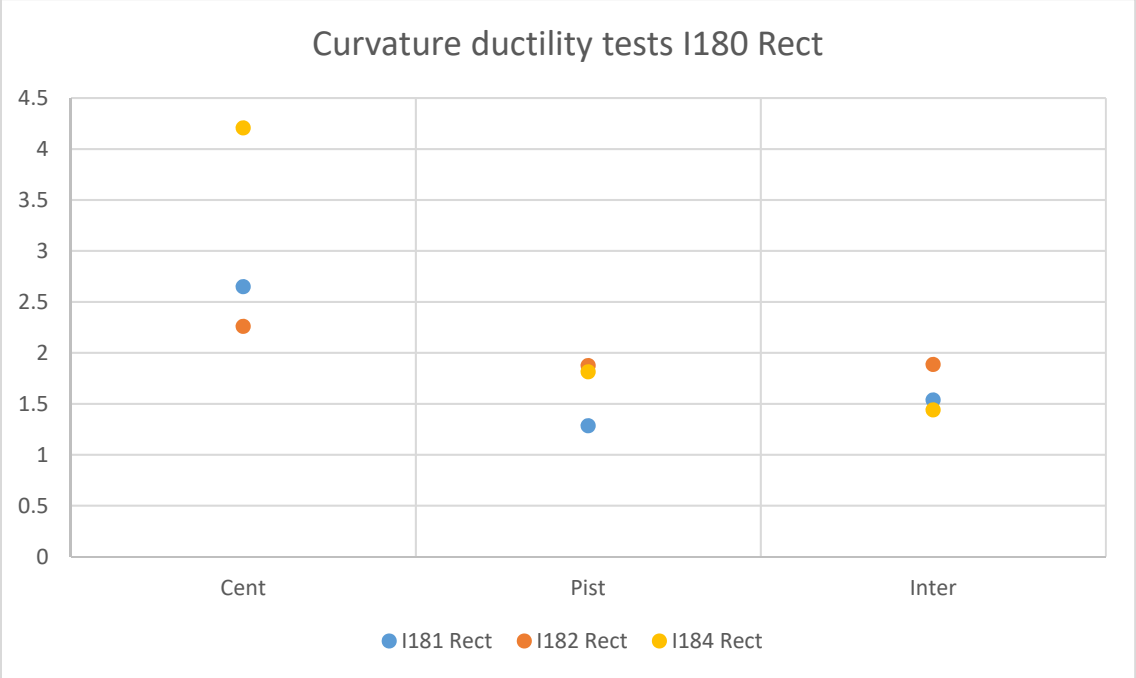

Figure 4.2-6 Curvature ductility for tests I180 Rect

A comparison between the curvature obtained from the displacement transducers placed at midspan and the curvature obtained from the simulations was performed. The simulations were performed with the multilayer flexion simulator and with TINSA (Total Interaction Non-linear Sectional Analyse) (Bairán and Marí, 2006a, 2006b). For the four tests, the simulations matched the experimental results in the beginning of the test and in the yielding branch. The main differences occurred between the cracking point and the yielding of the longitudinal reinforcement. As can be seen in Figure 4.2-7, the experimental stiffness is between the predictions of the two simulations. The changes in the stiffness were less abrupt in the experiments than in the simulation.

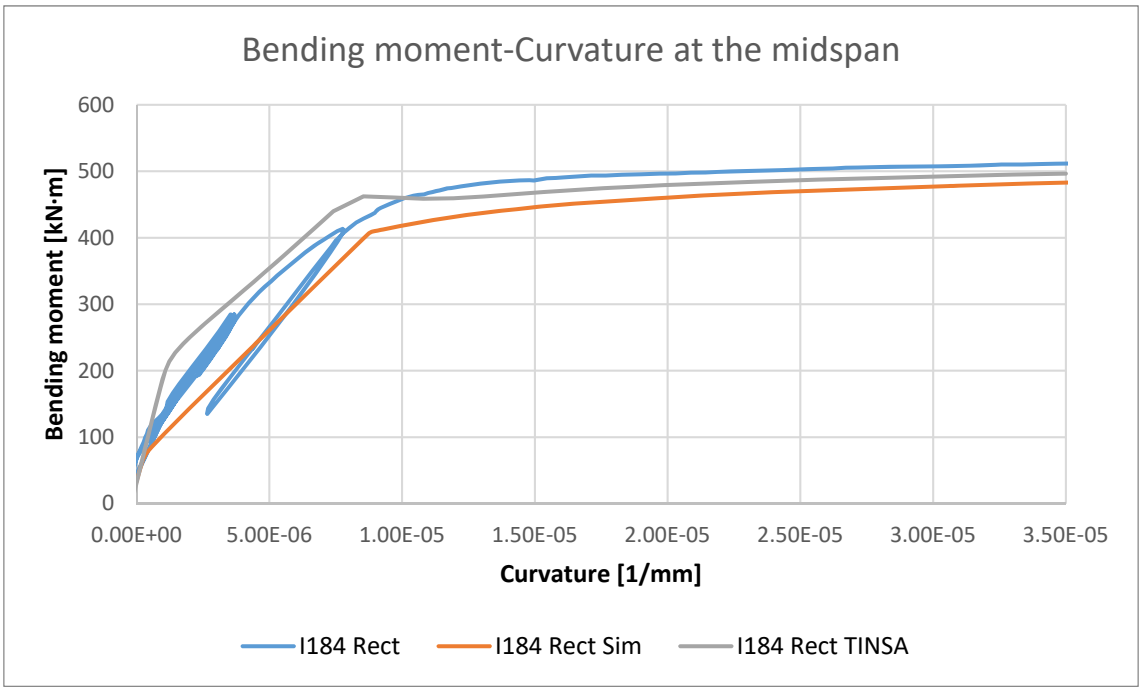

Figure 4.2-7 Bending moment-curvature comparison between models and experimental results for tests I184 Rect

4.2.2.3 Plastic hinge length evolution

Figure 4.2-8 and Figure 4.2-9 show the loading history for both tests I181 Rect and I184 Rect, beams with 4 and 2 strands respectively. The orange squares represent the time and external force for which the stress of the strain gauges overcome, for the first time in the test, the yielding level. In all the cases, the first sections to exceed this limit were placed between sections *M1* and *M2*, spite the reduction in bending moment suffered by sections 1 and 2 (up to 20%) due to the tension shift (Section 4.2.1).

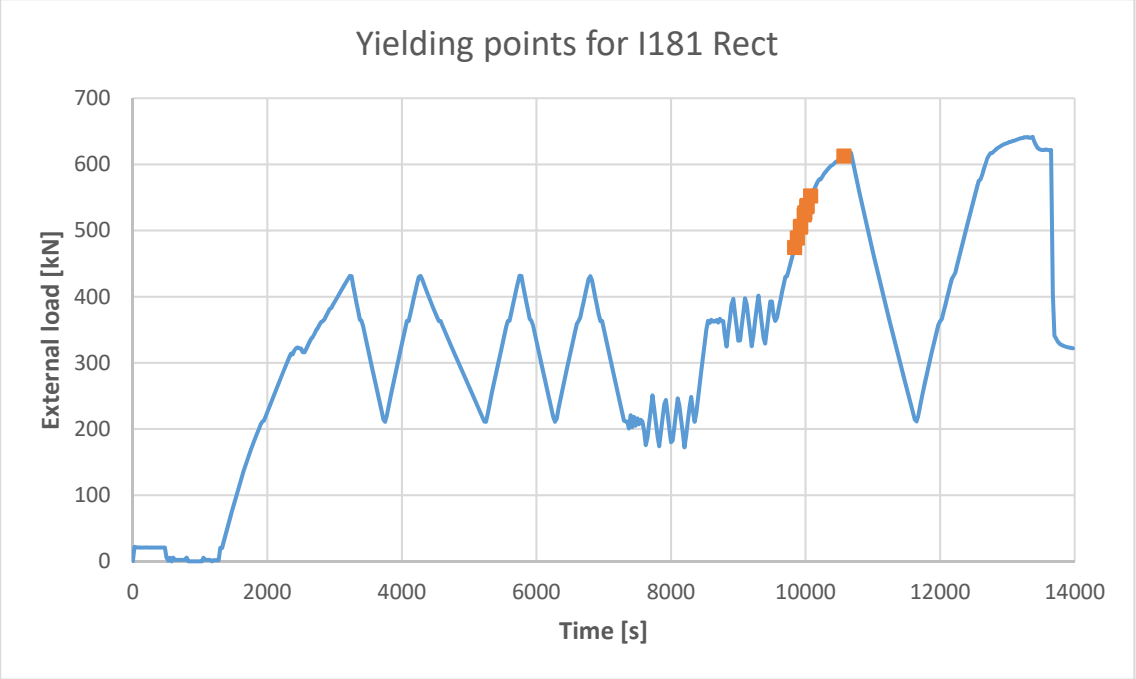

Figure 4.2-8 Load and time for the yielding of the longitudinal reinforcement, in test I181_Rect

For the 4 strands specimens (test I181 Rect and I182 Rect), the prestressing force used to establish the load protocol was slightly greater than the prestressing force applied with the strands. Therefore, the longitudinal reinforcement yielded before reaching the predicted yielding bending moment. This difference produced important yielding strains in the reinforcement before unloading to quasi permanent level (as can be seen in Figure 4.2-1). In turn, for beams with 2 strands, the longitudinal reinforcement yielded just when it was predicted, in the hold. The strains did not increase significantly, hence, the deformations did not spike. This difference between 2 or 4 strand tests was reflected in Figure 4.2-1, by the position of the loop generated after the yielding load level. The tests with important strains had the loop far away of the previous loops than the beams with 2 strands.

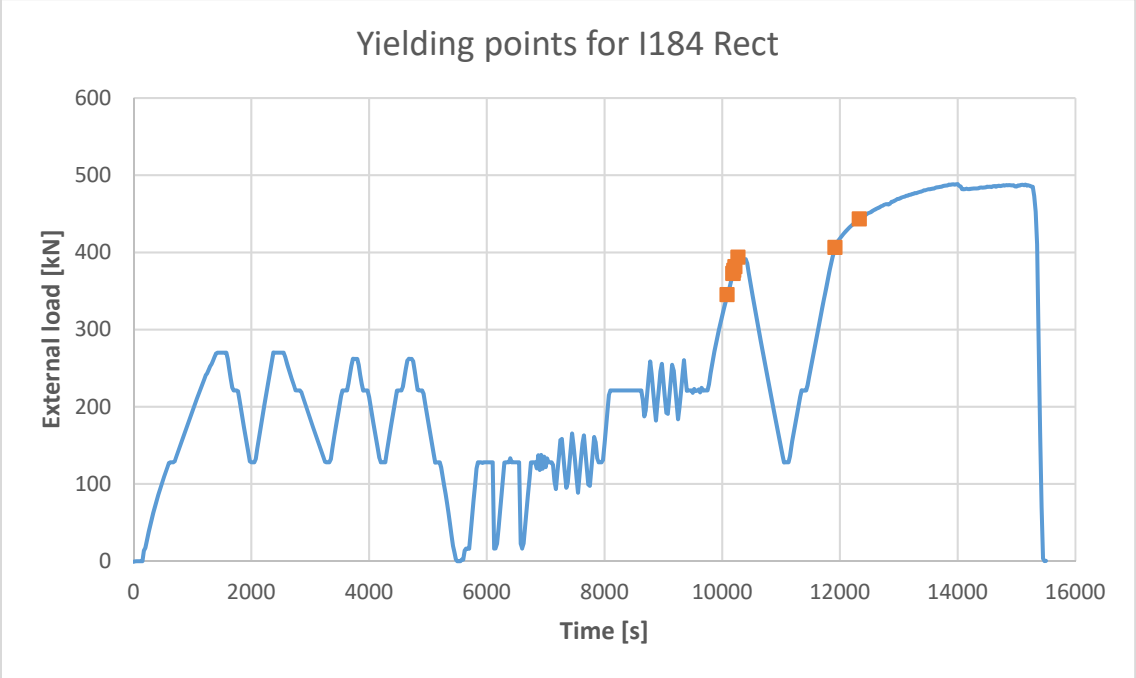

Figure 4.2-9 Laod and time for the yielding of the longitudinal reinforcement, in test I184_Rect

The different behaviour between beams with 4 and with 2 strands affects the plastic hinge length. Figure 4.2-10 and Figure 4.2-11 show different plastic hinge lengths for beams I182 Rect and I184 Rect, respectively. The evolution of the strains and stresses of the reinforcement was obtained using the strain gauges in sections 1 to 4 on the ordinary longitudinal reinforcement. The stresses, at all the length of the span, were obtained interpolating the information from the strain gauges. The plastic hinge length is the distance between the section M2 to the last point of reinforcement that has yielded. Beams with 4 strands had larger plastic hinge lengths than the 2 strands tests.

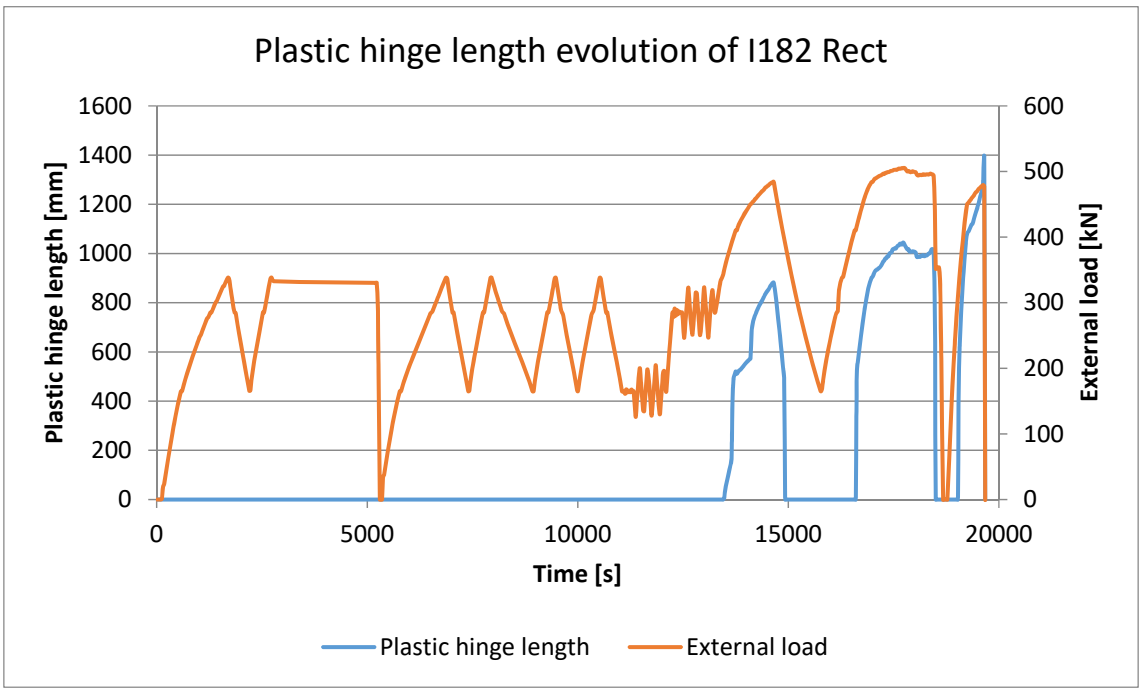

Figure 4.2-10 Evolution of the plastic hinge length of the test I182 Rect

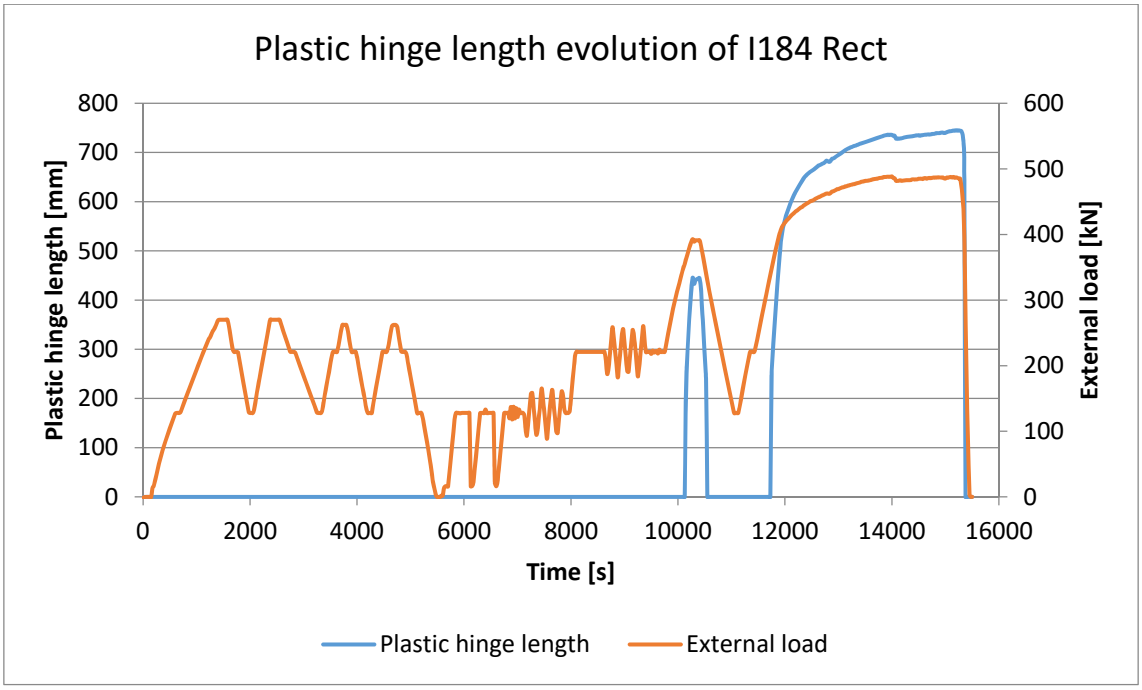

Figure 4.2-11 Evolution of the plastic hinge length of the test I182 Rect

The beams I181, I182 and I184 presented similar prestressing area or ordinary area. Tests I181 Rect and I182 Rect had the same prestressing reinforcement but I182 had a third of ordinary reinforcement respectively. Their plastic hinge length was 1006mm and 1451mm, respectively, therefore the beam with higher ordinary reinforcement had smaller plastic hinge length. However, the maximum plastic hinge length of test I182 Rect was not obtained under the maximum external force. The plastic hinge length under the maximal shear stress was 1044 mm (Table 4.2-5). In turn, the tests I181 Rect and I184 Rect had the same ordinary reinforcement but with different prestressing reinforcement area. The plastic hinge length in test I184 Rect was 745 mm, therefore the tests with larger prestressing reinforcement had a larger plastic hinge.

Table 4.2-5 Plastic hinge length calculated from the strains and stresses of the strain gauges

	I181 Rect	I182 Rect	I182 Rect (max Load)	I184 Rect
Plastic hinge length (mm)	1006	1451	1044	745

Figure 4.2-12 presents the diagram of bending moment for the ultimate state for the three tests, from the support to the applied load (Sections *R* and *M2*). The dashed lines are the yielding bending moment reduced by the tension shift, obtained in Section 4.2.1. For tests I181 Rect and I182 Rect, the yielding moment correspond to the strain gauges of section 1. In the case of I184 Rect, the strain gauges in section 1 did not yield and the bending moment was obtained with the strain gauges of section 2.

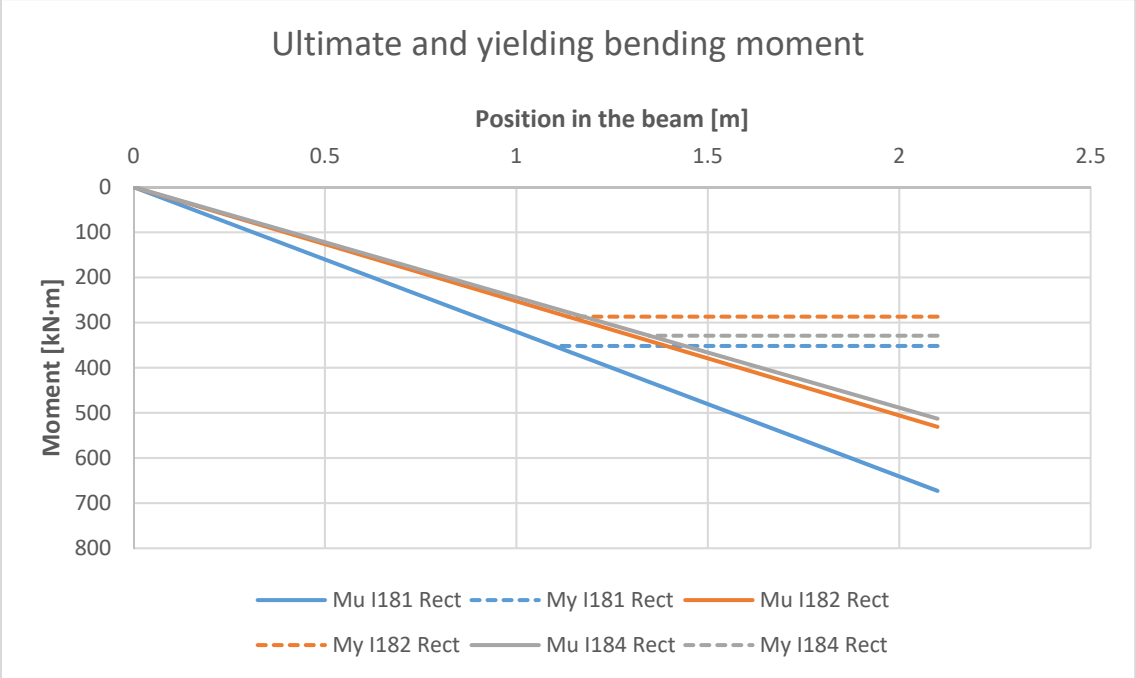

Figure 4.2-12 Comparison of the diagram of bending moment in ultimate state with the reduced yielding bending moment due to tension shift

Table 4.2-6 presents the results of the intersection of ultimate bending moment and yielding bending moment. These lengths are very similar with the distances obtained with the previous method for the maximum shear load. In this case the difference between tests I181 Rect and I182 Rect (both with 4 strands) is very small and the beam with smaller amount of ordinary longitudinal reinforcement had smaller plastic hinge length.

Table 4.2-6 Plastic hinge length obtained from the intersection of bending moment diagram and yielding bending moment

	I181 Rect	I182 Rect	I184 Rect
Plastic hinge length (mm)	1001	965	753

4.2.2.4 Tangent stiffness post-yielding

To analyse the behaviour of the beams post-yielding, the stiffness of the beams was calculated between the yielding of the first rebar and the maximum load. This tangent stiffness is the ratio between bending moments and curvatures between the two instants described before (Figure 4.2-13). This analysis was not performed on the tests I182 Rect and I183 Rect. During the latest stages of Tests I182 Rect, one of the sensors (InfCent 2 of Figure 3.6-11) fell off the beam. The sensor fell before reaching the failure point, therefore the tangent EI could not be calculated. Tests I183 did not reach its maximal deformation before the sudden unloading, therefore it is not included in this comparison.

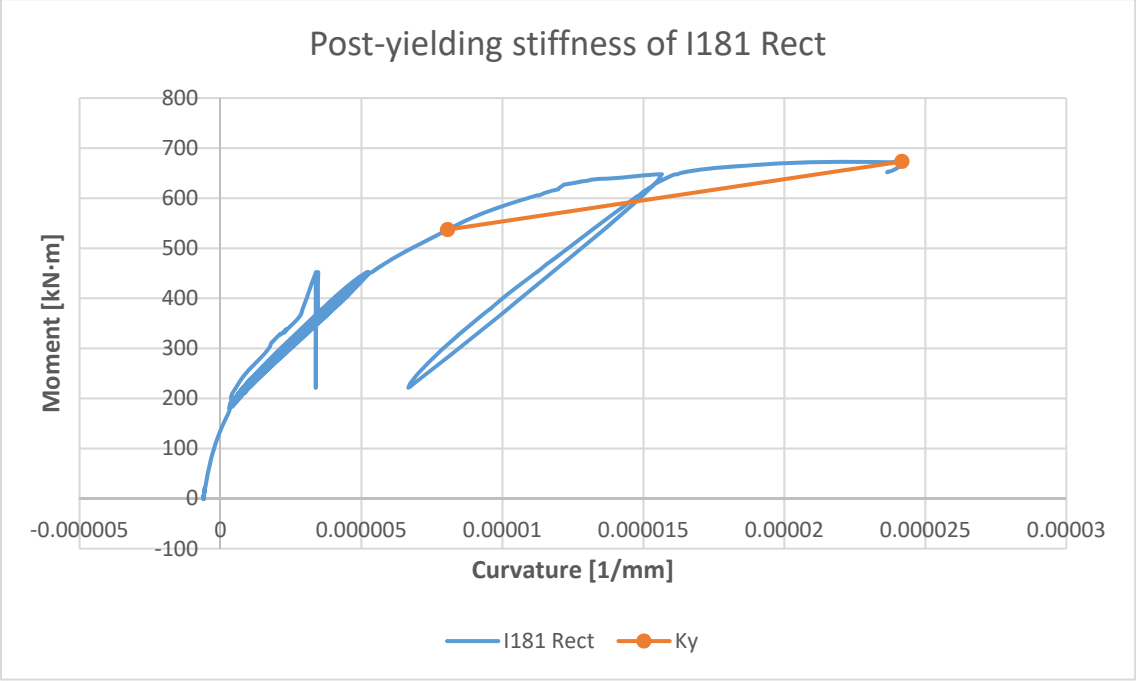

Figure 4.2-13 Tangent post yielding stiffness of tests I183 Rect

Table 4.2-7 Tangent EI obtained from yielding to failure. Table 4.2-7 presents the tangent EI of the two tests. These two tests had the same amount of ordinary reinforcement but the tests I181 Rect had twice the amount of active reinforcement. The tangent EI of tests I181 Rect was 2.42 times larger than I184 Rect tangent EI.

Table 4.2-7 Tangent EI obtained from yielding to failure

	I181 Rect	**I184 Rect**
Tangent EI	8.44E+04 kN·m^2	3.49E+04 kN·m^2

4.2.3 Post yielding behaviour of monitored reinforcement

Strains and stresses of the reinforcements in the final branches were compared in Figure 4.2-14, Figure 4.2-15, Figure 4.2-16 and Figure 4.2-17, for tests I181 Rect and I184 Rect. In beams I181 and I182, the strains grew significantly during yielding. The strain gauges of sections 4 and 5 increased their strain during the yielding hold. Some strain gauges that did not failed, doubled their strains. Once the load decreased to the quasi-permanent level, the bars showed compression stresses over 100 MPa, due to the important plastic strains and due to the prestress force.

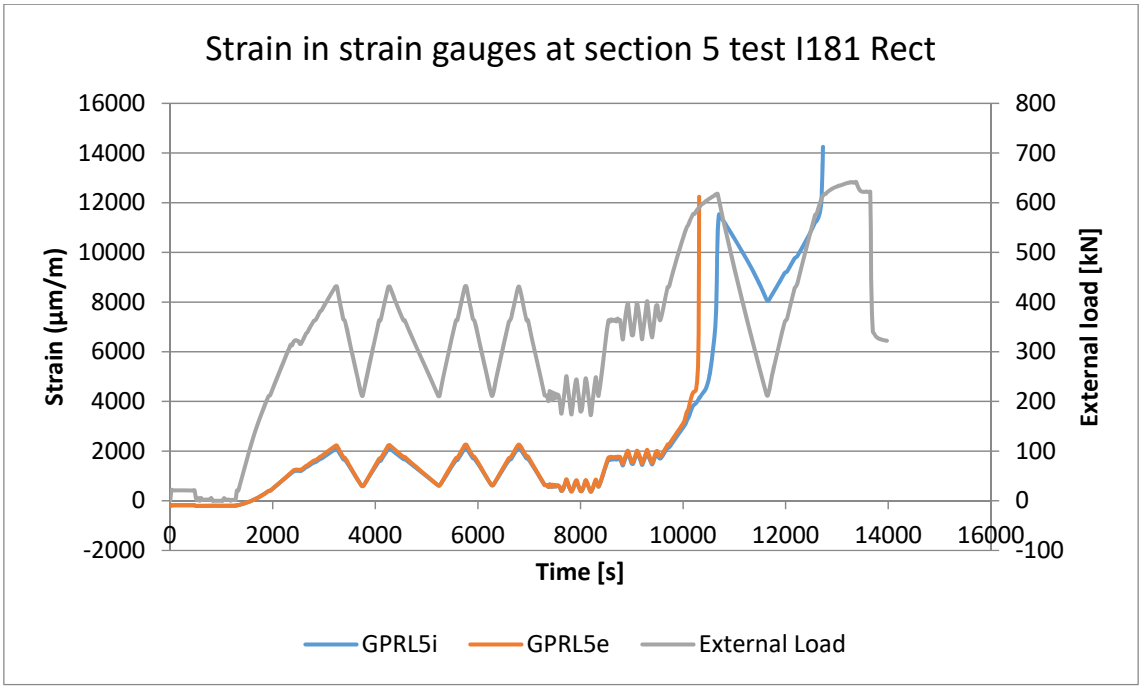

Figure 4.2-14 Strain gauge GPRL5i registered the loading and unloading process, having important strains in the last quasi-permanent load level

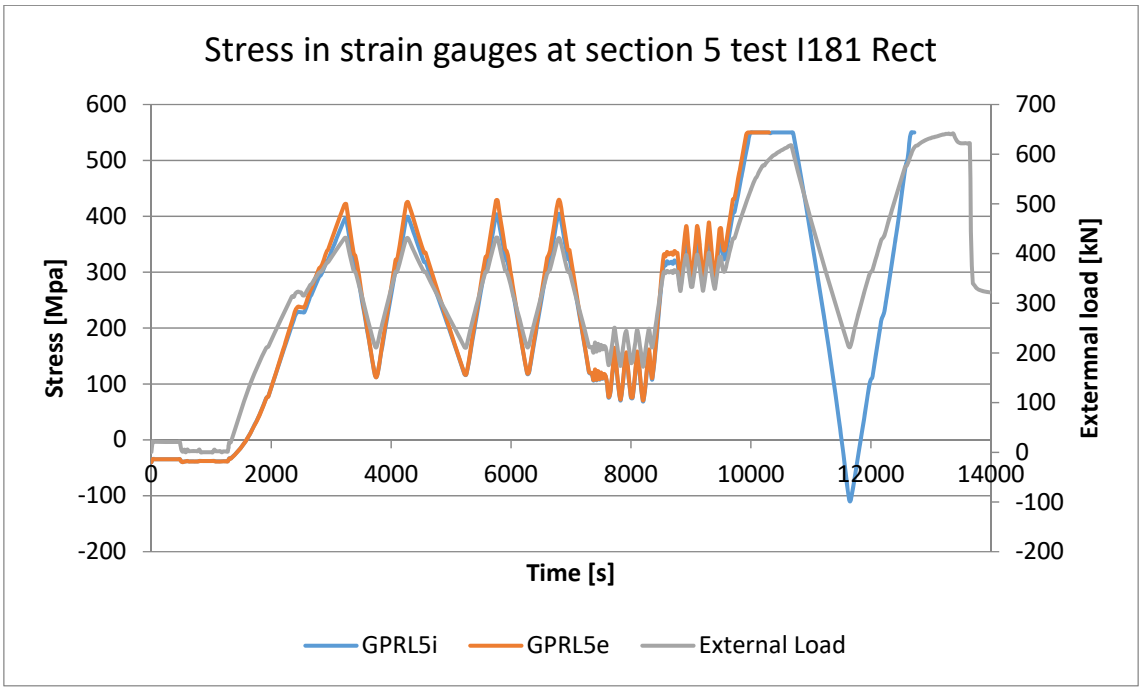

Figure 4.2-15 GPRL5i was compressed post peak due to an important plastic deformation of the bar

In turn, the bars in beams I183 and I184 reached the yielding point but did not showed significant strains increases. After unloading to the quasi-permanent load, strains were slightly higher and always in tension. When the load increased again, the strain gauges registered important peak deformation and then failed.

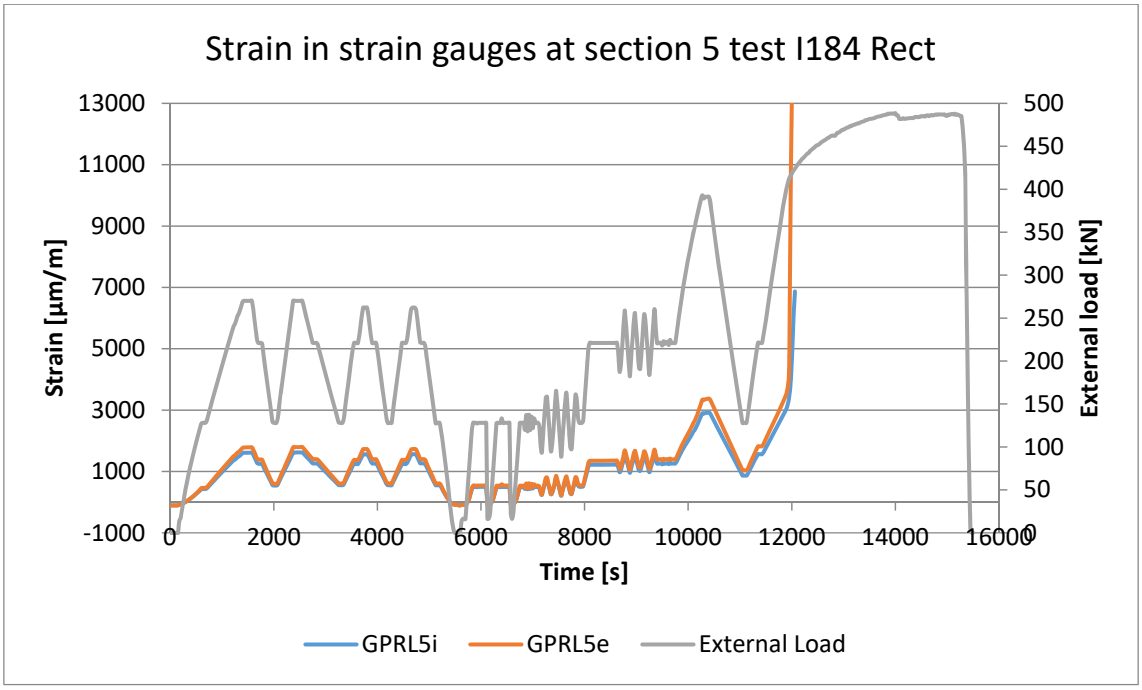

Figure 4.2-16 Strain of the strain gauges did not increase significantly during the yielding level

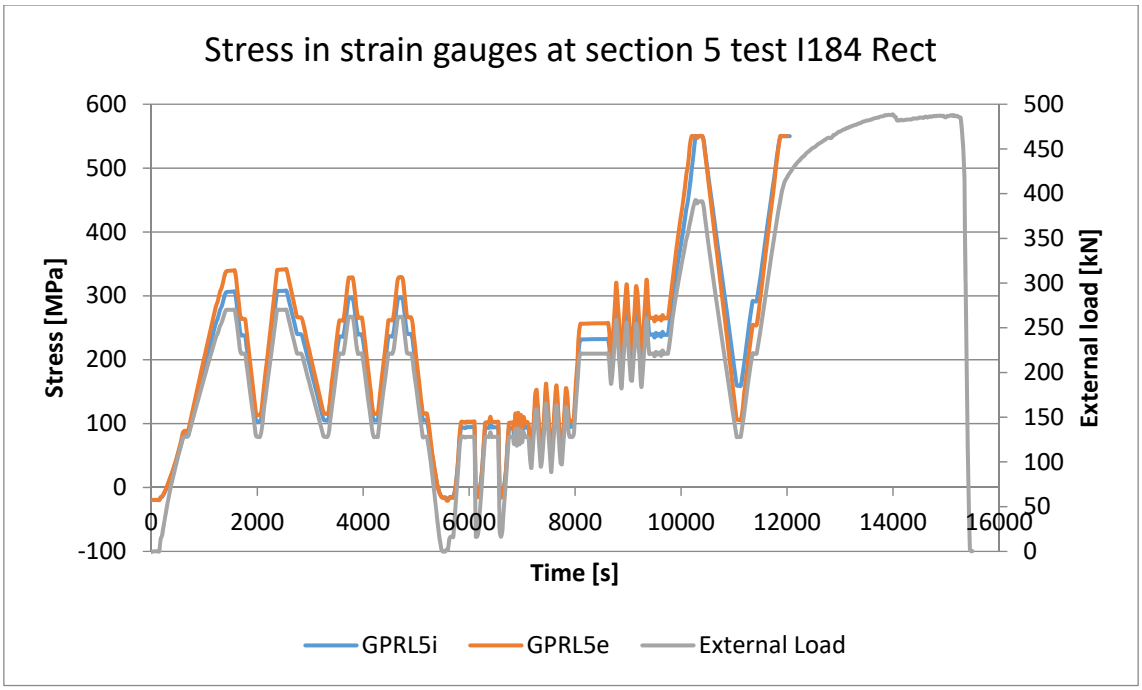

Figure 4.2-17 The stress post yielding peak was very similar to the previous quasi-permanent values

Figure 4.2-18 shows the average strains recorded by strain gauges in sections 4 and 5. As observed in this figure, the initial slope of the curves is similar between beams with the same amount of strands. The initial strains are all negative due to the prestress force compressing the concrete. When strains reached the yield level, the beams are grouped by failure bending moment. The loop after reaching yielding load level can be seen for all the tests, but not for test I182 Rect. The strain gauges of I182 Rect failed before the unloading from yielding load level to quasi-permanent level.

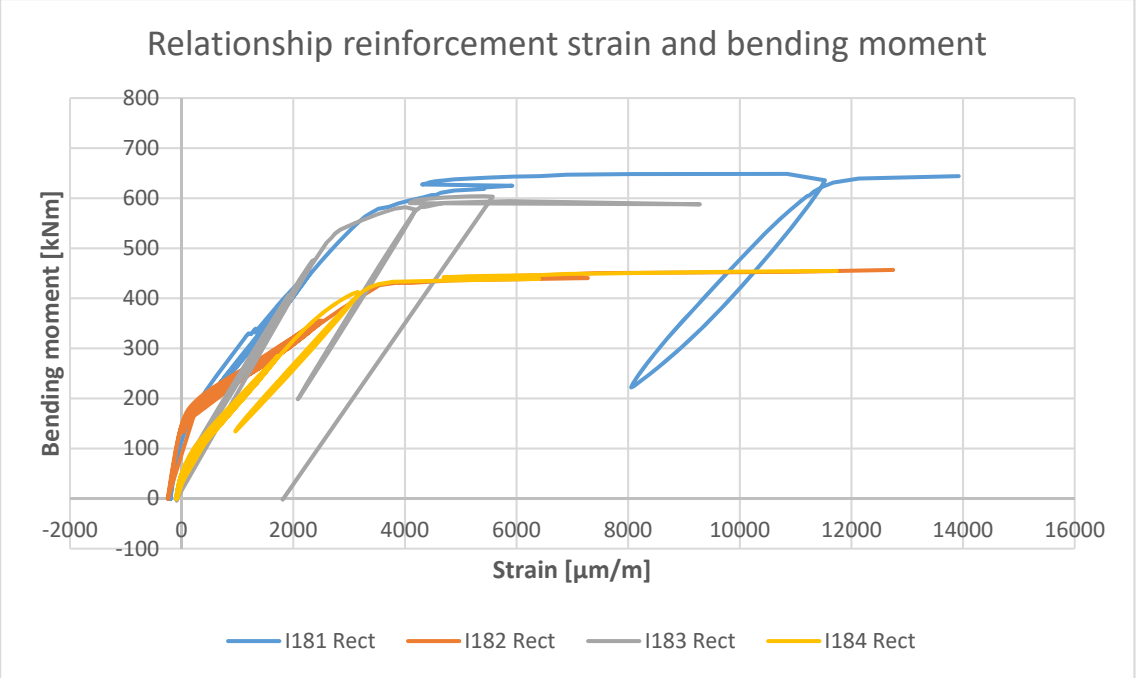

Figure 4.2-18 Average strain obtained from the strain gauges placed between sections M1 and M2

4.3 Performance of tests specimens in service

The design of the experimental campaign divided the four test into two groups, according to their cracking bending moment. The initial behaviour of the beams was analysed through the data recorded from the strain gauges and the recorded deflection. The load protocol was divided in two types of cycles: slow load speed and fast load speed. The slow cycles were used to obtain the influence of cyclic loads and the evolution of the reinforcement stresses (Figure 4.3-1). The fast cycles enable equivalent damping analysis and increased the amount of information to analyse the evolution of strains, stresses and deflections in PPC under cyclic loads.

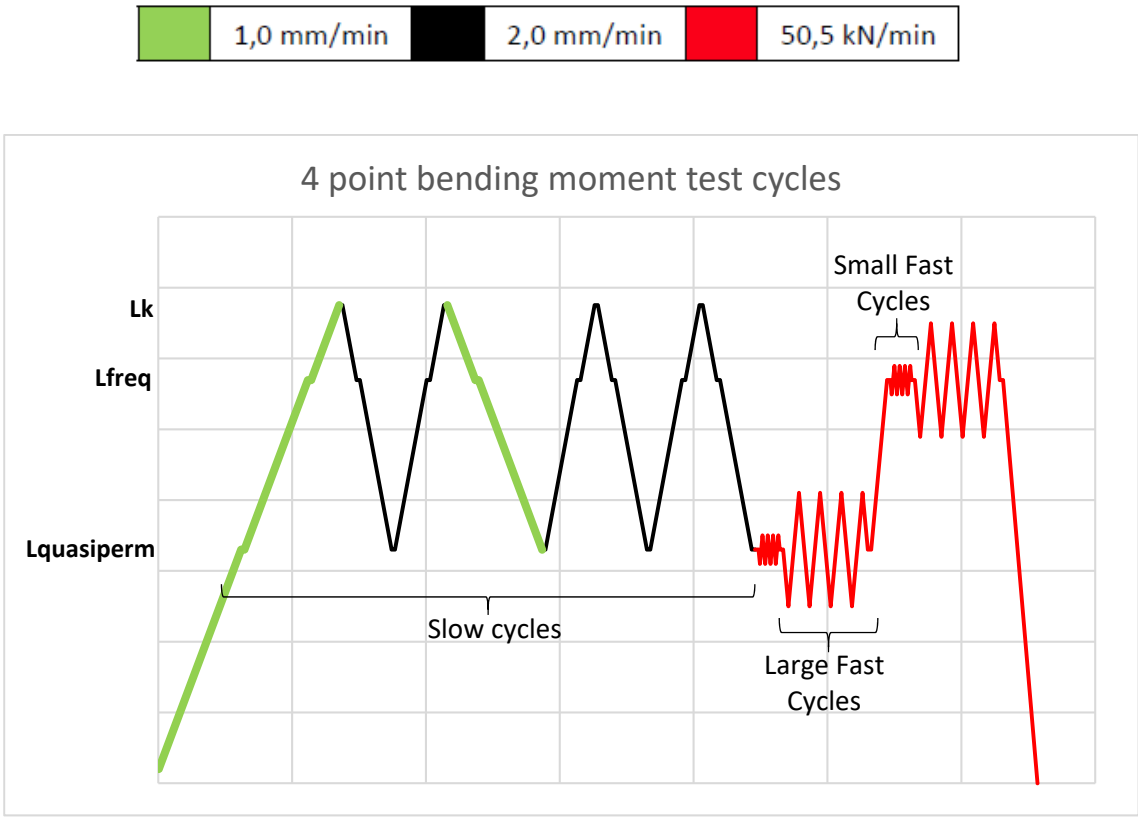

Figure 4.3-1 Load protocol in service

These tests were performed using the Set-up 3 for four-point bending test. As explained in Section 3.4, these tests were performed after the shear tests. In all the cases, the previous tests had already partially cracked regions 2 and 3 and modified the prestressing stress of the strands.

As described in Section 3.5, the slow cycles had 4 cycles between quasi-permanent level and characteristic level having a hold on the frequent level. The fast cycles were divided in 4 blocks. The first two blocks were centred in quasi-permanent level and the last two were centred in frequent level. The first and third block were called small fast cycles and the second and last block were called large fast cycles.

4.3.1 Stress evolution of longitudinal reinforcement

4.3.1.1 Analysis during the slow cycles

In Figure 4.3-2, the average strain recorded between the two loaded sections is shown. These strains correspond to the beginning of the tests, from the initial loading ramp up to the characteristic level. For tests I182 and I183, two ramps are provided. During those tests, some incidents with the instrumentation and the jack occurred and the tests had to be re initiated. For the test I182 Rect, this happened during the slow cycles (as can be seen in the beginning of the Figure 4.2-10). In the case of the test I183 Rect, the incident occurred after all the cycles, when the tests was approaching the final state and it fell off the supports. As it can be seen, these unloading did not modified the service behaviour of the beams.

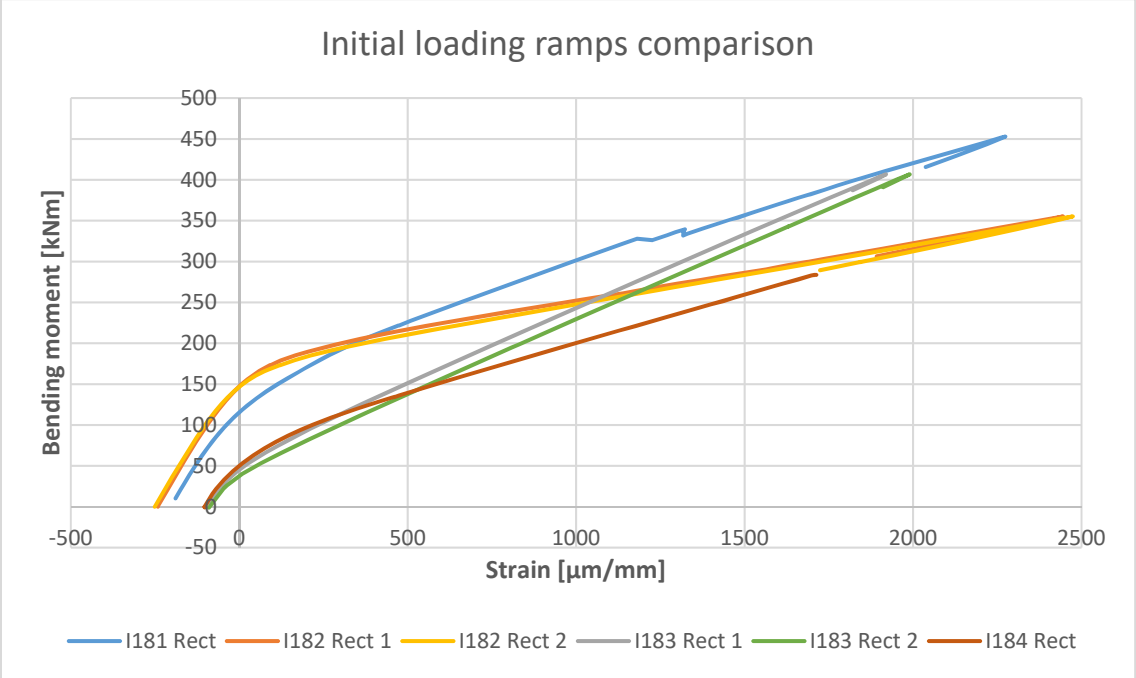

Figure 4.3-2 Average deformation of the strain gauges between sections M1 *and* M2

The initial strain of the ordinary reinforcements is in compression (negative values) due to prestressing in the section. Since the beams with 2 strands (I183 Rect and I184 Rect) had smaller prestressing force, the compression strain in the reinforcement was smaller than in the 4 strand cases. For both beams, the bending moment that produced tensile stresses in the longitudinal reinforcement was 50 kNm. In the case of the remaining two beams (I181 Rect and I182 Rect), the bending moment that generated tensile stresses was 114 and 150 kNm, respectively.

Since the beams were already cracked from the previous tests, once the strains turned to a positive value the cracks opened and the stiffness of the beams changed. The bending of the curves of Figure 4.3-2 for the beams I181 Rect and I184 Rect were similar, in both cases the amount of longitudinal reinforcement was 6Ø16. Beam I182, with the smallest amount of reinforcement, had the lowest slope once the reinforcement was under tensile strains. The point where the slope changed was 175 kNm, half of the characteristic load level. This was the highest slope change of all the cases. This beam had the biggest difference between the amount of ordinary and prestress reinforcement.

All tests had four initial cycles where the load changed from the quasi-permanent level to the characteristic level. The evolution of the stresses of the longitudinal reinforcement was analysed through the cycles and through the numerical simulations. The stresses in each level are compared and their progression is analysed in this section. For the frequent level, the influence of the loading and unloading process was studied. In Figure 4.3-3, the experimental and simulated tensile stress were compared. The tensile stress recorded in the first loading step was very similar to the value predicted by the simulation, the difference is of 3 MPa. The second time the load decreased to 221 kN, the tensile stress changed, and was 30 MPa higher than the previous one, and, after 5 cycles, the stress increased 40 MPa.

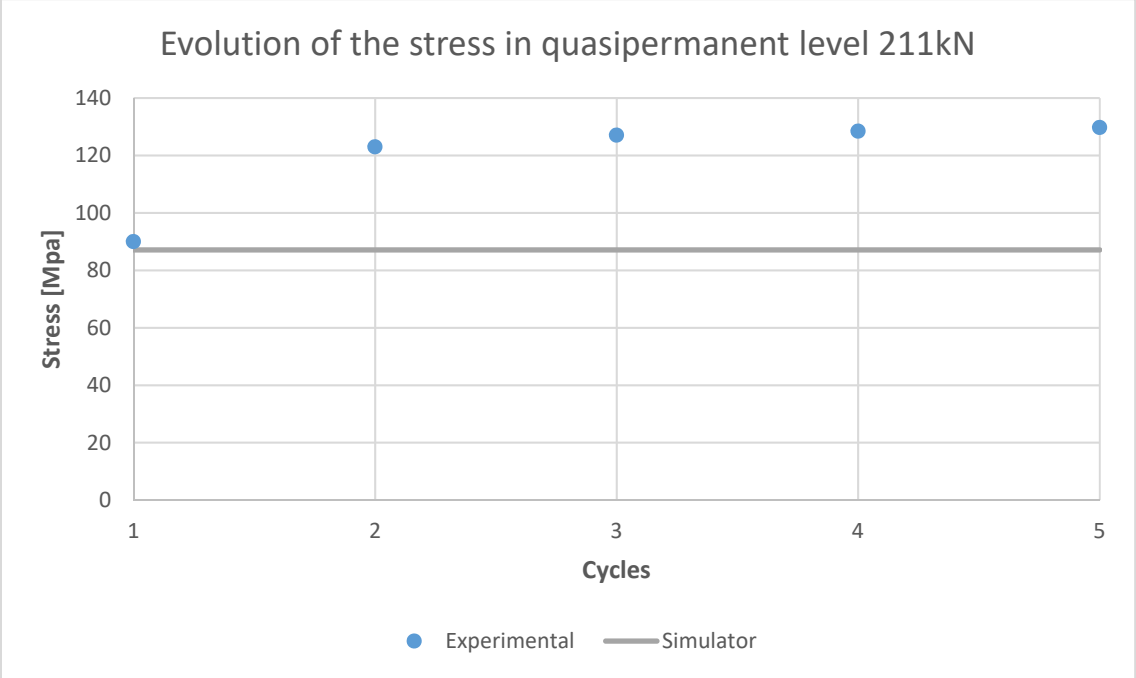

Figure 4.3-3 Average stress in the longitudinal strain gauges 4 and 5 on the test I181 Rect

The four tests showed a similar response, the first time the load level was reached, the simulated load and the experimental load were similar. The subsequent times, the stress augmented and tends to stabilize. The increment did not depend on the stress magnitude, it was between 10 and 40 MPa. In the case of beam I182, the increase in tension was of 157%, since the stress was very small.

Using Equation 2.2-1 to compare the increase of stress between the simulation and the higher stress during the cycles in quasi permanent level provides an α factor of 10.64 (Section 4.2.2.1). Where the tests with higher amount of equivalent reinforcement area had higher stress differences.

For the frequent load level, the influence of loading and unloading in the stress of the reinforcement was analysed. Figure 4.3-4 and Figure 4.3-5 show an example of the difference between the 4 and 2 strand beams, respectively. In Figure 4.3-4, the gap between loading and unloading is over 20 MPa, and both curves show the same pattern. The simulated value was closer to the first time the load level was reached. On the other hand, for the beams with 2 strands, the stress had a low increase and the simulated value was the average stress during loading.

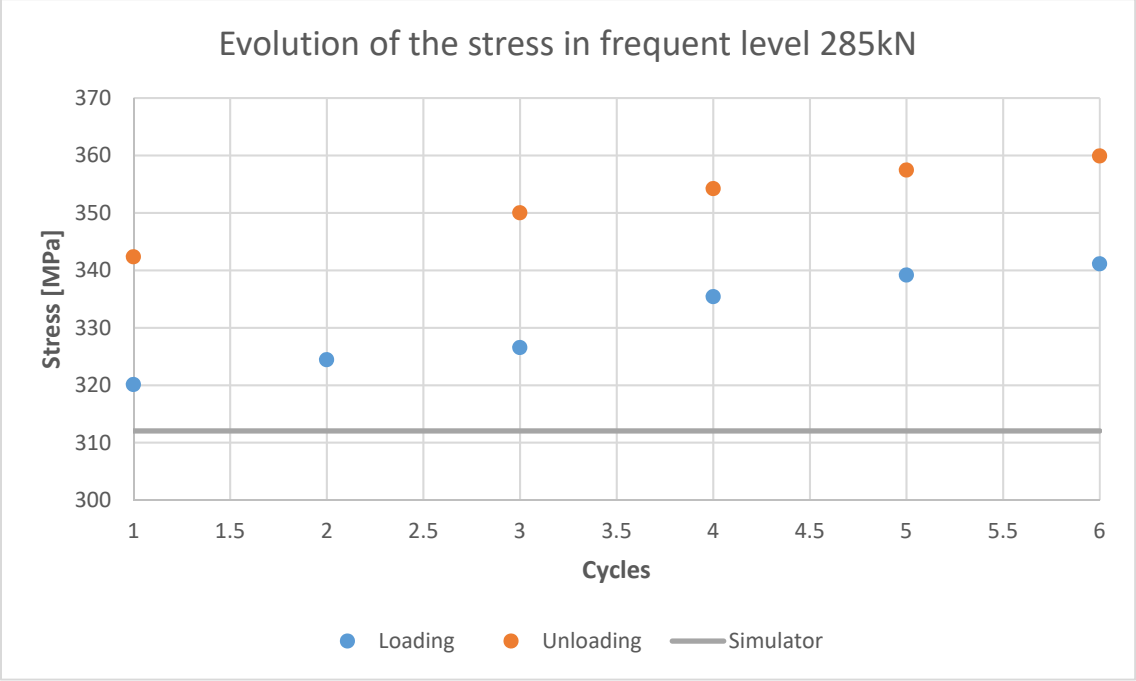

Figure 4.3-4 Average stress in the longitudinal strain gauges 4 and 5 on the test I182 Rect

For the beams with 4 strands (Figure 4.3-4), there was a big difference between the behaviour during loading and unloading. In both tests, the difference was initially of 20 MPa, but in beam I181, the difference reduced progressively to 10 MPa. Although in both cases the stress increases away from the simulated values.

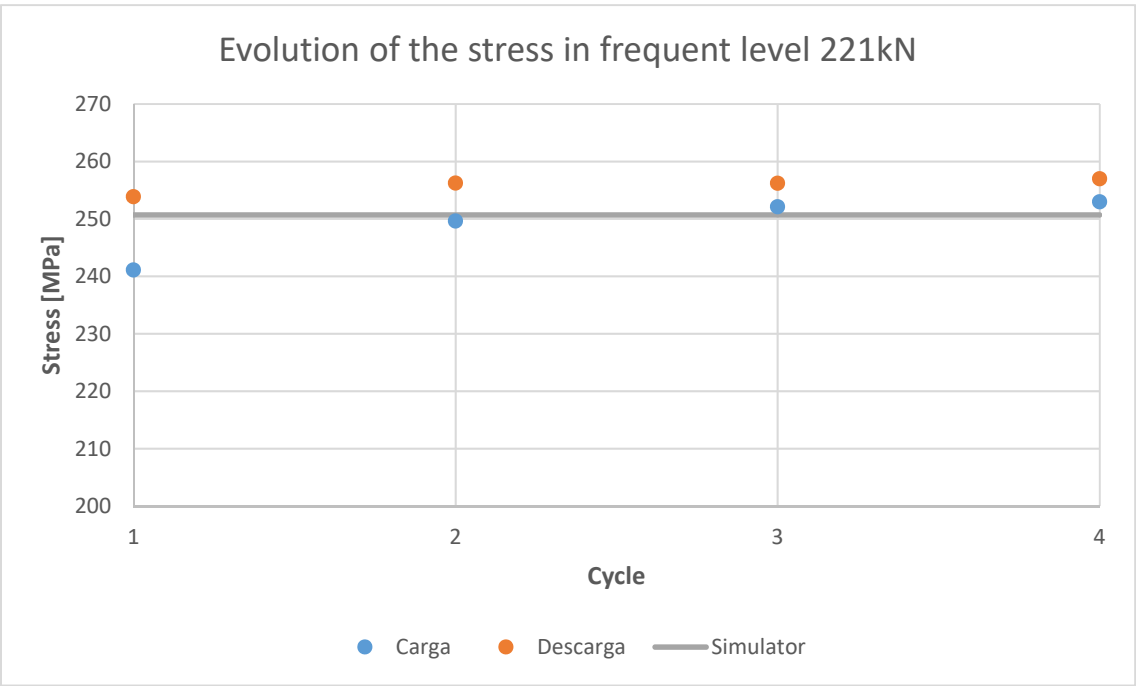

Figure 4.3-5 Average stress in the longitudinal strain gauges 4 and 5 on the test I184 Rect

The information obtained from the characteristic level showed a similar behaviour. The increase of stresses for beams with 4 strands was higher than for beams with 2 strands. On the other hand, there was not a reduction on the stress increment after subsequent cycles. The difference between the first

and second cycle was very similar to the difference between the two last cycles. The trend of increase of stress was constant.

The stresses predicted by the simulations were very close to the experimental results in the first load branch. The cycling process increased the strains and stresses. The average difference between the simulation and the experimental results was 26 MPa (29%), 23 MPa (7%) and 11 MPa (2%) for the load levels of quasi-permanent, frequent and characteristic, respectively. The tests with smaller prestress had smaller differences.

4.3.1.2 Analysis at quasi-permanent level

After the slow load cycles, fast load cycles were applied. The average stress in sections 4 and 5, recorded on the fast cycles performed at the quasi-permanent level, was lower than the stresses obtained during the slow cycles. In Figure 4.3-6, the stress during the three set of cycles at quasi-permanent level are shown, the slow and the two fast cycles (small and large). The stress decreased during the small fast cycles. The stresses of loading and unloading were very similar. During the large cycles, the stresses went down again, and there was a difference between the loading and unloading stresses. Conversely, the rebars stresses decreased with the number of cycles. The final cycle had the smallest stress of the fast cycles. Although, the smallest stress of quasi-permanent level was the recorded on the initial loading.

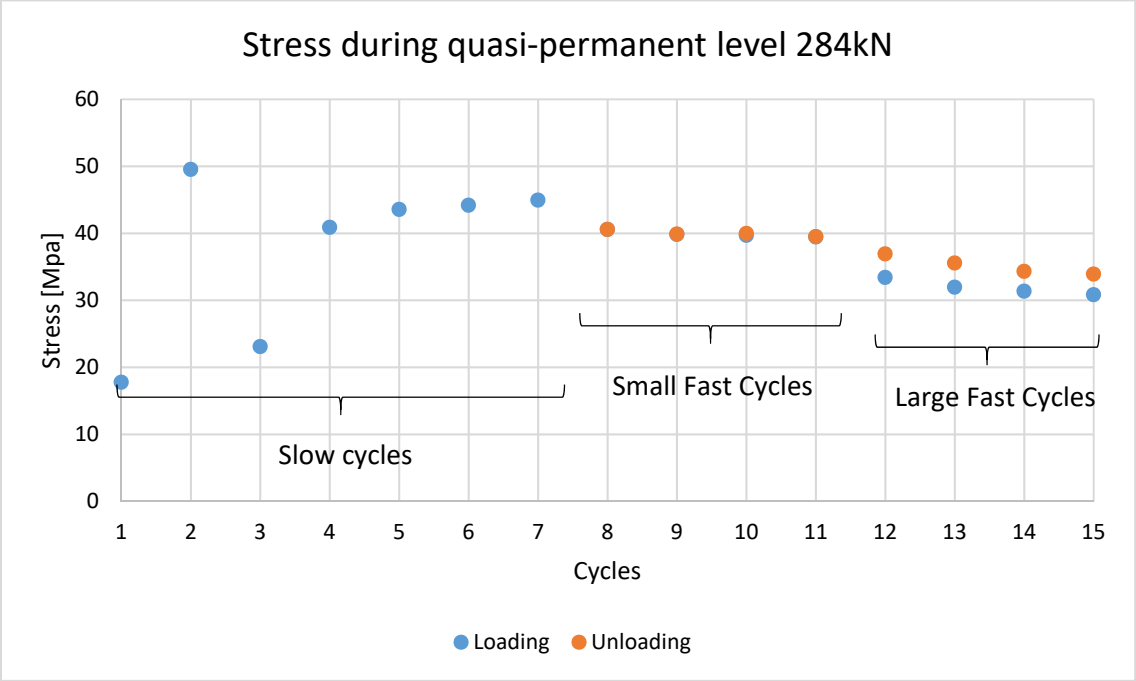

Figure 4.3-6 Evolution of the average stress in sections 4 and 5 during all the cycles for testI182 Rect

4.3.1.3 Analysis at frequent level

The cyclic behaviour at the frequent load level was different; the stresses had a very small increase. In the small-fast cycles, the stresses for loading and unloading were almost the same, very similar to the stress of the last cycle of the slow cycles. Figure 4.3-7 shows the results of the test I181 Rect at the frequent load level. Focusing on the data recorded for the slow cycles in the loading branches, the stresses increased significantly (25 MPa of increase from cycle 1 to 4).

It is worth mentioning that between cycles 4, end of the slow cycles, and cycle 5, beginning of frequent fast cycles, the quasi-permanent fast cycles were performed. Despite the application of those cycles, the difference of stresses between the stress of cycles 4 and 5 was small and it was similar to the difference between other cycles. During the small fast cycles, the stresses tend to a constant value. During the large cycles, the stresses grew again but with a stabilizing trend.

The unloading stresses described a different pattern. In the slow cycles, the unloading stresses were higher than the loading values. For the small fast cycles, they reduced to similar values than the loading process. Finally, with the large fast cycles, the difference grew again, but kept reducing with successive cycles. The trend of the stresses was horizontally asymptotic. The smaller amplitude of the small fast cycles did not generate differences between the branches.

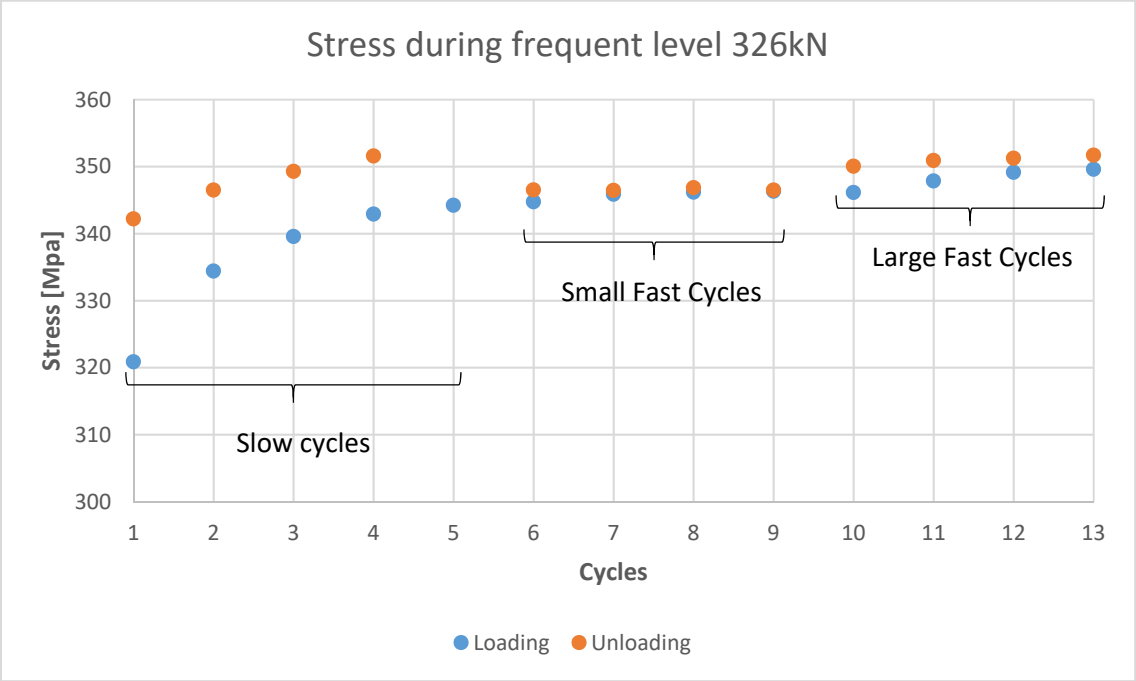

Figure 4.3-7 Evolution of the average stress in sections 4 and 5 during all the cycles for testI181 Rect

In the I184 Rect test, after the slow cycles, the beam was completely unloaded and then the fast cycles of quasi-permanent level were performed. The order of the frequent fast cycles was inverted, the large fast cycles were performed before the small fast cycles (Figure 4.3-8). This was due to an error with the load protocol of the jack. The problem was solved without unloading the beam but the order of the cycles had to be changed. The stresses of cycle 5 and 6 correspond to the stresses of a load hold at frequent level, after the total unload and the first block of fast cycles at quasi-permanent level. In this holds the stress was lower than the stresses of cycle 4, but higher than cycle 1. During the large set of fast cycles, the stress increased up to the 4th cycle. The stresses during the small fast cycles were constant. The trend of the unloading stresses was similar to the unloading previously commented.

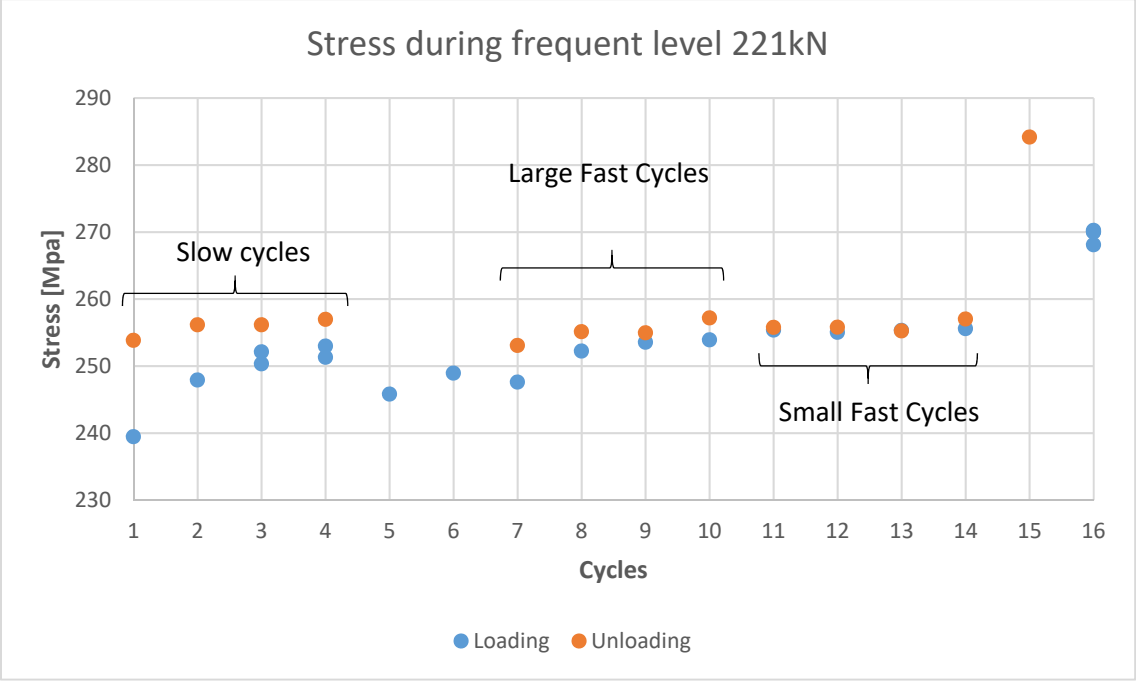

Figure 4.3-8 Evolution of the stress in sections 4 and 5 during all the cycles for testI184 Rect

In the test I183 Rect and I184 Rect (2 strands beams), the difference between the loading and unloading stresses was smaller than for the 4 strand beams (I181 and I182). However, in both cases the stresses tended to converge, reducing the increase of stress after each cycle.

4.3.1.4 Analysis at characteristic level

On the characteristic level, all the beams increased the stress of their rebars after each cycles. The load protocol of I184 Rect suffered some problems and the characteristic load level was slightly overcome. Moreover, the difference between frequent and characteristic load was exactly 40 kN. This matched the increase of load of the large fast cycles. Therefore, as can be seen in Figure 4.3-9, there are loading and unloading branches for this characteristic analysis, plus the stress corresponding to the peak of the large fast cycles centred in frequent load. These stresses were lower than the ones of the fourth cycle, but with an increasing trend. After reaching the yielding load level, in cycles 9 and 10, the stress increased.

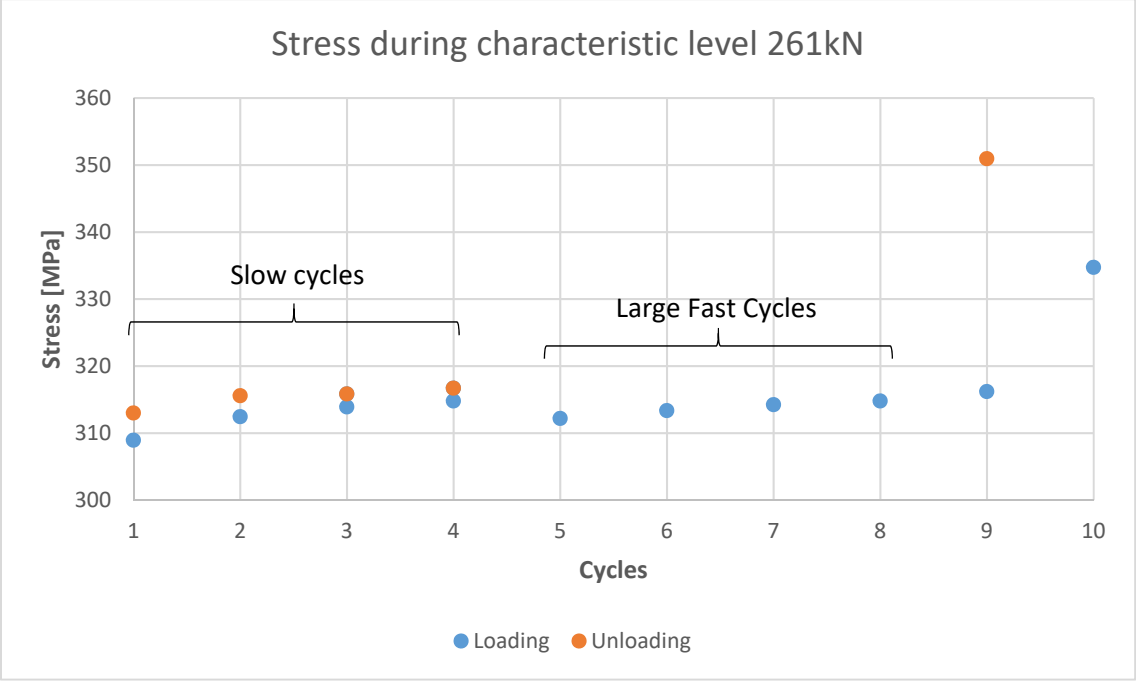

Figure 4.3-9 Evolution of the stress in sections 4 and 5 during all the cycles for testI184 Rect

4.3.2 Deflection behaviour

The information obtained from strain gauges show the localized response of the sections where the sensors were placed. The deflection of the beam shows a general behaviour of the beam during the serviceability loads. By using the vertical displacement transducers placed at midspan, the evolution of the deflection due to repetitive cycling loads can be analysed as well as the hysteretic behaviour of the PPC. A new load level was added to perform the analysis, called "Extra load level" (Lextra in the figures). This extra load level was used to compare the loading and unloading behaviour. Figure 4.3-10 shows the external load of the test I181 Rect and the deflection at midspan of all the load levels.

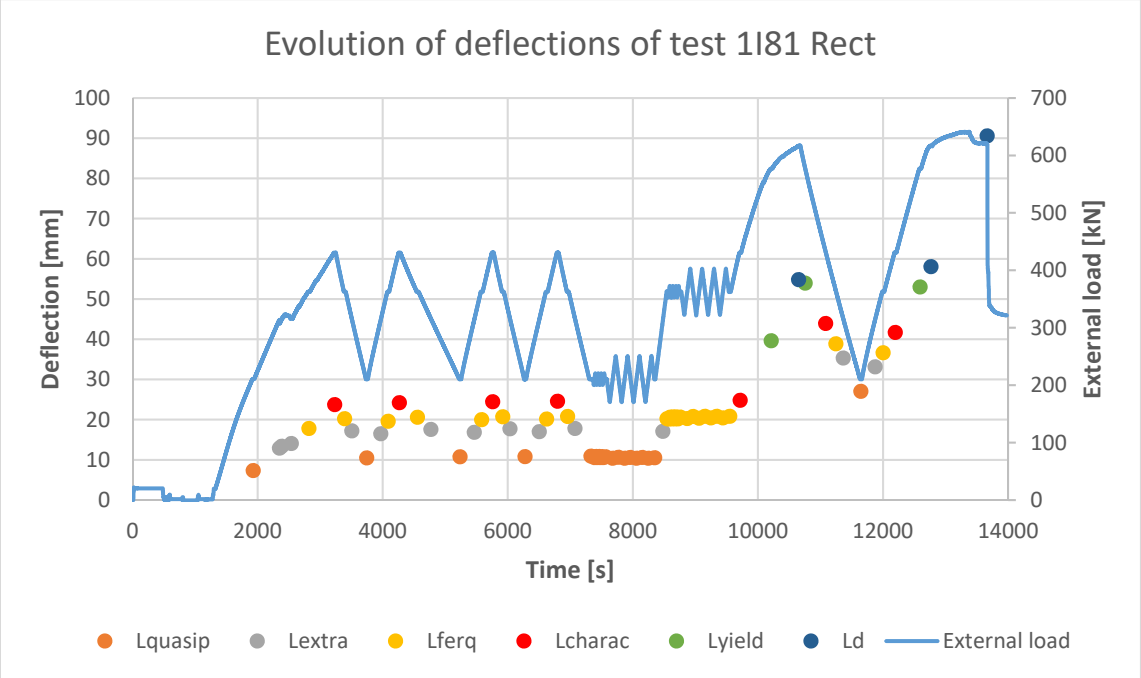

Figure 4.3-10 Deflection at midspan, for the load levels of the I181 Rect test

Figure 4.3-11 is a detailed view of the initial part of the test. In these first 4 cycles, the deflections increased through the cycles for all the levels; although the variation between deflections is decreasing. The difference between loading and unloading also decreases and it was higher on the extra level. The deflections for the characteristic level (peak of the cycles) were very similar, the cycling process did not affected the behaviour of the beam.

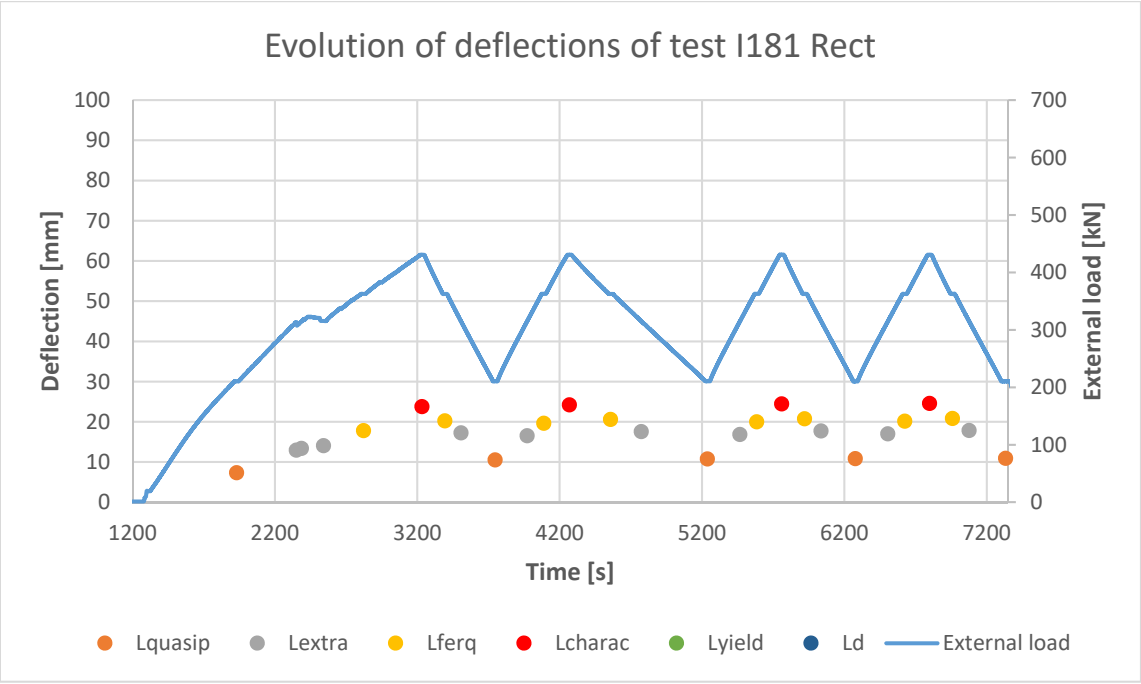

Figure 4.3-11 Zoom of the deflection of Figure 4.3-10.

4.3.2.1 Evolution of deflection in quasi-permanent level

In Figure 4.3-6, it was observed than the stresses decreased during the fast quasi-permanent cycles. The same phenomena was observed for the deflection, in Figure 4.3-12. The deflection loading branch in quasi-permanent level decreased after each cycle. The test I184 Rect showed the most important reduction of deflection between slow and fast cycles. As it was already seen in Figure 4.2-16, between those cycles the tests was stopped and the specimen completely unloaded. The fast cycles were performed before loading again the beam to characteristic level. This difference with the rest of tests generated a smaller deflection on the fast cycles.

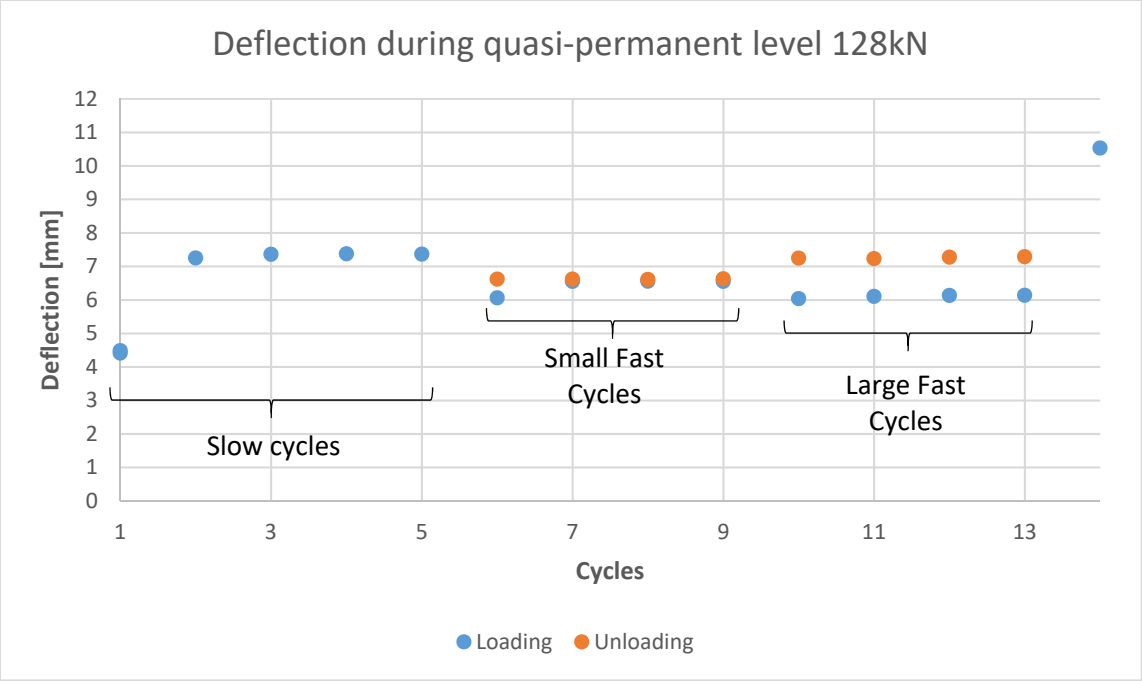

Figure 4.3-12 Deflection at midspan for test I184 Rect

In all four tests, the difference between loading and unloading branches for the small fast cycles was smaller than for the large fast cycles. On the beams with 2 strands, I183 and I184 (Figure 4.3-12), the unloading deflection obtained on the large fast cycles was higher than the loading deflection obtained on the small fast cycles. On the other hand, for the 4 strand beams, the unloading branch of a cycle was inferior to the loading branch of the previous cycle (Figure 4.3-13). The extra prestress closed the cracks when the load was reduced, reducing the deflection.

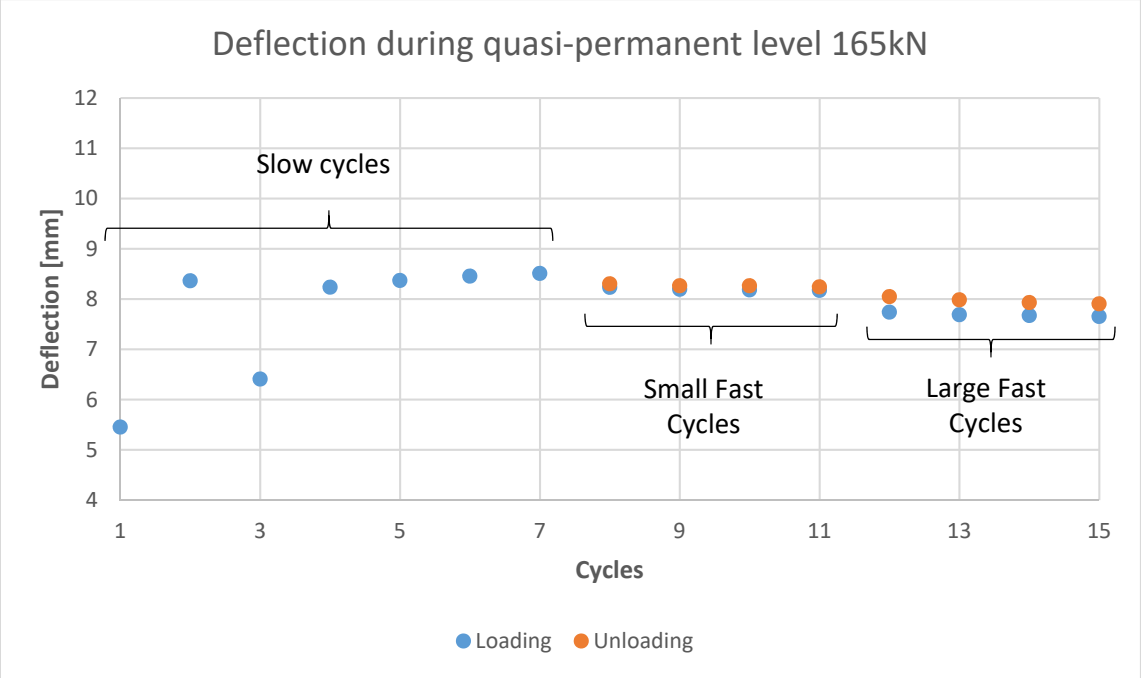

Figure 4.3-13 Deflection at midspan of a 4 strands beam, test I182 Rect

The α factor (Equation 2.2-1) was calculated for the difference between loading and unloading branch in deflection for the last fast cycle. The α factor with smaller error was 6.22. The differences were smaller for the tests with larger amount of equivalent area of reinforcement.

4.3.2.2 Evolution of deflection in frequent level

Like for the case of the stress analysis, in the frequent level the loading, the deflections increased for all tests except for I183 Rect (Figure 4.3-14). In tests I182 Rect (Figure 4.3-16), I183 Rect and I184 Rect, the difference between loading and unloading deflection was higher in the large fast cycles than in small fast cycles. For test I181 Rect, the difference between loading and unloading for the two fast cycles is very similar; but in the fast cycles, the increment of deflection was higher (Figure 4.3-15).

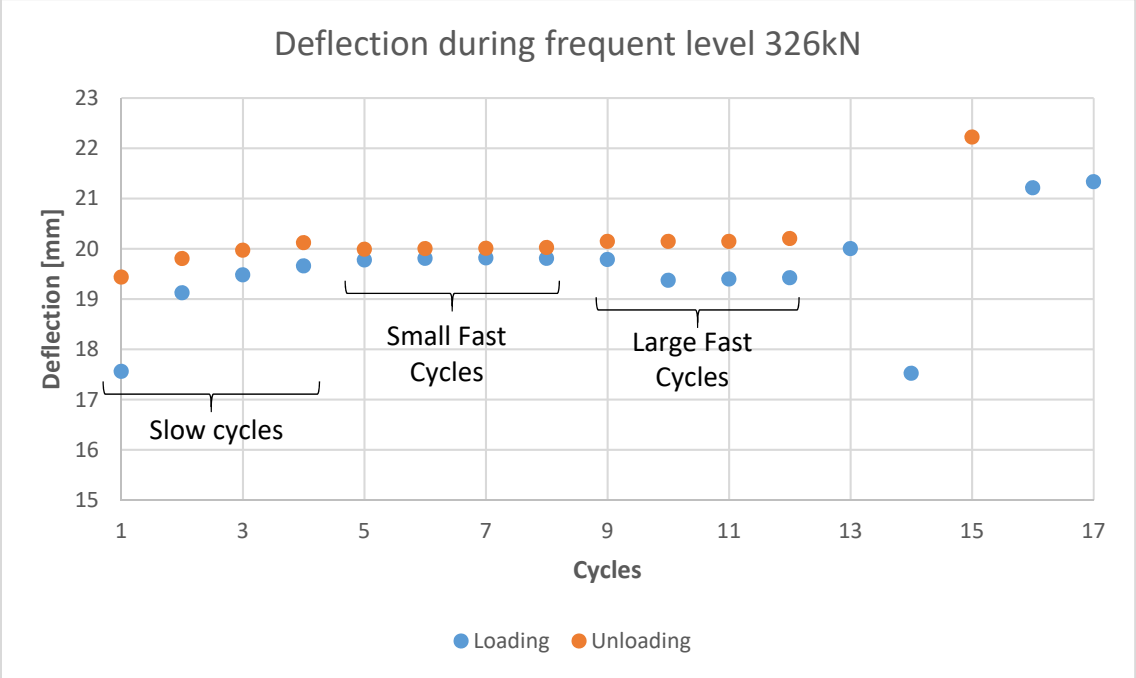

Figure 4.3-14 Deflection at midspan of test I183 Rect

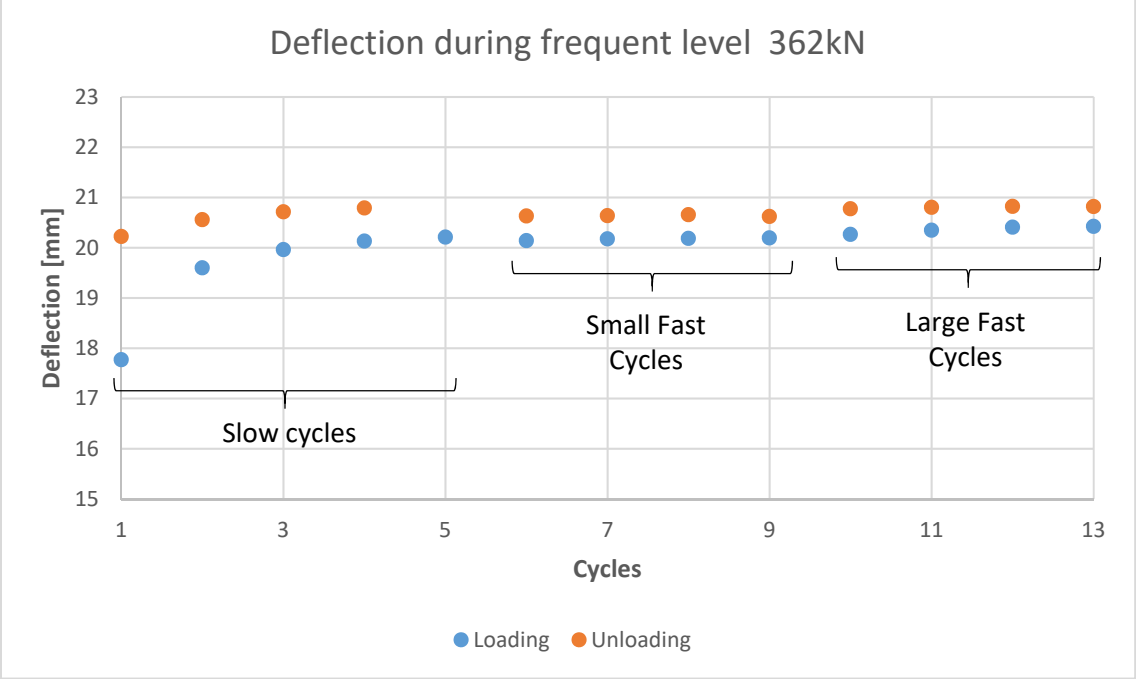

Figure 4.3-15 Deflection at midspan of test I181 Rect, with similar differences between loading and unloading for all fast cycles

Figure 4.3-16 shows the progressive increase of the deflection in the I182 Rect test. During the small-fast cycle, the difference between loading and unloading deflection was reduced, being almost equal in the in the last cycle. In the first cycle (cycle 12) of the large-fast cycle, the deflection was slightly lower than the previous cycle, but it grew for the subsequent cycles. As observed, the specimen did not behave linearly, the precedent states of the structure modified the response of the structure. This case showed the importance of the load history

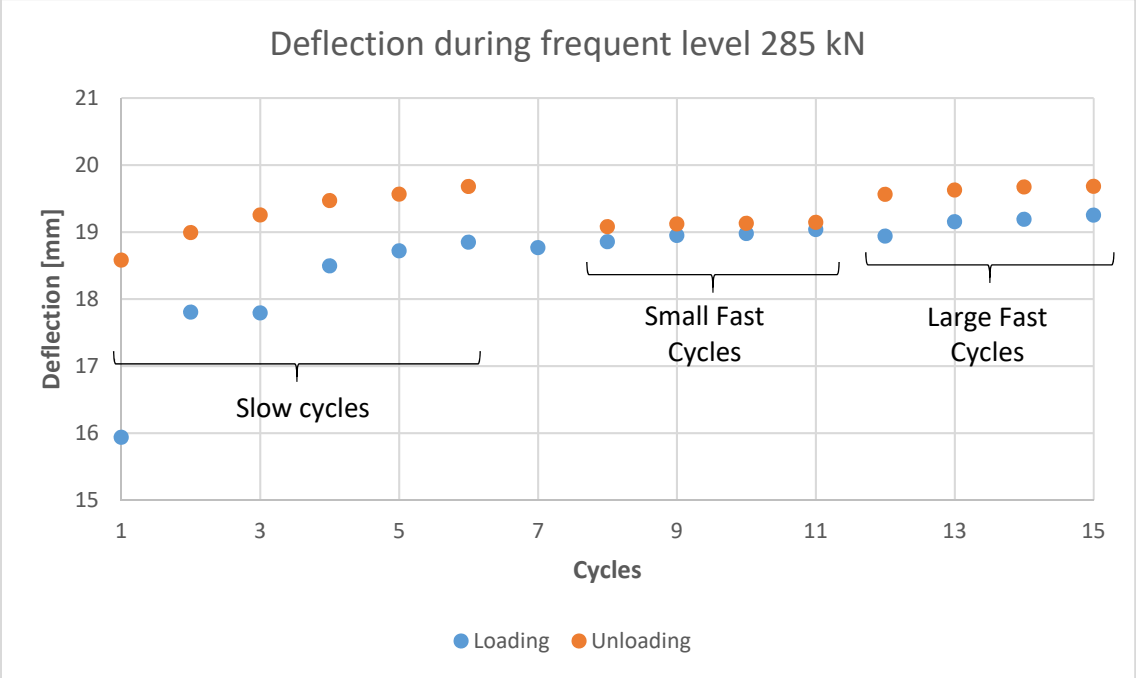

Figure 4.3-16 Deflection at midspan of test I182 Rect, increasing progressively after each cycle

The equivalent area (Section 4.2.2.1) was calculated using the difference between the loading and unloading branches of cycle four, the last slow cycle. In this case, the α factor (Equation 2.2-1) was 4.23 and the beams with higher equivalent area had smaller deflection differences. The α factor was also computed using the difference between branches for the last cycle of the large fast cycles. The relation between areas was 9.14 and, like in the previous cases, the differences between loading and unloading decreased when the equivalent area increased.

4.3.3 Analysis of equivalent damping in service situations

The control of bridge vibrations is carried out to analyse the serviceability of the structure. The damping of a structure depends on the materials and the stiffness of the structure. PPC has a behaviour between reinforced concrete (RC) and totally prestressed concrete (TPC). Therefore, the damping ratio of PPC is also between the damping ratios of RC and TPC.

An equivalent damping analysis was performed using the deflection, of the displacement transducer placed at midspan of the beam, during the large fast cycles. These cycles had hysteretic behaviour. Table 4.3-1 presents the equivalent damping ratios obtained with the method presented in (Jacobsen, 1930; Grant, Blandon and Priestley, 2005). Because the midspan Temposonic of test I184 Rect was not working properly, the data of this case was computed by using the deflection of the transducers under the loaded sections *M1* and *M2.* The damping ratios obtained for the frequent level are higher than the ratios obtained for the quasi-permanent level; hence, the ratios of the 4 strand beams are lower than the other ratios.

Table 4.3-1 Equivalent damping recorded during the wide cycles

	Equivalent Damping	
	Lquasi	Lfreq
I181 Rect	3,5%	5,8%
I182 Rect	3,6%	3,6%
I183 Rect	4,9%	8,7%
I184 Rect	10,9%	11,2%

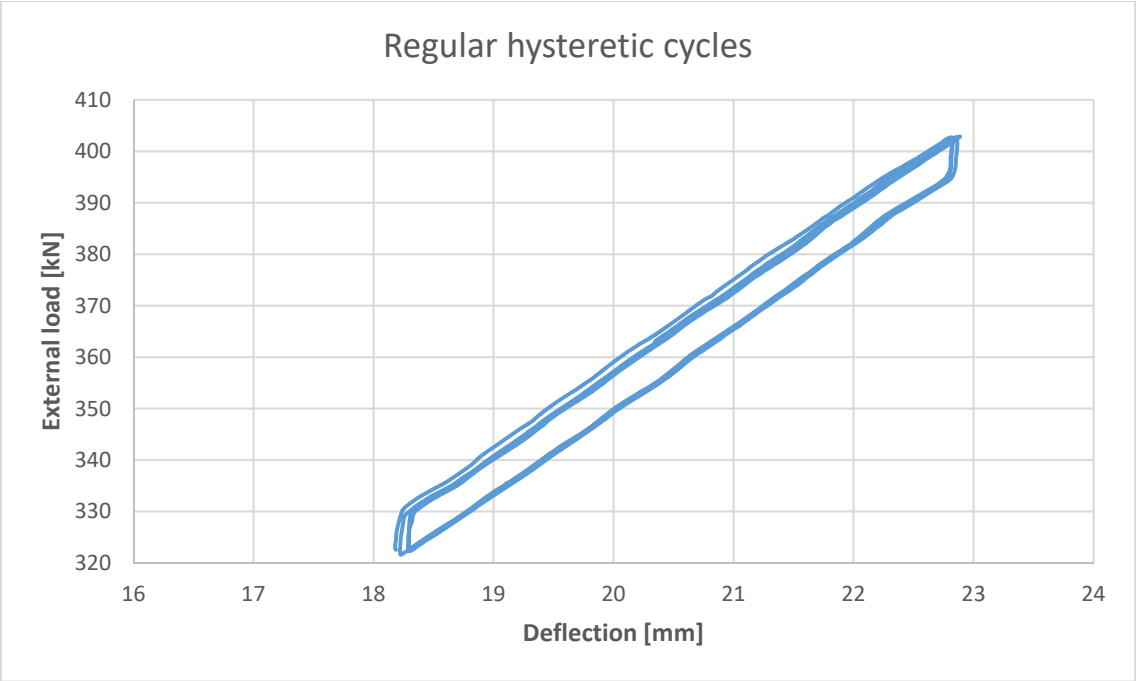

Figure 4.3-17 Load vs deflection of the beam I181, for the frequent load level

Figure 4.3-17 shows an example of the hysteretic cycles described by the beams. As observed, for the same load level, the deflection changed depending on the type of branch: loading or unloading. At the beginning of each ramp, the stiffness of the beam was very important and the load varied more than the deflection. When the external load had varied enough, the deflection slope started to change. This effect created a gap between the two branches. Tests I181 Rect, I183 Rect and I184 Rect showed a behaviour similar to Figure 4.3-17 or Figure 4.3-18 for the two load levels. The stiffness of the branches was very similar.

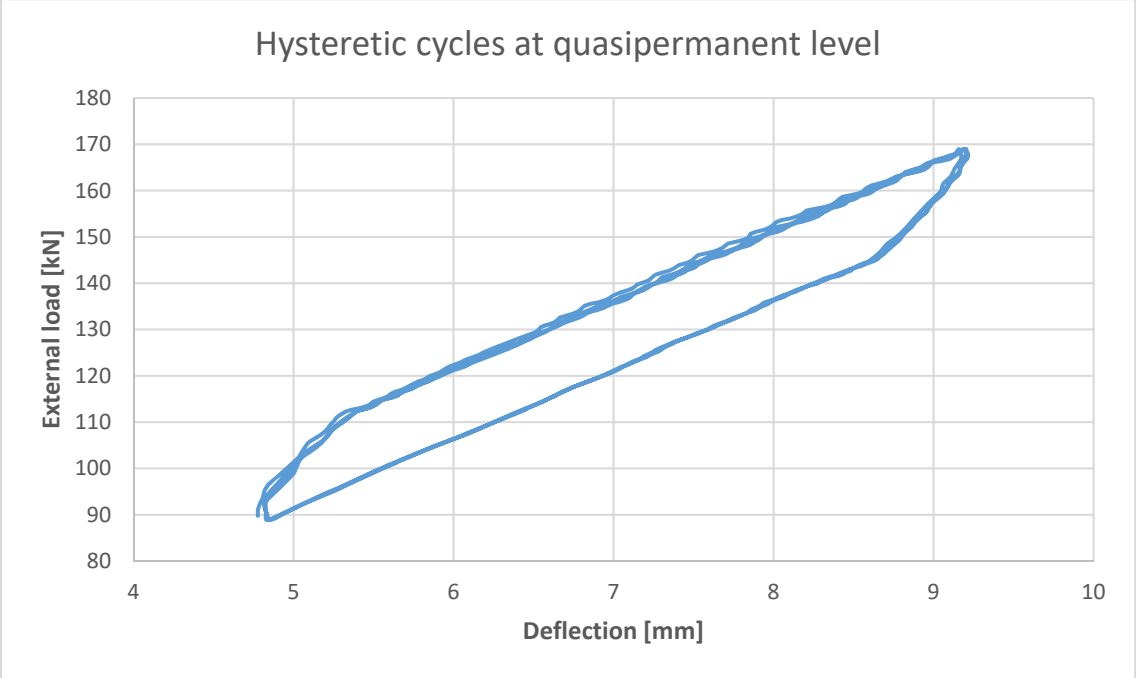

Figure 4.3-18 Load vs deflection of the beam I184

Beam I182 Rect behaved differently. In quasi-permanent level, the hysteresis loop had both branches follow similar paths. There was a progressive variation of the stiffness generating an area between the branches but not like in previous specimens. Figure 4.3-19 shows the hysteretic cycles for the quasi-permanent level. The shape of these loops is completely different to the other cases. Its branches have two very distinct stiffness. When comparing this figure with the data of test I182 Rect, shown in Figure 4.3-2, it can be seen how the loops are replicating the behaviour of the initial loading of the test. In this case, the load level was closer to the cracking load that the change of stiffness was observed in this loop.

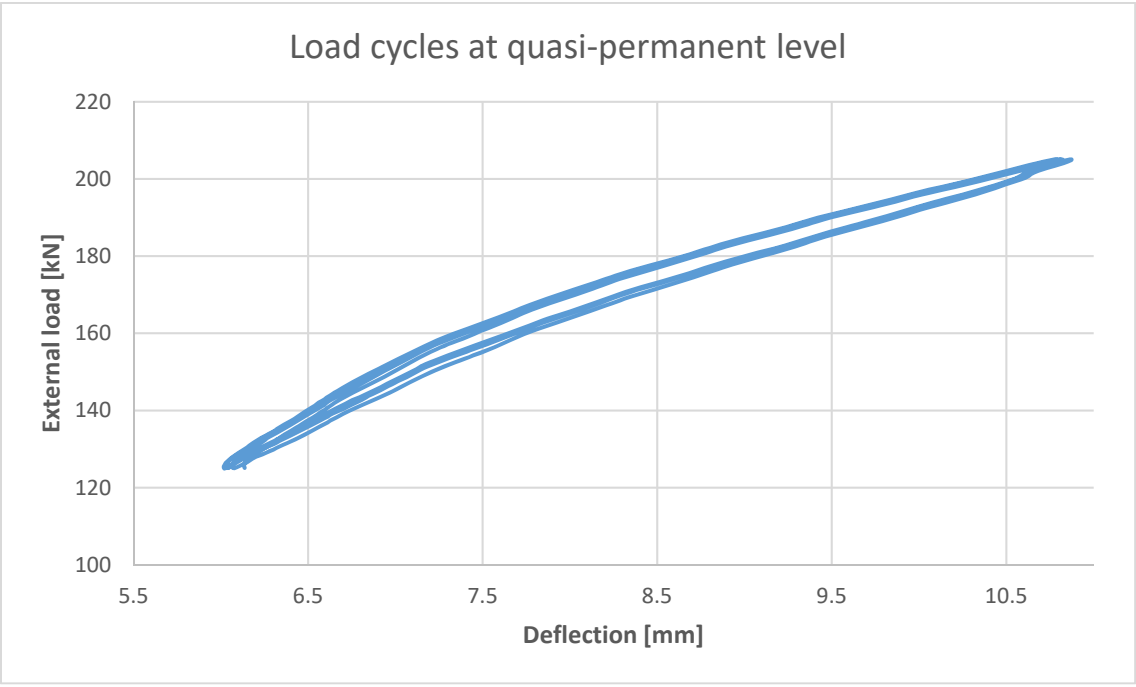

Figure 4.3-19 Load vs deflection of the test I182 Rect for large fast cycles of 40 kN at 165 kN of external force.

All beams showed more damping in the frequent level than in the quasi-permanent level, except for the test I182 Rect (see Table 4.3-1). This difference was associated with the double stiffness of the loops in quasi-permanent level.

The influence of the equivalent area in the damping ratios can be established with the method explained in Section 4.2.2.1. The α factor (Equation 2.2-1) was 5.11 for the quasi-permanent load level. For the frequent level, the factor was 8.94. In both cases, the information of tests I182 Rect was dismissed. In the two load levels, the tests with higher equivalent area had smaller damping ratios.

4.3.4 Study of the stiffness evolution

Using the deflection obtained with the vertical transducers (Figure 3.6-8) and the Euler-Bernoulli beam theory, the flexural stiffness (EI) was calculated. It was assumed that EI was constant in the entire beam. Therefore, the obtained stiffness from each sensor is an average value of the global stiffness. The EI average was calculated averaging the EI from all the sensors.. The deflections were obtained from the transducer placed under the loads, in the centre of the beam and in the middle of the lateral span, between *M2* and *R* (Figure 3.6-8).

Figure 4.3-20 shows the evolution of the stiffness after reaching the yielding load. In the first part of the test, the stiffness decreased when the applied load increased but also increased when the load was reduced, slow and fast cycles alike. After yielding load, the beam was unloaded and the stiffness did not recover, and continues decreasing. When the load increased again, the stiffness also increased. Finally, when the load reached again the yielding level the stiffness recovered to the old level and started to decrease again until the end of the test. During the entire test, the difference between the stiffness was 10 % (in average).

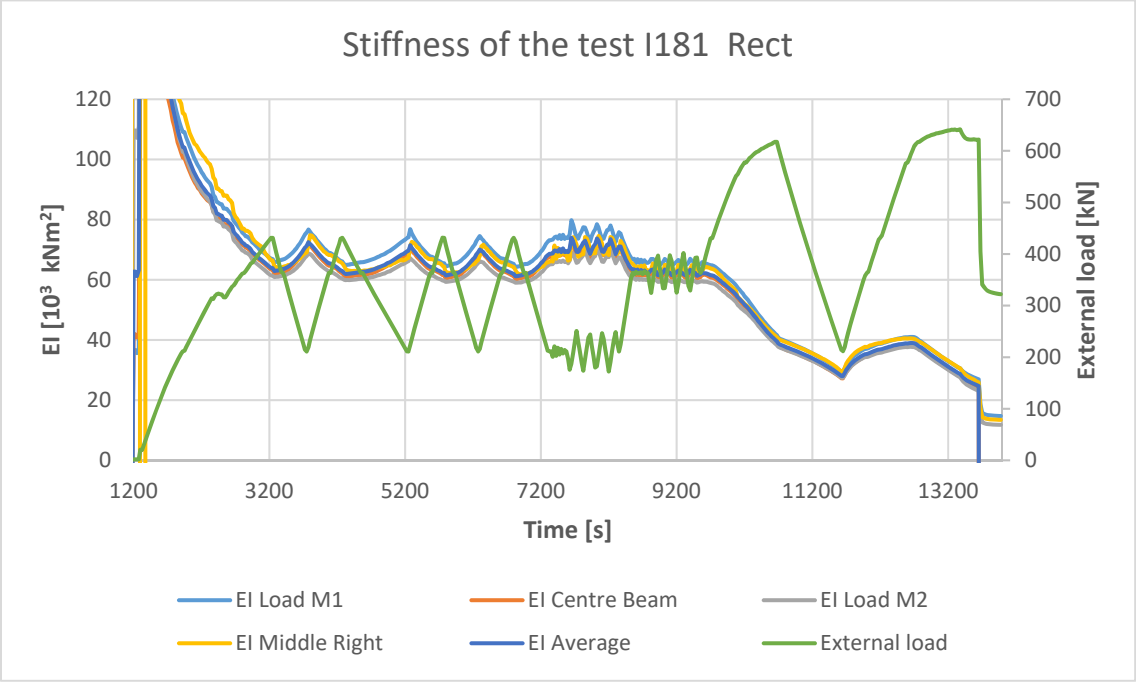

Figure 4.3-20 Stiffness of the test I181 Rect, obtained from the deflection of the beam

For test I182 Rect, as can be seen in Figure 4.3-21, the stiffness values obtained for different deflections are very similar. During the first cycle, before the long hold, the stiffness variation was smaller than during the subsequent cycles. Like in the previous test, the stiffness and the load varied inversely before the yielding point. In between yielding load levels, the behaviour was inverted, and, when the load decreased, the stiffness decreased. When the load reached the yielding load again, the stiffness started to decrease.

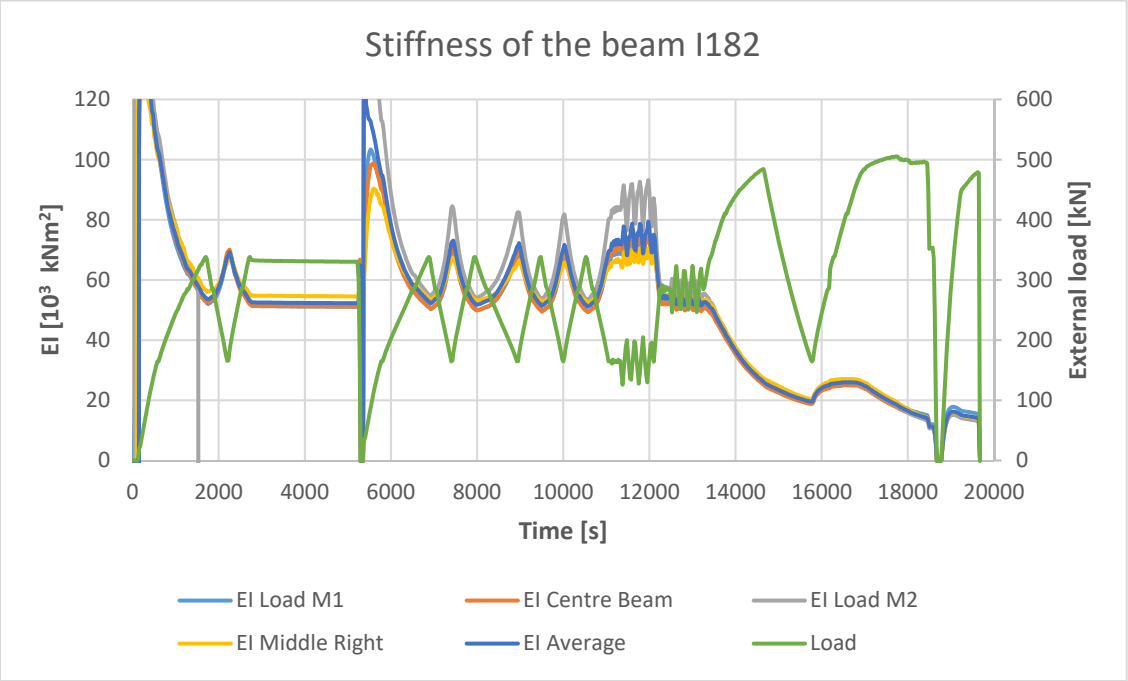

Figure 4.3-21 Stiffness of the test I182 Rect, obtained from the deflection of the beam

Test I183 Rect showed a behaviour different from the two previous tests. As it can be seen in Figure 4.3-22, the stiffness and the load grew and reduced at the same time after surpassing the characteristic level for the first time. After the fast cycles, the load increased and the stiffness decreased. In the second 7750, the test had to be stopped to check the jack. The test was then resumed. After this stop, the difference between the stiffness provided by each sensor had increased. The stiffness obtained through the displacement transducer placed close to section *R* was the biggest one. Even though all of them behaved similarly, the stiffness reduced while the load increased. Like in the other tests, when the load reached the yielding level, the behaviour changed, and, as the load decreased, the stiffness decreased.

Figure 4.3-22 Stiffness of the test I183 Rect, obtained from the deflection of the beam

In test I184 Rect, several displacement transducer used to determine the beam deflections failed. The sensors placed in sections *M1* and *M2* were the only working properly. As it can be seen in Figure 4.3-23, the stiffness were not as smooth as in the other tests. During the behaviour of the stiffness in relation with the load was not stable. There were several instants when the relationship was not continuous.

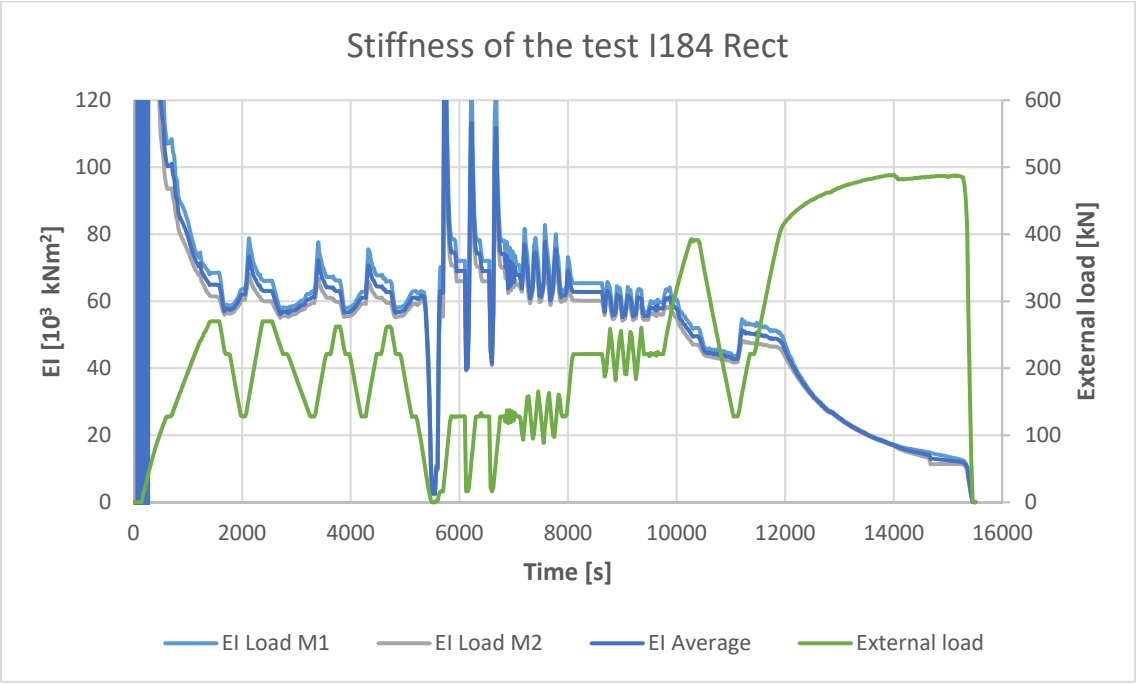

Figure 4.3-23 Stiffness of the test I184 Rect, obtained from the deflection of the beam

The average stiffness of the beams, during the slow cycles, was similar. Some differences on the variation of the stiffness were appreciated due to the cycles. Figure 4.3-24 shows a detailed view of

the slow cycles. Test I182_Rect was divided in two to remove the long hold. The second part of the test I182 Rect show the larger variation in the value of the stiffness, afterwards tests I184 Rect, I181 Rect and finally I183 Rect. In all the cases, the subsequent cycles had a smaller stiffness, even though the variation was small. Tests I183 Rect and I184 Rect had very irregular curves, the other two curves are smooth.

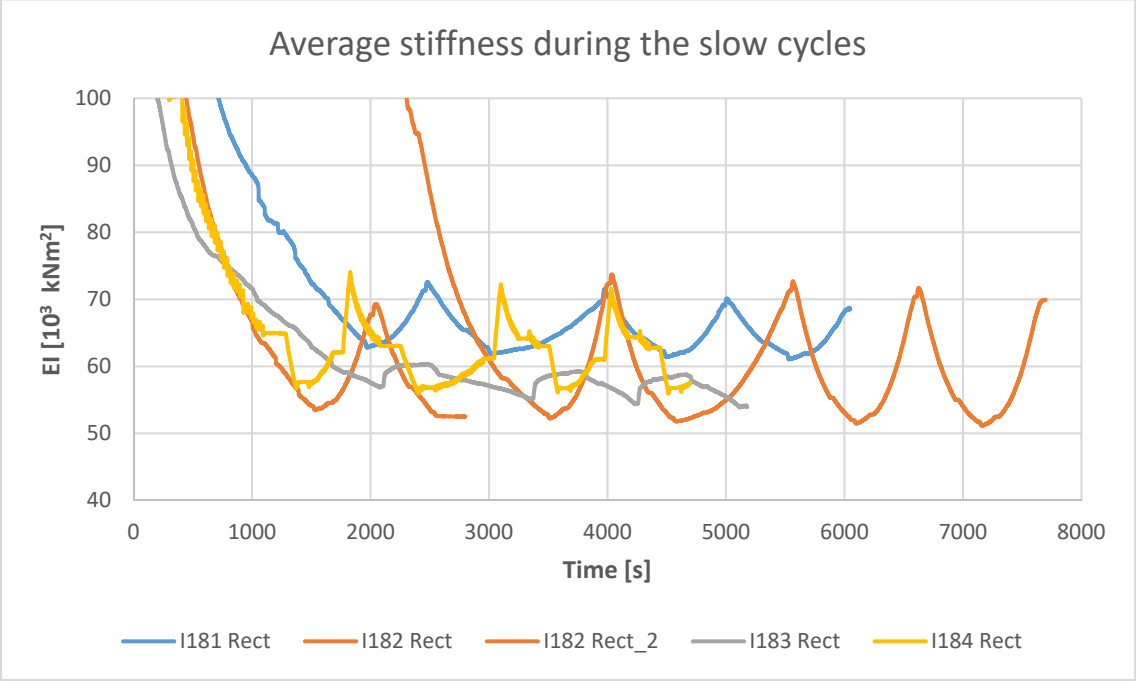

Figure 4.3-24 close up on the average stiffness during the slow cycles

Figure 4.3-25 shows the evolution of the stiffness and the load (solid and dashed lines, respectively) for tests I181 Rect and I182 Rect (4 strands) from the end of the cycles until failure. In both cases, the stiffness decreased until reaching quasi-permanent level. The slope of the EI curve changed when the load reached the yielding load, but in both branches (loading and unloading) the stiffness decreased. Between quasi-permanent and yielding level, load and stiffness increased. When the load reached the yielding level and entered in the plateau, the stiffness decreased.

Test I182 Rect was completely unloaded and then reloaded, the beam was severely damaged and the beam failed before reaching the previous load. In this extra cycle, it can be observed that the stiffness increases until reaching the yielding load. At that point, the load increased and entered in a plateau but the stiffness decreased. The stiffness at yielding load was inferior in this loop than in the previous iterations.

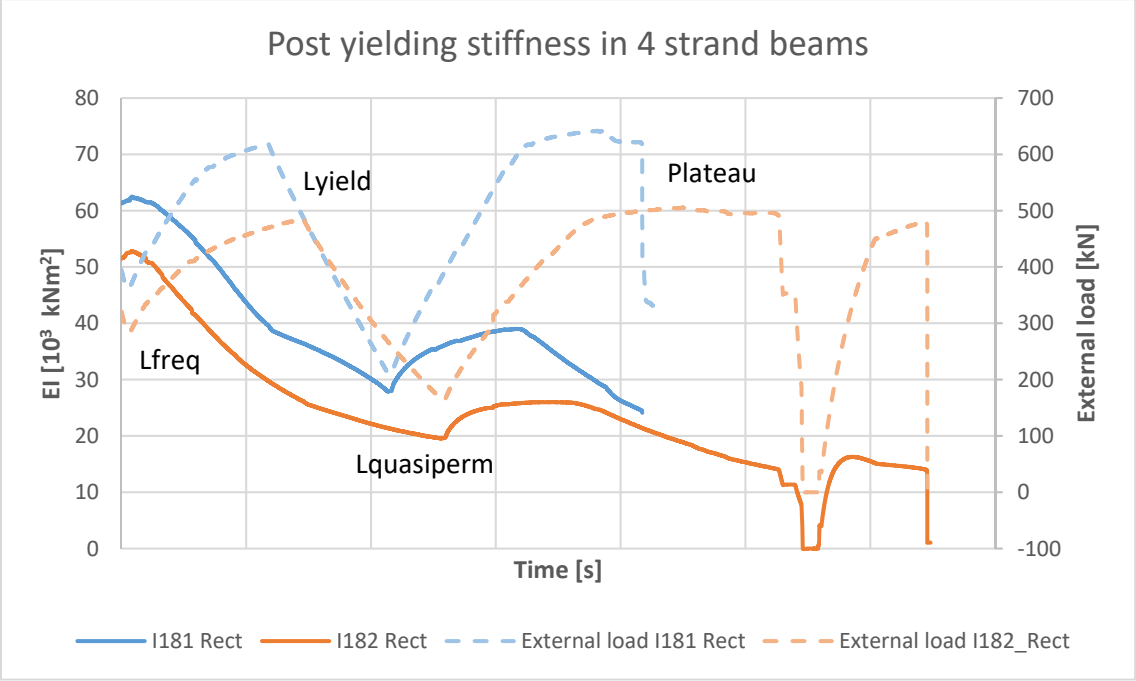

Figure 4.3-25 Evolution of the stiffness in beams with four strands after reaching the yielding load level

For beams with two strands, (Figure 4.3-26) the general behaviour was similar to the previous case. The stiffness decreased between frequent level and quasi-permanent level. Then the stiffness increased until reaching the yielding level again. At that point, the stiffness decreased until failure. However, the behaviour was more erratic than in the previous case. After quasi-permanent level, there was an important increase of stiffness. For tests I183 Rect, the increase of stiffness after the long hold was almost insignificant. For the tests I184 Rect, the decrease of stiffness after yielding load level was very important.

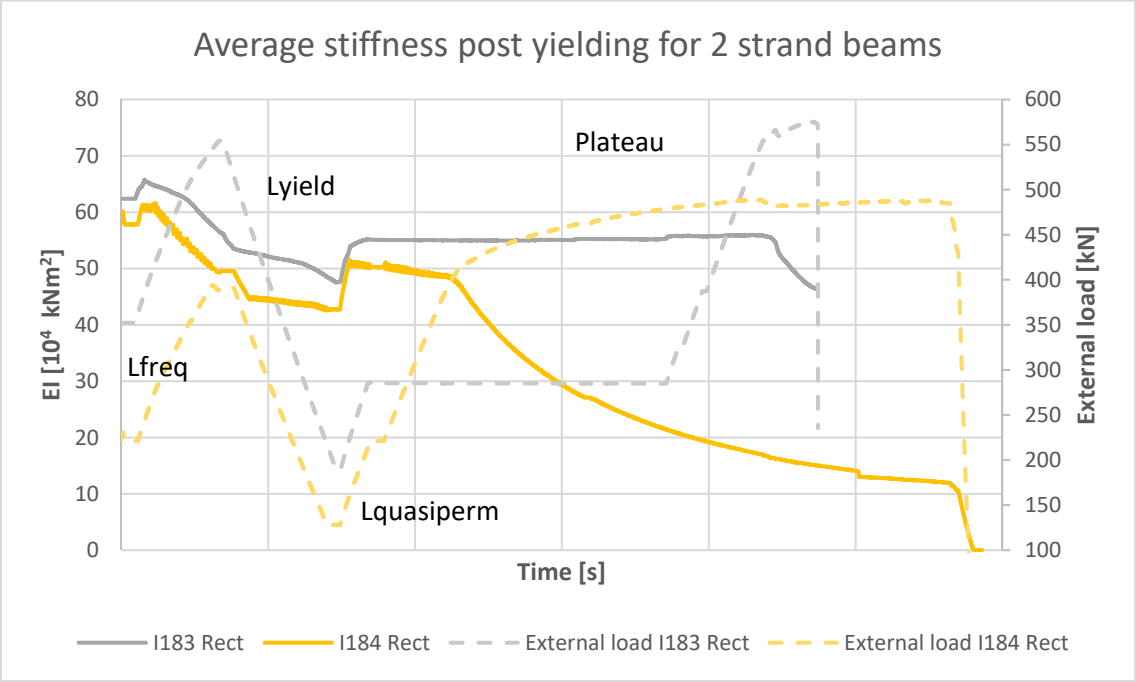

Figure 4.3-26 Evolution of the stiffness in beams with two strands after reaching the yielding load level

4.4 Final conclusions of four-point bending moment tests

This chapter includes a discussion of the tests results obtained during the four-point bending test performed in beams I181, I182, I183 and I184, analysing the behaviour at service and failure. To study the behaviour in service, the load protocol described cycles between quasi-permanent and characteristic load level.

Test I183 Rect suffered a sudden unloading after performing the fast cycles. This event affected the behaviour of the beam and it was reflected at the final deflections and the flexural response. However, during the first stages of the test, the behaviour of the beam was as predicted and could be compared with the rest of the beams in equal conditions.

As can be seen in the analysis of the stress on the rebars, the shear produced an important tension shift. Therefore, yielding of the reinforcements occurred at lower external forces. The reduction of bending moment was 7.5%, 20 % and 30 % for sections 3 to 1, respectively. These important reductions allowed large plastic hinges. In some cases, the deformations recorded by the strain gauges were very important and when combined with the effect of the prestressing forces, the rebars were under compression in the unloading branches.

Beams with higher failure load had smaller deflection ductility ratio. A decrease on the amount of reinforcement (ordinary or active) produce an increase of the ductility. Table 4.4-1 shows the relationship between the ductility and the different amounts of reinforcement. In this case, the equivalence factor α is 5.25.

Table 4.4-1 Relationship of areas and deflection ductility

	I181 Rect	I182 Rect	I184 Rect
Ductility	2,4	3,1	3, 8
Asl [mm^2]	1206	471	1206
Ap [mm^2]	560	560	280
Equivalent Area [mm^2]	4146	3411	2676

The plastic hinge length evolution showed that beams with higher amount of prestressing area, had larger plastic hinges. The influence of the amount of ordinary reinforcement on the plastic hinge length was very small.

The bending moment campaign was designed to obtain the same behaviours in service or in failure. The failure loads and cracking moments were correctly predicted and the behaviour of the beams was as expected. However, during service and due to the cycling process, the stress of the reinforcement was higher than expected. The stresses, obtained in the first loading ramp, matched the predicted stresses of the simulations, but the stress increased with the cycling process (an average of 29% for the quasi-permanent load level). The differences were larger in the high-prestressed beams. The difference between the simulated stress and the stress at the final cycle at quasi-permanent level was compared with the amount of reinforcement and showed that the α factor between reinforcements was 10.64.

A stress difference between loading and unloading branches was observed. The unloading branches had always bigger stresses. The difference between branches and between experimental and

predicted stresses was more important in high-prestressed beams. The branch difference in high-prestressed beams was the double as in low-prestressed cases.

The previous discussion was performed taking into account the slow cycles and was independent of the load level. However, when the fast cycles are analysed, the load level introduced important behaviour differences. For quasi-permanent cycles, the stress decreases after every loop. However, the last and lowest stress of the fast cycles is always higher than the stress recorded in the initial ramp of the test. The cycles performed at frequent load generate an increase of stresses in the reinforcements. If the cycles are performed at low load levels, with the reinforcement stress under 140MPa, the stress decreased. But if the cycles are performed at higher load levels, with the stress of the reinforcement between 250MPa and 350 MPa, the stress of the reinforcements increases.

The same comparison was performed with the midspan deflection. The deflection in the slow cycles increased with the amount of performed cycles, like the reinforcement stress. But a more stable deflection is reached in fewer cycles. In all the cases, the increase of deflection was around 3mm for the quasi-permanent level and reduced to 2.3mm in the frequent level. In frequent level, differences between loading and unloading branches were observed. This difference was related with the amount of reinforcement on the beam. Beams with higher amount of reinforcement had smaller deflection variations. In this case, the ratio between passive and active reinforcement was 4.26. The characteristic level did not experience any increase of deflection.

For the fast cycles centred in quasi-permanent level, the deflection on the loading branches was smaller than the last cycle of the slow cycles. In all cases, the deflection of the loading branch in the large cycles was smaller than the deflections of the small cycles. However, the deflection of the unloading branches for the 2 strand tests was higher than the deflection of the small cycles. The difference between branches determined an α factor of 6.27. Therefore, higher equivalent area generated smaller differences between deflections.

In the fast cycles centred in frequent load, the deflection tend to increase after each cycle. All the values were higher than the last slow cycle. The difference between loading and unloading branches was more important for the lowest prestressed beams. The α factor was 9.21, showing that the influence of the prestress was more important than in quasi-permanent.

The hysteretic analysis showed that the beams with smaller amounts of prestressed reinforcement had larger equivalent damping. For the frequent load level, the I182 Rect test did not follow the general trend and the hysteretic loops were different from the other cases. The ratios between passive and active reinforcement were 5.11 and 8.94 for quasi-permanent and frequent load levels, respectively. Therefore, in both cases the equivalent damping decreased when the equivalent area increased.

5 Shear Behaviour of Partially Prestressed Concrete Beams

5.1 Introduction

This chapter presents the results of the shear tests performed for this thesis on partially prestressed concrete (PPC) beams. Twelve PPC specimens were tested. They were divided in three groups. The first group consists of beams of 120 mm of web thickness, and were tested using the Set-up 1. (Section 3.4) The second group consisted of the same beams but using the Set-up 2. After performing the first test, the position of the supports was changed to perform the second test in the other end of the beam. The third group contained the beams of 180 mm of web width and used the Set-up 1.

As in the bending moment tests, the two main goals of the test were to capture serviceability behaviour and the failure load. To do so, a two steps protocol was designed. The initial step would perform 4 cycles of loading-unloading on the serviceability load levels. The final step consisted on loading up to a level where most of the stirrups would have yield, an unloading to quasi-permanent level and a final loading ramp until the failure of the beam. All the tests were performed using displacement control.

Additionally, each element of the group had a different combination of number of strands, longitudinal reinforcement and reinforcement spacing. Groups 1 and 2 had the same reinforcement but the lay out of the strands were different. The ratio between bending moment and shear (M/V) was also different. The Groups 1 and 3 share the same M/V ratio and the amount of stirrups, but the longitudinal reinforcement was switched and the width of the web was 180 mm.

5.2 Performance of test specimens in failure

As for the bending moment tests, the predicted failure load was used to define the load protocol. The shear resistance of sections with variable width could be obtained with a wide range of formulas or programs but the dispersion of results would be very wide. From previous studies carried out on the department (Pujol, 2018), it was expected that high degree of conservatism of the codes equations to predict the shear resistance. Therefore, advanced non-linear shear resistant models were used to predict the shear capacity of the specimens. In particular, the software TINSA-EVO (Total Interaction Non-linear Sectional Analysis Evolutive) (Bairán and Marí, 2006a, 2006b), Response2000 and CONS-

Shear (Ferreira, 2013) were used to calculate the shear resistance of the beams. The difference between the different models was up to 70%, with an average difference with the experimental result of 20%. A new analytic formulation was presented: the compression chord capacity model (CCCM) (Marí *et al.*, 2015; Cladera *et al.*, 2016). This new formulation took into account all the parameters that were modified on the different beams.

To perform the first test, I122 Incl, the resistance load was computed using the different models and using the average resistance, the load protocol was composed. The CCCM formulation predicted a failure load of 428,9 KN. The rest of the models predicted values in between 500 and 600 kN. The failure load for the test was 414 kN. The same process was used for the tests I122 Rect and I124 Incl.

On the test I124 Incl, the CCCM formulation predicted a failure load of 385 kN, TINSA 557 kN, CONS-Shear 493 kN and Response 2000 322 kN. The beam failed after reaching 392 kN. The formulation was predicting the failure load very accurately, so to compose the rest of the load protocols, only the CCCM resistance was used.

Table 5.2-1 Failure load comparison between experimental and CCCM formulation of group 1

	I-121 Incl	I-122 Incl	I-123 Incl	I-124 Incl
Experimental	510 kN	414 kN	391 kN	392 kN
CCCM	557 kN	429 kN	406 kN	385 kN
Ratio	1.09	1.04	1.04	0.98

Table 5.2-2 Failure load comparison between experimental and CCCM formulation of group 2

	I-121 Rect	I-122 Rect	I-123 Rect	I-124 Rect
Experimental	548 kN	429 kN	426 kN	404 kN
CCCM	543 kN	398 kN	419 kN	392 kN
Ratio	0.99	0.93	0.98	0.97

Table 5.2-3 Failure load comparison between experimental and CCCM formulation of group 3

	I-181 Incl	I-182 Incl	I-183 Incl	I-184 Incl
Experimental	618 kN	539 kN	524 kN	430 kN
CCCM	612 kN	542 kN	467 kN	461 kN
Ratio	0.99	1.01	0.89	1.07

Table 5.2-4 Statistical data from the shear tests

Mean	Standard Deviation	C.O.V.
1,00	5,62%	5,63%

As could be seen on Table 5.2-1,Table 5.2-2 and Table 5.2-3, the CCCM formulation predicted correctly the behaviour of the beams. This formulation takes into account the amount of stirrups, the T shape of the section, the presence of active and passive reinforcement and the M/V ratio. The average ratio between experimental and predicted shear resistance was 1.00 and a standard deviation of 5.62%

(Table 5.2-4). Figure 5.2-1 compares the experimental and analytical predictions with CCCM. The dotted lines in the figure represents the +/- 5% and 10 % variation from the predicted results.

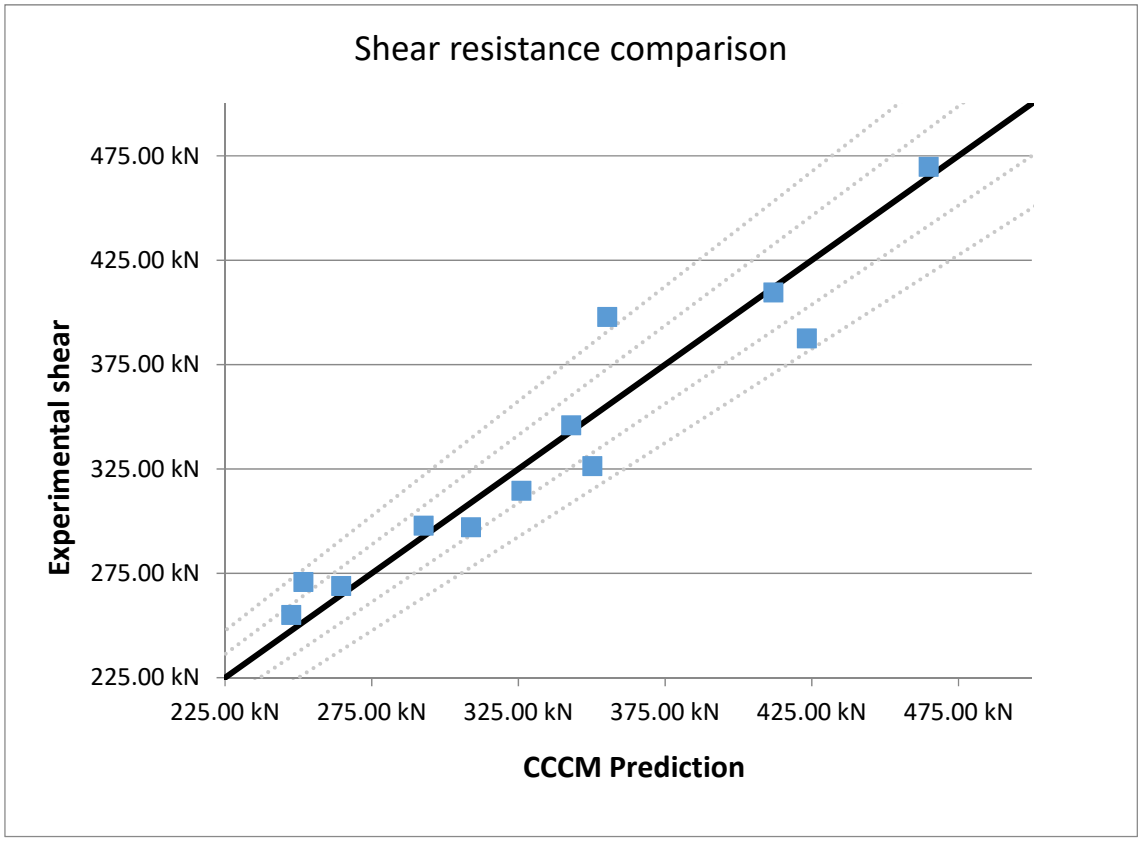

Figure 5.2-1 Comparison between the experimental shear resistance and the predictions of CCCM, with the +/-5% and 10%

The Table 5.2-5 present all the failure values for the shear tests and the predictions with CCCM. The Table 5.2-6 and the Table 5.2-7 present the ratios between external load and shear and bending moment for the two different tests set-ups.

Table 5.2-5 Comparison between experimental results and predictions

		Experimental			Prediction			
Beam	Test	External Load	**Shear**	Bending Moment	External Load	**Shear**	Bending Moment	Error
I_121 Incl	Shear	510,00 kN	**387,60 kN**	697,68 kNm	556,93 kN	**423,26 kN**	761,87 kNm	-9,20%
I_122 Incl	Shear	414,00 kN	**314,64 kN**	566,35 kNm	428,90 kN	**325,96 kN**	586,74 kNm	-3,60%
I_123 Incl	Shear	391,00 kN	**297,16 kN**	534,89 kNm	406,28 kN	**308,77 kN**	555,79 kNm	-3,91%
I_124 Incl	Shear	392,00 kN	**297,92 kN**	536,26 kNm	385,05 kN	**292,64 kN**	526,75 kNm	1,77%
I_181 Incl	Shear	618,21 kN	**469,84 kN**	845,71 kNm	611,57 kN	**464,79 kN**	836,63 kNm	1,07%
I_182 Incl	Shear	539,00 kN	**409,64 kN**	737,35 kNm	541,90 kN	**411,84 kN**	741,31 kNm	-0,54%
I_183 Incl	Shear	523,52 kN	**397,88 kN**	716,18 kNm	467,41 kN	**355,23 kN**	639,42 kNm	10,72%
I_184 Incl	Shear	429,56 kN	**326,47 kN**	587,64 kNm	460,72 kN	**350,15 kN**	630,27 kNm	-7,25%
I_121 Rect	Shear	547,89 kN	**346,04 kN**	726,68 kNm	543,01 kN	**412,68 kN**	742,83 kNm	-2,22%
I_122 Rect	Shear	429,00 kN	**270,95 kN**	568,99 kNm	398,46 kN	**302,83 kN**	545,09 kNm	4,20%
I_123 Rect	Shear	425,92 kN	**269,00 kN**	564,90 kNm	418,86 kN	**318,34 kN**	573,00 kNm	-1,43%
I_124 Rect	Shear	404,00 kN	**255,16 kN**	535,83 kNm	391,91 kN	**297,85 kN**	536,13 kNm	-0,06%

Table 5.2-6 Ratios for the long span shear test, Incl side

Ratio	
Shear	Bending Moment
0,76	1,37

Table 5.2-7 Ratios for the short span shear test, Rect side

Ratio	
Shear	Bending Moment
0,63	1,33

The specimens showed different failure modes. They were grouped in two different types of failure, plus an other case that was not classified (Table 5.2-8). The first mode of failure was governed by the failure of the concrete on the compression chord (Figure 5.2-2). The concrete region in-between the top end of the inclined crack and the jack position spalled, reducing automatically the load and the longitudinal reinforcement of the flanges would be completely bended. In the second group, web failure, once the maximum load was reached, the width of some cracks would increase, yielding the stirrups, until the load decreases. In the end of the test, all the deformation was concentred in one or two cracks (Figure 5.2-3). The last group the failure could not be clearly attributed to one of the previous cases.

Table 5.2-8 Failure modes of the shear tests

Compression chord failure	Web failure	Other
I123 Rect	I121 Incl	I123 Incl
I124 Rect	I122 Incl	
I181 Incl	I124 Incl	
I182 Incl	I121 Rect	
I183 Incl	I122 Rect	
I184 Incl		

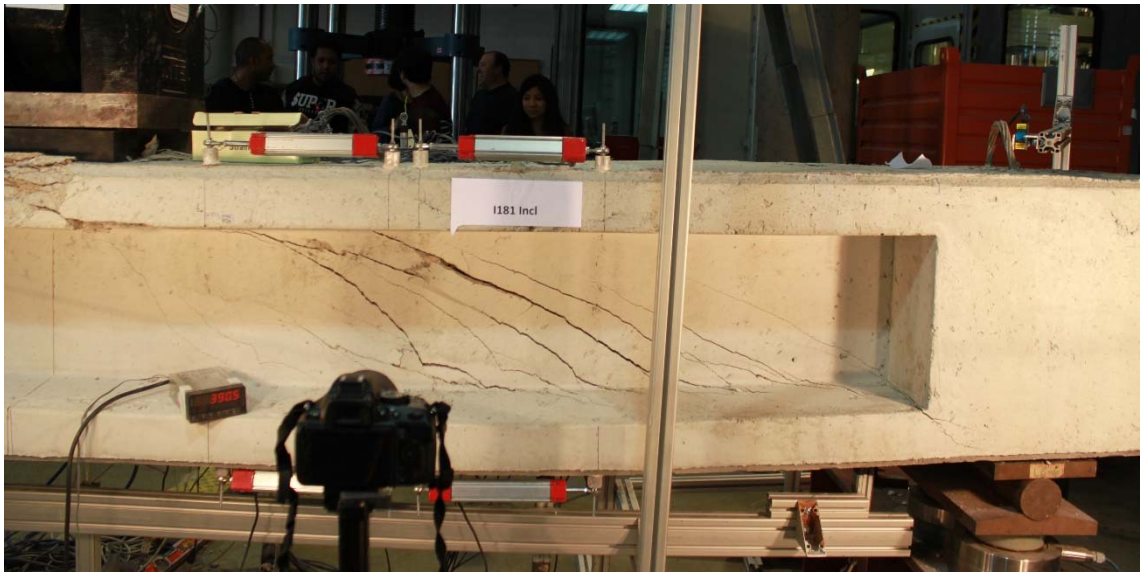

Figure 5.2-2 Compression chord failure in tests I181 Incl

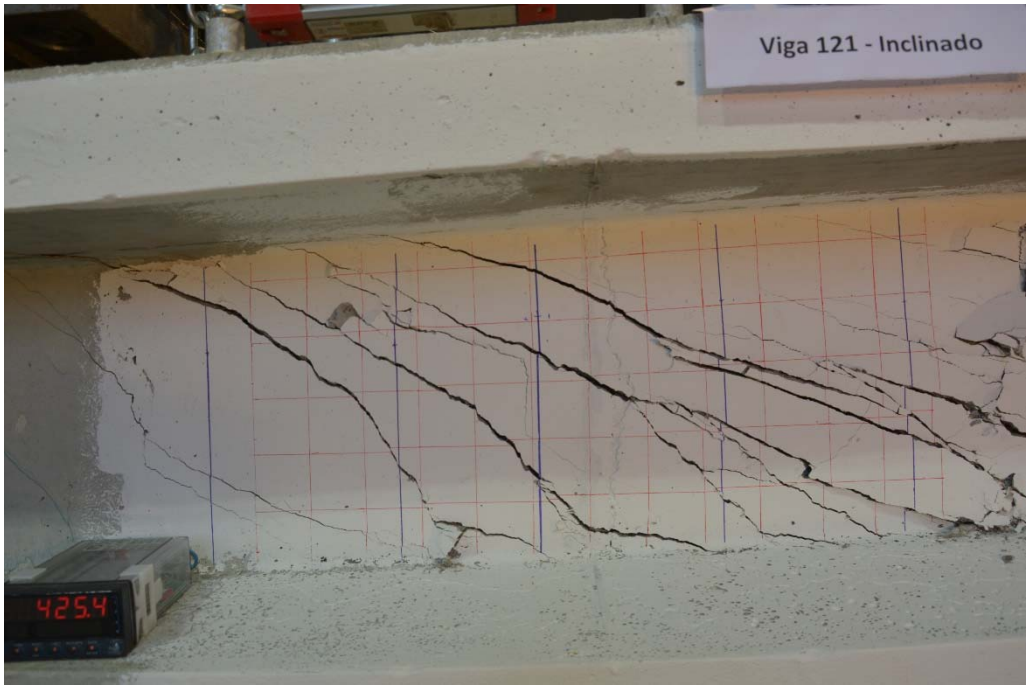

Figure 5.2-3 Web failure of tests I121 Incl

As above mentioned, the current codes and formulations were not able to take into account the behaviour of our beams. Figure 5.2-4 compares the theoretical shear resistance of the twelve tests using different codes, the CCCM and the experimental results. The used codes were *Eurocode 2* (EC 2) (European Committee for Standardization, 2004), the Spanish concrete code (EHE 08) (Comisión permanente del Hormigón, 2008) and the American Concrete Institute (ACI 318-11) (ACI Committee 318, 2008). All the codes severely underestimated the resistance of the beams. The code that presented the biggest error was the *EC 2*, with errors from 100% up to 300%. The CCCM is the best model to predict the shear behaviour of the tests.

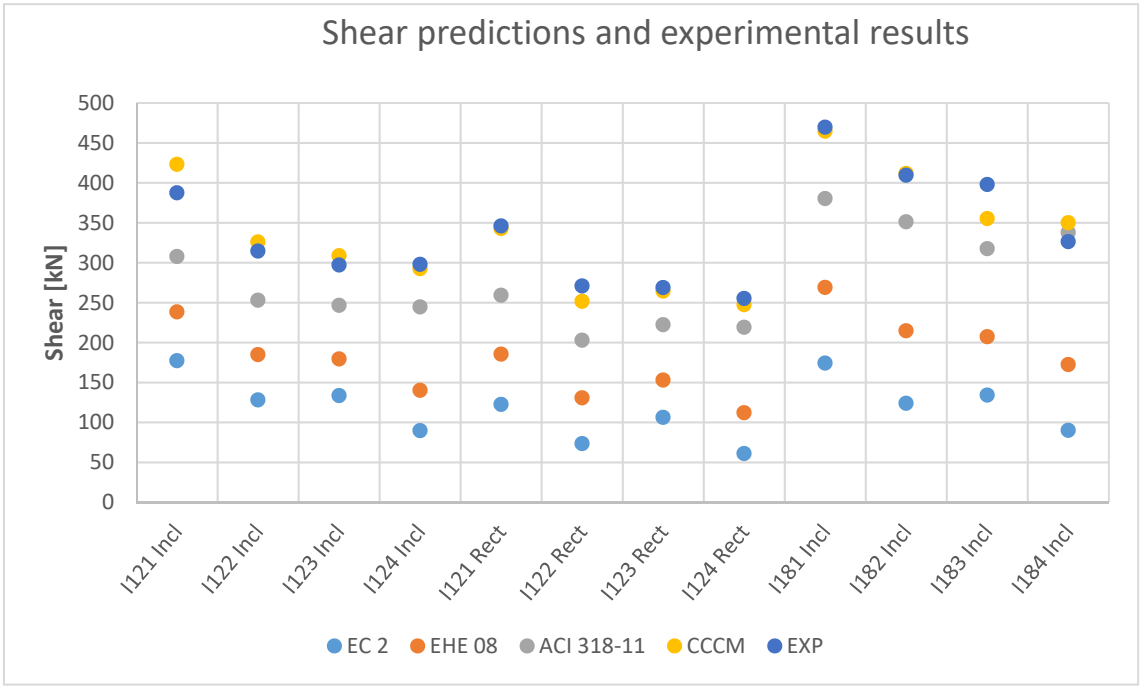

Figure 5.2-4 Comparison between the different formulations and the experimental results

To analyse the behaviour of the PPC beams to the variation of the prestressing load, web width and amount of stirrups without the interference of the different concrete resistances, all the cases were recalculated . The new parameters were: a concrete resistance of 40 MPa, an initial prestressing stress of 1150 MPa and without taking into account the vertical component of the prestressing. Figure 5.2-5 shows the results of this comparison. The beams are regrouped by number of strands, width size and stirrup spacing. Therefore the first element of the three groups are shown together. Then the second elements and finally the third element of the group.

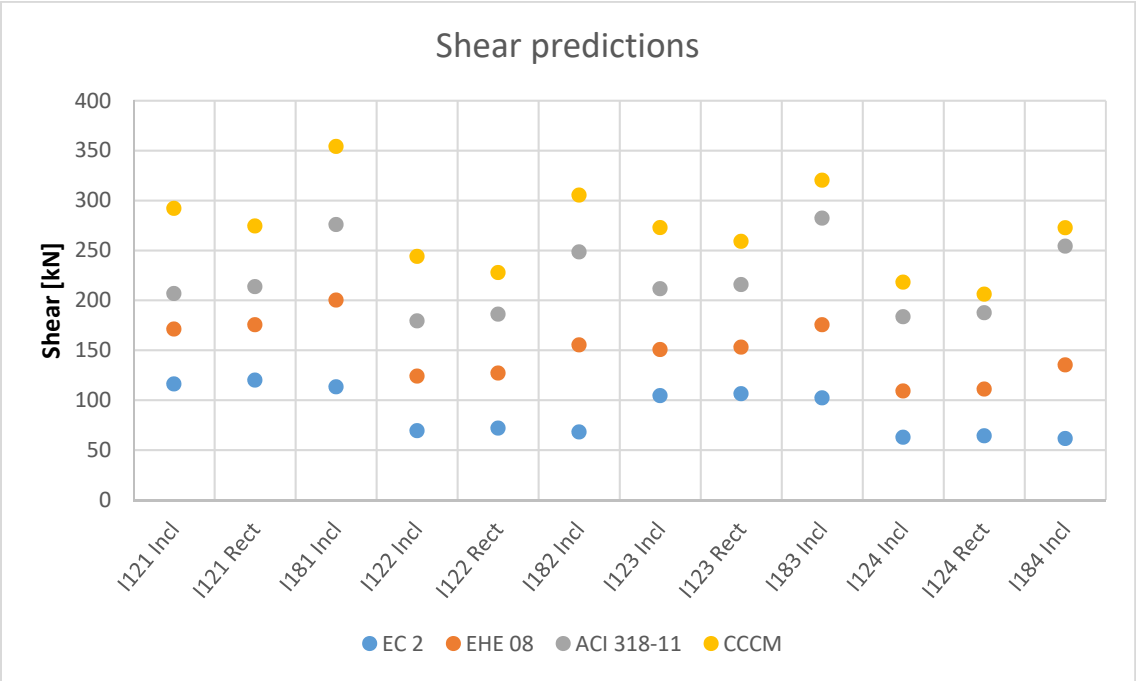

Figure 5.2-5 Shear resistance for normalized beams without vertical prestressing component

Using the EC-2, two set of shear resistances were obtained. The first and third trio had a higher resistance and the second and fourth a lower resistance. The common point of the tests in each group is that they all have the same amount of stirrups. Since the EC-2 does not take into account the contribution of the concrete, the different geometries does not affect the resistance. EC-2 underestimates the resistance of all the sections.

The EHE 08 formulation is composed of the contribution of the stirrups and the contribution of the concrete in the web. The stirrups contribution is calculated, as in the EC 2. Adding the concrete contribution reduces the difference to the CCCM level. As can be seen in the Figure 5.2-5, the third element of each trio has always a higher resistance than the other two elements. The formulation takes into account the increase of the web width but que contribution of the concrete to the overall resistance of the section is too small. The position of the strands are not taken into account either.

The ACI formulation takes into account the two contributions. For the beams with the same width and the same ratio of stirrups, beams 1-3 and 2-4, respectively, the tests with smaller prestress had higher shear resistance. On the other hand, the influence of the width of the web was similar to the CCCM. Even if the formulation was generally underestimating the shear resistance, this was the best code formulation to predict the shear resistance.

5.2.1 Deflection ductility

Using the same procedure as in Section 4.2.2.1, a ductility analysis was performed. This analysis compares the deflection of the beam when the linear behaviour stops to the final deflection. This parameter shows the difference between deflections and provides a reference of how ductile the beams were.

The envelope of load-deflection was obtained using the information gathered by the sensor under the load. The ductility of the tests is between 1.4 and 1.75 (Figure 5.2-6), independently from the amount of stirrups, number of strands or the width of the web. The test I183 Incl had the lowest ductility, the beam failed just after reaching the maximum load.

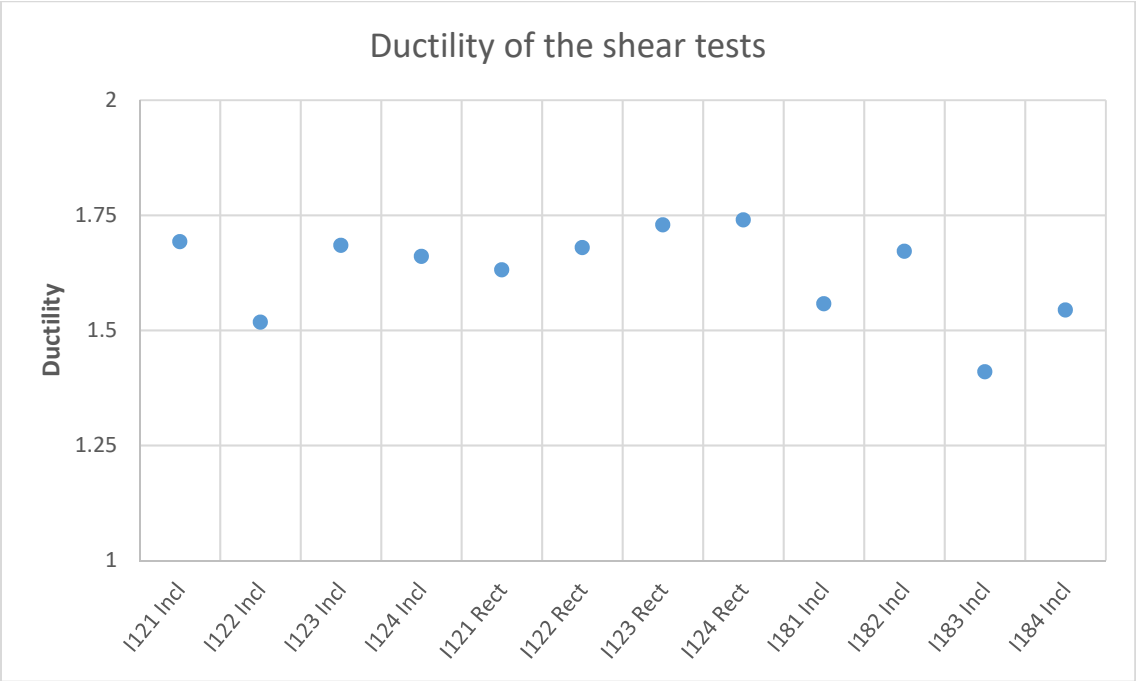

Figure 5.2-6 Ductility of the tests

Figure 5.2-7 shows the deflection at the three states used to perform the ductility analysis. The first information is the deflection when the behaviour of the beam change due to yielding (blue dot). The second information is the deflection of the beam at maximum load (orange dot). The last information is the deflection when the load has decreased to a 90% of the maximum load (grey dot).

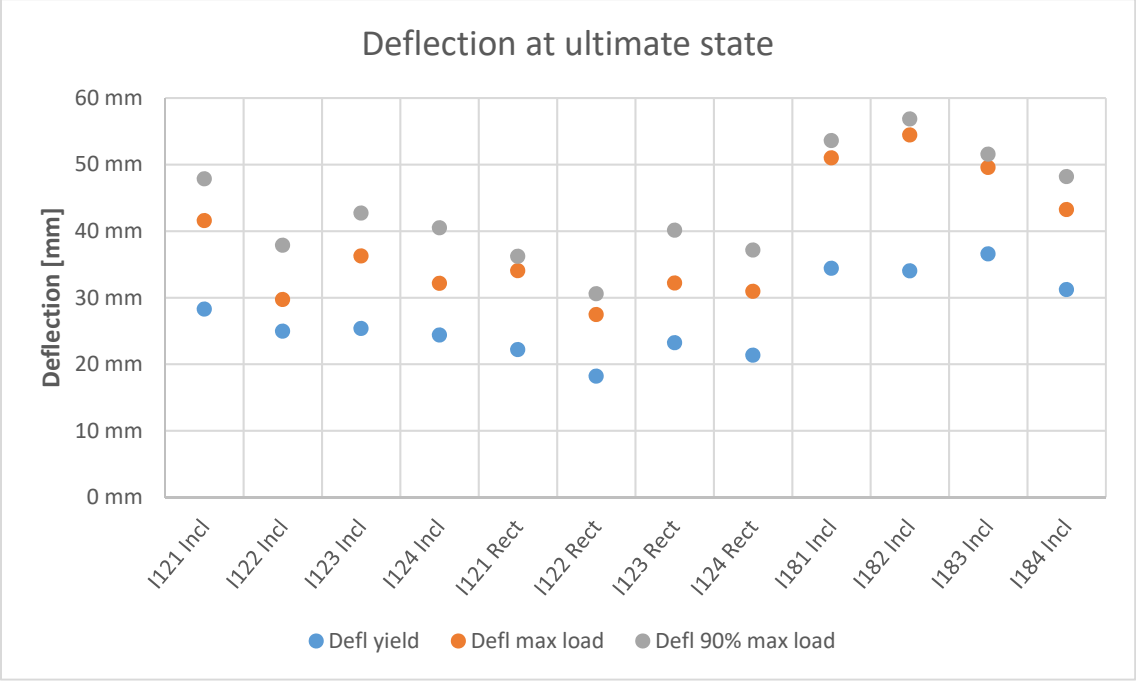

Figure 5.2-7 Deflection at yielding point, maximal load and at 90% of maximal load post peak

The beams with 180 mm of web width had larger final deflections, but a very fast decrease of shear resistance after reaching the maximum load. On the other hand, the beams with 120 mm of web width could keep deflecting after reaching the maximal load without losing that much resistance.

Figure 5.2-8 and Figure 5.2-9 show two examples of ductility analysis. The envelope of deflection is in blue and the theoretical linear response and the final deformation are drawn in red. In Figure 5.2-8, the deflection of the test I123 Incl shows a relatively progressive softening behaviour after reaching the maximum shear resistance. During the execution of the tests, the failure of the 120mm web width beams was not explosive and happened after important deflection and decrease of the jack's load.

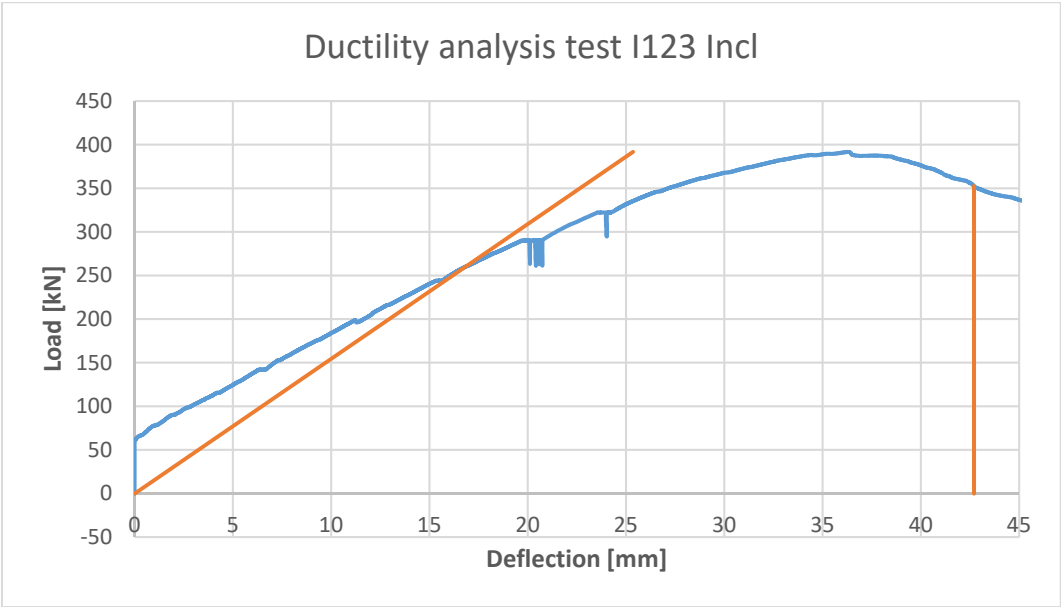

Figure 5.2-8 Envelope of the external load for the I123 Incl test

On the other hand, the beams with 180mm of web width had an abrupt decrease of resistance after reaching their maximal load. The beams did not deflect much after maximal load and the failures of the beams were very explosive and sudden. (Figure 5.2-9).

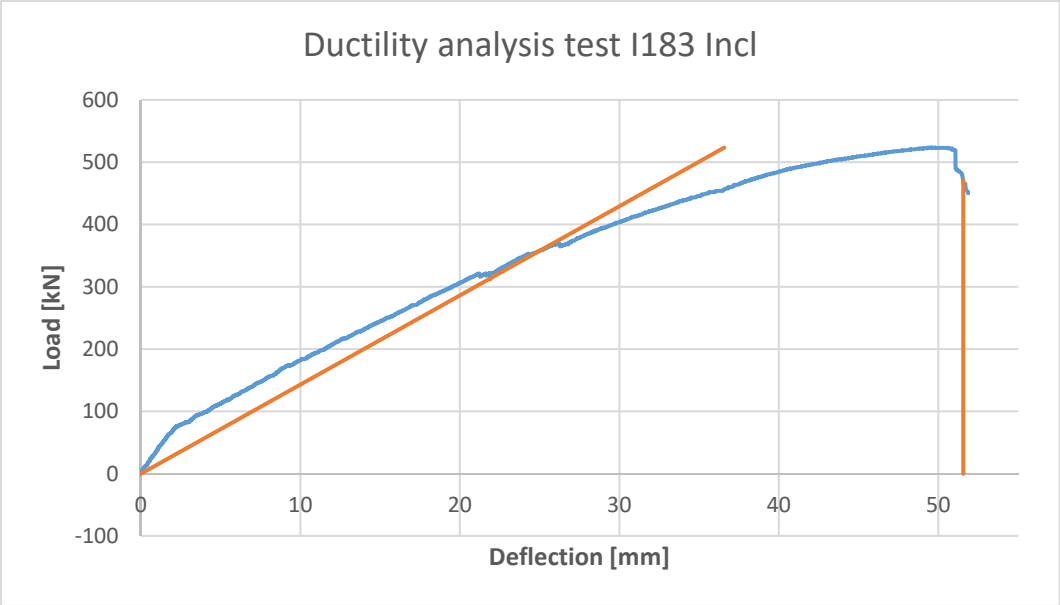

Figure 5.2-9 After reaching the maximum load, beams with 180 mm of web width had sudden failure

5.2.2 Study of the $\cot\theta$ in failure

The angle of the compression field is used in several formulations and codes. Even if this angle and the angle of the cracks (θ) is not the same, normally this assumption is made because they are very close. Therefore analysing the angle θ would provide important information to describe the behaviour of shear resistance in PPC.

Figure 5.2-10 presents the $\cot\theta$ of the crack angle for the maximum load situation. The $\cot\theta$ for all the tests is over 2, in two cases the values are over 2,5. Two variables were used to analyse the influence of the geometrical and mechanical parameters of the tests over the $\cot\theta$. The same variables were also used in the serviceability analysis. The first variable was the stress ratio (SR) between the average prestressing stress and the tensile strength of the section (Equation 5.2-1). The second variable was the ratio of transverse reinforcement (ρ_{st}) (Equation 5.2-2).

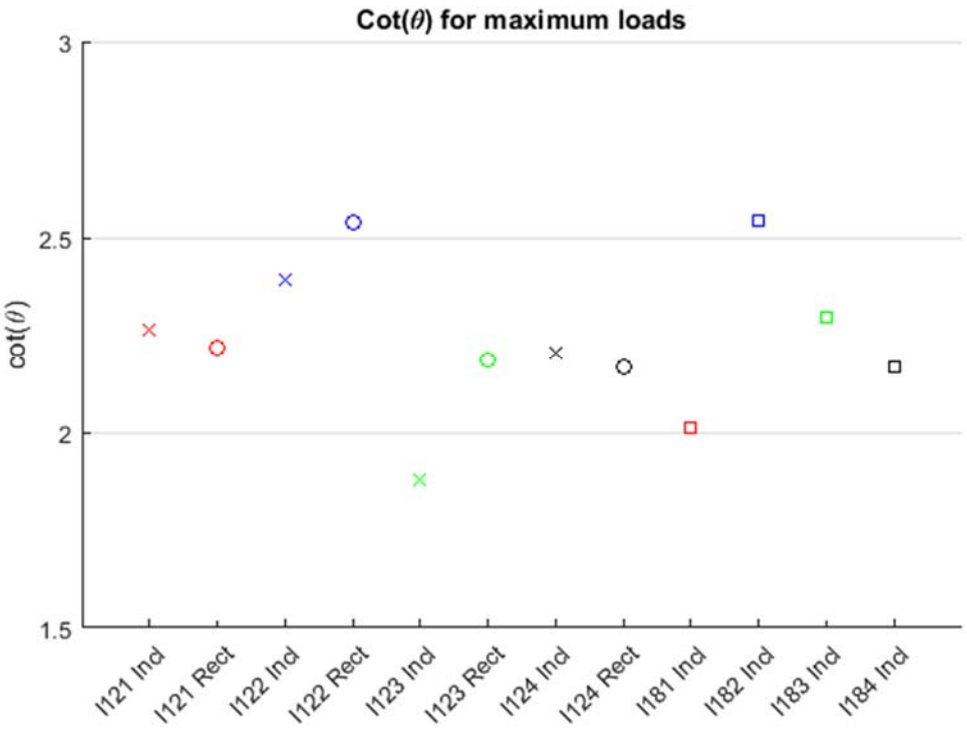

Figure 5.2-10 Cotangent of the crack angle at maximum load

$$SR = \frac{\sigma_c}{f_{ct}} = \frac{P/A_c}{f_{ct}} \qquad 5.2\text{-}1$$

The SR takes into account the number of prestress cables, the difference of web width and the difference between concretes. Figure 5.2-11 shows the influence of this variable over the angle of the cracks. In this case the influence is very small, very different DS had the same $\cot\theta$. In all the cases the $\cot\theta$ was high.

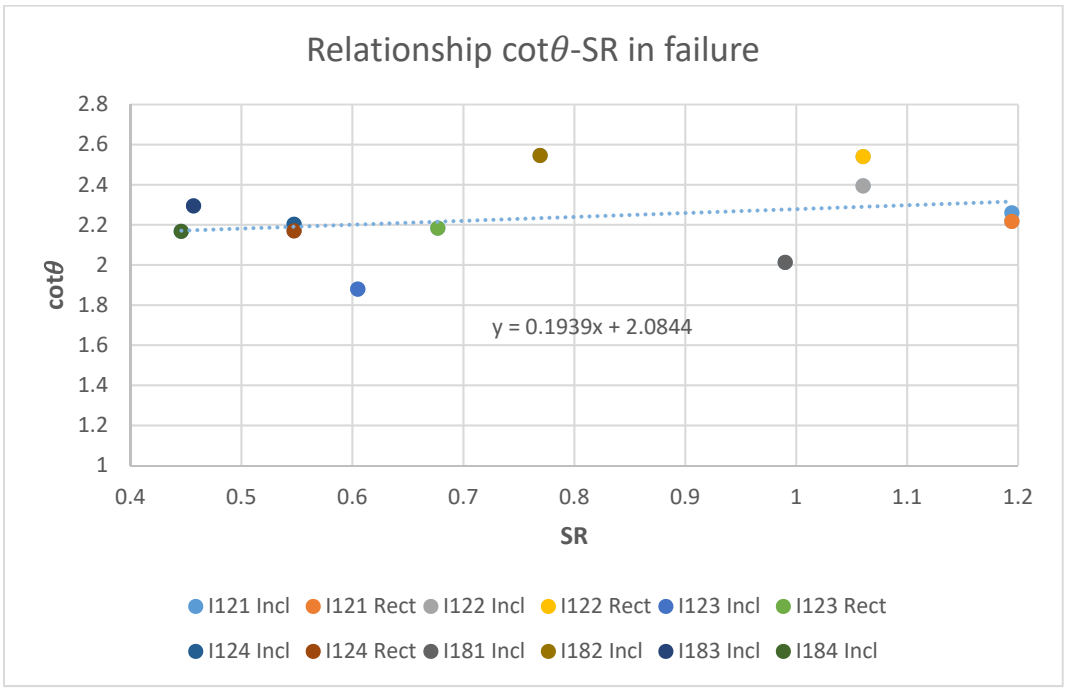

Figure 5.2-11 Influence of the SR over the cotθ in the failure situation

$$\rho_{st} = \frac{A_{st}}{b_w \, s_{st}} \qquad 5.2\text{-}2$$

On the other hand, ρ_{st} takes into account the stirrups present in the beam. Figure 5.2-12 shows a more important influence of the stirrups to establish the angle of the cracks. Increasing the amount of transversal steel reduces the $\cot\theta$.

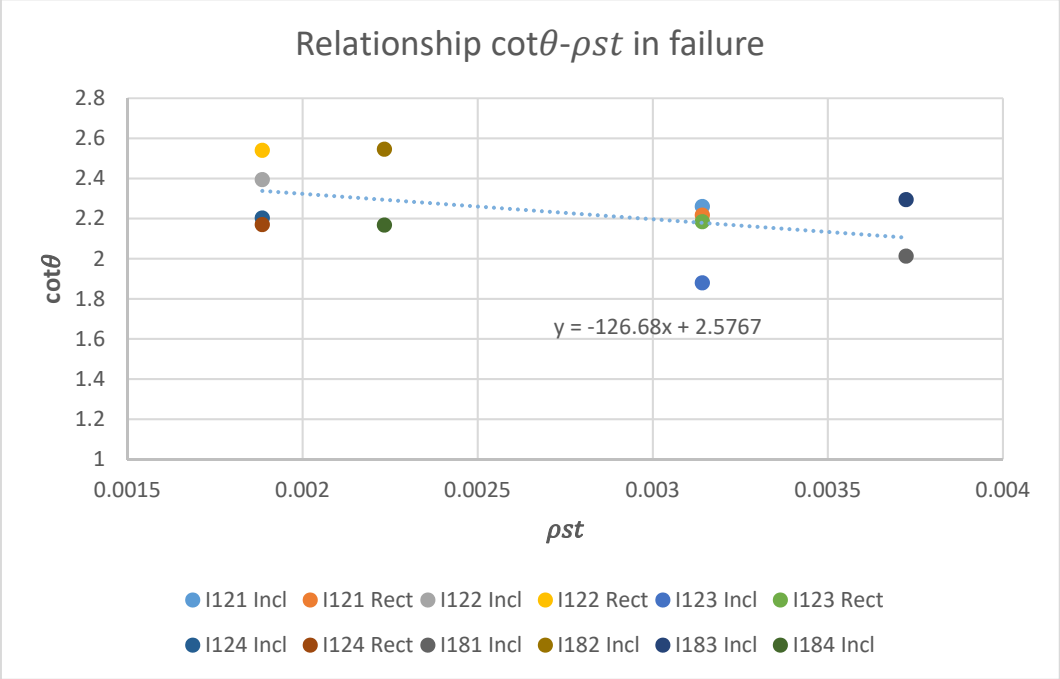

Figure 5.2-12 The amount of stirrups has an important influence on the angle of the cracks in failure

The previous two figures compare the $\cot\theta$ with the variables one by one. Using the equation 5.2-3, a multivariable linear regression was performed to obtain the cross correlation of the influence of the variables. Figure 5.2-13 shows the plane and the three parameters of the equation. The circles represented the elements over of the plane. The squares represented the elements under the plane. The projection of the points on to the plane was drawn as a red line. The average error of this equation is 5%

$$\cot\theta = a \cdot SR + b \cdot \rho_{st} + c \qquad 5.2\text{-}3$$

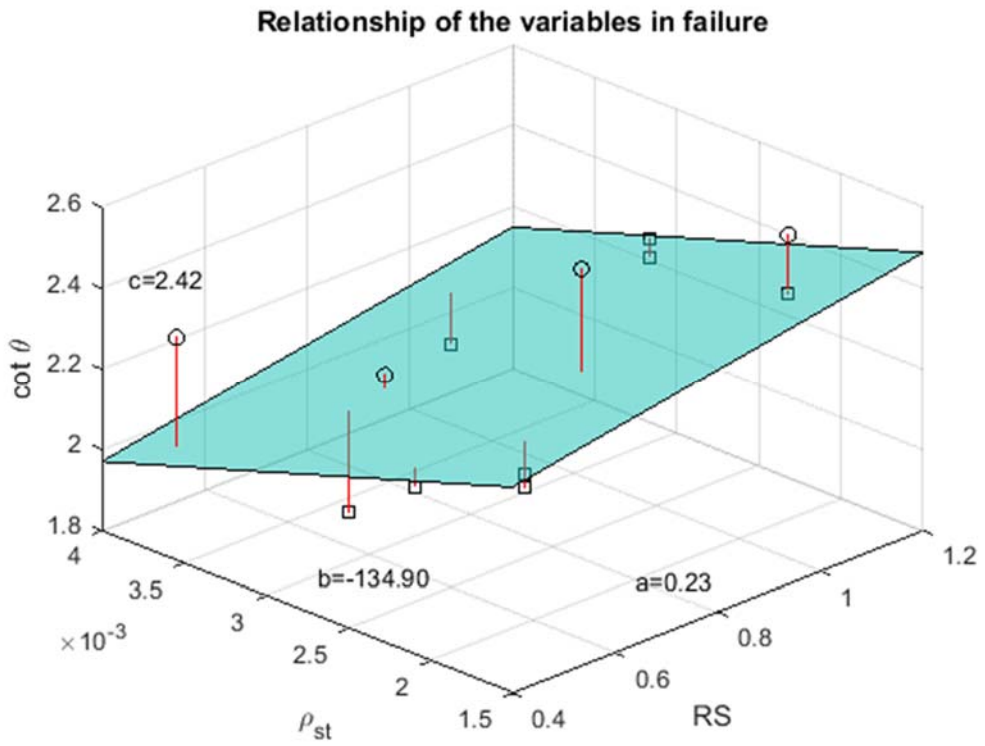

Figure 5.2-13 Plane representing the relationship between the three variables and the parameters of the plane, with a 5% error

The CCCM formulation uses an analytical calculation to obtain the cot θ (Marí *et al.*, 2015). Figure 5.2-14 presents the comparison between the two variables. The formulation slightly underestimates the cot θ with an average error of 10%.

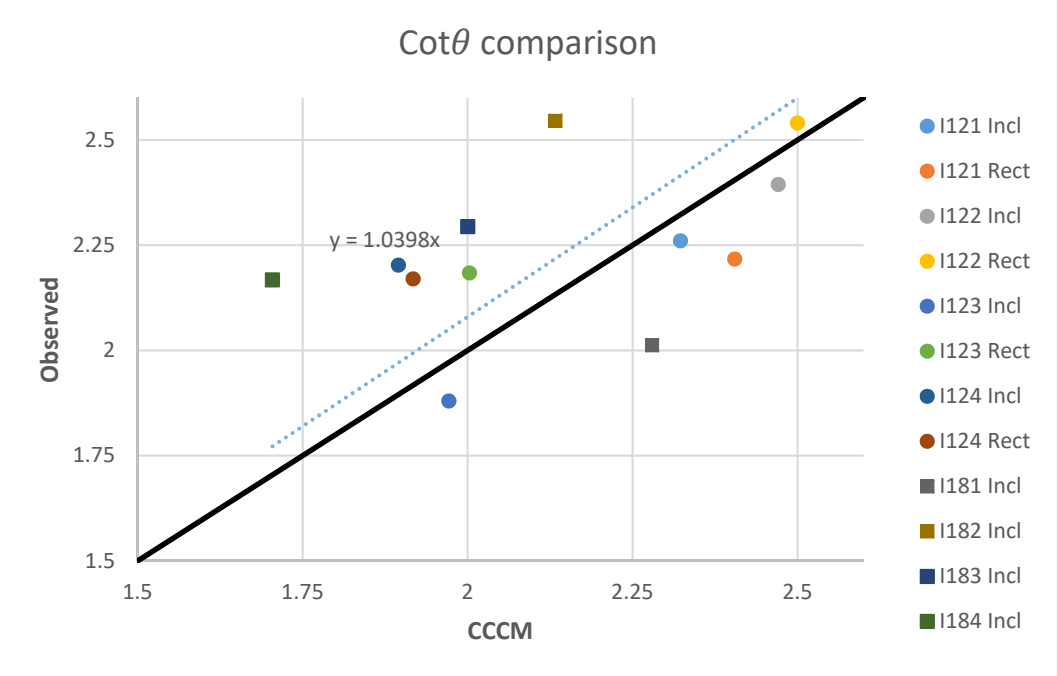

Figure 5.2-14 Difference of 4% between observed and analytic value

5.3 Performance of tests specimens in service

One of the main goals of this dissertation is to analyse the behaviour of the PPC under important shear stresses in the serviceability state. The previous theoretical analyses implied that, in the initial states of loading, shear cracks would appear on the web of the beam. These cracks were going to be inclined to an angle below 45º due to the presence of the prestress force. The stirrups would suffer an increase of stress when the cracks progressed. The strain gauges should record the evolution of the tension during the loading cycles and the photogrammetry captured the crack width evolution.

The deformation recorded by the strain gauges in the longitudinal reinforcement was always under the yielding threshold (Figure 5.3-1). The observations performed on the top and the bottom of the beams during the test showed very thin cracks. They were vertical and they were held within the flanges.

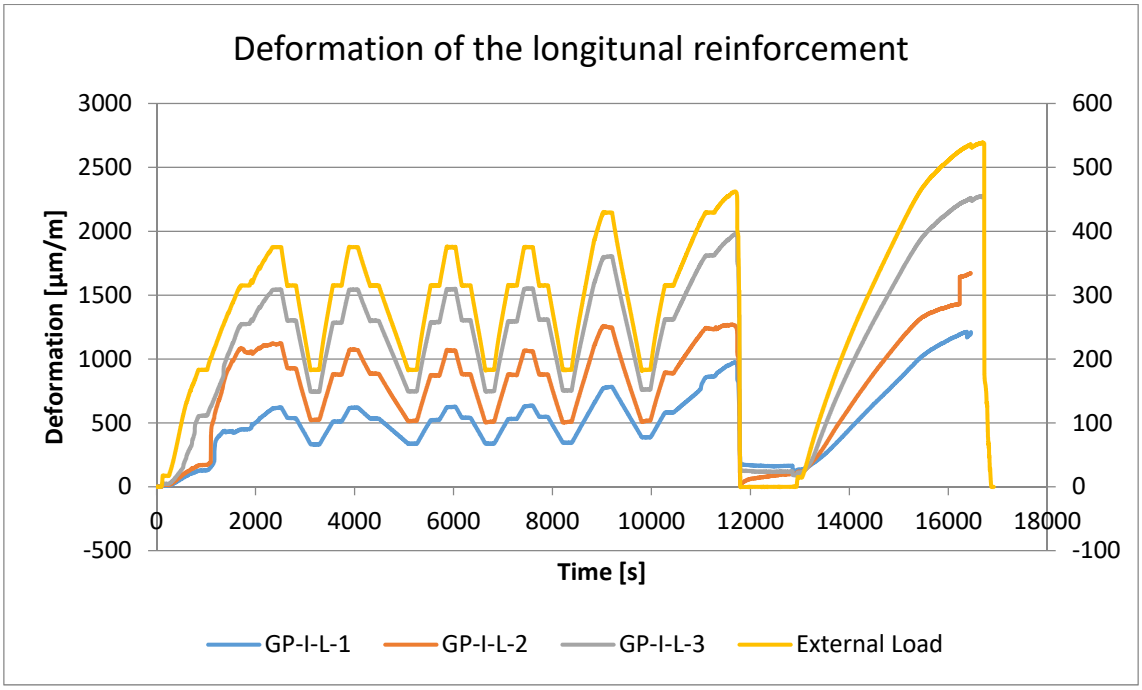

Figure 5.3-1 Evolution of the deformation of the longitudinal reinforcement for the test I182 Incl, obtained from the strain gauges.

5.3.1 Study of the $\cot\theta$ in service

In turn, cracks appeared on the web at the beginning of the tests, near to the flanges and with angles between 45 and 90 degrees. These cracks were wider than the vertical ones present on the flanges. As the test advanced, the crack pattern developed and the average angle of the cracks was getting lower. After the first cycle, the crack pattern remained unchanged through a large load range. When the load increased, approaching the failure load, new cracks appeared crossing old cracks with flatter angles, slightly reducing the average angle. Due to the presence of the flanges and the change of sections, the cracks tend to get horizontal on the top and bottom of the web (as it can be seen on the group of photographs in Figure 5.3-2).

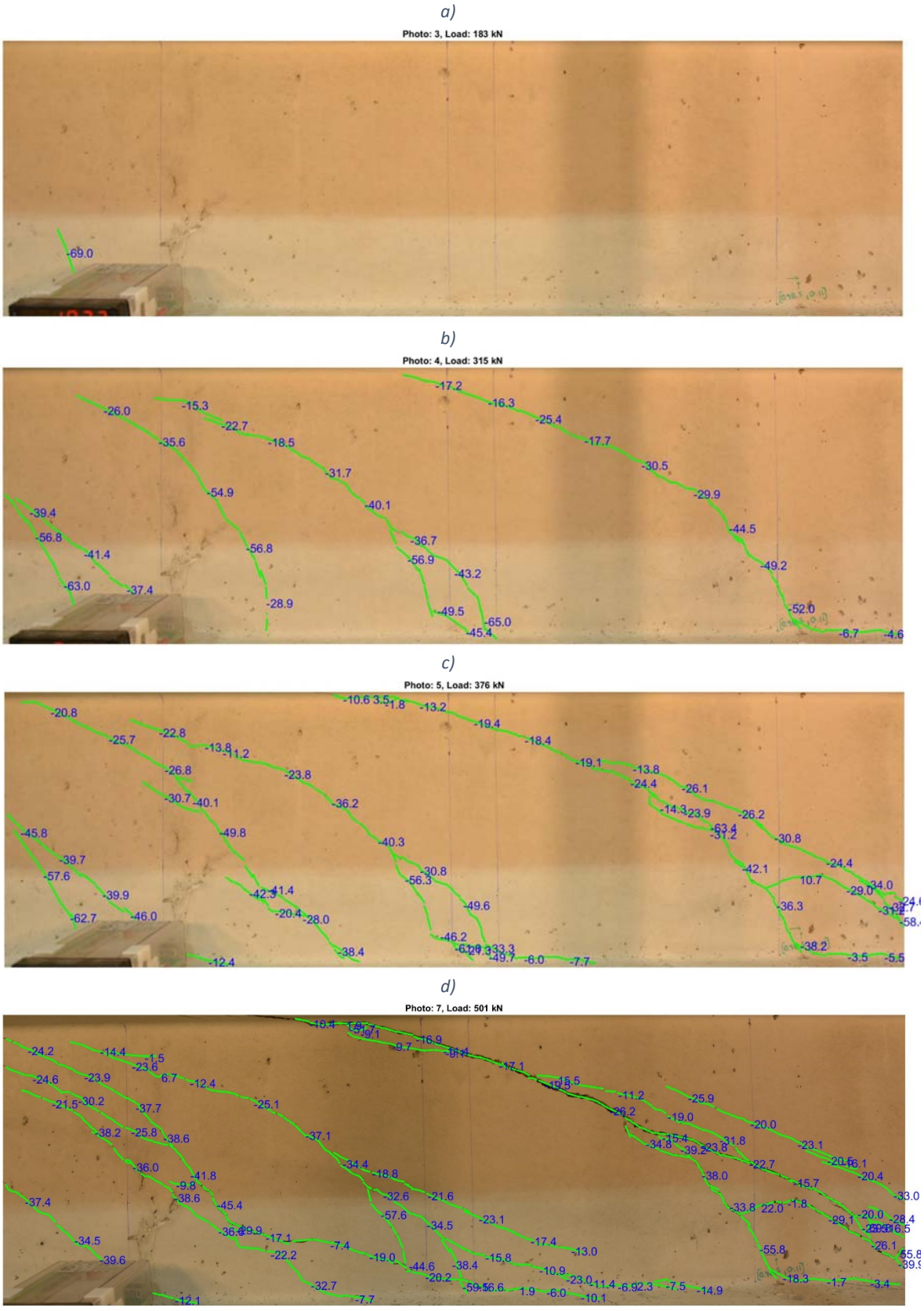

Figure 5.3-2 Crack angle of the test I182 Incl. Pictures a, b and c show the evolution during the first load levels and d the situation on the last states of the test. The average angle of the pictures was 69º, 33º, 28º and 24 respectively

This phenomenon repeated itself through all the tests. Figure 5.3-3 shows the important reduction of the angle in the first moments of the test. At the beginning of the test, the angles tend to vertical, due

to the bending moment. When the load increased, the shear cracks appeared with a flatter angle. As it can be seen in **Error! Reference source not found.** b and c, new cracks appear reducing the average angle. This occurred in all the cases and progressively reduced the average angle. The reduction of the angle is in average a 16% from the serviceability state to the maximal load.

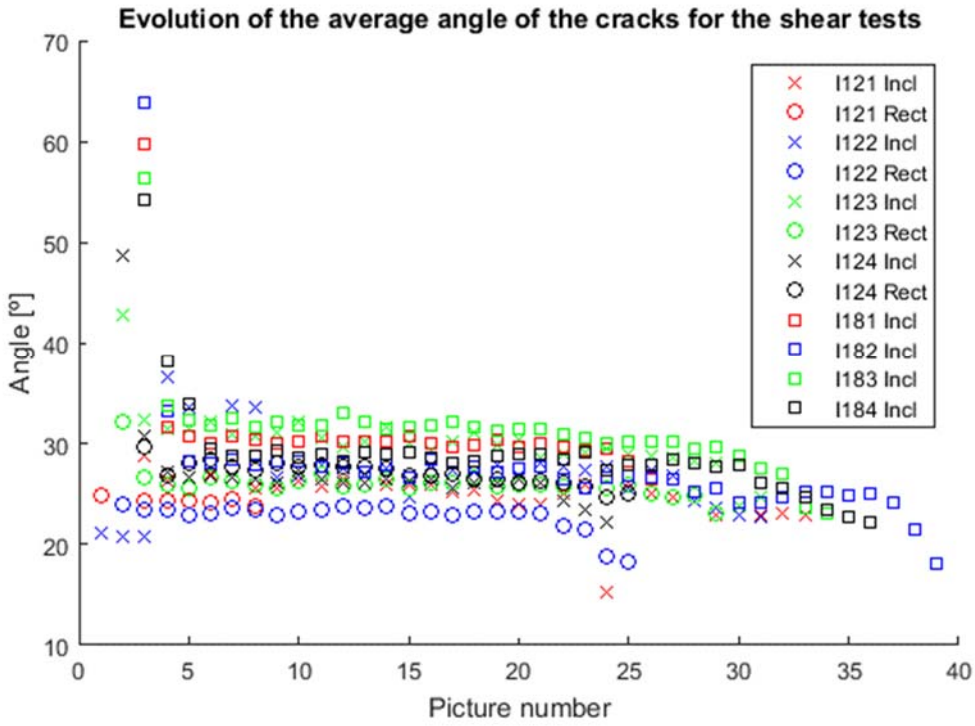

Figure 5.3-3 Evolution of the average angle of the tests, showing an important variation on the initial moments and a low decrease during the test

The angle of the shear cracks is relevant, as it was considered close to the inclination of compression stress fields in the region in shear. Most code formulations use the inclination of the compression field to determine the number of stirrups activated in a particular region and, consequently the contribution of the transversal reinforcement to the shear resistance. The formulations take the cotangent of the angle ($\cot\theta$) to determine the contribution of the stirrups. The Figure 5.3-4 shows the evolution of $\cot\theta$ during service load cycles. During the cycles, the value of $\cot\theta$ did not vary significantly. The range of $\cot\theta$ of the shear crack angle, for these tests, was between 1.5 and 2.4, during the serviceability loads.

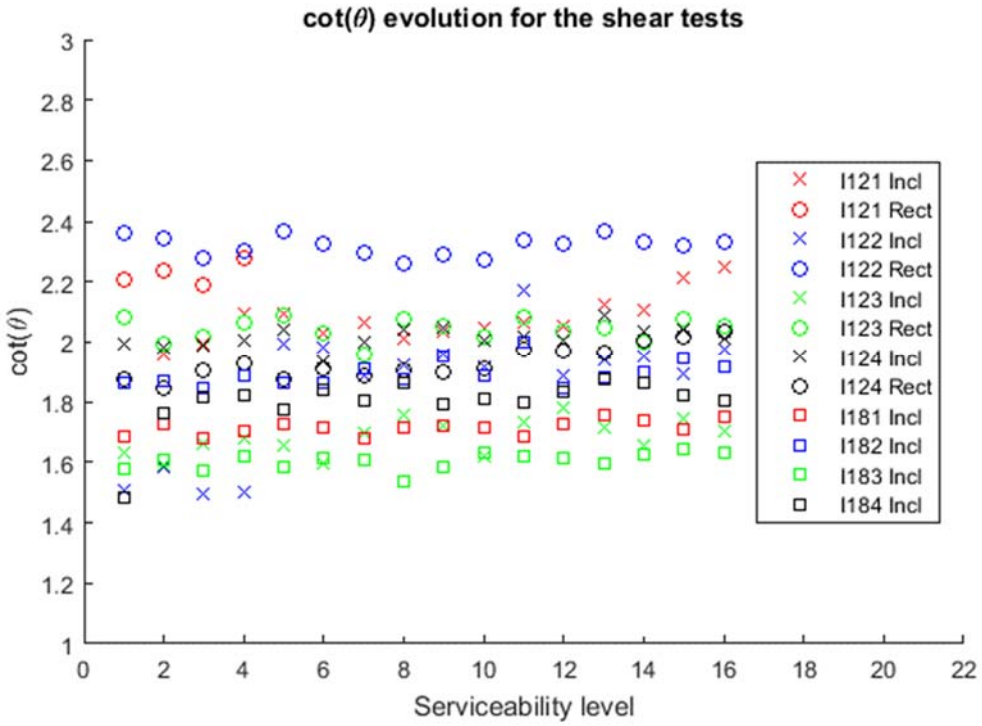

Figure 5.3-4 Cotangent evolution of the angles during serviceability loads

The test I122 Incl showed an important variation at the first stages of the test. However, it was attributed to a change of the photographed area and on which the cracks inclination was averaged. The pictures framing was too small and was only focusing on a very small part of the web. When the frame was opened and more cracks were added to the analysis, the angle was modified.

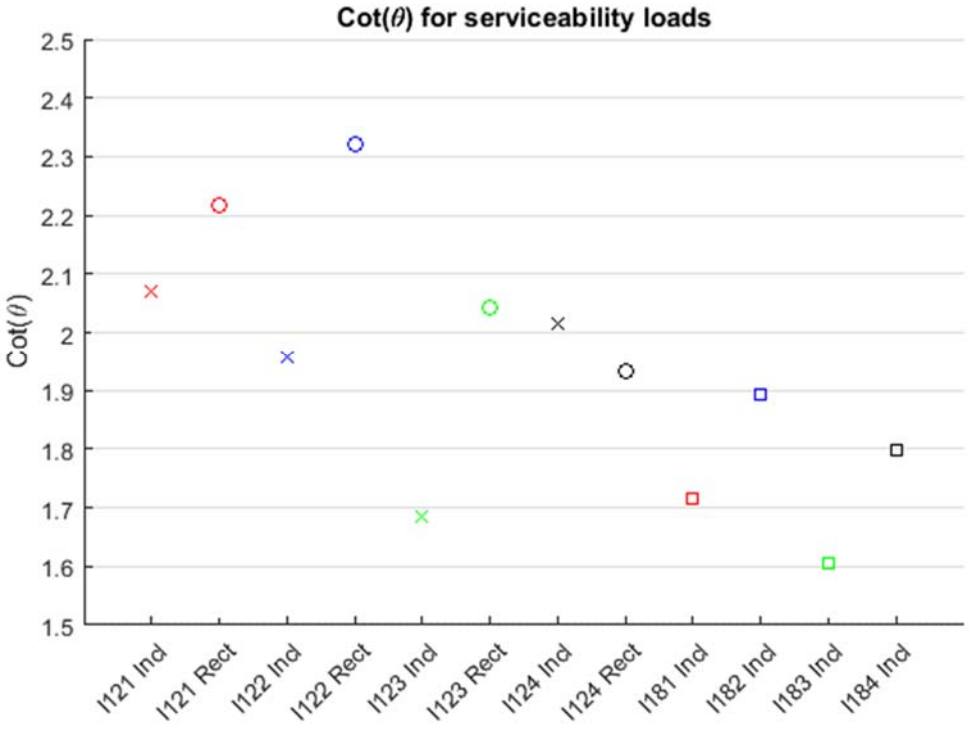

Figure 5.3-5 Average cotangent of the angles during serviceability loads

Figure 5.3-5 presents the average $\cot\theta$ of the crack angle during the serviceability loads. The values were comprised between 1,6 and 2,35. The same variables used for the failure situation were used in service analysis. The first variable was the stress ratio (SR) of the section (Equation 5.2-1), a ratio between the compression stress of the concrete and the tensile stress of the concrete. The second variable was the stirrup density (Equation 5.2-2).

The dimensionless stress had a relevant importance to define the $\cot\theta$. The evolution of the angle is linked with the value of the SR, an increase of the SR leaded to the rise of the $\cot\theta$. Figure 5.3-6 shows the trend of the evolution.

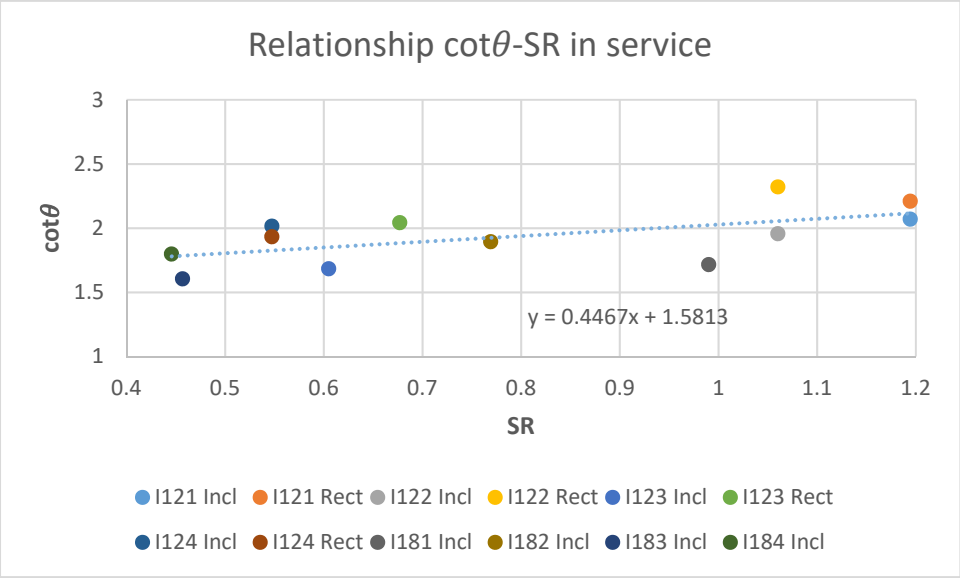

Figure 5.3-6 A strong relationship between the cotθ and SR.

The amount of transversal steel had the same effect in service and failure. The relationship between the variables is the same, but in failure all the $\cot\theta$ were a 12% higher.

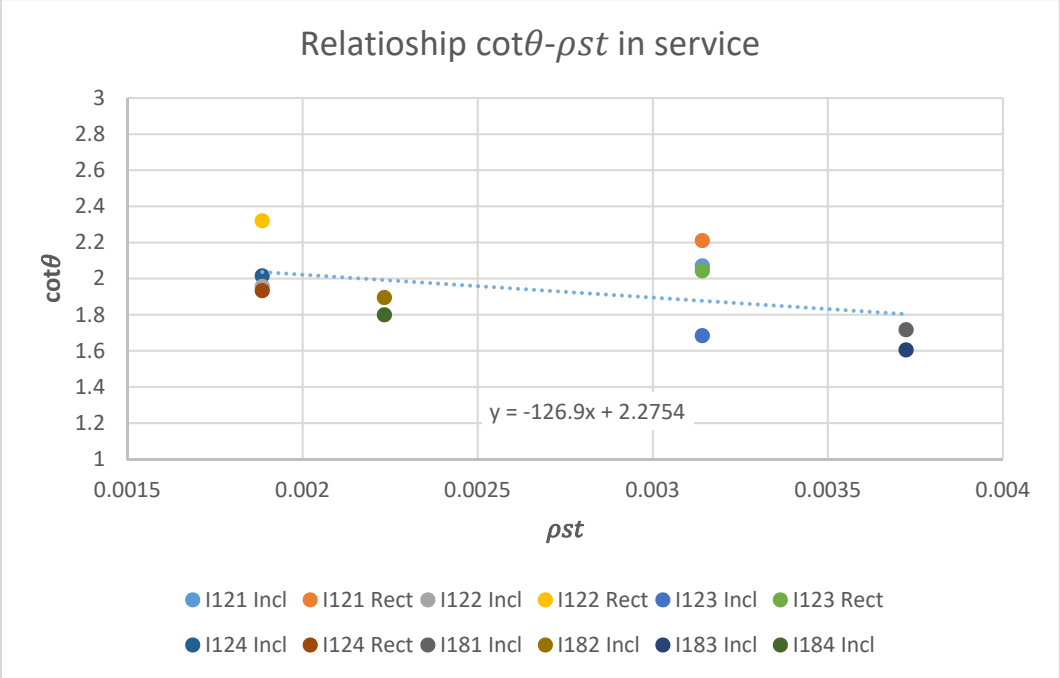

Figure 5.3-7 Similar relationship between the two variables in service and failure

As in the case of the failure analysis, a multivariable linear regression was applied to the $\cot\theta$ and the variables SR and ρ_{st}. The parameters of the equation 5.3-2 and the plane representing the relationship of variables is showed in Figure 5.3-8. In this case and as it was already described in the previous figures, both variables affect the value of the angle of the cracks.

$$\cot\theta = a \cdot SR + b \cdot \rho_{st} + c \qquad 5.3\text{-}1$$

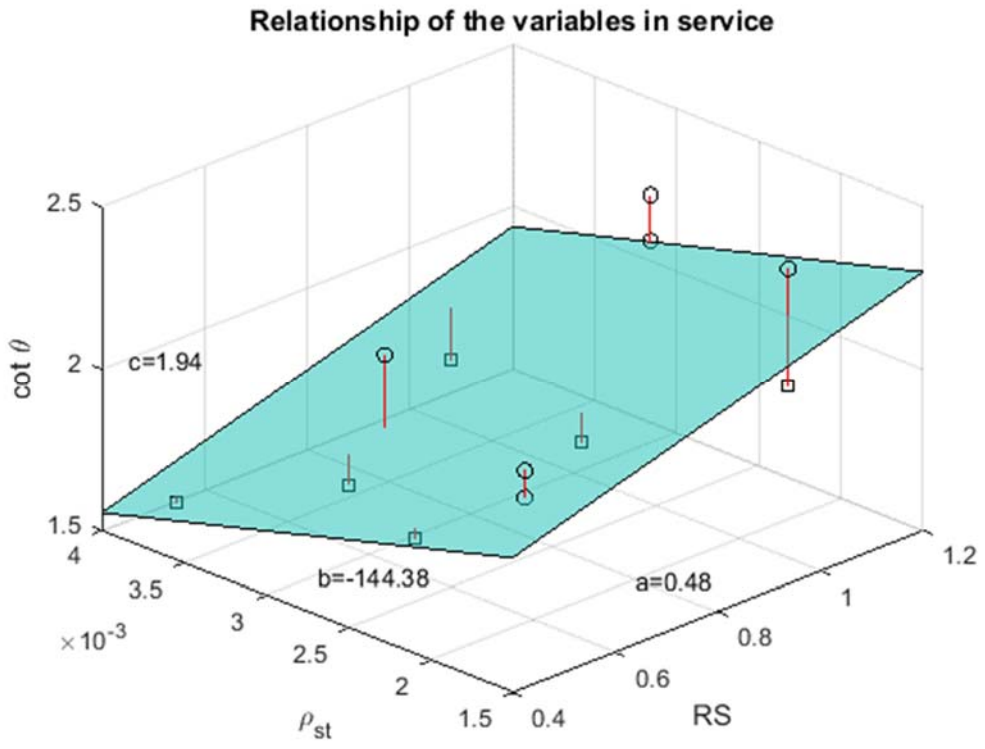

Figure 5.3-8 Plane representing the relationship between the three variables (Equation 5.3-1) in service, with a 5% error

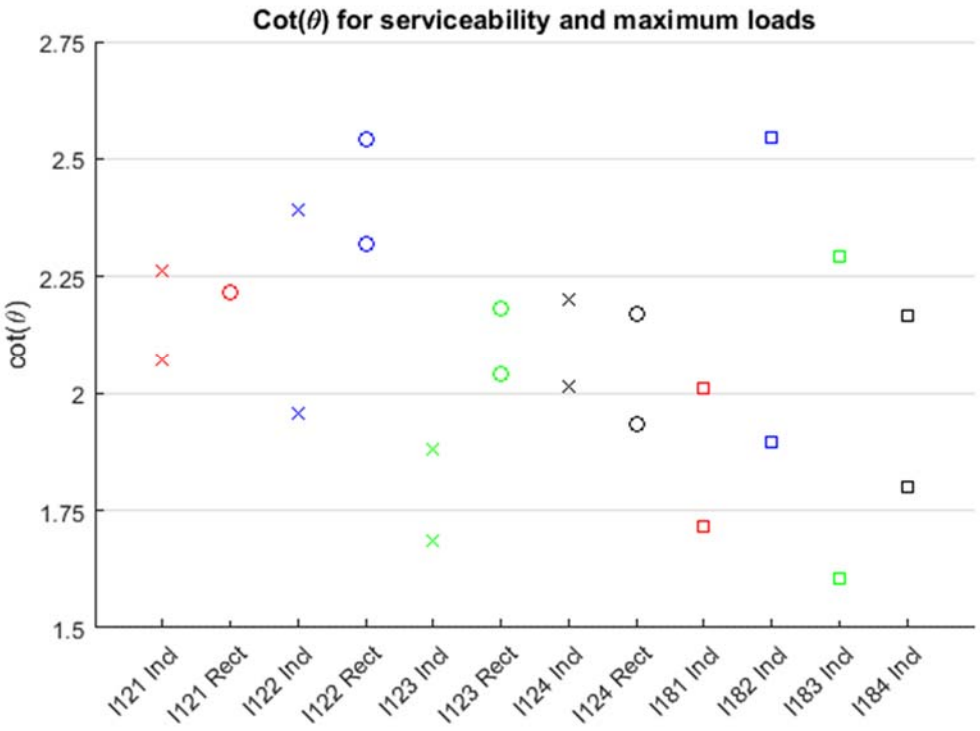

Figure 5.3-9 Comparison of the cotangent in serviceability and under the maximum load

The value of $\cot\theta$ increased at the end of the test, reaching its maximum value at the end of the test. Figure 5.3-9 shows the average $\cot\theta$ during service loads and the $\cot\theta$ under the maximum load reached by the beam (merging Figure 5.2-10 and Figure 5.3-5). The average increase in $\cot\theta$ was 17.8%. The beams of the test 120 Rect had an increase of 9,6%, the 120 Incl 13,2% and the tests with a web width of 180mm reached an increase of 28.8%.

5.3.2 Analysis of the crack spacing

The cracks of these tests were not parallel (Figure 5.3-10 and Figure 5.3-12). The distance between cracks would increase or decrease depending on where or how their distance was calculated. To homogenize this operation, the cracks were divided in small segments of similar inclination. The average crack angle of the picture was used to calculate the perpendicular direction between cracks (Figure 5.3-10).

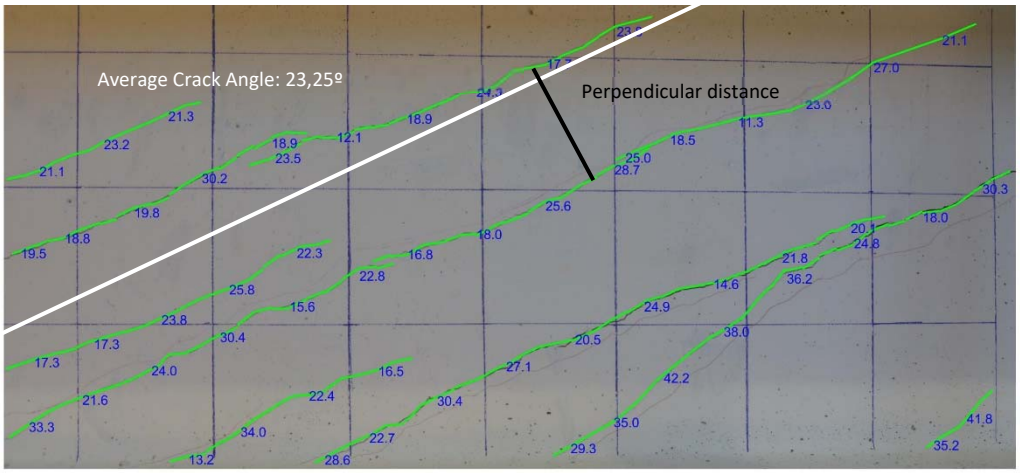

Figure 5.3-10 Crack angles of the test I122 Rect under 244 kN of external load on the loading ramp of the fourth cycle. The average crack angle was 23,25º and the perpendicular direction was used to compute the distance between cracks.

Figure 5.3-11 shows the evolution of the crack spacing for the different tests. Almost all average crack spacing during service loads laid within the range of 55 and 75mm. No relationship between the geometrical and mechanical parameters of the beams and the crack spacing was obtained. The cycling loading process did not affected the crack spacing. The value of the crack spacing kept stable after the first loading cycle.

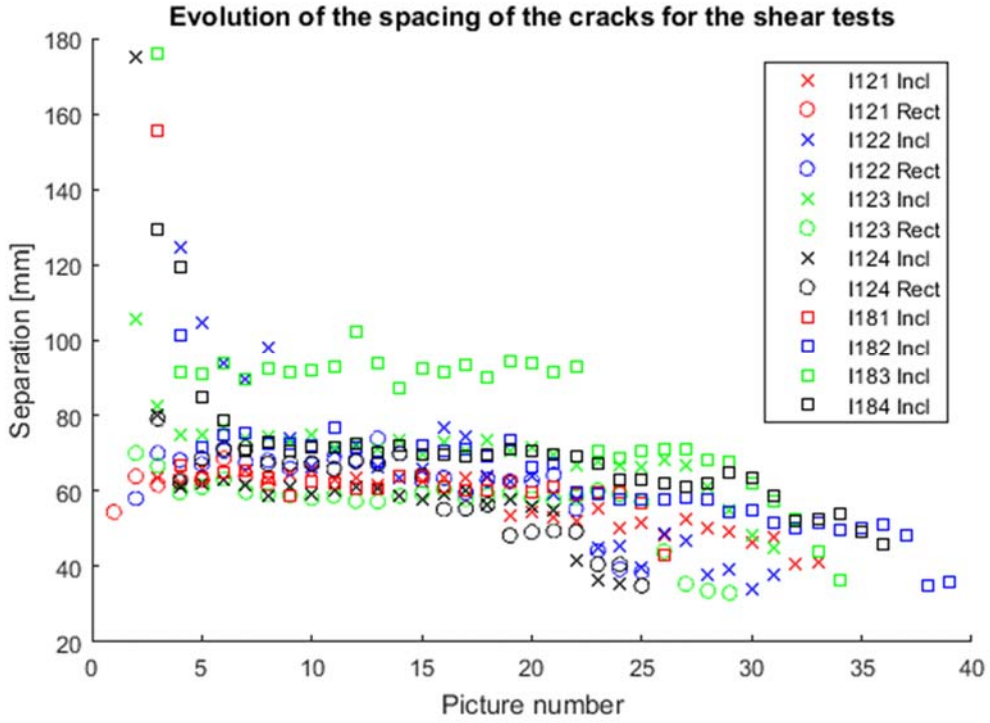

Figure 5.3-11 Average spacing of the cracks in each picture of the tests

The test I183 Incl had higher spacing until the first yielding level force was reached. An important crack appeared crossing the web reducing the spacing between cracks. This crack connected pre-existing cracks (Figure 5.3-12 and Figure 5.3-13). This kind of cracks appeared also in other cases. Normally they connected the middle of a crack with the bottom of the next crack. In this case, the crack

connected the top of a crack with the bottom of its neighbour, reducing severely the spacing between cracks. The spacing dropped from 92,8mm to 70,3mm, a reduction of 28%.

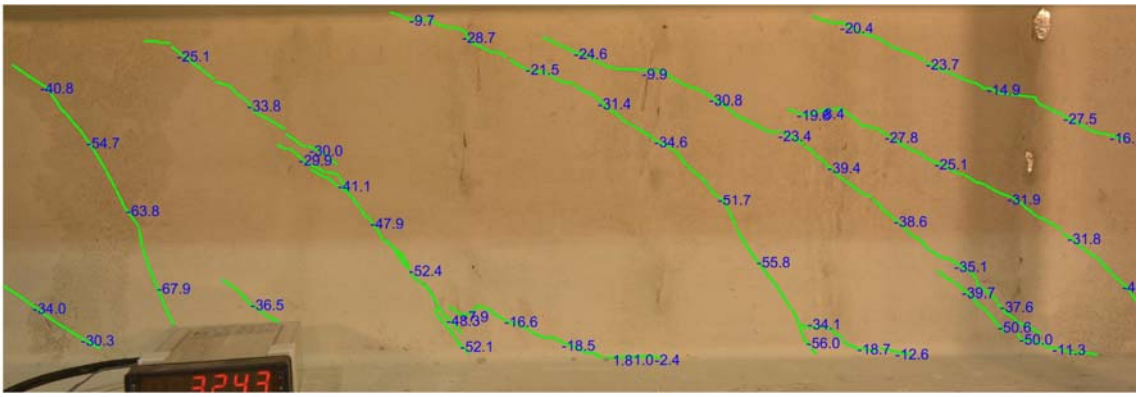

Figure 5.3-12 Picture num 22 of test I183 Incl at 325 kN of external force with the crack angle overprinted. With an average crack spacing of 92,8 mm

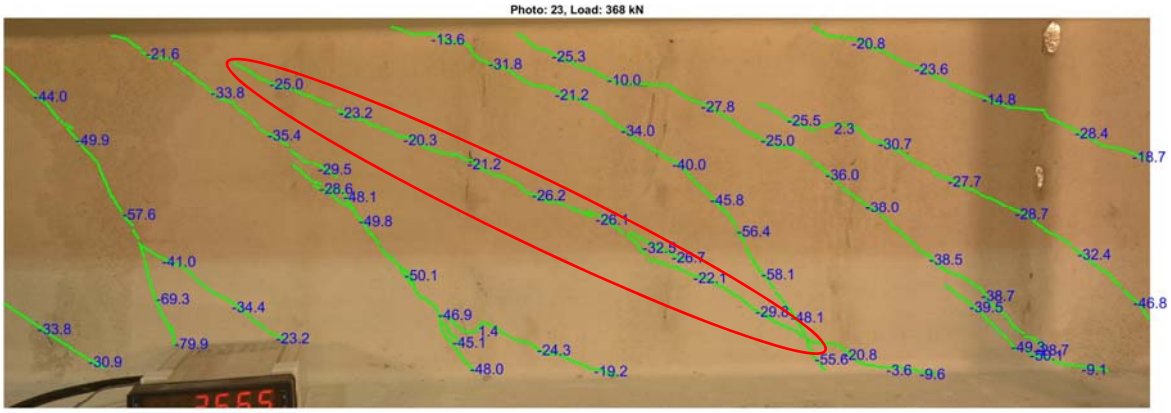

Figure 5.3-13 Picture num 23 of test I183 Incl at 366 kN of external force with the crack angle overprinted. With an average crack spacing of 70,3 mm

As it has been seen in previous images (Figure 5.3-10, Figure 5.3-12 and Figure 5.3-13), the crack pattern was not a parallel nor crack spacing was uniform in the region. The distance between crack segments was a very variable value. Cracks were grouped or connected, in some cases they did not develop the full height of the web or they changed their inclination.

The spacing between cracks was a very heterogenic value but the crack patterns repeated and showed different distributions depending on the web position of the crack. In the upper part of the web, two crack patterns usually appear. The first pattern consisted in very spread cracks because some of the cracks did not developed completely from the bottom to the top. The second case was the opposite, when the cracks developed they got closer, due to a change of their angle when they ascend.

In the centre of the web if the angle of the cracks was similar, their distribution was uneven. However, in most cases the angle was not homogeneous, so the angle would vary depending on the point where the spacing was computed. Finally, the bottom part of the web. In this part, most of the cracks ended in a very flat angle and most of the times the crack split in two branches.

To take into account the variation of the values of the spacing, a comparison of the maximum spacing was performed. To obtain the maximum spacing for each picture, the lognormal distribution of the segment spacing was performed. Figure 5.3-14 shows the values of crack spacing that represented the 95% of the observed values.

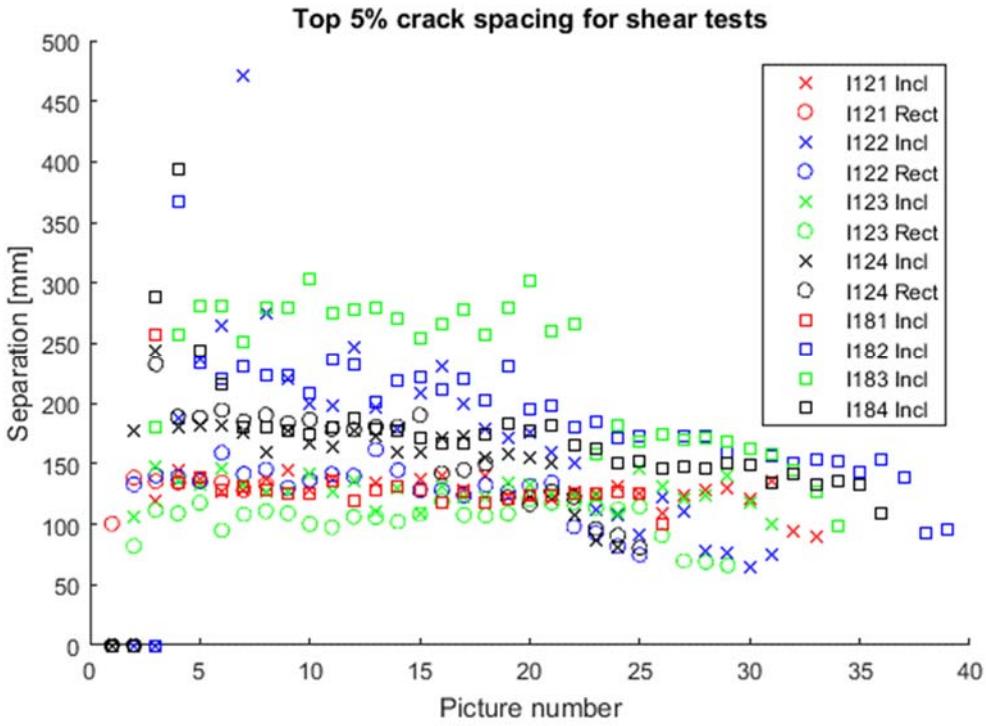

Figure 5.3-14 Top 5% crack spacing showing a higher spacing for the beams with stirrups each 250mm

After excluding the test I183 Incl for the reasons previously commented, an important difference was observed. When the top 5% of the cracks was taken into account, there was a bigger dispersion over the results, there were important differences between tests. The group of tests with a spacing between stirrups of 250mm (test blue and black in Figure 5.3-14) had a bigger crack spacing than the rest of tests. Showing that the stirrup distribution has an influence on the maximum crack spacing.

Figure 5.3-15 and Figure 5.3-16 show the horizontal projection of the crack spacing. This projection was performed with the average crack angle. This projection is the distance between the cracks on the same direction than the stirrups. Figure 5.3-15 shows the tests with a stirrup spacing of 150 mm. As it can be seen, all the tests (excluding I183 Incl) had an average spacing under 150mm.

Meanwhile, Figure 5.3-16 shows the tests with 250 mm stirrup spacing. Their horizontal spacing was not limited by the 150 mm bound neither they reached the 250 mm boundary. In this figure, without the upper boundary, the test with higher amount of strands had a higher horizontal crack spacing. The horizontal crack spacing was only limited by the stirrup spacing in the tests with smaller stirrup spacing.

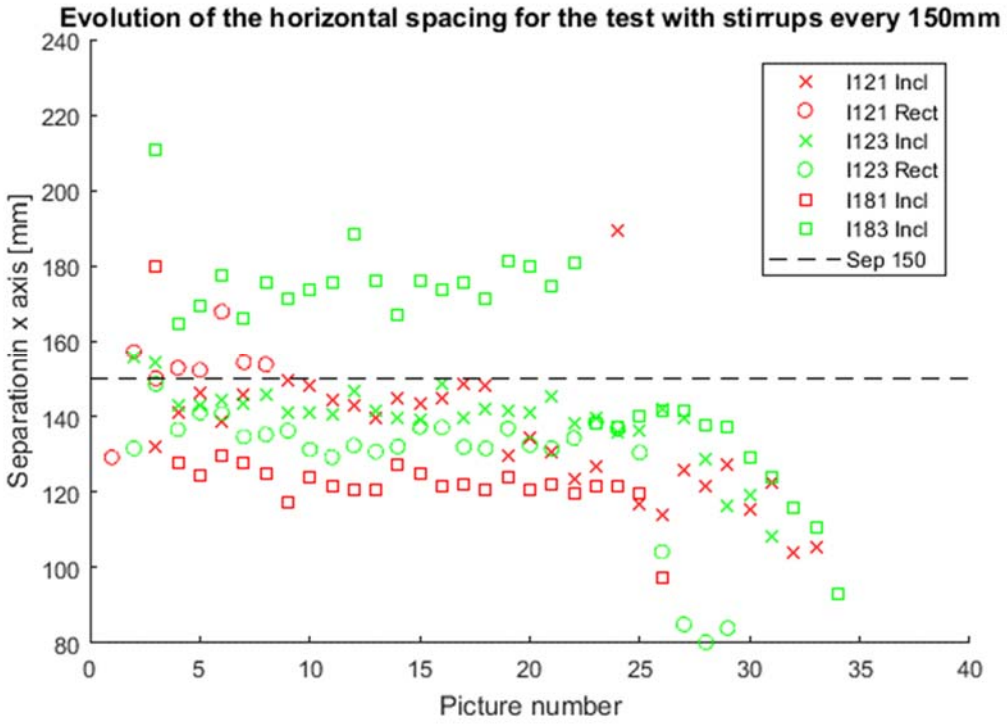

Figure 5.3-15 Stirrup spacing of 150mm compared with the crack spacing

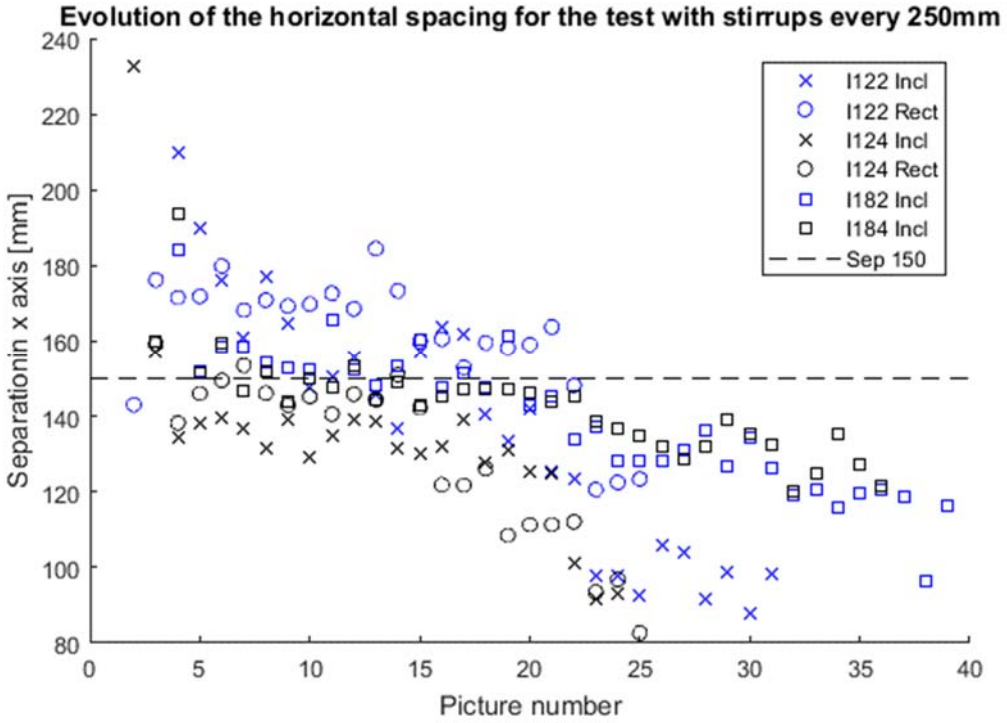

Figure 5.3-16 Comparison of the stirrup spacing with the crack spacing

5.3.3 Strains and stresses in the vertical reinforcement

As it can be seen in Figure 5.3-17, the strain gauges of the stirrups where placed on the centre of the stirrup, and 11cm up and down the stirrup. The strain gauges were placed to collect the deformation occurred on the web between the load section and the support section, in the smaller span side. During the test, and due to multiple factors, several strain gauges suffered problems and stopped sending reliable information. 20% of the strain gauges failed during the first load process, a 17% failed during the cycles representing serviceability. 60% of the strain gauges where recording information until the maximal load.

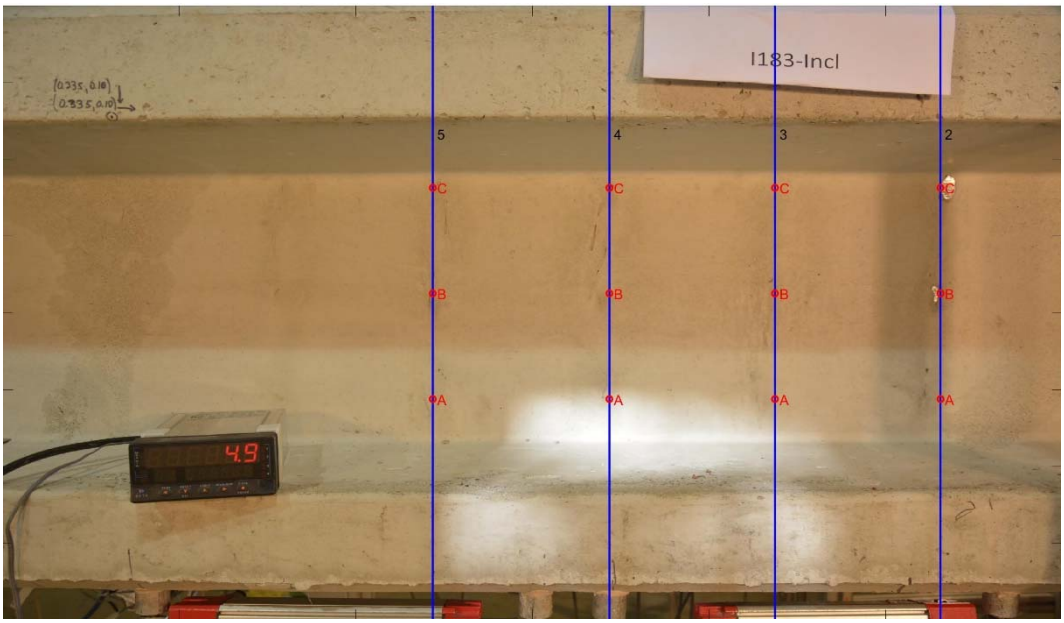

Figure 5.3-17 Position of the strain gauges in test I183 Incl

The yielding in these bars was not simultaneous in the monitored points. 40% of the strain gauges registered yielding of the reinforcement for the first time during the first loading ramp. 23% registered yielding after the serviceability cycles, on the ramp to the yielding load. 20% of the strain gauges finally registered yielding during the last ramp or after pick load. Finally, 14% of the strain gauges did not reach steel yielding strain, the 75% of this cases are strain gauges placed on the position A or C.

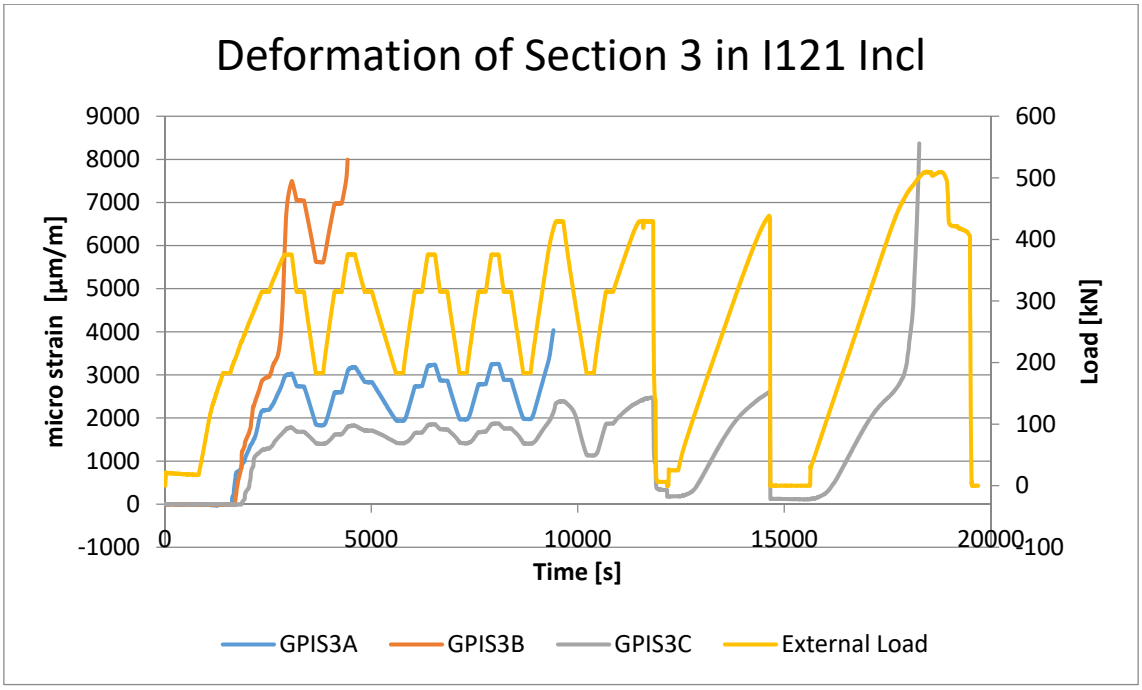

Figure 5.3-18 Example of different strain gauges reaching important deformation and breaking

This information showed that, the strain gauges that showed initial yielding, strain kept increasing through the serviceability cycles, increasing their deformation and finally the strain gauges could not resist the important deformations (like GPIS3A in Figure 5.3-18). It was also observed how, after each cycle, the final deformation of the strain gauges on the valleys had grown (Figure 5.3-19). The increase of strain was due to the cycling process. The concrete is damaged by the appearance of cracks and in some parts the stirrups had yield.

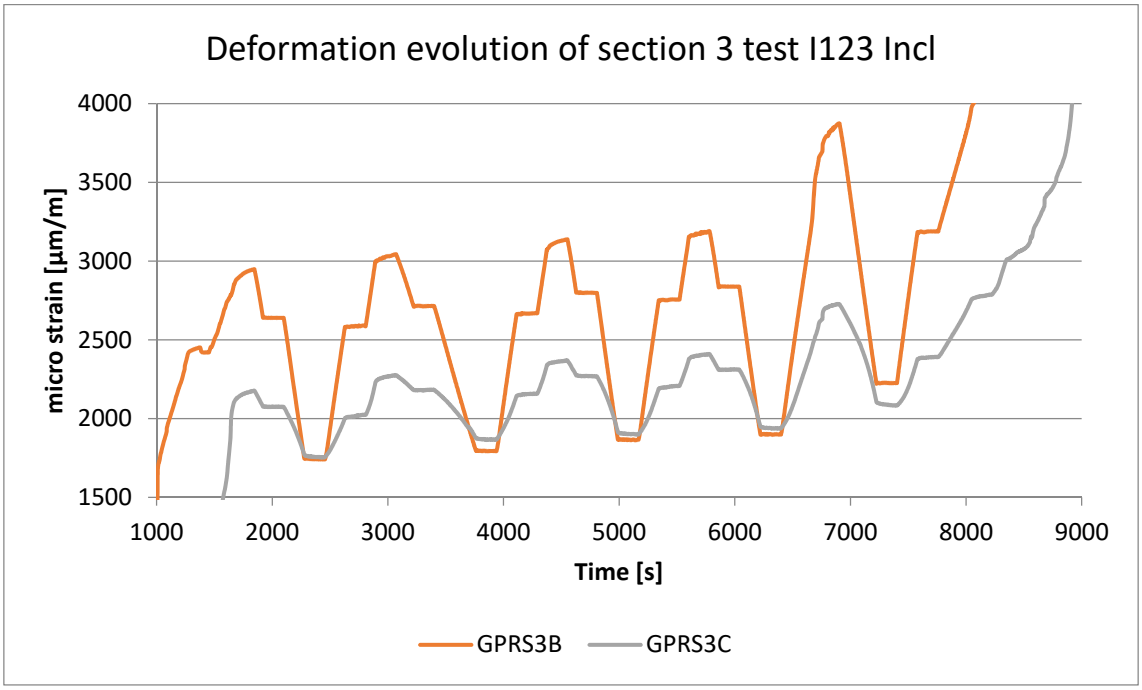

Figure 5.3-19 Increase of the deformation in the valleys after every loop

Even if the strains increased in every cycle, in some cases, the stress at unloading decreased after several load cycles (Figure 5.3-20). The different behaviour depended on the stress state of the stirrup. If during the loading branch, the yielding point was not reached, the stress at unloading branch would increase under subsequent load cycles. On the other hand, if the stirrups had yield, the stress on the quasi-permanent level will decrease after each cycle (like strain gauge GPRS3B).

If a stirrup had not yield, its stress-strain relationship is linear, and the stress would perfectly follow the trend of the deformation. Strain gauge GPRS3C (shown in the above figures) is an example of this kind of behaviour. In some cases, the deformation recorded by a strain gauge decreased and so it did its tension.

In the cases where the stirrups had overcome the yielding deformation, the ratio of deformation over applied load increases significantly, therefore the deformation at each peak increases in every loop. In the unloading branch, two phenomenon affect the stirrups. The first one is due to the linear behaviour of the steel of the stirrups. The second one is due to the prestressing force.

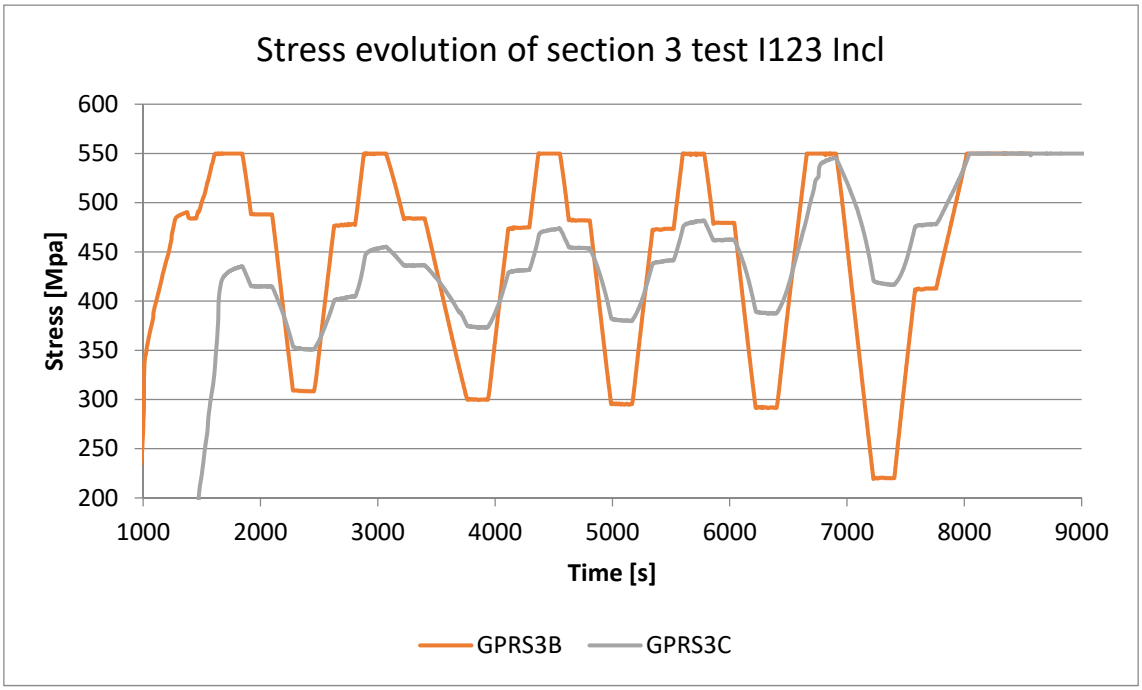

Figure 5.3-20 Different behaviour of stirrups due to yielding

The first phenomena unloads the stirrup from a yielding state to a linear state. The variation of strains is linearly dependent to the external force and independent of the current strains at the stirrup at the moment of unloading. Since the loading protocol is the same for each loop, the variation of deformation during the unloading had to be the same.

Meanwhile, the tendons are constantly in a linear behaviour, they always compress the specimen and try to close the cracks. During the unloading branch, the stresses in the stirrups reach again their original value but the cracks are still opened due to the yielding deformation. The strands close the cracks adding compression to the stirrups, therefore the deformation of the stirrups decrease. This second phenomena generates a higher variation of the tensile stress of the stirrups at unloading. The decrease of tension is higher than in the non-yielded case.

5.3.4 Observed and calculated crack width

The formulations presented in several codes use the deformations in the web and the spacing of the cracks to predict the crack width. Using the information showed in Figure 5.3-17 and the crack spacing obtained using photogrammetry, this formulation could be used to predict the crack with for the tests. This process consisted in calculating the distance between the two cracks that flanked the strain gauges. The direction used to calculate the spacing was the average angle of the cracks for the picture under analysis. The deformation would be the deformation of the respective strain gauge.

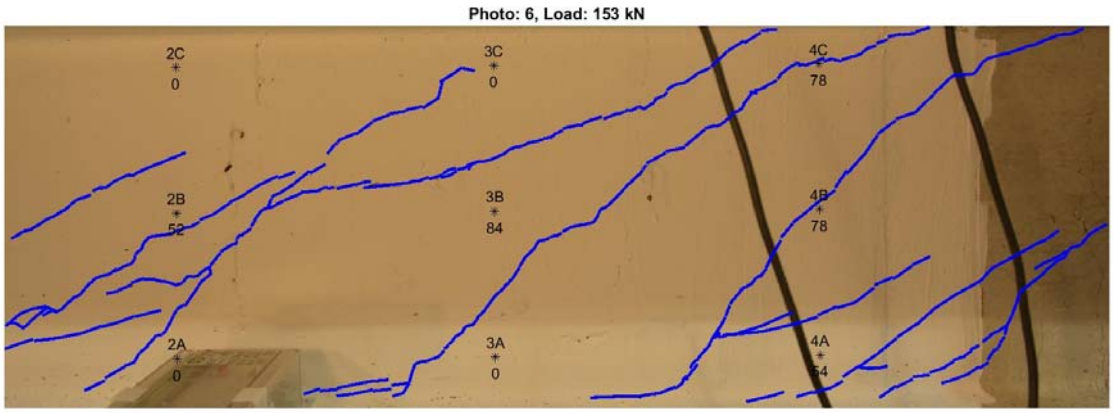

Figure 5.3-21 Distance between cracks computed form the strain gauge position. Test I124 Incl [mm]

Figure 5.3-21 shows the distances computed form the position of the strain gauges. Some strain gauges were not placed between cracks, this could change due to the evolution of the cracks. In case of a strain gauge was not between cracks in a picture, it was assumed the distance was 0 and this data was not used for further analysis.

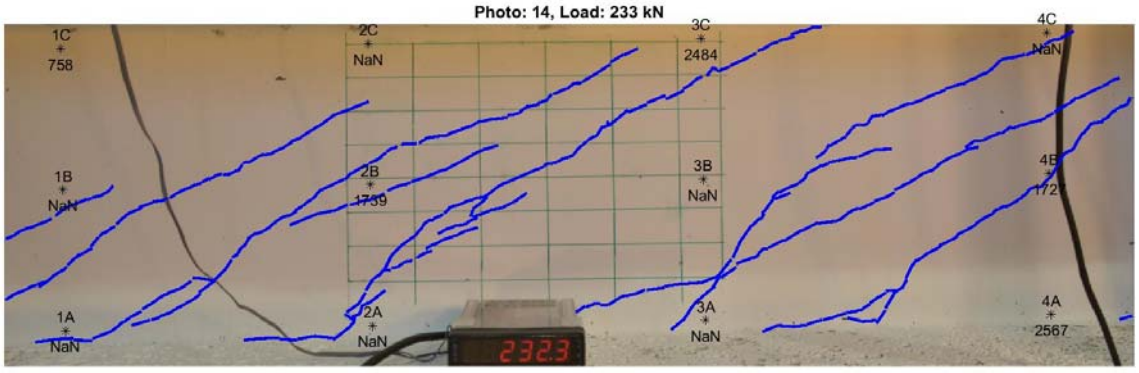

Figure 5.3-22 Deformation of the strain gauges. Test I124 Rect [μm/m]

Figure 5.3-22 shows the deformations obtained by the strain gauges and its position on the web. In the cases where there were no information or the data was clearly inaccurate the image would show a not a number (NaN) tag. As it can be seen, the amount of strain gauges that failed was significant.

However, the use photogrammetry allowed obtaining an accurate value of crack spacing width. Obtaining the angle and the spacing of cracks with previous technologies was complicated, and required and important use of resources. The use of strain gauges to obtain the deformation in rebars has been proven as very effective and accurate. However, the use of the two values to obtain the crack width has been proven inaccurate. Figure 5.3-23 shows the crack width using the combination of the two technologies. As an example, it can be seen how 4B is a wider cracks than 4C but the formulation

provides the opposite result. This problem repeated through all the pictures and disqualified this process to know the crack width of the tests. The deformation value obtained from the strain gauges was the parameter that putted off the process.

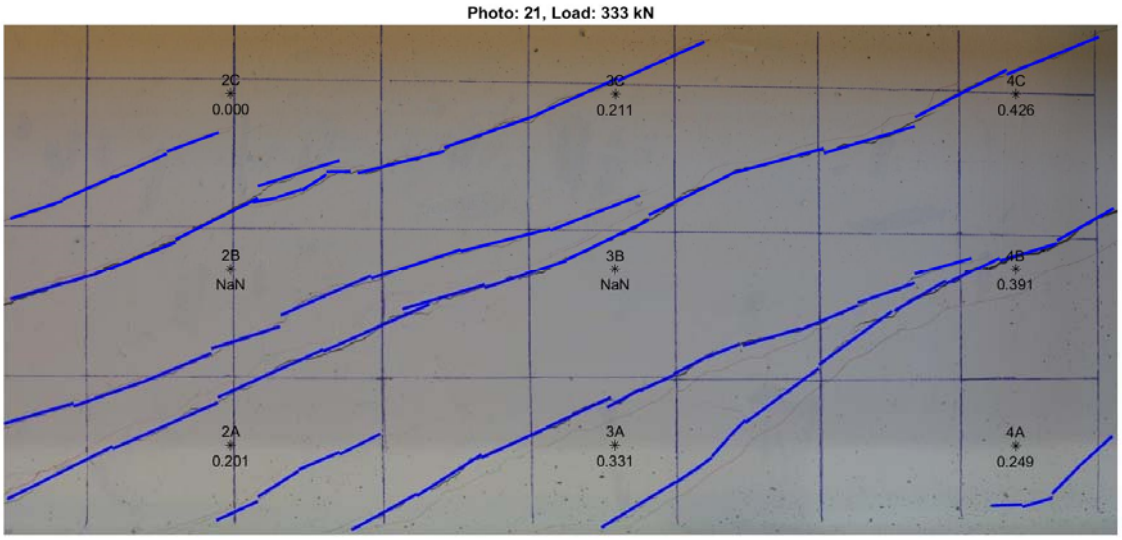

Figure 5.3-23 Crack width in the strain gagues. Test I122 Rect [mm]

5.3.4.1 Evolution of the crack width using photogrammetry

Using the programme developed in this Thesis, described in the Chapter 0, it was possible to obtain the crack width using only the information of the photographs. The software analysed the pictures and calculated the width of the cracks using the light variation of the pixels and the intensity of the pixels in the crack. Figure 5.3-24 shows the crack widths obtained with the software. These results were checked against real crack widths measurements, comparing different regions of a picture and comparing tests between them. The crack width obtained from the pictures was then considered valid.

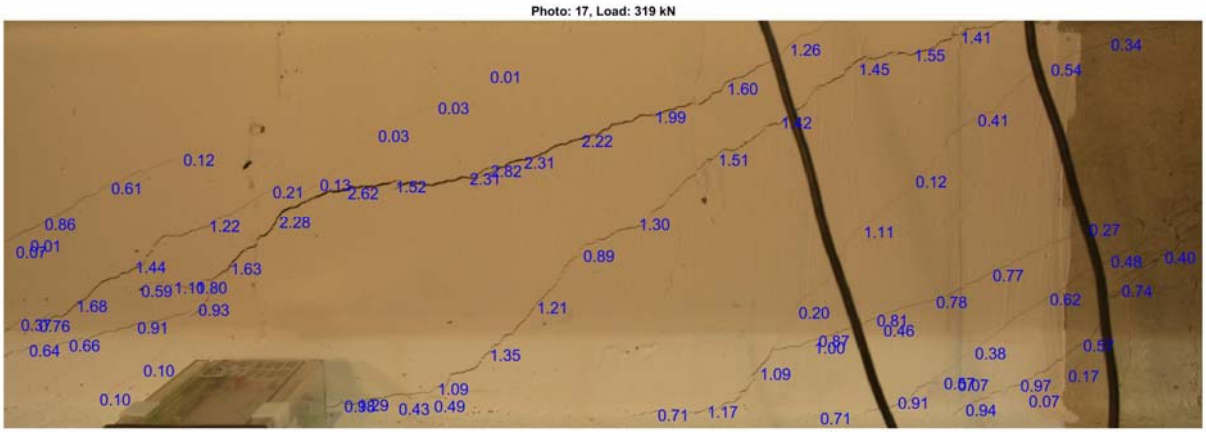

Figure 5.3-24 Crack width of test I124 Incl [mm]l

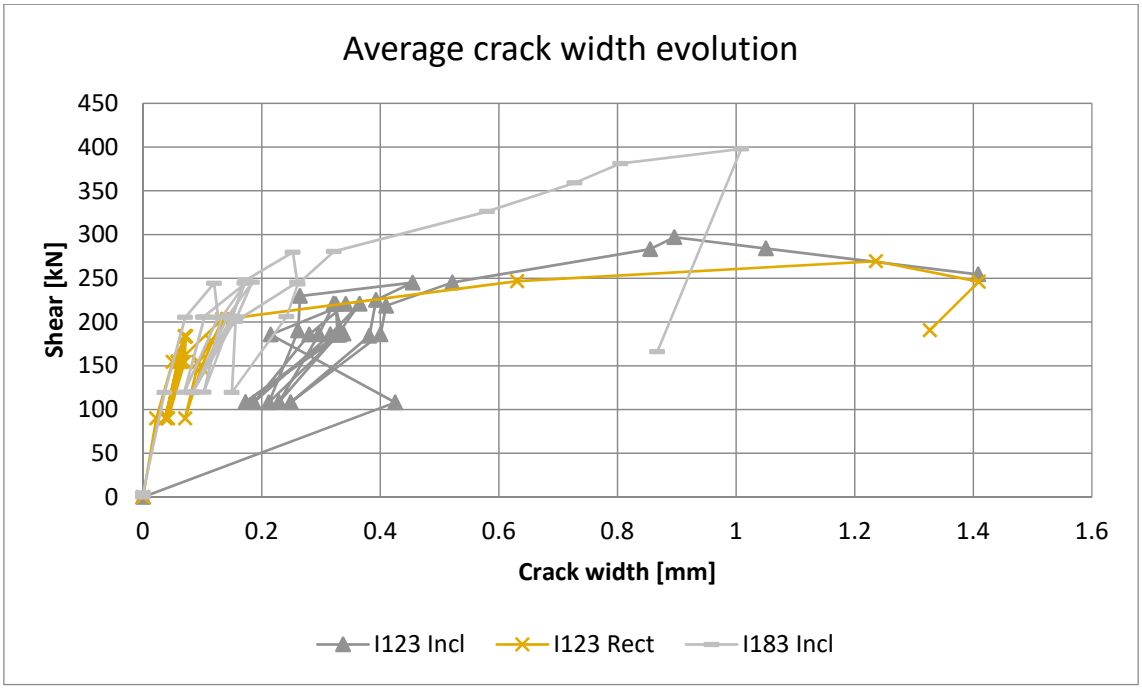

Figure 5.3-25 Relationship between crack width and shear for the third tests of each group

Figure 5.3-25 shows the evolution of the crack width of the tests. It can be seen that the beams with lower web width got higher average crack width. The tests where the pictures were not taken from a single picture frame (changing on the position or zoom of the camera), had blurrier curve and had to be removed from some analysis of the general behaviour. On the other hand, when the frame was constant during the entire test, the evolution of the curves was smoother. Like in Figure 5.3-26, where the cycles and the general evolution of the crack width was clearly noticeable.

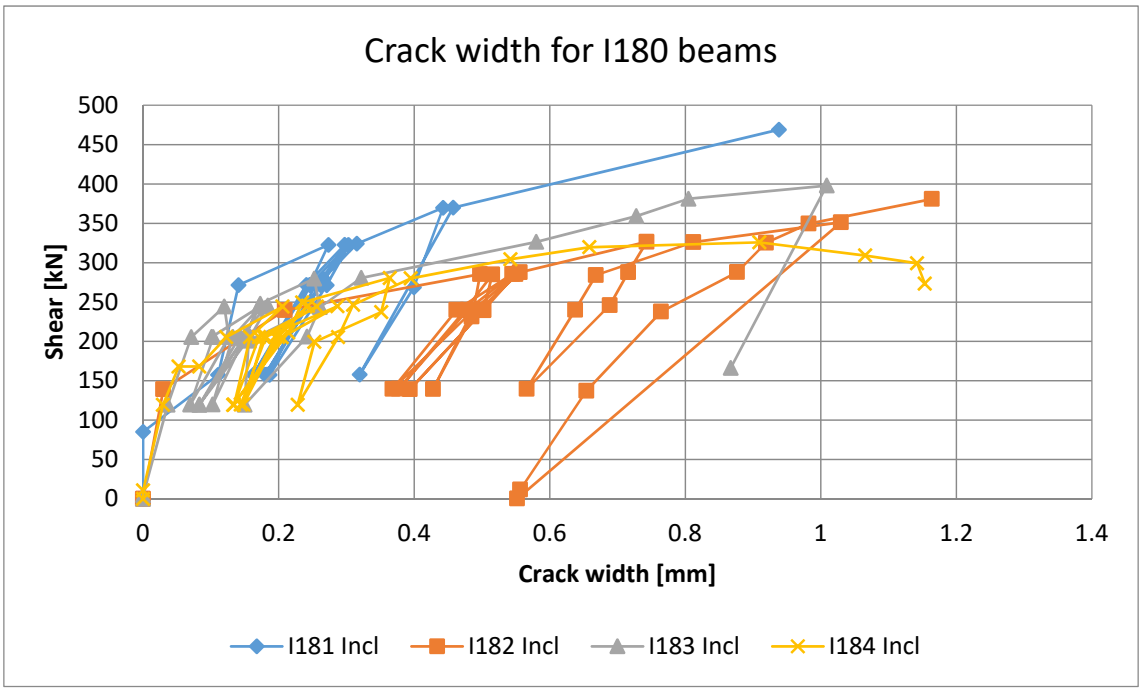

Figure 5.3-26 Evolution of the average crack with of the beams with 180mm of width

The tests performed on the straight layout side of the beams (specimens with Rect suffix) also had adequate pictures, and could be used to analyse the evolution of the crack width. The eight cases in Figure 5.3-26 and Figure 5.3-27 showed a similar behaviour. The beams with lower amount of stirrups had bigger crack width, but the beams with higher amount of strands had higher shear crack width. Test I121 Rect could only be photographed entirely after the beginning of the second cycle. The same behaviour was maintained when the maximum crack width in the pictures was analysed.

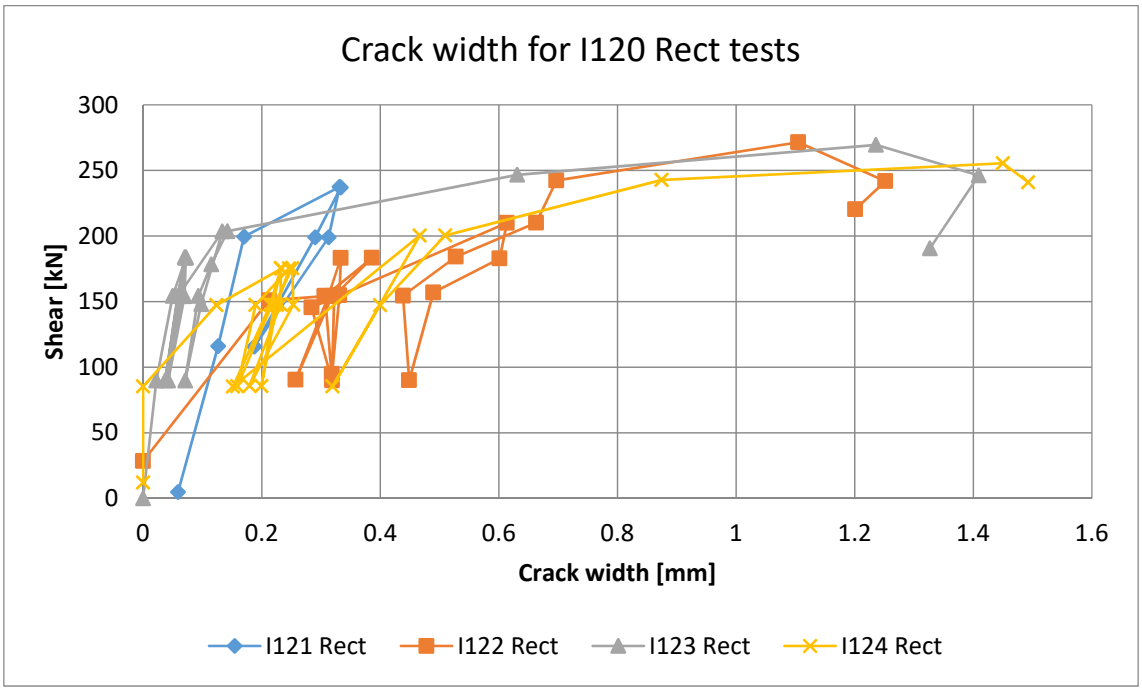

Figure 5.3-27 Evolution of the crack width of the beams of 120 mm of web and horizontal lay out

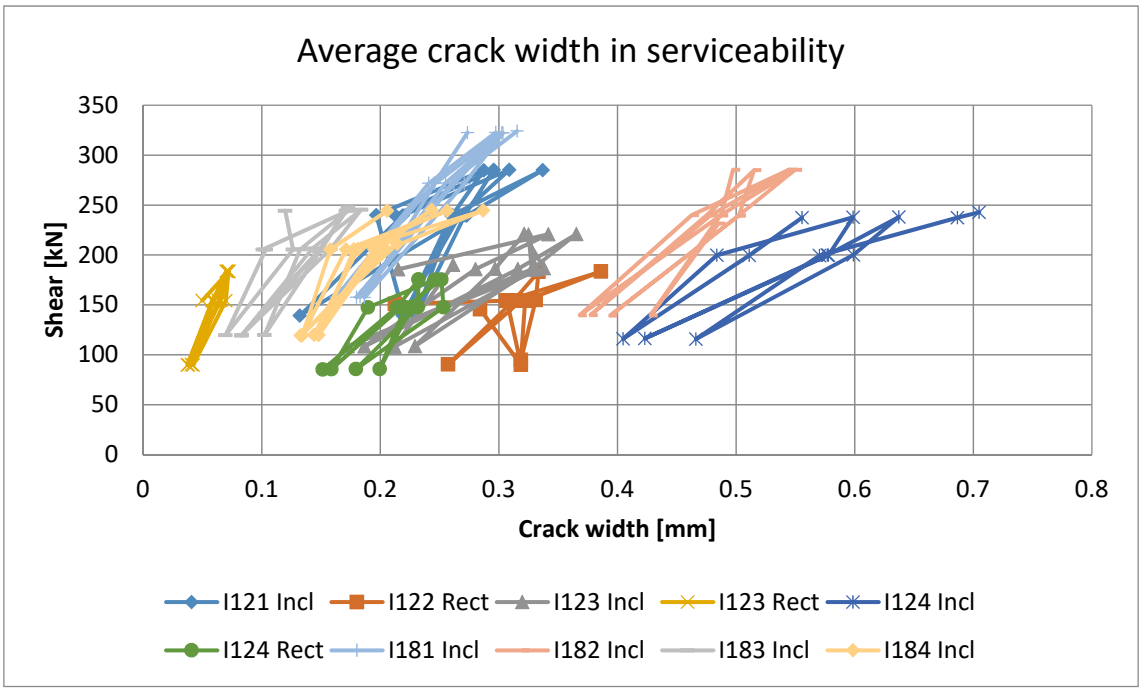

Figure 5.3-28 Crack width during the cycles. Evolution of width due to repetitive load

Figure 5.3-28 shows only the average crack width of the cycles. The information prior to the first peak and the information of the yielding ramp and failure ramp had been removed. The beams with important crack width had bigger difference between the peak and the valley of the cycle. This would mean that the stiffness of the beam has been reduced. Figure 5.3-29 presents the average crack width the beam presented at the peak and valley loads. The difference between the peak and the valley is proportional to the crack width.

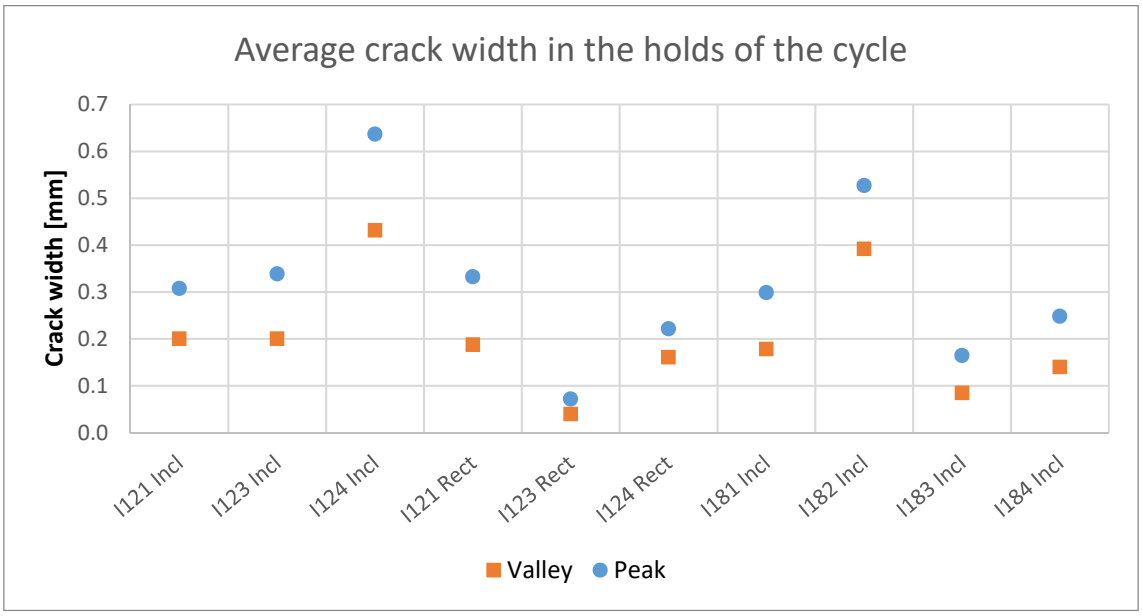

Figure 5.3-29 The average of the crack widths obtained in every load level

The cycling process also abased the stiffness of the beams. The crack width in peaks and valleys increased with the cycles. Figure 5.3-30 shows the variation of crack width on the peaks and valleys, comparing the values of the first and the last cycle. The positive variations implied that, after subsequent cycles, the crack opening increased. Tests where less than two cycles were recorded were not taken into account.

It can be seen how, in some cases, the final crack width was smaller than the initial value. This would imply that the loading process has generated more cracks and the deformation has been distributed between the cracks, reducing the average crack width. Even though, in most of the cases, the variation was positive for the peak and the valleys. In these cases, no new cracks appear and the increase in deformation suffered by the strain gauges was absorbed by the pre-existing cracks.

In most of the cycles, either during service or post-yielding loads, the crack width was bigger during the unloading ramp and smaller during the loading part. This effect was also seen in the deflection curves and the strain gauges deformations. At the beginning of a change in the direction of the load, the stiffness of the beam increased. The friction in the cracks should explain this increase in the stiffness of the beam. This effect also generates a hysteretic effect.

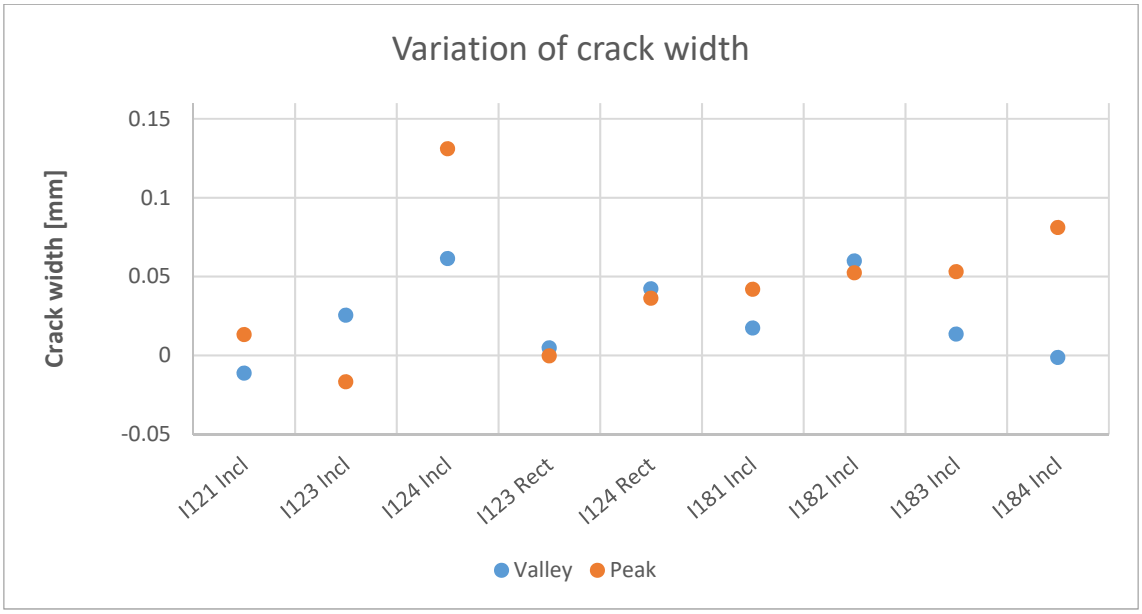

Figure 5.3-30 Difference of crack widths between the first and the last loop, for the peaks and the valleys of the cycles

Figure 5.3-31 shows the maximum crack width observed in serviceability levels. Test I122 Rect and I123 Incl have been removed. The stickers and lines drown on the surface of the beam interfered with the computation and the values could not be taken into account. In average, the maximum crack opening were 7.0 times bigger than the mean crack opening. Each test had the same ratio for all its pictures. The lower ratio was 4.4 and the highest 13.8. This exemplified the variance of behaviour to predict a characteristic crack width for shear tests.

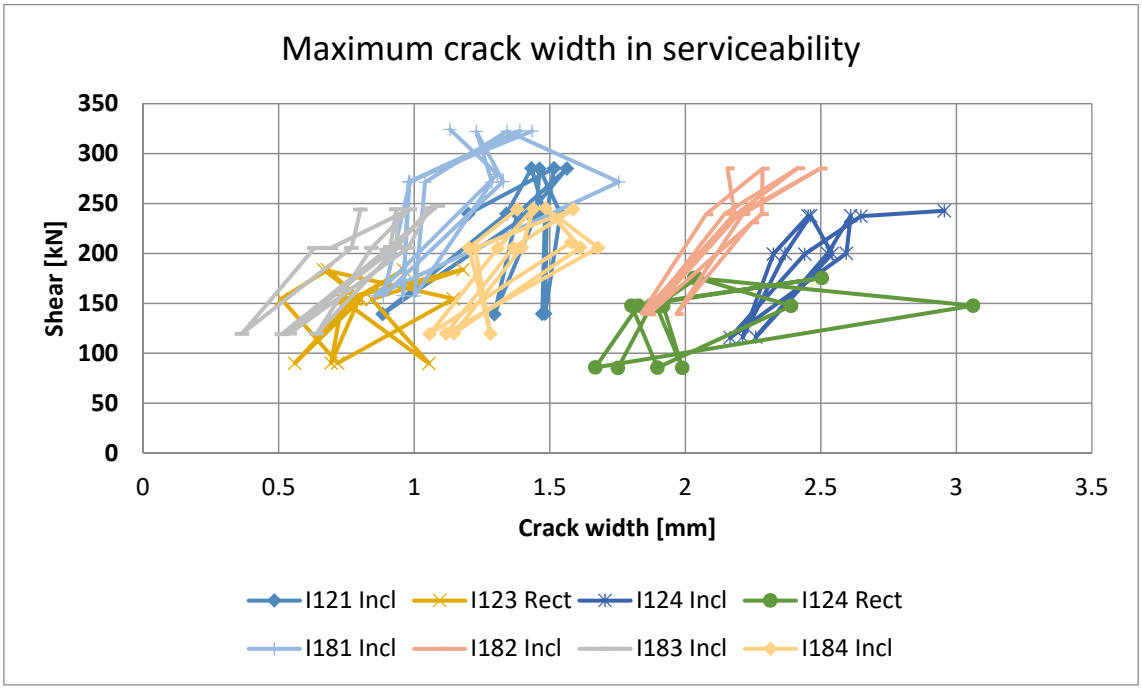

Figure 5.3-31 Biggest crack widths during serviceability

The values of angle and crack width used in Figure 5.3-32 were obtained from the intermediate holds performed in the cycles. The test I124 Incl had higher service loads than the other beams, resulting from the loading protocol, which was defined based on the predicted maximum load. Taken this into

account, and removing its results from the analysis, it can be seen how the value of $\cot\theta$ and the crack width are related. The beams with lower prestressing force had smaller crack width and their angle was more vertical. The beams with 4 strands, had bigger crack widths and the cotangent is also bigger. With the beams with smaller amount of stirrups having bigger cracks and cotangent values.

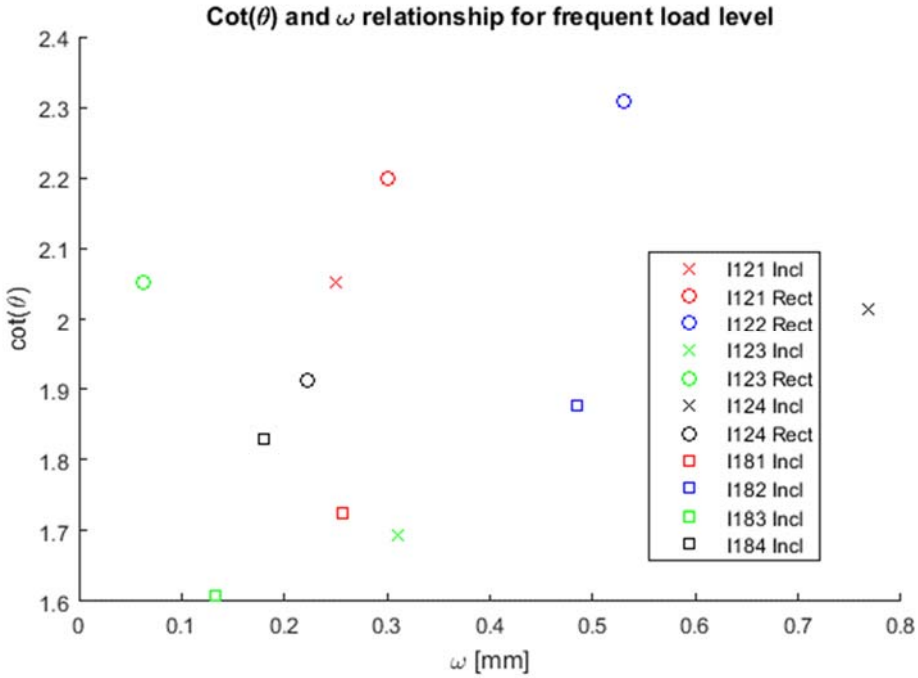

Figure 5.3-32 $Cot(\theta)$of the crack angle during the intermediate loads

To generate the Figure 5.3-33, the same criteria was used. The information was collected from the intermediate load levels. When analysing the influence of the crack spacing and the crack width, an important consideration had to be made. The test I183 Incl had a smaller load ratio than the rest of the specimens, and not all the cracks had developed. As it was observed in Figure 5.3-11, after serviceability load level, the crack spacing of this test reduced drastically to values similar than the other tests. Due to this difference, this test was considered as an outsider and was not used in the analysis of the influence of the spacing in the crack width.

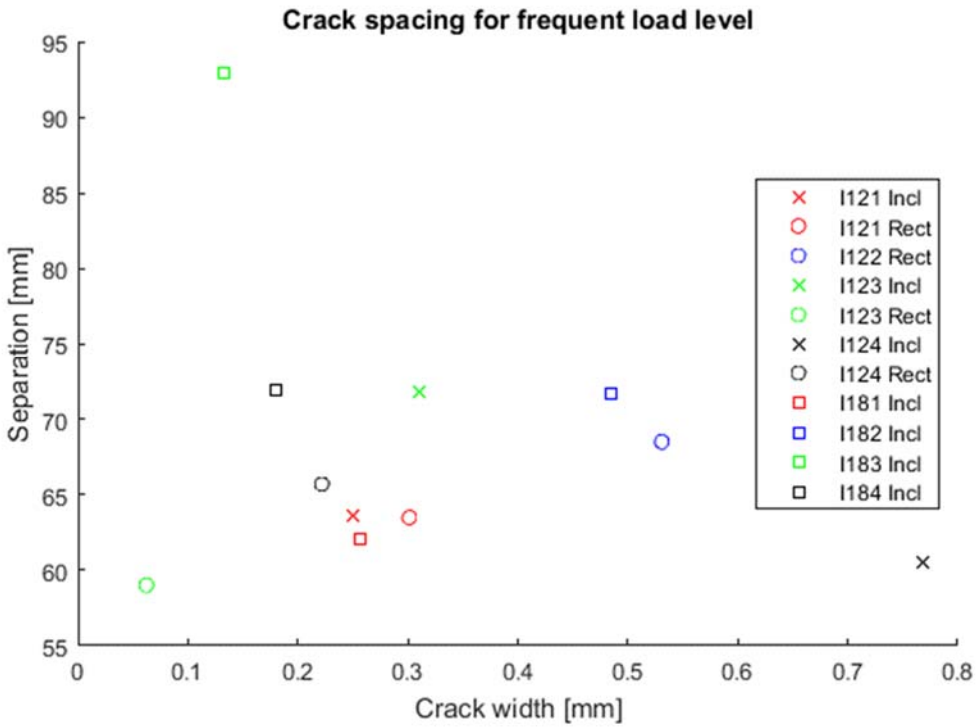

Figure 5.3-33 Relationship between crack width and spacing

The range of values of crack spacing was small. No relationship could be established between the spacing and the crack width. The two precedent figures showed that the angle of the cracks and its spacing was established by the geometrical and mechanical properties of the beam. These properties would greatly affect the crack size while the spacing and the angle of the cracks would not. These two parameters would set the amount of stirrups crossed by the cracks or the amount of times a stirrup would be crossed by cracks and in combination with the other properties of the beam, the crack width could be predicted.

5.3.4.2 Proposed cracked width formulation

To predict the crack width of a beam, EHE 08 (Comisión permanente del Hormigón, 2008) uses the equation 5.3-2. Where the deformation on the web times the distance between cracks is the crack opening. As mentioned above, the stirrups during the test were locally yielded but the global behaviour of the structure does not behaved as yielded. The two inputs of the equation were obtained from the images and the theoretical deformation of the stirrups. The deformation was obtained using the shear resistance of the stirrups in EHE 08 code (Equation 2.3-1).

$$\omega = s \cdot \varepsilon_w \qquad 5.3\text{-}2$$

$$V - V_p = \frac{As}{st}\,\sigma_s\, z\, \cot\theta \qquad 5.3\text{-}3$$

$$\varepsilon_w = \frac{V - V_p}{\frac{As}{st}\,E\, z\, \cot\theta} \qquad 5.3\text{-}4$$

The shear resistance of the stirrups (Equation 2.3-1) is the ratio between the area of stirrups and their spacing times the tension of the stirrups, the lever arm and the cotangent of the angle of the trusts. In the cases where the lay out of the strands was not flat, the vertical component of the prestressing force helped to resist the shear force, so it would have to be subtracted. With Equation 5.3-4, the

deformation of the stirrups can be obtained. This deformation would take into account the variation of the shear force and the change in the angle of the cracks showed in Figure 5.3-3

The stirrups yielded during the test, the deformations obtained using the equation 5.3-4 also reported deformations over the yielding limit. The equation uses a linear relationship between strain and stress (young modulus). Therefore, the strains obtained from the equation were smaller than the deformations of the strain gauges. To analyse the difference between the two values, an energy balanced hypothesis was considered; hence, the equating the theoretically elastic area below the σ-ε curve, to the area of an elasto-plastic σ-ε behaviour, Figure 5.3-34. The first area represents the deformation over the yielding point and the increase of stress. The second area would be the increase of deformation due to the limitation of stress.

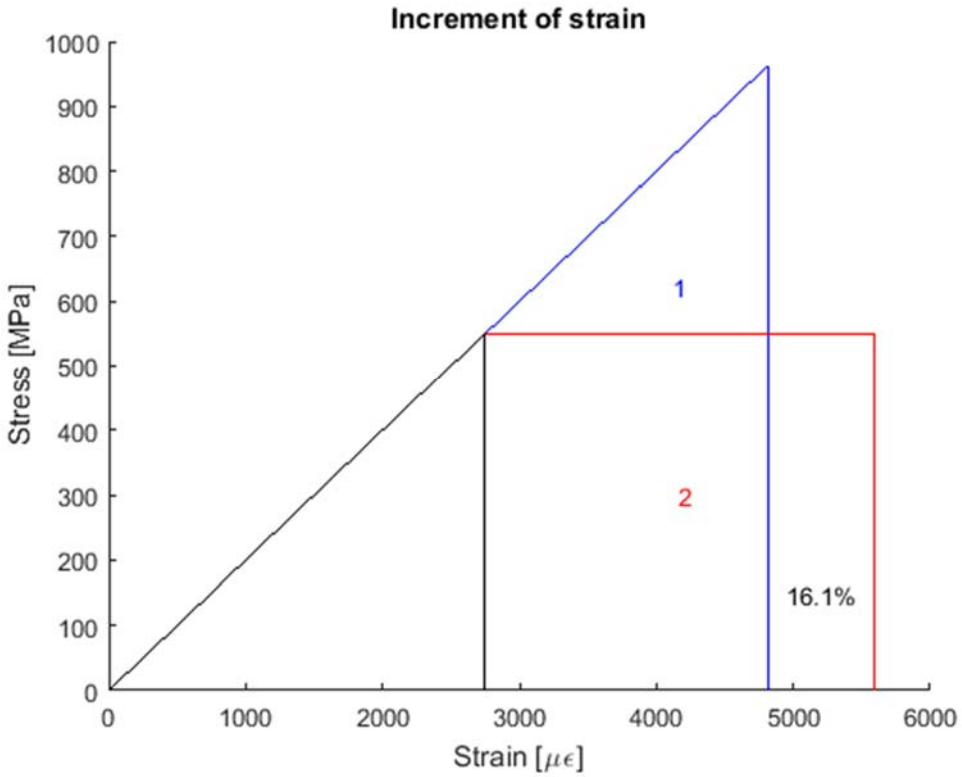

Figure 5.3-34 Increment of 16,1% of the area when the yielding deformation is exceeded by 75% (4812,5 με)

The equation 5.3-6 shows energy balance, where the unknown parameter is the post-yielding strain: ε_s. σ_s is obtained using Equation 5.3-5, from Equation 5.3-4. Equation 5.3-7 presents the final solution that depends on the stress or strain obtained by the formulation of the code. When applied to the strains of the tests, the variation between deformations was very small and the transformation was not taken into account.

$$\sigma_s = \frac{V - V_p}{\frac{As}{st}\ z\ \cot\theta} \qquad 5.3\text{-}5$$

$$\frac{{\sigma_s}^2 - {f_y}^2}{2\,E_s} = f_y\left(\varepsilon_s - \frac{f_y}{E_s}\right) \qquad 5.3\text{-}6$$

$$\varepsilon_s = \varepsilon_y \frac{\left(\frac{\sigma_s}{f_y}\right)^2 + 1}{2} \qquad 5.3\text{-}7$$

Using the crack spacing presented in Figure 5.3-11 and the deformation obtained with equation 5.3-4, an analytical value of crack width (ω) was obtained. The comparison of the analytical and observed crack width showed that the analytical crack width could only be taken into account for serviceability loads. In the firsts stages of the tests, the angle of the cracks are due to bending moment stressed and the formulation do not show good results. When the loads start to increase leaving the serviceability range, the increase in deformation was underestimated by the formulation and the values of crack width are too small. Figure 5.3-35 shows an example of the behaviour of the two variables. The ω obtained by the photogrammetric software is the blue curve. The ω calculated via formulation is presented in black. Finally, the red curve is the observed ω vs analytical ω.

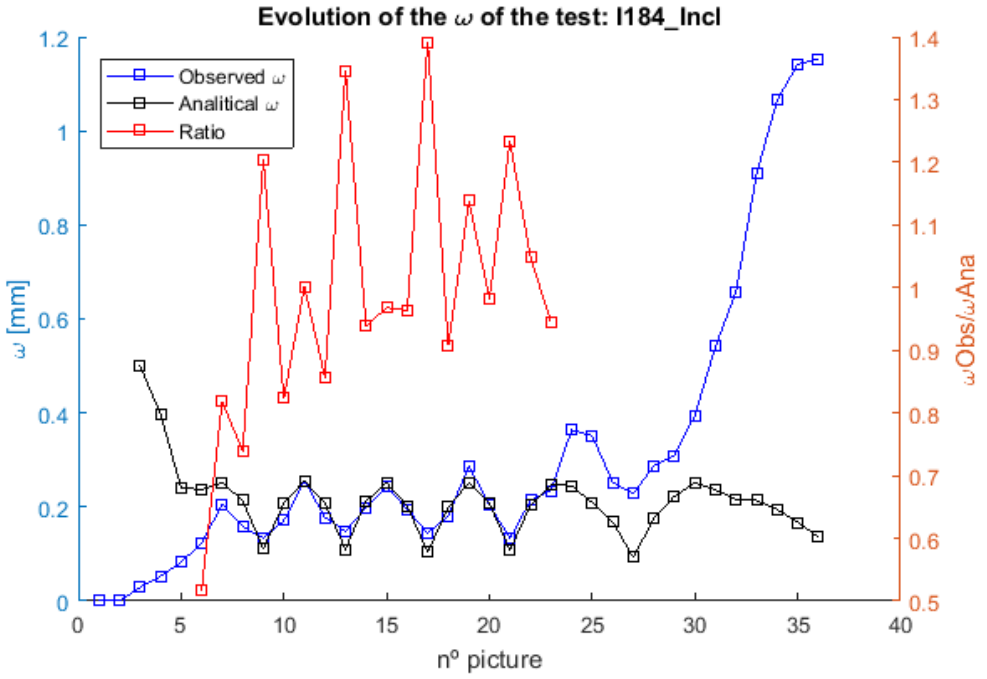

Figure 5.3-35 Comparison of the two crack width and the ratio between them

From the 339 photographs analysed, 171 were taken under service loads and with crack angles not governed by the bending moment stresses. For each one of these 171 photographs, the ratio of observed and analysed ω was calculated. Finding the correction factor between the two crack widths would allow to predict the crack width using the equation 5.3-8.

$$\omega = \beta \cdot \omega_{calc} \qquad 5.3\text{-}8$$

A lognormal distribution was assumed for the distribution of the observed and predicted ratio. The Figure 5.3-36 shows the probability (PDF) and cumulative (CDF) distribution function of all the ratios in serviceability. The average ratio was 1.33, the percentile 0.90 was 2.86 and the 0.95 was 3.55.

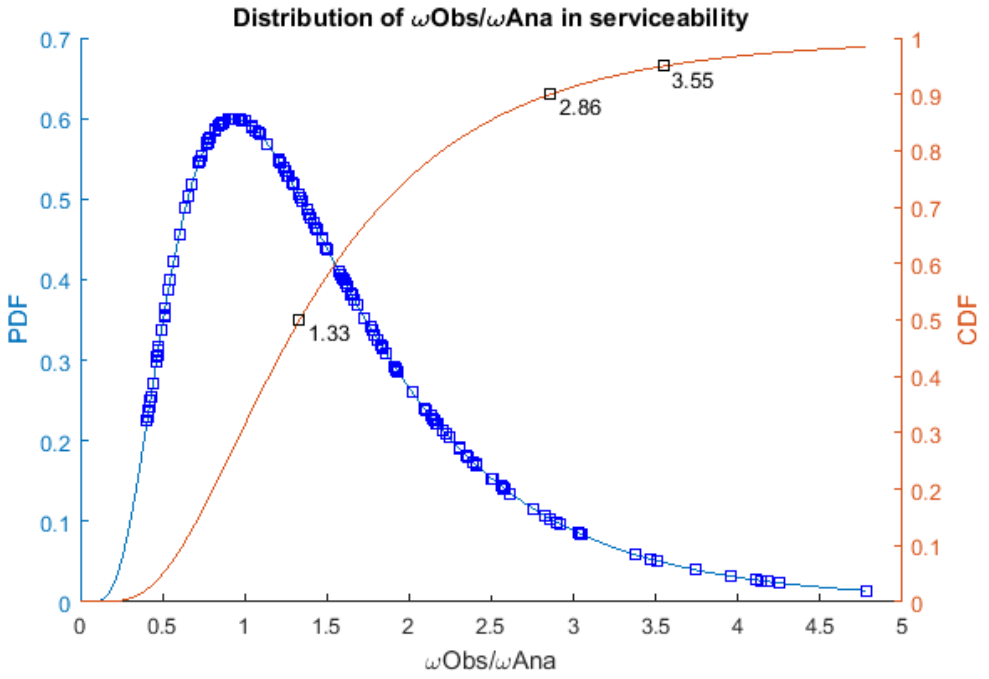

Figure 5.3-36 Lognormal distribution of ratios in serviceability with 2.86 and 3.55 as the percentile 90% and 95%, respectively

The bigger ratios of the set were the crack widths obtained on the valleys of the cycles. The formulation predicted that the unloading would close the cracks more than it did. Figure 5.3-37 is a clear example of how in the valleys the analytical crack width was smaller than the observed one. On the other hand, the frequent level and characteristic level showed stable and smaller ratios. Since the crack control formulations are generally performed in the frequent level, a statistic analyse erasing the valley ratios was performed.

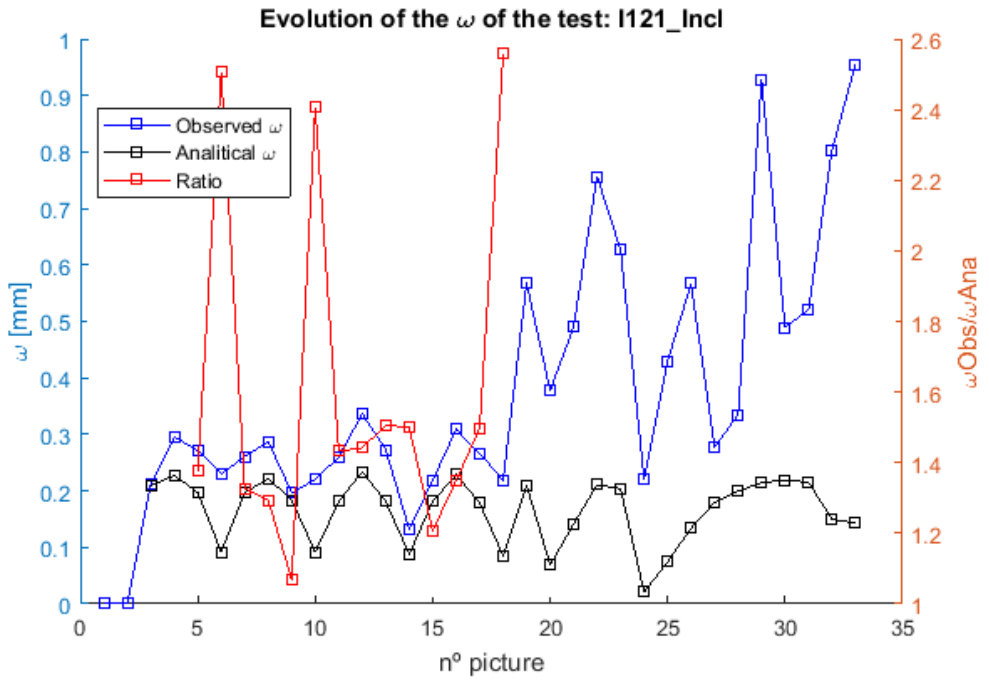

Figure 5.3-37 Important increase of the ratio at the valleys. The cracks tended to close less than predicted by the formulation

By removing the valleys, the number of ratio samples was reduced to 128. The percentile 0.95 was reduced to 2.99 with an average value of 1.22 (Figure 5.3-38). These parameters could be used as the β of equation 5.3-8, and for design purposes and to ensure a proper safety factor the percentile 90% of 2.45 could be used. Therefore, if the calculated average crack width is multiplied by 2.45, the obtained crack width would be superior to the real one a 90% of the times.

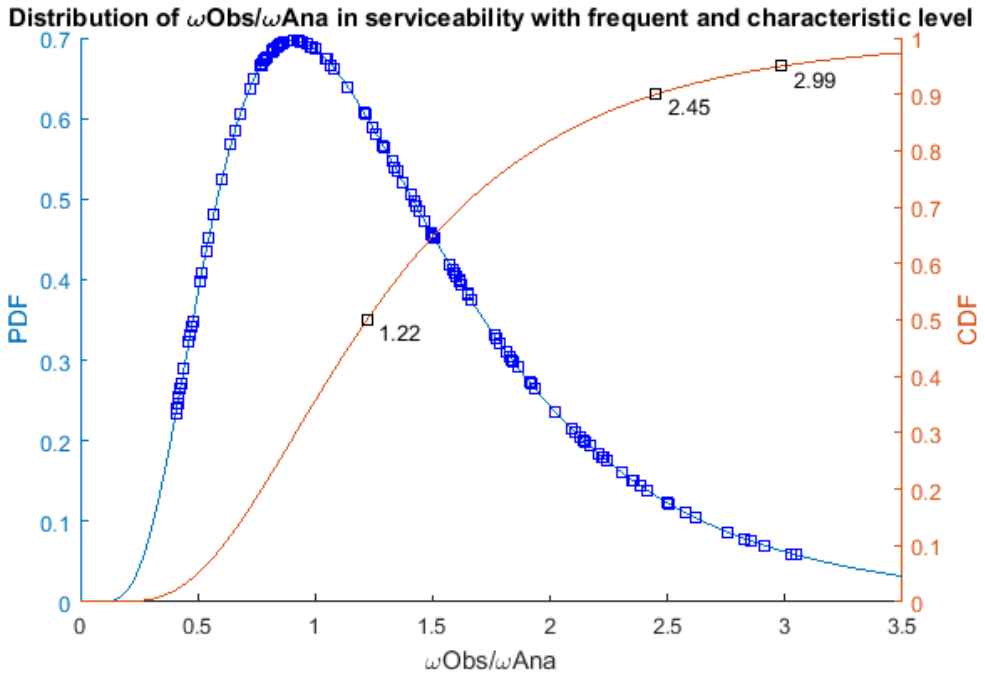

Figure 5.3-38 The lognormal distribution without the valleys had a 2.45 and 2.99 ratio for the percentile 90% and 95%, respectively

If the equation 5.3-8 is used to compute the ω of quasi-permanent load levels, the appropriate β to use is the one founded in the analysis of Figure 5.3-36, $\beta = 2.86$. On the other hand, if the ω has to be calculated for higher serviceability loads, a smaller β =2.45, could be used.

5.3.5 Analysis of the deflection

The degradation of the stiffness of the beams observed in Figure 5.3-30 was also observed analysing the deflection of the beams. During the load cycles, the stiffness of the beams changed significantly generating important differences between the loading and unloading branch. This process resulted in a progressive increase of the deflection in the peaks and valleys of the load protocol.

Figure 5.3-39 shows the loops generated by the deflection during the cycles. The difference between the loading process and the unloading process is due to the opening and closing of the cracks. The deflection difference between the two branches was in average 2.0 for the beams with 120 mm web width. This effect was more subtle on the beams with 180mm of web width (Figure 5.3-40) and the deflection difference was 1.2 in average.

For all the cases, the global behaviour started with an initial stiffness, corresponding to the un-cracked section. After this point has been surpassed, a new stiffness appears, decreasing as the load increases. Suring the cycles, the tangent stiffness was an intermediate stiffness, between the un-cracked and the stiffness obtained post cracking. This stiffness remained constant independently of the load level.

Reaching loads under the cracking load did not changed the behaviour. Only been altered when the cracks are closing or opening near the peaks and valleys of the cycles.

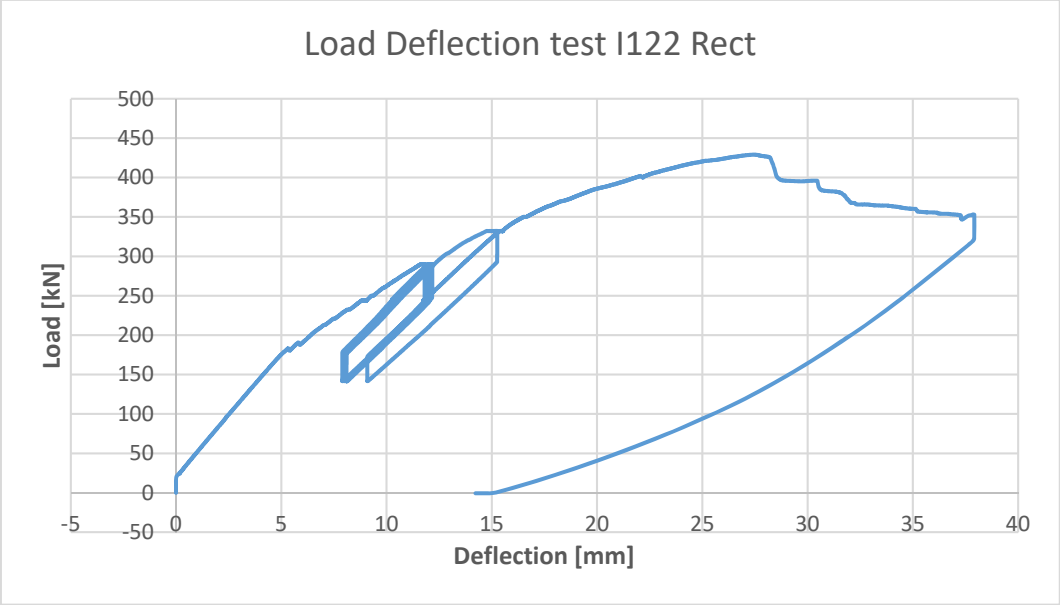

Figure 5.3-39 Deflection of the section under the jack

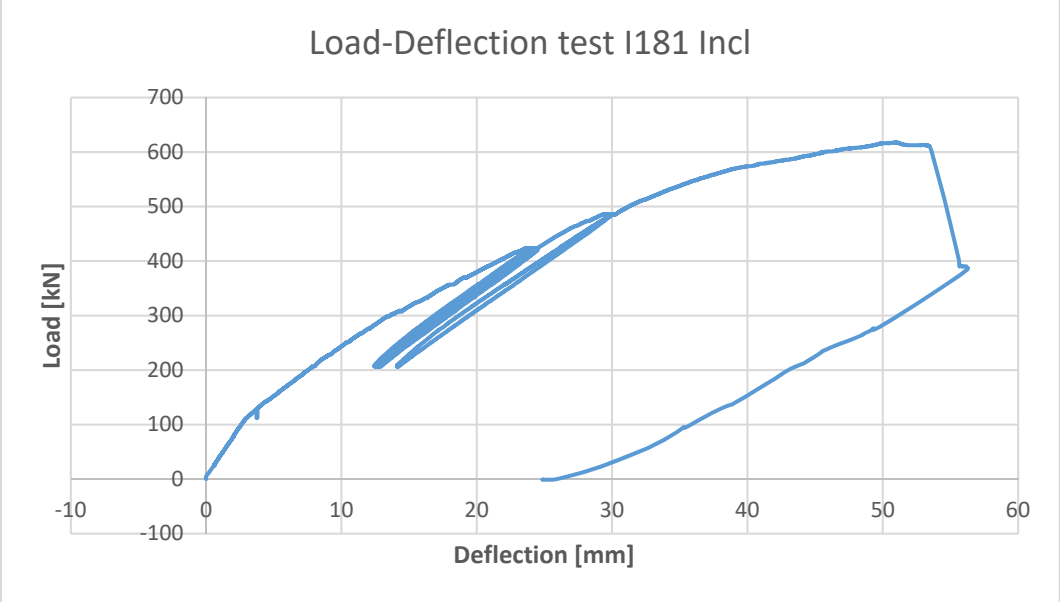

Figure 5.3-40 More subtle cycles for the beams of 180 web width

The test I124 Incl (Figure 5.3-41) had a mixed behaviour. The unload process developed like all the beams of 120 mm, but in the loading branch, the stiffness was constant until 250 kN was reached and then the stiffness changed. The abrupt changes of stiffness did not occur near the valleys of the load protocol. The divergent behaviour occurred in the middle of the loading branch.

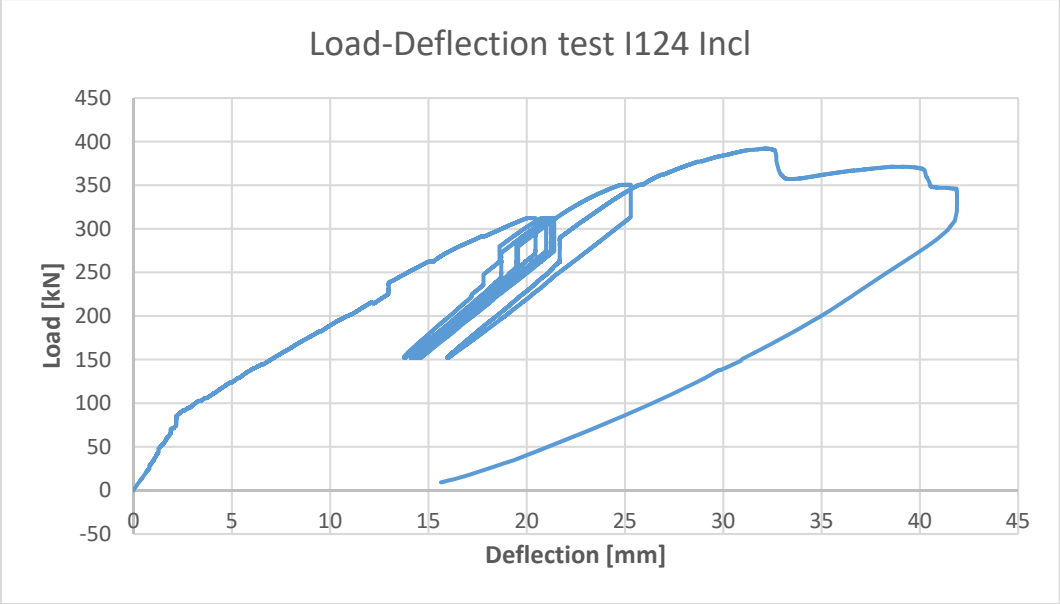

Figure 5.3-41 the test 124 Incl presented a mixture of the two behaviours

The degradation of the stiffness due to the cycling process generated an increase of the deflection after each cycle. This behaviour was observed in all the beams and for all the load levels. Figure 5.3-42 shows, for a beam with 180 mm, the evolution of the deflection at the frequent load level. The difference in the first cycle is bigger because the beam had not suffered previous damage. The fifth cycle reached the yielding load. Comparing this cycle with the sixth value of loading (post yielding load) showed clearly the degradation the beam suffered with an important increase of the deflection.

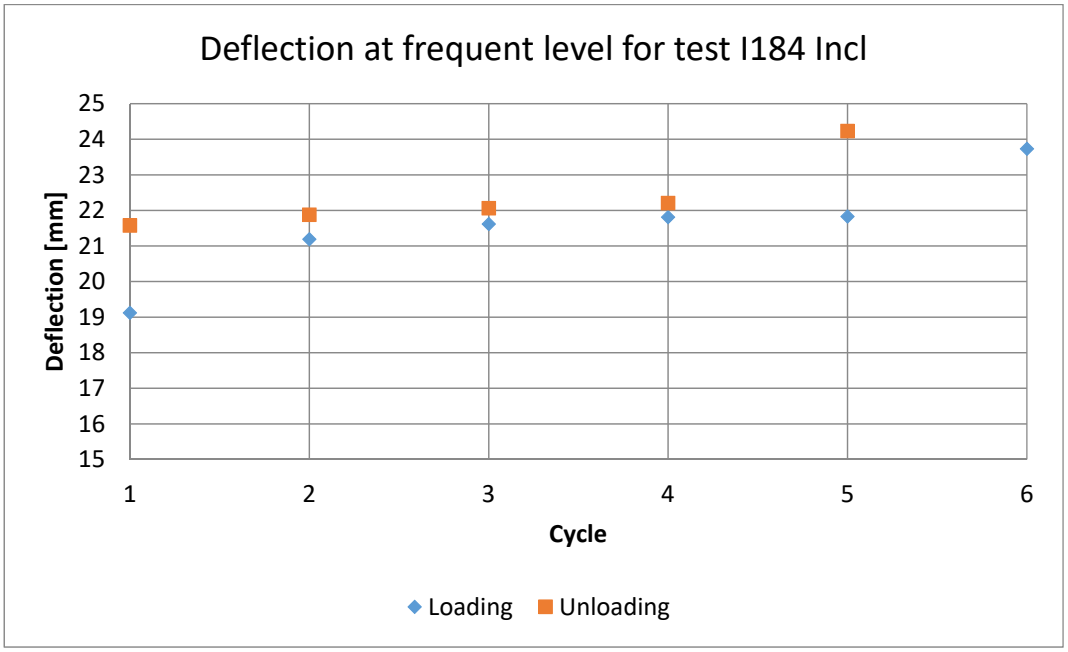

Figure 5.3-42 Evolution of the deflection for the first 4 serviceability cycles and the yielding load cycle

The beams, where the difference between the two branches was important (Figure 5.3-43), showed similar increases of deformation after each cycle than the previous cases, including the transition from cycle five to six. Even if during the cycles there was an important variation of stiffness, the global

behaviour was similar. For all the tests, the degradation due to repetitive cycles was very similar and generated an increase of deflection after each cycle.

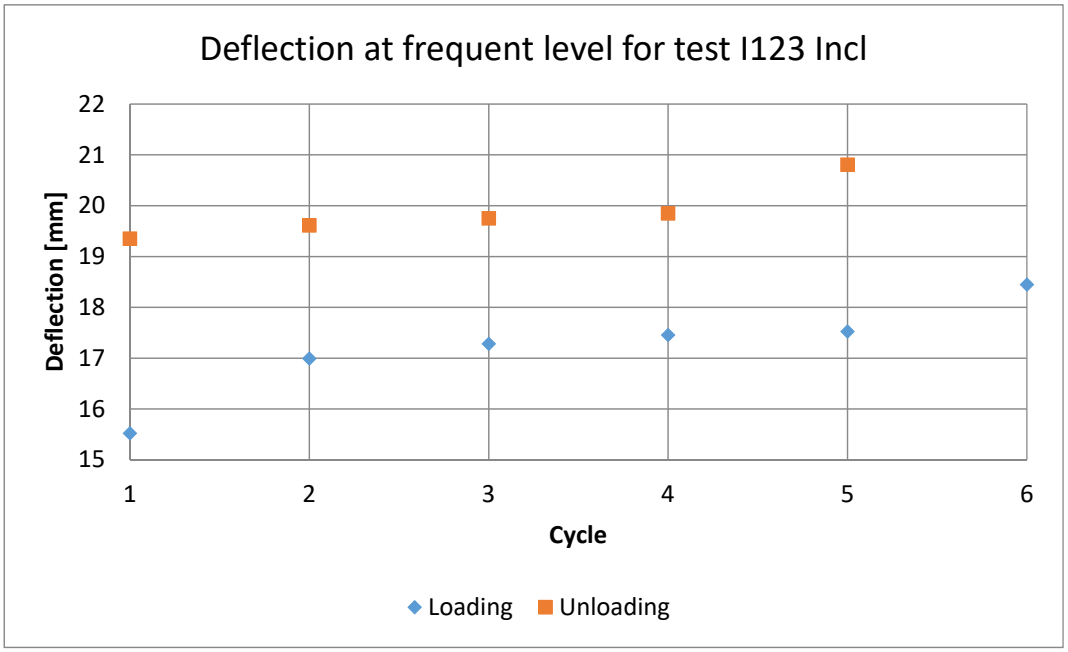

Figure 5.3-43 Important difference between the deflections in the loading and unloading branches

All the beams had an unloading branch with a loading speed half of the regular speed. Both speeds were slow enough for not to consider any dynamic effect. The different speeds did not generate any difference in the behaviour of the deflection of the beams. Neither the degeneration of the stiffness was affected by this loading speed change.

5.4 Final conclusions of the shear tests

This chapter analyses the shear behaviour of PPC through an experimental campaign, taking into account the influence of the stirrups, the prestress reinforcement and the web width. During this test, the strain and stresses in the reinforcement, the crack patterns at service and failure and the deflection of the beams was analysed. Moreover, the shear strength of the specimens was compared with several formulation, analysing the influence of each parameter on the formulations and the best formulation.

The comparison of the experimental shear resistance and the CCCM prediction showed a very good fit (Figure 5.4-1). The average of the ratio, experimental load over prediction, was 1.004, with a standard deviation of 5.62% and a COV of 5.63% (Table 5.2-4). The analysis of the failure modes established that half of the tests failed by the compressive chord. The rest had a web failure, even though the simulations did not foresaw it and the web resistance was from 1.5 to 2 times higher than the failure load.

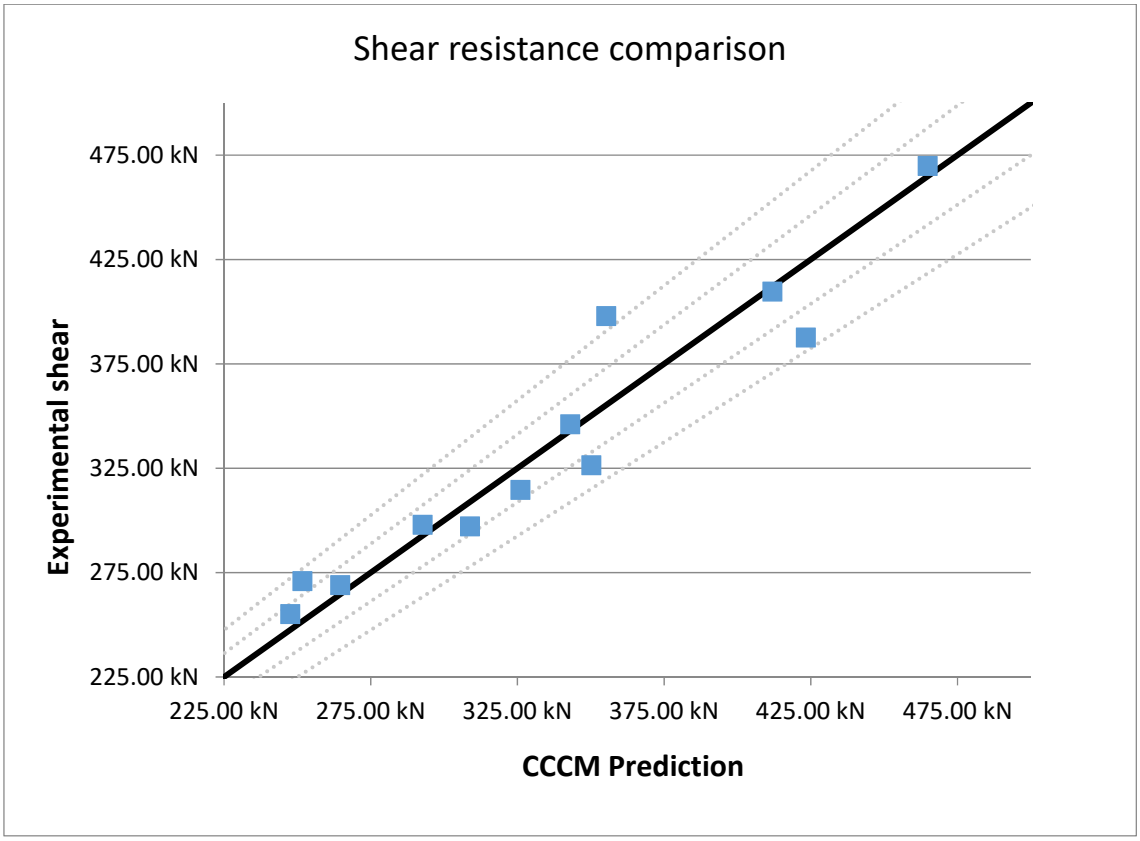

Figure 5.4-1 Comparison between the experimental failure load and the predictions of CCCM, with the +/-5% and 10%

The experimental results were also compared with other formulations, these formulations provided smaller shear resistances. The formulation that provided the biggest difference was the EC 2, then EHE 08 and finally the ACI 318-11 (Table 5.4-1 Statistical comparison between different formulations and the experimental results Table 5.4-1).

Table 5.4-1 Statistical comparison between different formulations and the experimental results

	EC 2	EHE 08	ACI 318-11	CCCM
Average	3.00	1.88	1.22	1.00
Stand Dev	63.0%	19.9%	9.5%	5.7%
COV	21.0%	10.6%	7.8%	5.7%
Max	4.18	2.27	1.33	1.12
Min	2.19	1.63	0.97	0.92
Percentile 5%	2.21	1.64	1.08	0.92

To compare the influence of the different parameters in the shear resistance, all the tests were normalized using the same concrete resistance (Figure 5.2-5). EC 2 does not take into account the concrete shear resistance, moreover the width of the web. EHE 08 takes into account the width of the web but underestimate the concrete resistance. The formulation only takes into account a third of the shear resistance obtained with the CCCM, due to the neglecting of the concrete in the flanges. The ACI 318-11 provides higher shear resistance, 72% respect the CCCM.

As it can be seen in Figure 5.4-2, there is a trend in the behaviour of the ACI. It provides better results for tests with smaller amount of prestress and with smaller amount of transversal reinforcements.

When the Incl tests were compared, the tests with 180 mm of web width also showed better results than the 120mm web thickness. The 180 tests had smaller stresses in the concrete due to the prestress since their concrete area was bigger. The CCCM is the only formulation that assumes a smaller shear resistance for the flat layouts.

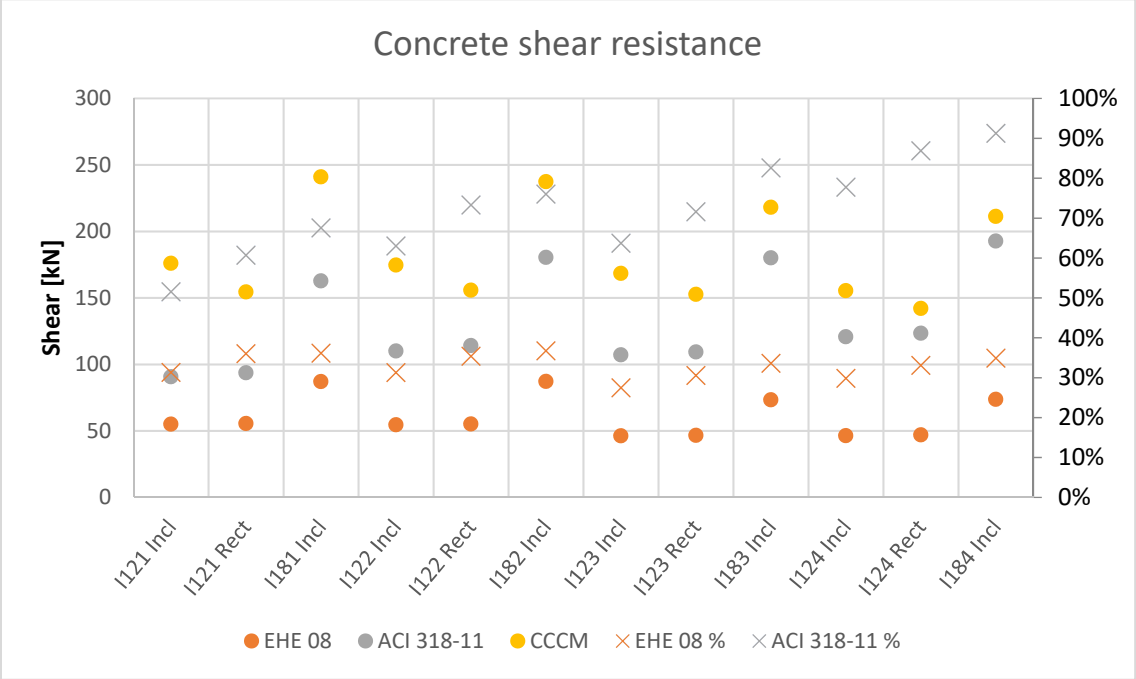

Figure 5.4-2 Relationship of concrete shear resistance between formulations.

The ductility of the shear tests was inferior to the four-point tests. The average ductility for all the tests was 1.63, the tests with 120mm of web with had an average ductility of 1.67 and the 180mm web with of 1.55. The tests with 180mm web width had very small increase of deflection post peak. The failure of the beams was very brittle.

The $\cot\theta$ of the shear cracks angle at maximum load was between 2 and 2.5. A linear relationship between the $\cot\theta$, the stress ratio (SR, Equation 5.2-1) and the transversal reinforcement (ρ_{st}) was established. The $\cot\theta$ increases with the SR but decreases with the ρ_{st}(Figure 5.2-13). The variation is more important for the ρ_{st} CCCM underestimates the $\cot\theta$ in 10%.

At the beginning of the test, cracks appeared on the concrete, mainly in the web and with diagonal direction. In service, the angle of the cracks did not change (Figure 5.3-3). Even if the cracks were different in each test, some patterns were observed. The main pattern was that the spacing between cracks was not constant. It was not the same between two pairs of cracks nor between two cracks at different heights. The form of the cracks also repeated. The cracks started on the bottom of the web with angles over 45º. The cracks developed form both ends. On the joint of the web-flange, the cracks were horizontal. On the middle high of the web, the angle of the cracks decrease under 45º (Figure 5.3-2).

The angle of the cracks was constant during service and established after the fist-loading ramp. The $\cot\theta$ for all the test was between 1.5 and 2.4. In service both parameters, SR and ρ_{st}, had the same influence on the angle of the cracks. The behaviour is the same as in failure but the influence of the parameters is higher. In the case of the SR, the influence has doubled.

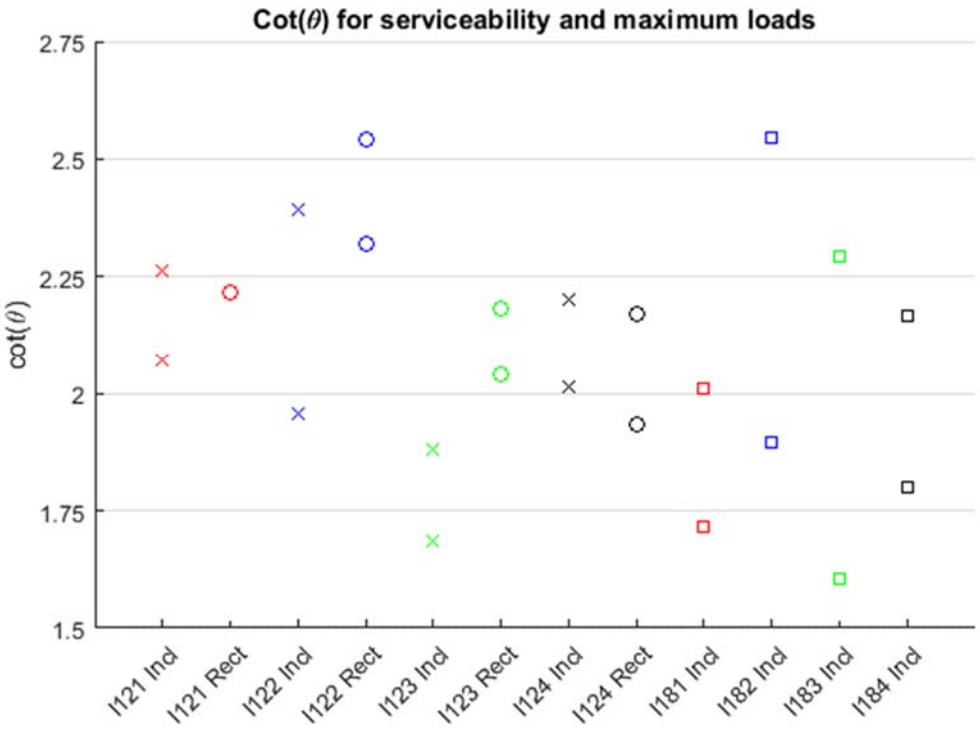

Figure 5.4-3 Comparison of the cotangent in serviceability and under the maximum load

The value of $\cot\theta$ reached its maximum value at the end of the test. Figure 5.4-3 shows the average $\cot\theta$ during service loads and the $\cot\theta$ under the maximum load reached by the beam (merging Figure 5.2-10 and Figure 5.3-5). The average increase of $\cot\theta$ was 17.8%. The beams of the test 120 Rect had an increase of 9.6%, the 120 Incl 13.2% and the tests with a web width of 180mm reached an increase of 28.8%.

Like the angle of the cracks, the spacing between cracks was established during the first loading ramp and remained constant during service. In the final stages of the tests, the spacing decreased. The average distance between cracks in service was between 60 and 80 mm. When the top 5% of the spacing was taken into account, the range went from 100 to 250mm. In this case, the test with higher stirrup spacing had bigger crack spacing. Moreover, the tests with stirrup spacing of 150mm had maximum crack spacing under 150mm.

When the horizontal spacing was analysed, the same conclusion was obtained. The horizontal spacing was always under the stirrups spacing. For the beams with stirrups every 150mm, the spacing was between 120 and 150. The beams with 250mm between stirrups had a spacing between 130 and 180mm.

Unlike longitudinal reinforcement, the strains reached by the stirrups were very important and in several cases too big to be recorded by the strain gauges. 83% of the strain gauges registered yielding strains, 40% during the first loading ramp. The ratio of strain gauges that failed during the test was 40%. Important differences were observed from the three strain gauges in each stirrup. The strain increase was very localized. The increase of strain could affect only one of the strain gauges of a stirrup (Figure 5.3-18). In many cases one of the parts yielded, increasing the strain of the strain gauge to its limit and failing.

Due to the different situations inside a single stirrup, and the important strains observed in the stirrups, the cycles produced different effects on the stirrups. In some cases the cycling effect increase the strain and stress in the stirrup. However, when the yielding stresses had already being reached, the stresses decreased even if the strains increased. In some cases almost compressing the stirrups (Figure 5.3-20). The concentration of strains could produce strain peaks that lead to yielded situations.

The software developed for this dissertation (Chapter 0), allowed to compare the crack width from different pictures. In service, the beams with lower amount of stirrups had higher shear crack width and the beams with higher prestressing stress had higher shear crack width. The stirrups absorb the tensile stresses, therefore higher amount of stirrups reduce the strains and crack width. Meanwhile, the prestressing reinforcements establish the angle of the tensile field. Lower prestress lead to steeper angles therefore a higher contribution of the stirrups. Higher prestress produce flatter angles hence less contribution of the stirrups and the shear stresses have to be resisted by other mechanisms (such as tension stiffening.

It was also observed, when comparing the cracks width in the valleys and peaks (Figure 5.3-29), that the crack width size and the range of it was independent of the shear load. While, the size of the cracks determined the range between peak and valley crack width.

In most of the tests, the cycling process did not produce new cracks to redistribute the strain, so the repetition of the cycles increased the size of the cracks. In the cases were the increase of crack width is not equal for peak and valley, the peak crack widths increase always more than the valley crack width.

For these tests, the maximum crack width was in average 7.0 times bigger than the average crack width with a standard deviation of 3.44. In each test, the ratio between maximum crack width and average crack was constant.

A new model to predict the average shear crack width in service was presented. This model uses the deformation of the stirrups to calculate the crack width (Equation 5.3-4). This model was compared with the experimentally observed crack width (β) and a statistical analysis was performed. The average β taking into account all the service pictures is 1.33 and the β representing the percentile 90% is 2.86. When the valleys are taken out, the average β is 1.22 with a 90% percentile of 2.45.

The deflections observed during the cycles showed different stiffness on each branch. These differences generated an area inside the deflection curve. These areas were smaller in I180 tests, with an average difference between deflections of 1.2 versus a difference of 2.0 for the rest of the tests. In all the cases, the deflection of the beam increased after each iteration. No relationship was observed between the range of deflection of the cycles and the increase of deflection after each cycle.

6 Photogrammetry

6.1 Introduction

The main goal of an experimental campaign is to obtain the real response of the tested specimens. The response can be a wide range of parameters but, in all the cases, a sensor has to be used to obtain the value of the parameter. The gathering of this information is a necessary part of the experimentation. In civil engineering, and in the study of concrete beams, the main parameters are obtained with sensors that are placed on the surface of the beam or inside of it; such as load cells, strain gauges or displacement transducers. All these sensors are widely used and verified in the past.

These sensors are basically divided in two categories:

-The first category contains the sensors of 1-point. These sensors are placed in a specific location of the beam and provide information about that point. They do not provide direct information about any other point of the specimen. Most of the sensors used are in this category, load cells, pressure transducers or strain gauges.

-The sensors of the second category are 2-point sensors. This kind of sensors will provide the relative information about their two ends. These sensors are used to obtain relative displacement inside a beam or the deflection of the beams. Using the variation of the distance between the ends and the initial spacing, they can also be used to determine the average strain between the two ends. The sensors only record the variation of the distance between the two ends, regardless of the direction.

All these sensors provide an accurate measure at their specific location. To control events with uncertain location, the usual solution is to place several sensors trying to hit the correct position. In the case of crack width, the sensors will have to be placed over the crack and in the correct angle, otherwise the information provided by the sensors would be useless. Taking into account the economical limitations in research, the amount of sensors that can be used is limited so its use would be inefficient and could imply the loss of important information.

In the case of the shear tests conducted in this research, the shear crack opening is a very important information. Shear crack patterns are very hard to predict, so it is impossible to place the sensors on the optimum location and direction before, damage appears, to be able to read the opening of the

cracks. One the other hand, placing the sensors after damage initiates introduces safety issues and the information prior to the initial damage cannot be captured.

One possible solution to this problem is found on novel photogrammetry techniques. Photogrammetry is a contactless technique that analyses the pixels of an image and allows to obtain the displacement or measurements of parts of the image. All the surface captured in the photograph could be used to obtain information, allowing a less precise knowledge of where and how the cracks are going to appear.

Since the analysis is based on the pixels, the resolution and the scale of the image will determine the precision of this method. After performing the test, the images are processed with specific software. These programmes can generate a wide range of information from crack location to displacements field. They can focus on the behaviour of a unique picture or analyse the evolution of a set of pictures.

These methods will gather information of a region of the specimen, not only from one or two points. This would allow a wider range of scouting and reduce the amount of useless observations. Through the analysis of the images, a lot of information about the cracks can be obtained, as the position, the angle, the spacing and the width. Each picture is analysed independently and will provide information about the state of the specimen, without the need of previous knowledge.

6.2 Digital Image Correlation

Digital Image Correlation (DIC) is a photogrammetric technique developed during the seventies. It was not used in civil engineering until lately (Tung, Shih and Sung, 2008; Pan *et al.*, 2009; McCormick and Lord, 2010). This technique will provide the displacement and strain field of every point of an image. DIC compares a reference picture (usually the initial picture of a test) with the following pictures and find the displacements of the different parts of the image. This technique has been implemented in several software (Jones, 2015; GOM, 2019).

To correlate the reference image into the rest of the images, the surface of the specimen has to be painted. To uniform the surface and help the software, the surface is initially painted in white. Then a dark speckled pattern is painted (Figure 6.2-1). This pattern is going to be the target of the correlation. The test has to be under a constant illumination, any variation could be inferred as a variation of the surface.

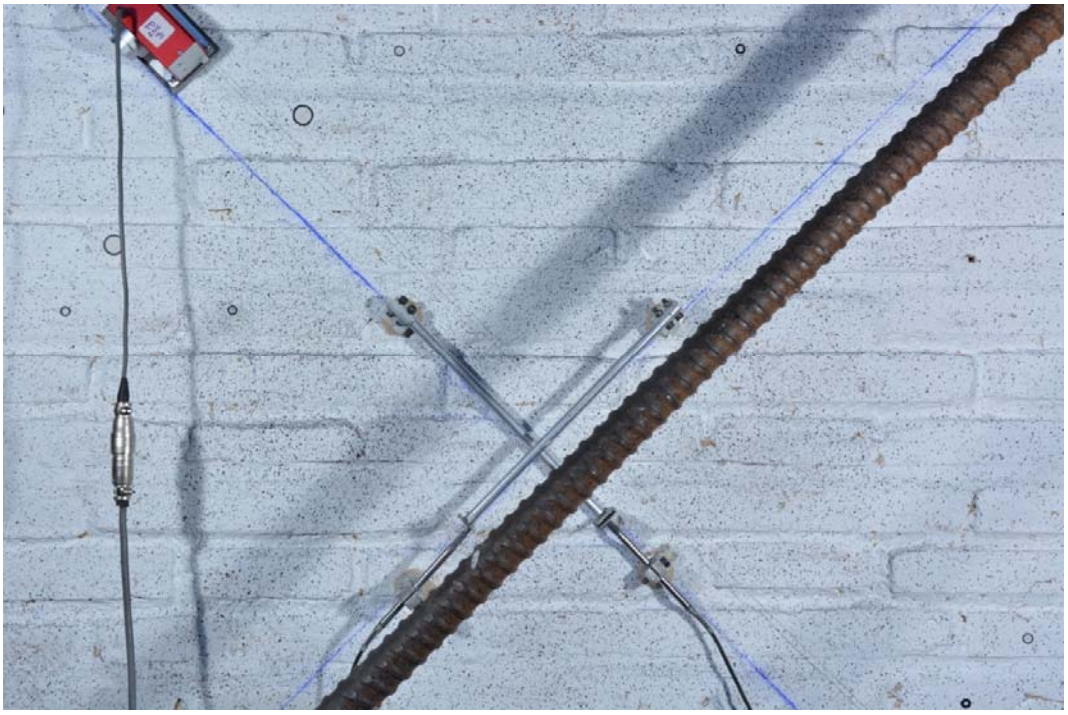

Figure 6.2-1 Surface of masonry wall with speckled pattern (courtesy of García Ramonda)

The reference photograph has to be taken at the beginning of the test in a load free state. As many pictures can be taken to analyse the behaviour of the specimen, the software will generate a web over the reference picture. In each node of the web, a subset of the reference picture will be selected. The program will look for this subset on all the following images. Since the pattern is random, there is only one match for each subset in the pictures.

In each picture, the subsets from the reference image are found. The position of the subsets can be different. The difference between the centres of the subsets from the reference picture to the analysed pictures will determine the displacement field. With the difference between displacements the strain field is obtained. This method provides the displacement and strain field of a series of images(Figure 6.2-2).

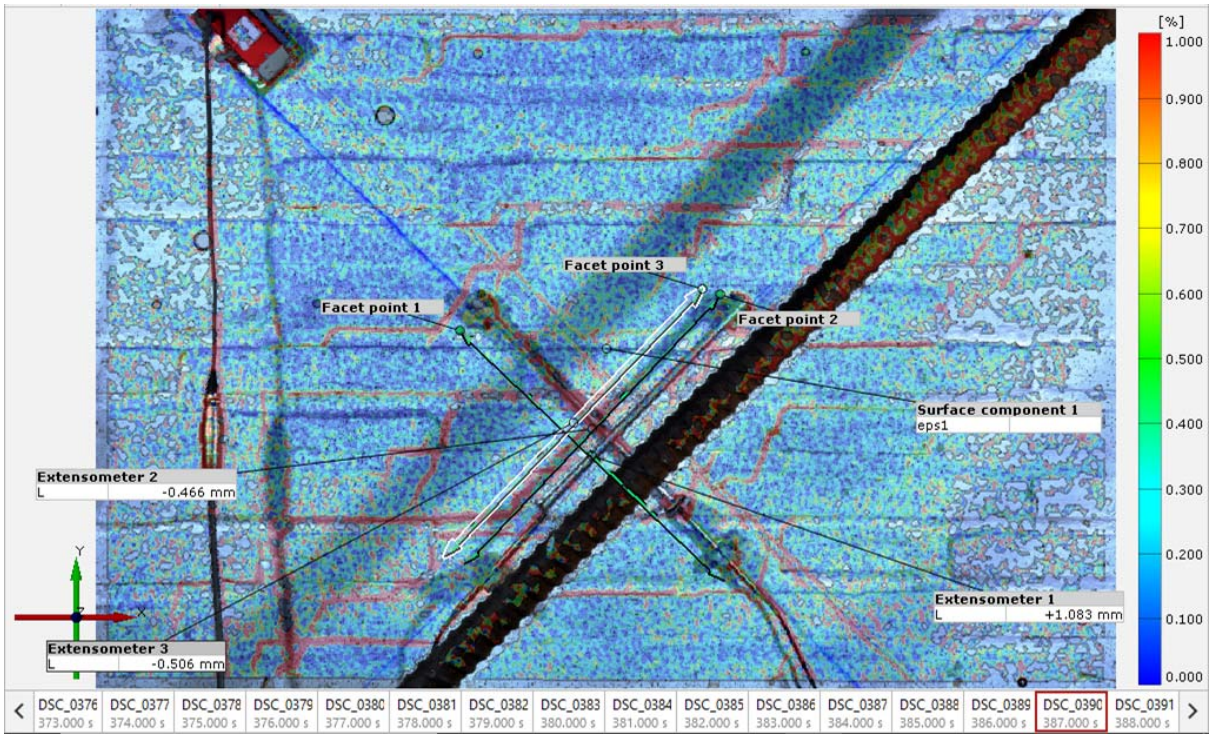

Figure 6.2-2 DIC analysis using GOM performed in a masonry wall (courtesy of García Ramonda)

The distance between the nodes will determine the density of points where the displacement field is calculated. The size of the subset will determine the accuracy of the method and the spatial resolution. To increase the resolution of DIC, "subpixel" interpolation is commonly used. This technique would determine the position of the subsets interpolation the intensity of the pixels. This approach allows obtaining movements to a finer resolution than the resolution of the original image.

At the beginning of this experimental campaign, a photogrammetric software was being developed by the members of our department (Sanchez, 2017). This software was specifically design to locate and analyse cracks. Therefore, DIC was not used in this campaign.

6.3 Methodology

The technique developed in this Thesis analyses the pictures of specimens to study the crack pattern and its evolution. From each picture, the program obtains the following parameters: crack width, angle and spacing of the cracks. Afterwards, the evolution of these parameters can be analysed. This technique requires an adequate set up of all the involved equipment (camera, lights, labelling…). During the test, pictures should be taken with a certain frequency or alternately at the relevant steps of the test. Finally, after the test, the pictures are analysed by the software to obtain the cracks and its characteristics.

The first step is to establish the area of the sample that wants to be photographed. This depends on the type of process that wants to be analysed and the amount of information to be collected. Since the information that cameras can capture (via number of pixels) is limited, the size of the area of interest is inversely related to the precision that could be obtained by this process.

The camera has to capture all the region of interest (ROI). The movements of the ROI (such as deflection) have to be taken into account. The camera has to be placed in a parallel plane to the sample. If this condition is not satisfied, the image is going to be out of proportions. The area has to be adequately illuminated. The quality of the light can modify significantly the results of the analysis. It is recommended to use steady illumination, hence direct current lamps should be use when possible. One should avoid at all-time sun light or lights that could be affected by moving objects that create shadows during the tests.

The last parameter of the camera is the shooting frequency. It was observed that the best method to record the tests is to set an automatic shooting timer. This technique has two important benefits. The first one, and more important, is that ones the camera has been placed, no interaction with it is needed, it is not going to move during the whole test. Neither on shooting (blurry images) nor changing the position of the camera with respect the specimen. The second one is that setting a timer will allow a simpler and efficient analyse of the results and assure no data is lost by a missing shoot. The problems with this technique is that if the test is too long the camera can run out of battery or if the frequency is too low some relevant moments can be missing.

Once all these steps have been completed, and before starting the test, a picture of the sample has to be taken with the presence of a ruler or scale. This scale has to be placed in the same plane that is going to be further analysed. If several areas had to be analysed, a reference for each ROI is needed.

To allow the software to follow the ROI over several images with important displacement a reference has to be added to the specimen. At least 4 points have to be clearly identified on the specimen. These points will function as trackers for the programme. A scatter distribution will improve the results of the analysis.

During the test, it is mandatory to make direct measurement of some crack widths. This will allow the programme to obtain the crack width of all the cracks. The programme compares the measures of the cracks in the images with the real information using the scale and some real measurements.

If during the test, the camera suffers any movement, all the previous steps had to be repeated to ensure the programme will have all the required information. Even if it is preferable to obtain all the information form one position, changing the position of the camera to focus in new information or in another ROI can be done, gathering again all the information about scale and crack width.

The first step in the software is to define witch part of the image is relevant (ROI). In the first picture of the analysis, a ROI has to be defined. Next the trackers have to be identified so the programme can search for them in the all the pictures too and automatically define the region of interest for all the pictures.

After the definition of the ROI and the trackers, the programme will transform all the pictures to b/w and run several subroutines that will identify the edges in the pictures and establish several threshold to eliminate edges that are not cracks. Finally, the user will check if all the pixels selected can be cracks. In case of discrepancies, the user can add or remove some pixels.

At this point, the software will group the pixels in cracks. It will group the pixels by proximity. In the case the groups are too big, it will split them to obtain smaller groups where the pixels are aligned. The pixels are now grouped in cracks of similar size and angle. The next step is to obtain the spacing

between the cracks. The programme performs several crack spacing calculations, like the horizontal spacing, the vertical spacing and some others.

For each crack the software will compute the crack width in three positions, at the ends and in the centre of the crack. The programme will calculate the crack width in the vertical and horizontal direction and then project them in the perpendicular direction of the crack. This is to improve the accuracy of the process. The measurements performed during the test are used in this part of the process to parametrize a curve that relates the crack width whit the darkness of the pixels.

The last part of the programme allows the visualization of all the information that has been computed. When the time and the load of the photos are added to the software, plots of the crack width evolution can be displayed. Maps of the crack pattern can also be displayed with specific information about, crack spacing, crack width or the angle of the cracks.

6.4 Programme

Once the area of interest is determined, the first part of the programme starts. Using the software developed in the thesis (Sanchez, 2017), the pictures are transformed to a black and white image and using edge detection, the pixels that belong to a crack are obtained. The edge detection process is very sensitive to light changes and intensities and do not provide accurate results for very big cracks, over several millimetres.

This programme was developed to analyse individually the images of a set of pictures, changing the light parameters to filter the cracks. To perform the crack detection of a large number of pictures, this approach was not effective, and an average set of parameters was used for each test. Therefore the precision of the crack detection was not satisfactory.

A new programme was developed form the software (Sanchez, 2017). The new programme uses the crack detection performed by (Sanchez, 2017) as an input to detect the cracks. The miss recognized cracks are erased and the non-recognized are added to the ones previously selected by the software. When all the cracks are correctly identified, a matrix of pixels represent the cracks of the picture.

The next part of the process groups the pixels in clusters. The programme checks for every founded pixel if there are other pixels of the list near it. When all the clusters are defined, it checks the number of elements in each group. If the amount of pixels does not overcome a certain threshold, it discards the group. The threshold depends on the scale of the picture and its goal is to erase too small groups that do not represent real cracks, like small imperfections on the surface of the specimen.

Once the groups contain a reduced amount of pixels, the programme checks the dispersion of the pixels. Since the angle of the cracks can vary between horizontal to vertical, a modified coefficient of determination (Equation 2.3-3) had to be implemented. The classical coefficient of determination (R2) is close to 0 for straight lines close to the horizontal or vertical direction. The modified method ($R2^*$) takes into account that the variance of these directions tent to.0 and uses the two directions to perform the analysis.

$$nDiv = \sum_i (Y_i - \bar{Y})^2 + \sum_i (X_i - \bar{X})^2 \quad 6.4\text{-}1$$

$$R2^* = 1 - \frac{\sum_i (Y_i - f_i)^2}{nDiv} \quad 6.4\text{-}2$$

This part of the code was designed to control the shape of the pixel groups. If the coefficient is too low, it means that the group of pixels does not have a linear shape. Normally representing small holes or imperfections on the concrete. On the other hand, for results too close to 1, the pixels shape is exactly a straight line. These results tend to be shadows on the image, instrumentation or lines drawn on the concrete. All this groups are erased, and these pixels are no longer considered for future analyses.

From this point on, all the pixels included in these groups are considered pixels belonging to a crack. Having groups of similar size improve the analyses. Therefore, the program looks to have groups that are not too big and where the shape is similar to a line. Initially the programme evaluates the distance between the two more distant pixels and if the distance exceed a threshold, the group is divided accordingly. With the correlation coefficient, the programme evaluates the shape of each group. When the shape of the group is too different from a line, the group is divided into sub groups that have better correlation.

After dividing the pixels in groups of a more regular size and with similar angle, the model establishes all the properties for the crack. Up to that moment, the properties are the number of pixels, their position, the length of the crack, and its angle. With the position and the angle, the model derives the crack spacing.

The programme computes the distance between cracks in several directions: horizontal, vertical, perpendicular, averaged, and two projected distances. It draws a line on the image starting from a point of the crack and find the first crack that is intersected by the line. The distance between the initial point and the intersection will be the spacing. The angle of the line will depend on the direction in which it is calculating the distance. The averaged distance uses the average angle of the cracks in the picture to draw the line. All the crack spacing are computed with the same angle.

For the two projected distances, the model uses distances previously calculated. The first projection uses the horizontal and vertical distance and projects them over the crack angle. The last projection calculates the horizontal distance between the two cracks but uses the mean angle between the two cracks to calculate the distance.

Since the angles of the cracks are different, some of these methods produce different crack spacing for two cracks that are side by side. The averaged and the second projected distance were created to obtain a distance that took the orientation into account without generating different spacing.

The calculation of the crack width is the last step performed by the program and has been by large the most complicated part to solve. At this point, the location and direction of the cracks have been determined. The problem lies in finding the exact position of the limits of the cracks, the lips of the crack.

6.4.1 Crack width

Initially, the software used the calculations done by the program developed in (Sanchez, 2017). This program analyses the pixels that are perpendicular to the crack. The pixels that represent concrete are brighter opposed to the pixels, placed inside the cracks, which are darker. The width of a crack is the distance between the light pixels. This system did not performed well in the tests and photographs of this thesis. The results were not reflecting changes on the cracks and the range of crack width was too small. A deeper analysis showed that these problems were not originated by the method but by the information obtained from the pictures.

The pictures were taken with a camera Nikon 5200 with a resolution of 6000x4000 pixels. This camera takes pictures using 24000000 sensors that do not record colour but light intensity. In front of the sensors a colour filter array (CFA) is placed, so each sensor only absorbs one of the three colours: Red, Green or Blue (Figure 6.4-1).

Figure 6.4-1 Sensor distribution in RGB configuration

The rawest information that can be obtained from this camera is a matrix 6000x4000 with a single number in each cell. This number is a related to an intensity of light for a specific colour. With this data, the camera or a program can apply a demosaicing algorithm (a colour reconstruction process) to present the image as a triple matrix of 6000x4000 elements were each cell of each matrix represents the amount of red, green and blue, that the pixels have to show, respectively.

This process consists in obtaining the three colours for each pixel. One of the colours come from the information provided by the sensor. The other two colours are obtained interpolating the values of that colour from the adjacent sensors. This method generates softening on the edges. The images do not have sharp edges.

If a band of sensors has half of its sensors hit by a white light and the other half by no light, the initial information store in the raw matrix will be 100% of the colour of the sensor and 0% of the colour respectively (Figure 6.4-2). When the process of colour reconstruction generates the colours on the bright side of the band, since all the sensors have 100% of their colour, the final colour will be white. On the dark side, the same process will occur and the final colour will be black. When the demosaicing reconstructs the colours of the boundary, it uses sensors from both sides, it mixes the two intensities blurring the edges (Figure 6.4-3).

Figure 6.4-2 Band of sensors half illuminated

Figure 6.4-3 Final colors after demosaicing, with the pixels of the edge in a grayscale

Demosaicing is a complex process that involves the information of several sensors to obtain the 3 colours of a pixel. To be able to compare the pixels in an easy way, the images were converted to black and white after performing the demosaicing. The triple matrix is turned in to a single matrix of scalars from 0 to 255. Where 0 represents the pixels lacking any light exposure, meaning they are black, and 255 the maximum light exposure, meaning they are white.

It was observed that after demosaicing and converting the image to b/w, two pixels side by side that should have shown the same light intensity (LI), could show important differences. The pattern of these pixels was very similar to the position of R or B sensors. The final conclusion was that, if the LI of the R or B sensors was very different from the G sensors, the demosaicing would generate oscillating LI, that could be perceived on the final b/w image. It can be seen Figure 6.4-1 that each row or column contains always G sensors, but they only contain R or B sensors. Therefore, when the programme had to analyse a column or row of pixels, it will take into account this LI oscillation and avoid it, changing the column or row.

On the original software, from (Sanchez, 2017),the crack width was calculated using the pixels perpendicular to the crack. Since the matrix is a discrete grid, a “line” of pixels was selected. For this thesis, that method is not appropriate. The level of zoom applied in the calculations is important, therefore the same pixels are used to calculate different angles and the distance between the centre of the pixels is different and is not taken into account.

Adding to this issues the fact that the software only uses one every two rows and columns, making impossible a proper “line”. Therefore the new programme calculates the width of the cracks in the vertical and horizontal direction and projects the width in the perpendicular direction of the crack. In extreme cases where the angle is close to the vertical or the horizontal direction, the program automatically dismisses the non-perpendicular direction.

The next figures present the values of the LI of a row of simulated pixels. They show different cracks using the raw data of the sensors or after interpolating the information. There are three situations: no-crack (blue), a crack with low LI (orange) and a crack medium LI (grey). The Figure 6.4-4 shows the raw data that would have been obtained by the sensors. The background of the image presents an oscillation due to the imperfection of the material that generates shadows. The two cracks are clearly different, the first crack has been detected by only one pixel and the variation of LI is important. On the other hand, the second crack is represented by two pixels but the variation of LI is small.

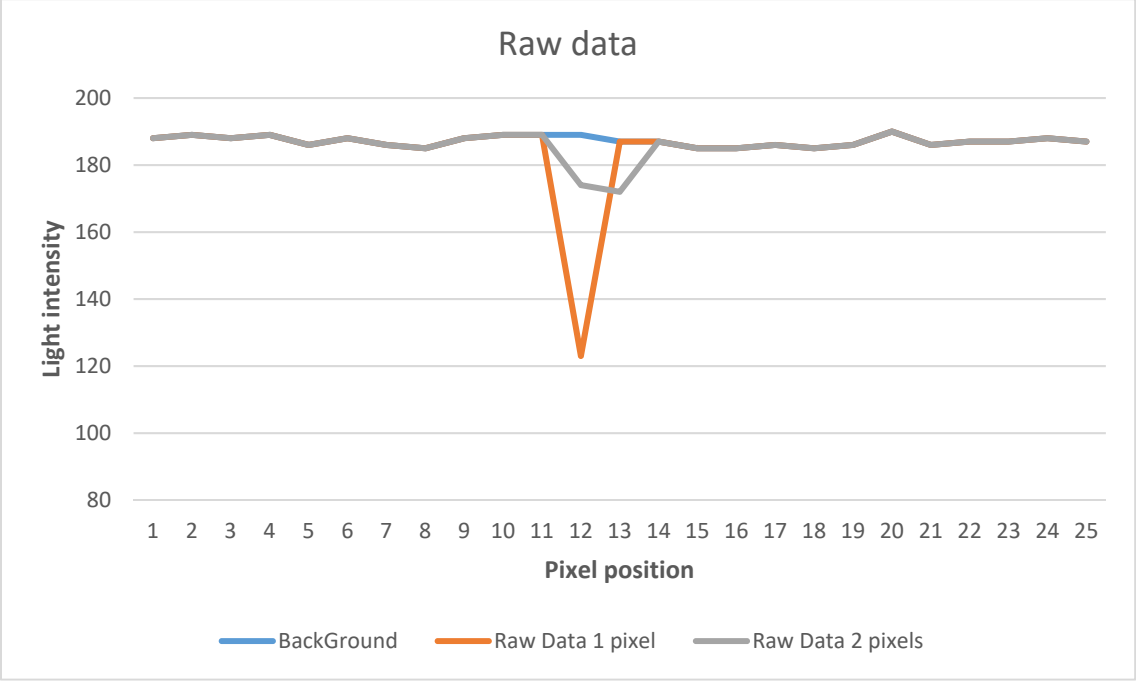

Figure 6.4-4 Raw color intensity

Figure 6.4-5 shows the same cracks after applying a demosaicing process to the three situations. The background is more homogeneous, and the edges of the cracks have dissipated, the two cracks have grown a pixel in each side and the variation of LI is smaller. The LI of the first crack has increased significantly but it maintains a clear valley shape. The second crack has almost the same LI but the sides of the valley are less clear. In real cases, the exact size of the valley can be complicated to obtain from the LI plots. Due to fluctuations of the back ground, small variations on the cracks or because the edges of the cracks are unclear, a better way to detect the sides of the valley needed to be implemented.

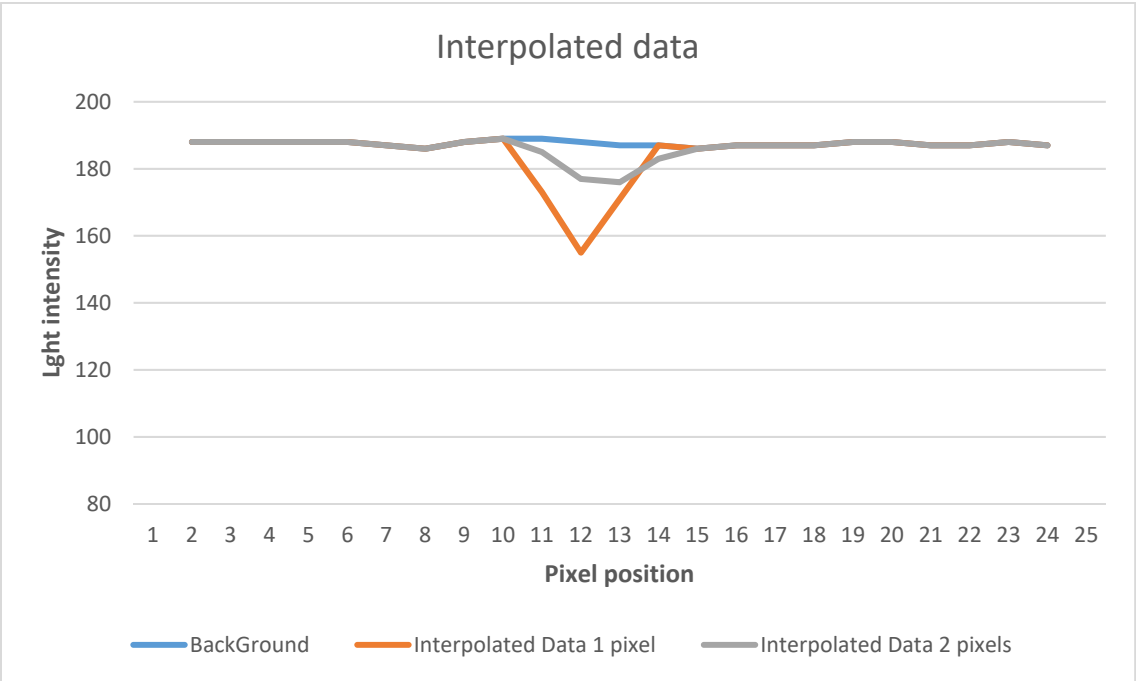

Figure 6.4-5 Interpoled data

Computing the LI gradient, by means of central differences, to the curves, the background and the sides of the valley appear clearly. Figure 6.4-6 shows for both curves the same pattern. The background part is stable near to 0. The peaks (maximum and minimum) of the differences are placed in the sides of the valley. This method simplifies the location of the edges and can be used independently of the mean value of the background, since it only cares about the variation of the LI.

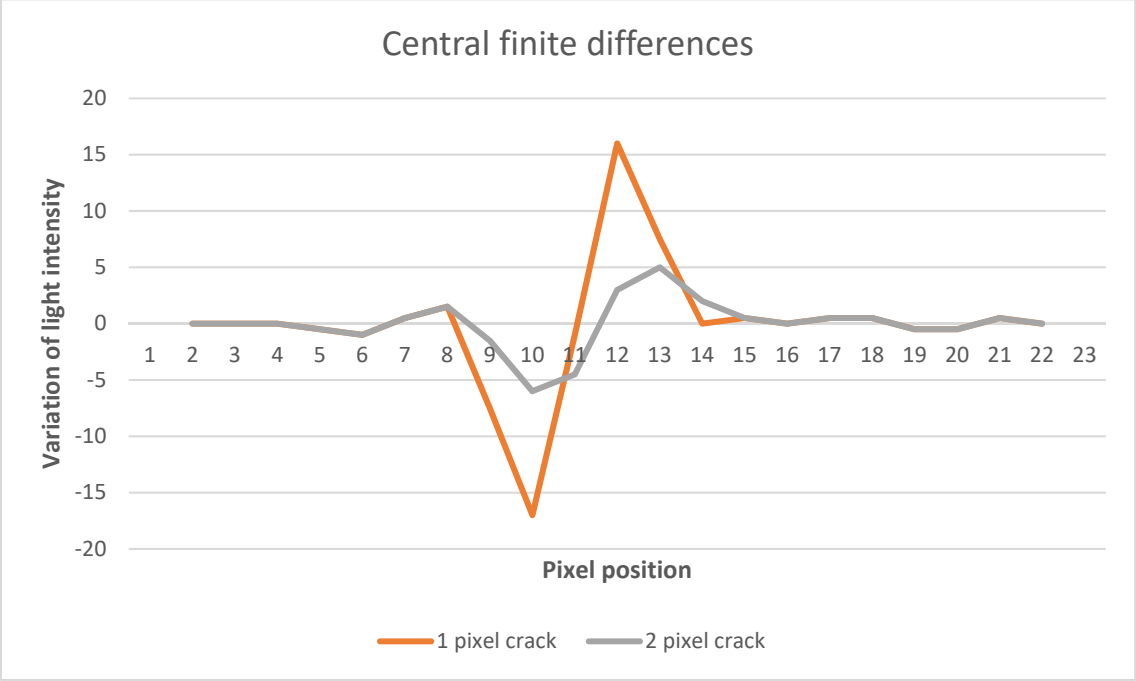

Figure 6.4-6 Central differences applied to the demosaicing data to found the edges

Since the real data was not perfectly homogenous, the following verifications had to be done: a) check that the minimum point of the valley was between the two peaks of the central differences, b) check that the difference between the maximum and the minimum of the LI curve was bigger than a threshold. If the first request was not achieved, the program could check for the next peaks on the central differences or check for the minimum between the two peaks. This decision depend on the distance between the new points or the LI amplitude. If the difference between the LI of the edges and the bottom of the crack was inferior to a threshold, the crack was dismissed and its width was reduced to zero. This threshold was different for each picture and was automatically computed with the contrast of the image and the average LI of the background.

As it has been observed with the gradient distribution, the edge of the valley can be easily spotted. The software will find, starting from the peaks and to the outside, the first position where the sign of the gradient changes. These positions are the background limits and the beginning of the valley (see Figure 6.4-7).

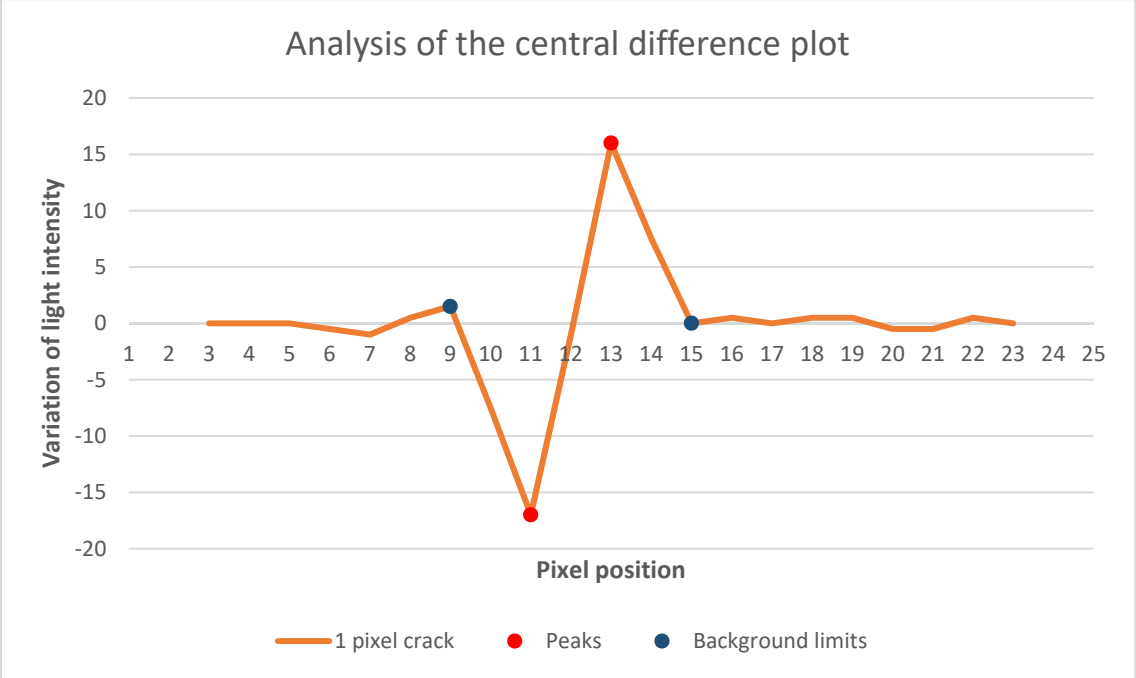

Figure 6.4-7 Points of interest in the central difference analysis

In order to take into account the variations of the background, the programme calculates the LI standard deviation and subtracts it to the LI of the limits. With this new values of LI, the programme computes the definitive limits of the valley by intersecting the values with the curve. Figure 6.4-8 and Figure 6.4-9 show the final curves, the theoretical limits of the background and the new limitation of the valley. This iteration on the computation of the edges of the valley was made to take into account the cases where the background has important oscillations and the edges of the valley were usually misinterpreted by the software.

At this point, the software was able to determine the size all the valleys with high accuracy but when the widths of the valleys were transformed in crack widths the results did not make any sense. The comparison between different sets of photos was impossible. The range between the different cracks was too small. In other words, the size of the valley was not the only parameter to know the size of the cracks.

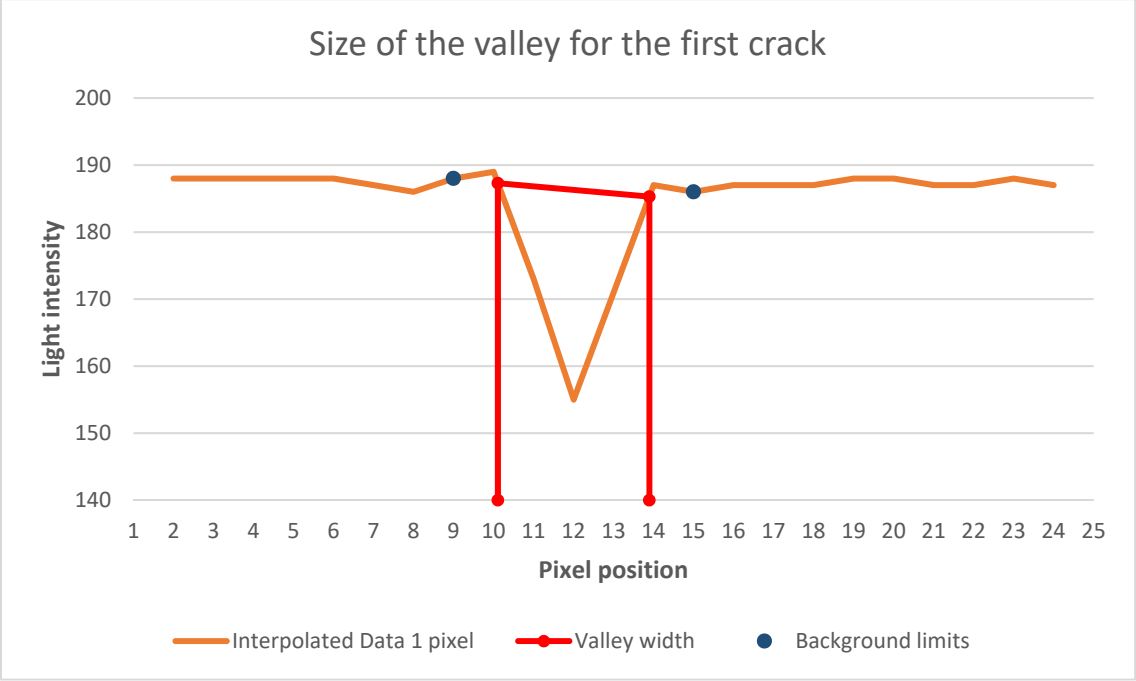

Figure 6.4-8 Final width of the valley reducing the noise of the background: 3.79 pix

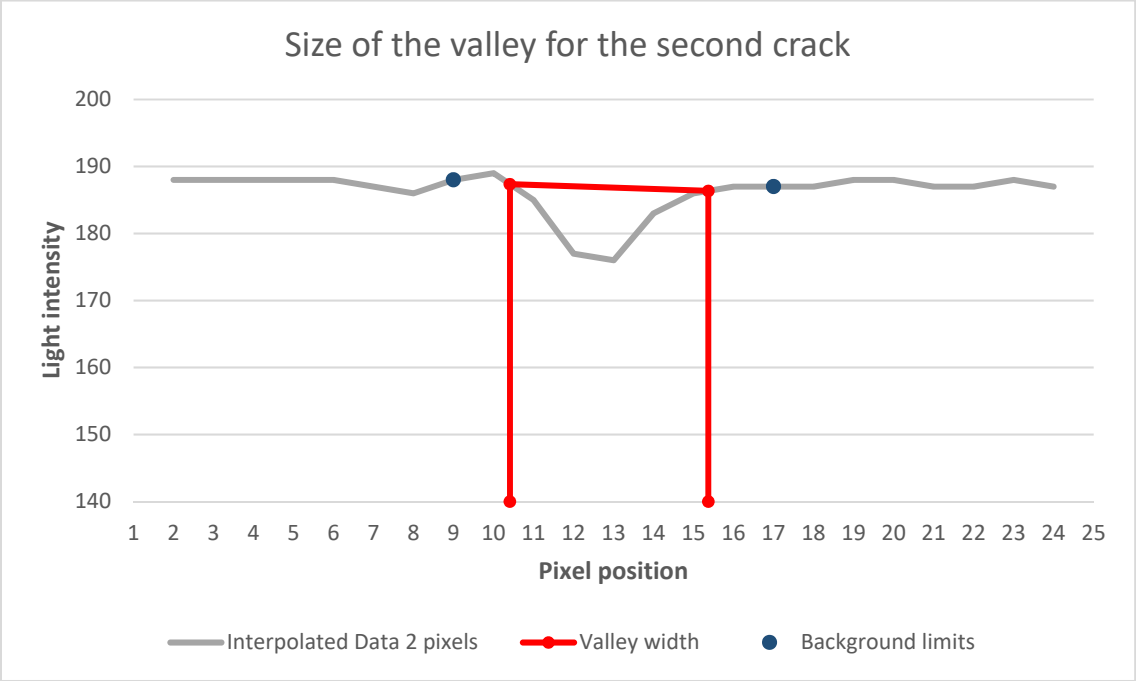

Figure 6.4-9 Final width of the valley reducing the noise of the background: 4.96 pix

After analysing small and medium cracks, it was observed that the size of their valleys was very similar but the difference between the LI was important and kept a pattern. The size of the cracks and their darkness were related. The more difference between the LI of the inside of the crack and the background ($MaxDif$), the more likely the crack was bigger. When this criterion was put together with the calculation of the valley width ($v\omega$), a reliable way to calculate the crack width (ω) was possible (Equation 6.4-3).

$$\omega = v\omega \cdot \beta_{\omega LI} \qquad 6.4\text{-}3$$

$$\beta_{\omega LI} = \left(1 + e^{-a\left(\frac{MaxDif}{\sigma Dif} - nLo\right)}\right)^{-1} \qquad 6.4\text{-}4$$

$\beta_{\omega LI}$ acts as a confidence factor. It is used to reduce the width of the valley if the $MaxDif$ is too small. If cracks with small $MaxDif$ are always small, it is considered that their size is more related to the process of demosaicing than to the size of the cracks they are representing. Conversely, if there is an important difference between the *LI* of a crack and the background, the size of the cracks is very similar to the size of the valley.

Equation 6.4-4 presents the sigmoid curve that generates $\beta_{\omega LI}$. This factor depends on the difference between the smallest LI of the analysed crack and the background of that crack ($MaxDif$). It has three parameters, σDif is the standard deviation of the central differences for the full picture. Its purpose is to take into account the illumination of the picture and standardize $MaxDif$ so all the pictures of a set use the same parameters. The last two parameters (a and nLo) are adjusted experimentally with observed crack width and are constant for each set of pictures. The slope of the curve (a) will define the range of gradients there is from a 0% of confidence to a 100% of confidence. The offset (nLo) will establish the 50% confidence ratio.

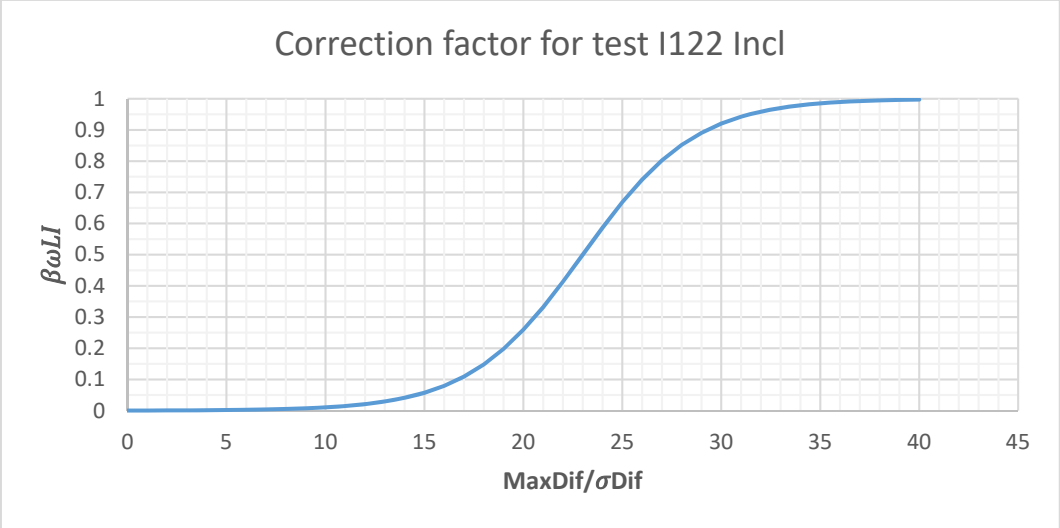

Figure 6.4-10 Curve of the correction factor used to obtain the crack width for the test I122 Incl

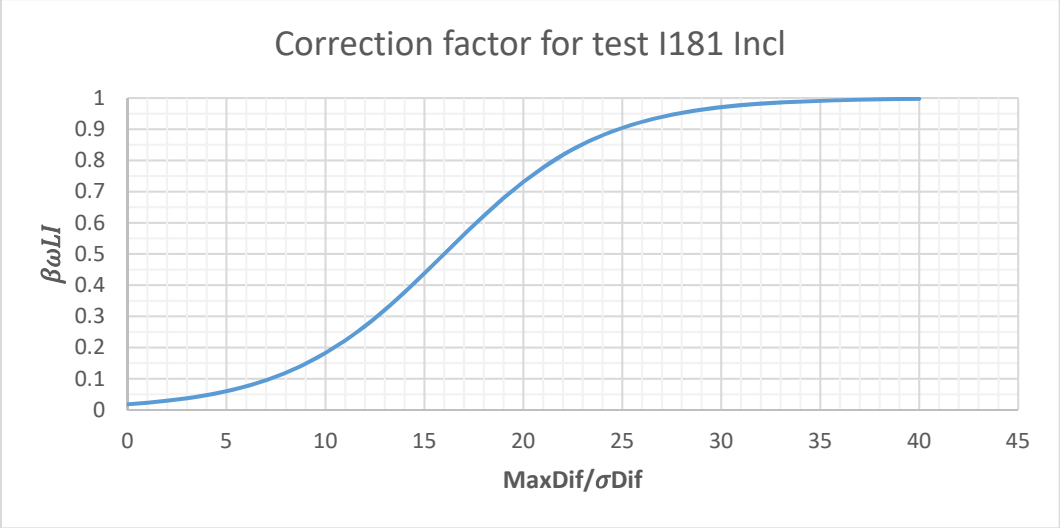

Figure 6.4-11 Curve of the correction factor used to obtain the crack width for the test I181 Incl

Figure 6.4-10 and Figure 6.4-11 show two examples of the correction factor. In the first case, the combination of the offset and the slope of the curve generated a threshold for the cracks. If the deepness of the valley is too small, the crack will not be taken into account. On the other hand, for the test I181_Incl, a wider range of cracks will be taken into account. These are two examples of the different curves used during the process of obtaining the crack width from the pictures.

At this point, the software has found the crack width in the two directions (vertical and horizontal). Using the angle of the crack, the programme weights the two crack widths. In case one of the two direction is the perpendicular to the crack, the programme only takes that one into account.

This process is performed three times for each crack: on its ends and on the centre. Then the programme computes the average value and store it.

6.5 Results

For a general visualization, the programme averages the crack width of a group of cracks and present the value on top of them.

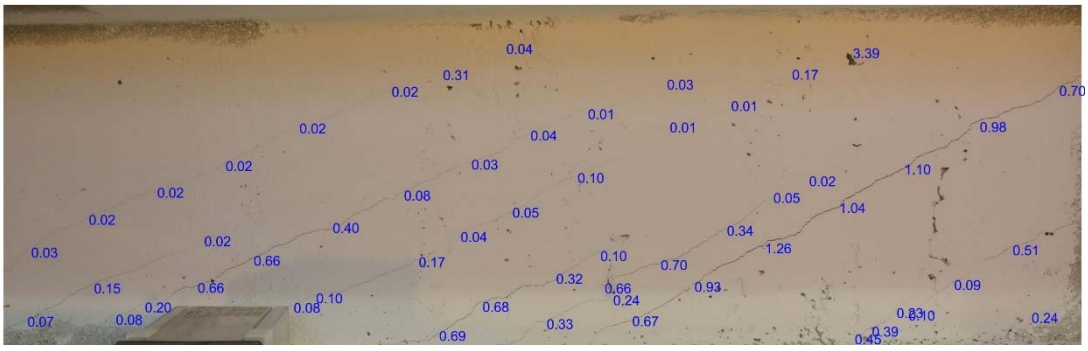

Figure 6.5-1 Picture of the I121 Rect under 315 kN

Figure 6.5-1 and Figure 6.5-2 show the results of the analysis performed with the programme to two different pictures of two different beams. The first image was taken in an early stage of the test and

the second one after several cycles. The size of the cracks is clearly different due to the process of loading and reloading.

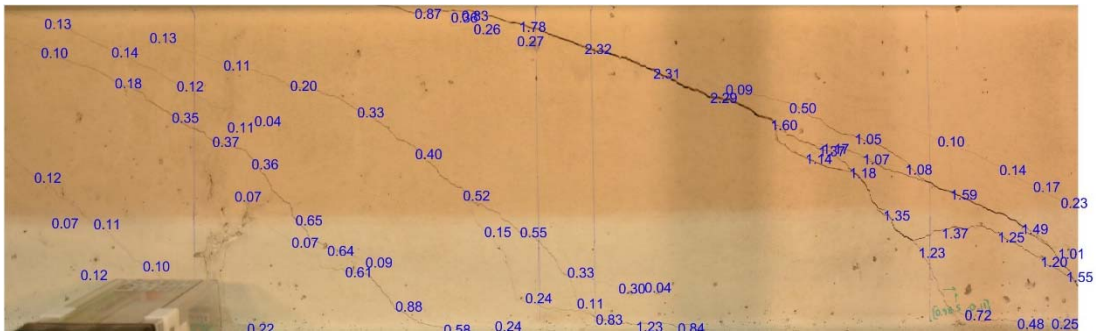

Figure 6.5-2 Picture of the I182_Incl under 326 kN

Using the information gathered through the test, the programme can establish the evolution of the average crack width or the maximum crack width. Figure 6.5-3 shows the evolution of the weighted crack width. In this case, the software takes into account the length of the cracks to average the width.

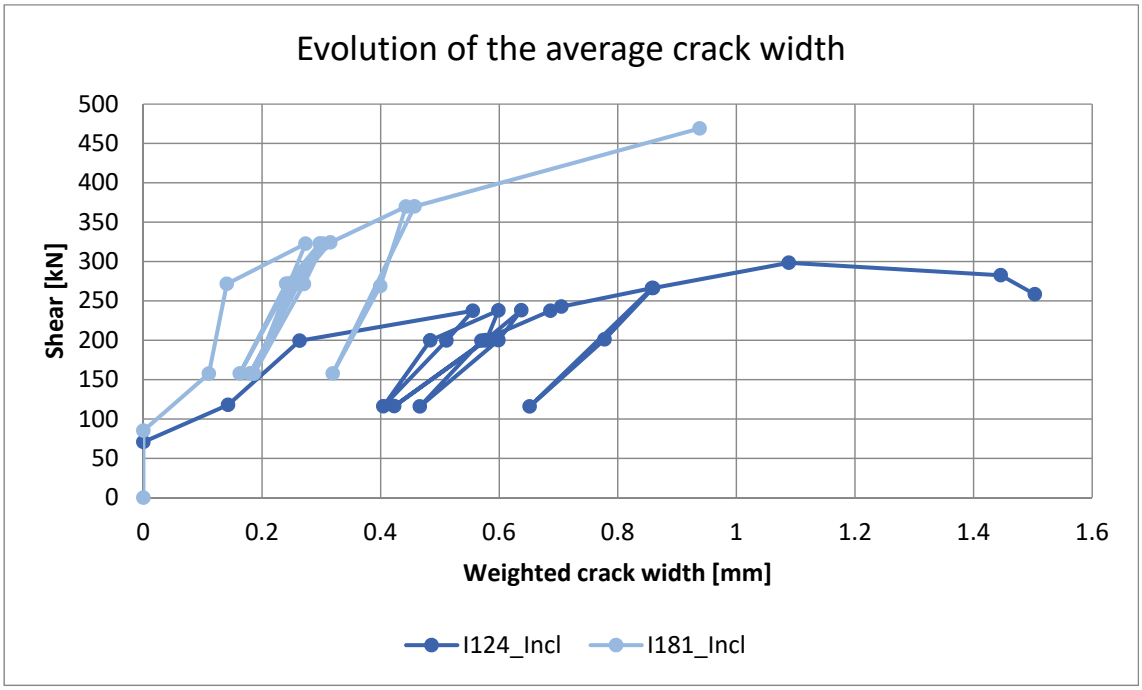

Figure 6.5-3 Evolution of the weighted crack width during different tests

6.6 Conclusions

The use of photogrammetry in structure laboratories is a new trend but has proven to have an enormous potential. The new approach of collecting data without having to glue any sensor to the specimen has provide very valuable information. Each picture contains information of many points of the specimen. The precision of the traditional methods is higher, but the target of each methodology is completely different. The photogrammetry can be used to fill he voids that the other instrumentations have left.

Applying this technique to crack pattern is an important improvement to the old techniques, based in pictures or direct observation during the test. The automation of the crack detection will allow obtaining the crack pattern faster and more efficiently. Before applying this technique, the process involved the manual detection and plotting of the cracks. This improvement has led to the possibility of tracking the whole process with hundreds of photos and analysing cycling process effortless.

The big upgrade that presents this software is the possibility of knowing the width of the cracks by analysing the pictures. All the cracks on the image are recorded and analysed. Previous to this, the only way of knowing the crack width was to do in situ measurement during the test, for all the cracks at all the positions, or place sensors at the specific place and angle where the crack will appear. This last possibility is still used in many tests, but it is only suitable if the cracking pattern is well known or forced in some manner, so the position of the crack to be monitored is known in advance. In the tests performed for this dissertation or in multitude of other tests, this pattern is unknown. For all of those tests, this new technology will allow to record the crack width and analyse its evolution during the test.

Photogrammetry is a technique that allows to know, in a simple and accurate way, the crack pattern of the shear tests. Analysing the pictures, the angle of the cracks, the crack spacing and the crack width are obtained. This information, when crossed with the load and the time when the pictures were taken, allows for an analysis of the evolution of the parameters. Performing this analysis would be impossible without photogrammetry. Tracking the evolution of crack width was the main goal of this task.

7 Conclusions and future research lines

This chapter presents the conclusions drawn from the performed research and the research lines that could be carried out in the future. The main objective of this Thesis was to analyse the behaviour of PPC beams in service and failure under shear and bending moment.

7.1 Conclusions for the four point bending moment test

Four tests were carried out to study the behaviour of PPC beams, under service loads and in failure. The beams were subjected to load cycles to study the evolution of the deflection and the stresses in PPC. An equivalent damping analysis was also carried out. From the performed experimental campaign, the following conclusions can be drawn:

- Since concrete is a heterogeneous material and its properties can vary from batch to batch, it is a high variance material. The dispersion of its properties affect the global behaviour of the concrete elements. This variability has to be taken into account when designing an experimental campaign because it could affect the relationship between the studied parameters.
- Performing two tests over the same beam was cost efficient; however, in some cases, cracking occurred in the region of the interest of the second test during the first phase. The first test affected the testing regions of the second test.
- The tension shift, due to shear-bending interaction, produced important increases of stress in the longitudinal reinforcement. Consequently, these bars yielded at lower bending moments than the theoretical value without shear forces; the reductions of the bending moments where 7.5% 20 % and 30 % less for the sections placed 1.95m 1.55m and 1.15m from the support, respectively. These important reductions allowed plastic hinge length up to 1 m. In some cases, the combination of yielded state and the prestressing forces closing the cracks in unloading branches generated compression stresses in the rebars.
- The tests with lower failure load showed higher deflection ductility ratios. Beams with less amount of active reinforcement showed larger ductility. While, the tests with less amount of conventional reinforcement showed a larger ductility. The plastic hinge length is larger in the tests with higher amount of prestress reinforcement.
- The increase of stress and strain in the rebars, due to the cycling loading process, has to be taken into account to design PPC elements and to calculate the crack width. The strain gauges, placed between the two load points, recorded differences with the predicted values of 29%,

7% and 2% in average for the quasi-permanent, frequent and characteristic load levels, respectively. This difference is due to the cracking of the section and the degradation of the cracks. The differences were more important in the tests with 4 strands. There were also stress differences between the loading and unloading branches. The lower bond capacity of prestressing strands could generate a larger difference between the experimental results and the predicted stresses.

- The fasts cycles were performed around a specific load level and showed the evolution of the stresses with smaller changes in the external force. If the stress of the strain gauges was under 140 MPa, the stress decreased. If the stress was over 250 MPa, the stress increase with the cycling load process.
- The deflection of the midspan has a similar behaviour than the reinforcement stress. There was an increase of deflection during the slow cycles. In the quasi-permanent load level, the increase was 3mm and reduced to 2.3mm in the frequent level. Important differences were observed between the loading and unloading branches at frequent level. The beams with higher amount of equivalent reinforcement showed smaller differences between branches, the higher prestress force kept the behaviour stable between both branches.
- In the fast cycles centred in the quasi-permanent load level, the deflection at midspan decreased and in frequent level the deflections increased. In all the cases, the tests with smaller amount of prestressing strands had larger differences between the deflection during the loading and unloading branches.
- The range of equivalent damping, computed after the energy dissipated in a load cycle, was in the range of 3.5% and 11.2%, with the beams with higher amount of reinforcement having lower equivalent damping.

7.2 Conclusion for the shear tests

Twelve beams were tested to study the shear behaviour of PPC at service and failure. The three main parameters of study were the web width, the prestress reinforcement the ratio and the amount of stirrups. A new model to compute the shear crack width was proposed and compared with the experimental information obtained from a new photogrammetric tool developed for this study. A new formulation for $\cot\theta$ in service and failure was also presented. From the comparison between experimental and theoretical shear failure strength, the following conclusions were drawn:

- Half of the beams showed a failure mode with splitting of the compression chord, the rest failed on the web, even if it was not predicted by the models. The Compression Chord Capacity Model (CCCM) showed the best accuracy predicting the shear resistance of the beams with an average ratio between the experimental and the theoretical ultimate shear force resistance of 1.0 and a standard deviation of 5.4%. All the other formulations underestimate que strength of the beams.
- The EC-2 had the worst results because it does not take into account the concrete contribution to the shear strength. The EHE-08 does not consider the T shape of the beam underestimating the concrete resistance. The ACI 318-11 does not take into account properly the stresses due to prestressing and to the interaction with the bending moment.

From the analysis of the experimental results, the following conclusions were drawn:

- Sensors had to be placed at several levels of the stirrups in order to capture local strain values in the transversal reinforcement. The strain in the reinforcement is crack dependant, with very important variation in the distribution along the stirrup and peaks of strains in the cracks. A correct protection of the strain gauges is very important to assure readings can be obtained during the entire test.
- The use of new technologies, as photogrammetry, can provide a very important improvement in the measurements obtained during the tests. Photogrammetry allows collecting information from large areas of the test, reducing the possibilities of missing information due to the lack of sensors or unexpected behaviour. A very important feature due to the cost of the experiments.
- The tests with 180 mm of web width showed a more brittle failure than the beams with 120 mm of web width. The ductility for those beams was 1.55. For the remaining tests, the ductility was 1.67. With an average ductility of 1.63, this ductility is clearly lower than the average ductility of 3.1 from the bending moment tests.
- The $\cot\theta$ of the shear cracks angle at maximum load was between 2 and 2.5. A linear relationship between the $\cot\theta$, the stress ratio $\left(SR = \frac{P/A_c}{f_{ct}}\right)$ and the transversal reinforcement (ρ_{st}) was established. The $\cot\theta$ increases with the RS but decreases with ρ_{st}. The influence of the parameter ρ_{st} is more relevant than the stress ratio (SR). For the maximum load, the amount of transversal reinforcement is more relevant than the prestressing force. The values of $\cot\theta$ used by the CCCM are always 10% lower than the experimental results.
- The cracks observed in the tests always showed two branches. The bottom branch had a steeper angle than the top branch. The cracks were not distributed evenly on the web; hence, the crack spacing was not uniform. Once the cracks were formed, during the first loading branch, their angle did no change for the remaining of the service part of the test. In the final stages of the test, some new cracks could appear and some of these cracks generated failure.
- During service, the angle of the cracks was constant and the $\cot\theta$ was between 1.5 and 2.4. In service both parameters, SR and ρ_{st}, had the same influence on the angle of the cracks. The behaviour is the same as in failure but the influence of RS has doubled. The maximum $\cot\theta$ occurred always at failure. The average increase of $\cot\theta$ was 17.8%. The beams of tests 120 Rect showed an increase of $\cot\theta$ of 9.6%, the 120 Incl of 13.2% and the tests with a web width of 180mm reached an increase of 28.8%.
- After the first loading ramp, the crack pattern stabilized. The average crack spacing did not change during the rest of the service cycles. In the final stages of the tests, the spacing decreased. The average distance between cracks in service was between 60 and 80 mm. When only top 5% of the observed spacing is taken into account, the range goes from 100 to 250mm. In this case, the tests with higher stirrup spacing have larger crack spacing. Moreover, the tests with stirrup spacing of 150mm had crack spacing between 100 and 150mm. The range of spacing for the tests with 250mm stirrups spacing was between 150 to 250mm. When the horizontal spacing was observed, the beams with stirrups spacing also had crack spacing under 150mm.

- Even at service, the stirrups suffered important strains and yielded. The variation of strains in a stirrup could be very important and localized, only affecting one of the strain gauges. Therefore, all the elongation was concentrated on a single part of the stirrup.
- During the cycling load process, the strain during the holds were analysed. Important differences were observed between the behaviour of yielded and non-yielded parts of the stirrups in the holds of the valleys (lower part of the cycles). On one hand, for non-yielded parts, the stress and strain of the holds increased after each cycle. On the other hand, in yielded parts during the valley holds, the strain increased while the stress decreased. This was explained because the strains during unloading increased due to successive yielding and unloading of the stirrup. In this scenario, the unloaded stress in successive cycles may be decreasing due to the effect of the prestress that tends to compress the stirrups and the cracks have been weakened and wider.
- At service, the beams with lower amount of stirrups showed higher shear crack width and the beams with higher prestressing stress had higher shear crack width. It was also observed, when comparing the cracks width in the valleys and peaks (Figure 5.3-29), that the crack width size and the range of it was independent of the shear load. While, the size of the cracks determined the range between peak and valley crack width.
- For the same service load levels, the shear crack width increased if the beams had a lower amount of stirrups. In the same way, beams with higher amount of prestressing steel had wider shear cracks. This was because, for beams with 4 strands the angle of tensile stresses is vertical, therefore parallel to the stirrups. Conversely, with less prestress the angle decreases and the tensile stresses had to be resisted by other effects, such as tension stiffening.
- It was also observed, that the range of crack width, between the peaks and valleys of the cycles, was independent of the shear force and depended on the crack width. Cracks with a larger crack width at service showed wider ranges of width between peaks and valleys of the cycles independently of the shear load.
- The ratio between the maximum crack of a picture and the average crack width was performed for all the pictures. All the pictures of the same test had a very similar ratio. The average ratio between all the tests was 7 with a standard deviation of 3.44.
- A new approach to calculate the average shear crack width at service was presented. The formulation takes into account the shear resistance of the stirrups to compute their strain (Equation 5.3-4). The formulation introduces a statistical factor, calculated from the crack width experimentally obtained (Equation 5.3-8).
- The ratio between the observed crack width and the proposed model was log-normally distributed. The statistical factor β related the observed crack width (from the software) with the crack width predicted by the proposed model. The average β, taking into account all the service pictures, was 1.33 and the β representing the percentile 90% was 2.86. When the pictures taken in quasi-permanent level were taken out, the average β was 1.22 with a 90% percentile of 2.45. Hence, for verification purposes of the shear crack width using the proposed model, a statistical factor of $\beta = 2.5$ is recommended.
- To obtain β, the cotθ was directly taken from the pictures. In case, the formulation has to be used without this information, the cotθ for service presented in Equation 5.3-1 can be used.

7.3 Future research lines

With all the information gathered in this study, some new lines of development have been raised.

- Perform a deeper statistical analysis of the average and maximal shear crack width to obtain confidence intervals and distribution function of the crack width to be able to perform risk analysis.
- Study of cyclic behaviour of PPC under fatigue loads (strains, deflection and stiffness) and seismic events (ductility and damping).
- Analyse widdle the cotθ in service and failure.
- Study the use in PPC beams of materials that are less affected by corrosion, like FRP or plastic.
- Analyse the use ultra high performance fibre reinforcement concrete (UHPFRC) in PPC beams to take advantage of the micro cracking.
- Extend the use of PPC in slabs and the influence of the 2D stresses.
- Analyse of PPC in continuous beams is been analysed by Noemi Duarte in her PhD study.

References

AASHTO (2010) *LRFD Bridge Design Specifications*. 5th edn. Washington, D. C.: American Association of State Highway and Transportation Officials.

Abeles, P. W. (1940) 'Saving Reinforcement by Prestressing', *Concrete and Constructional Engineering*, 35(3).

Abeles, P. W. (1945) 'Fully and Partially Prestressed Reinforced Concrete', *ACI Journal*, Proceeding(Jan), pp. 181–224.

ACI-ASCE Committee 423 (2000) *Report on Partially Prestressed Concrete ACI 423.5R-99*, *American Concrete Institute*.

ACI Committee 318 (2008) *Building Code Requirements for Structural Concrete (ACI 318- 08) and Commentary*. Edited by American Concrete Institute. MI: Farmington Hills.

Bachmann, H. (1984) 'Design of partially prestressed concrete structures based on swiss experiences', *PCI Journal*, 29(July-August), pp. 84–105.

Bairán, J. *et al.* (2014) 'Control de la fisuracion a cortante y flexión mediante pretensado parcial', in *VI Congreso de ACHE*, pp. 1–10.

Bairán, J. and Marí, A. (2006a) 'Coupled model for the non-linear analysis of anisotropic sections subjected to general 3D loading. Part 1: Theoretical formulation', *Computers and Structures*. Pergamon, 84(31–32), pp. 2254–2263. doi: 10.1016/J.COMPSTRUC.2006.08.036.

Bairán, J. and Marí, A. (2006b) 'Coupled model for the non-linear analysis of anisotropic sections subjected to general 3D loading. Part 2: Implementation and validation', *Computers and Structures*. Pergamon, 84(31–32), pp. 2264–2276. doi: 10.1016/j.compstruc.2006.08.036.

Bairán, J. and Marí, A. (2011) 'Método para el dimensionamiento de secciones parcialmente pretensadas con fisuración controlada o fatiga', *V Congreso ACHE*.

Bairán, J., Marí, A. and Duarte, N. (2011) 'Método para el dimensionamiento de secciones parcialmente pretensadas con fisuración controlada o fatiga', in *V Congreso ACHE*. Barcelona.

Bairán, J., Marí, A. and Duarte, N. (2012) 'Direct optimal design of partially prestressed concrete for controlled cracking or fatigue', in *fib Symposium*.

Bhide, S. B. and Collins, M. P. (1989) 'Influence of axial tension on the shear capacity of reinforced concrete members', *Structural Journal*, 86(5), pp. 570–581.

Casas, J. R. and Crespo-Minguillon, C. (1998) 'Probabilistic response of prestressed concrete bridges to fatigue', *Engineering Structures*, 20(11), pp. 940–947. doi: 10.1016/S0141-0296(97)00187-9.

CEB FIP (1978) *Code Modèle CEB FIP*.

Choulli, Y. (2005) *Shear Behavior of Prestressed I-Beams made with High Strength Self Compacting Concrete.*

Chowdhury, S. H. (2001) 'Crack Width Predictions of Reinforced and Partially Prestressed Concrete Beams: A Unified Formula', *Structural Engineering, Mechanics and Computation*. Elsevier Science, pp. 327–334. doi: 10.1016/B978-008043948-8/50032-1.

Cladera, A. *et al.* (2016) 'The compression chord capacity model for the shear design and assessment of reinforced and prestressed concrete beams', *Structural Concrete*, Accepted f(6), pp. 1017–1032. doi: 10.1002/suco.201500214.

Collins, M. P. and Mitchell, D. (1991) *Prestessed Concrete Structures*. Prentice Hall.

Comisión permanente del Hormigón (2008) *EHE -08 Instruccion de Hormigón Estructural*, *Ministerio de Formento*.

CSA (2010) *CSA-A23.3-04 Design of Concrete Structures, A National Standard of Canada (approved July 2007) (Reaffirmed 2010)*. Canadian Standards Association.

Darmawan, M. S. (2009) 'Service life prediction of partial prestressed concrete structures in a marine environment', in *1st Int. Conference on Rehabilitation and Maintenance in Civil Eng.*, p. 43.

Diana (2019) *Diana User's Manual*, *Diana FEA*. Available at: https://dianafea.com/manuals/d103/Diana.html.

Duro, L. *et al.* (2016) *Corrosión bajo tensión en el acero de pretensado: análisis mediante solicitación de fatiga*. Ministerio de Fomento, Centro de Publicaciones. Available at: https://books.google.es/books?id=-0ylAQAACAAJ.

Erlicher, S. (2014) 'Generic considerations on cracking based on tie experiments', in *CONCRACK 4*.

European Committee for Standardization (2004) *Eurocode 2: Design of Concrete Structures – Part 1-1: General Rules and Rules for Buildings (UNE-EN 1992-1-1)*.

European Committee for Standardization (2011) *Eurocode 2: Design of Concrete Structures – Part 1-2: General rules - Structural fire design (UNE-EN 1992-1-2)*.

Ferreira, D. (2013) *A model for the nonlinear, time-dependent and strengthening analysis of shear critical frame concrete structures*. UPC.

FIB (2010) *fib Model Code for Concrete Structures 2010*. doi: 10.1002/9783433604090.

Freyssinet, E. (1933) 'New Ideas and Methods', *Science et Industrie*, Jan.

GOM (2019) 'GOM Correlate Professional User's Manual', pp. 1–127.

Grant, D. N., Blandon, C. A. and Priestley, M. J. N. (2005) 'Modelling inelastic response in direct displacement-based design'. IUSS press.

Harajli, M. H. and Naaman, A. E. (1985) 'Evaluation of the Ultimate Steel Stress in Partially Prestressed Flexural Members.', *PCI*, 30(5), pp. 54–81.

Jacobsen, L. S. (1930) 'Steady forced vibration as influenced by damping', *ASCE Journal of Structural Engineering Mechanics Division*, 52, pp. 103–116.

Japan Society of Civil Engineers (2007) *Standard specifications for concrete structures*.

Jones, E. M. C. (2015) 'Documentation for Matlab-based DIC code'. University of Illinois.

Leonhardt, F. and Walther, R. (1962) 'Shear tests on single span reinforced concrete beams with and without shear reinforcement for determining the shear bearing capacity and the upper limit of shear stress', *Deutch Committee of Reinforced concrete*, 66(151).

Lin, T. Y. and Burns, N. H. (1981) *Design of Prestressed Concrete Structures*. 3rd edn. Edited by John Wiley & Sons.

Magnel, G. (1950) 'Prototype Prestressed Beam Justifies Walnut Lane Bridge Design', *ACI Journal Proceedings*, 47(12). doi: 10.14359/11993.

Marí, A. *et al.* (2015) 'Shear-flexural strength mechanical model for the design and assessment of reinforced concrete beams', *Structure and Infrastructure Engineering*, 11(11), pp. 1399–1419. doi: 10.1080/15732479.2014.964735.

Marmo, F., Serpieri, R. and Rosati, L. (2011) 'Ultimate strength analysis of prestressed reinforced concrete sections under axial force and biaxial bending', *Computers and Structures*, 89(1–2), pp. 91–108. doi: 10.1016/j.compstruc.2010.08.005.

McCormick, N. J. and Lord, J. D. (2010) 'Practical in-situ applications of DIC for large structures', in *Applied Mechanics and Materials*, pp. 161–166. doi: 10.4028/www.scientific.net/AMM.24-25.161.

Midas (2019) *Midas Fea User's Manual*, *Midas*. Available at: http://manual.midasuser.com/en_common/fea/296/whnjs.htm.

Mörsch, E. (1909) *Concrete-Steel Construction*. Edited by McGraw-Hill.

Naaman, A. E. (1983) *Prestressed concrete analysis and design: Fundamentals*. 2nd edn, *Techno Press 3000*. 2nd edn. doi: 10.1016/0262-5075(83)90035-0.

Naaman, A. E. (1989) 'Fatigue of reinforcement in partially prestressed beams', in *Structural Materials*. ASCE, pp. 377–381.

Naaman, A. E. *et al.* (2002) 'Stresses in unbonded prestressing tendons at ultimate: Recommendation', *ACI Structural Journal*, 99(4), pp. 518–529.

Naaman, A. E. and Founas, M. (1991) 'Partially prestressed beams under random-amplitude fatigue loading', *Journal of Structural Engineering*. American Society of Civil Engineers, 117(12), pp. 3742–3761.

Nakamura, E. (2011) *Shear database for prestressed concrete members*. University of Texas at Austin.

Nakamura, E., Bayrak, O. and Avendaño, A. R. (2013) 'Shear Database for Prestressed Concrete Members', *ACI Structural Journal*, 110(6), pp. 909–918. doi: 10.14359/51686147.

Pan, B. *et al.* (2009) 'Two-dimensional digital image correlation for in-plane displacement and strain measurement: a review', *Measurement Science and Technology*. IOP Publishing, 20(6), p. 62001.

PCI (1989) *Design for Fire Resistance of Precast Prestressed Concrete*. 2nd edn. Chicago: Fib.

PCI (1992) *Design Handbook : Precast and Prestressed Concrete*. 2nd edn. Chicago.

Pisani, M. A. (2000) 'Long-term behaviour of beams prestressed with aramid fibre cables: Part 2: an approximate solution', *Engineering Structures*. Elsevier, 22(12), pp. 1651–1660. doi: 10.1016/S0141-0296(99)00108-X.

Pujol, M. (2018) *Refuerzo a cortante de estructuras de hormigón armado con laminados de polímeros*

reforzados con fibras (FRP). Verificación experimental. Edited by U. P. de Catalunya. Universitat Politècnica de Catalunya. Available at: http://hdl.handle.net/2117/121015.

Ribas, C. (2013) *Resistencia a cortante de los forjados de vigueta pretensada y bovedilla*. Universitat Politècnica de Catalunya. Available at: http://www.tdx.cat/handle/10803/130815 (Accessed: 11 September 2019).

Ritter, W. (1899) 'Die Bauweise Hennebique Schweizerische Bauzeitung', 33(February), pp. 59–61.

Rodríguez, G. (2017) *Monitorización de estructuras de hormigón mediante sensores de fibra óptica distribuida*, *UPC*. UPC. Available at: https://www.tesisenred.net/handle/10803/458246.

Sanchez, L. A. (2017) *A system for crack pattern detection, characterization and diagnosis in concrete structures by means of image processing and machine learning techniques*. UPC.

Santamaria, A. J. and Arenas, J. J. (1985) 'Dimensionamiento de vigas continuas de hormigón parcialmente pretensado por condiciones estrictas de seguridad frente a rotura', *Hormigón y Acero*, 154, pp. 109–116.

De Silva, S. *et al.* (2006) 'Experimental Study on Shear Cracking Behavior in I-Shaped Partially Prestressed Concrete Beams', *Japan Concrete Institute*, pp. 817–822.

De Silva, S. (2008) *Shear cracking behavior and its design methodology for prestressed reinforced concrete beams*.

Simulia (2019) *Abaqus 6.13 Docmentation*, *Simulia*. Available at: http://dsk.ippt.pan.pl/docs/abaqus/v6.13/index.html.

Tung, S.-H., Shih, M.-H. and Sung, W.-P. (2008) 'Development of digital image correlation method to analyse crack variations of masonry wall', *Sadhana*. Springer, 33(6), pp. 767–779.

Tureyen, A. K. (2003) *Influence of Longitudinal Reinforcement Type on Shear Strength of Reinforced Concrete Beams without Transverse Reinforcement*. Purdue University.

Tureyen, A. K. and Frosch, R. J. (2003) 'Concrete Shear Strength: Another Perspective', *ACI Structural Journal*, 100(5), pp. 609–615.

Tureyen, A. K., Wolf, T. S. and Frosch, R. J. (2006) 'Shear strength of reinforced concrete T-beams without transverse reinforcement', *ACI Structural Journal*, 103(5), pp. 656–663.

Witchukreangkrai, E. *et al.* (2006) 'Evaluation of Shear Crack Width in Partially Prestressed Concrete Members', *Proceedings of JCI*, 28(1), pp. 823–828.

Wolf, T. S. and Frosch, R. J. (2007) 'Shear design of prestressed concrete: A unified approach', *Journal of Structural Engineering*, 133(11), pp. 1512–1519. doi: 10.1061/(ASCE)0733-9445(2007)133:11(1512).

Yoon, Y. S., Cook, W. D. and Mitchell, D. (1996) 'Minimum shear reinforcement in normal, medium, and high-strength concrete beams', *ACI Structural Journal*, 93(5), pp. 576–584.

Zakaria, M. *et al.* (2009) 'Experimental investigation on shear cracking behavior in reinforced concrete beams with shear reinforcement', *Journal of Advanced Concrete Technology*. Japan Concrete Institute, 7(1), pp. 79–96.

Zararis, I. P. I. P., Karaveziroglou, M. K. M. K. and Zararis, P. D. (2006) 'Shear strength of reinforced concrete T-beams', *ACI Structural Journal*, 103((5)), pp. 693–700. doi: 10.14359/51686733.